January 2009

Contributions To The Methodology Of Electrocardiographic Imaging (ECGI) And Application Of ECGI To Study Mechanisms Of Atrial Arrhythmia, Post Myocardial Infarction Electrophysiological Substrate, And Ventricular Tachycardia In Patients

Yong Wang
Washington University in St. Louis

WASHINGTON UNIVERSITY

School of Engineering and Applied Science

Department of Biomedical Engineering

Dissertation Examination Committee:

Yoram Rudy, Chair
Igor Efimov
Mitchell N. Faddis
Pamela K. Woodard
Arye Nehorai
Richard B. Schuessler

CONTRIBUTIONS TO THE METHODOLOGY OF ELECTROCARDIOGRAPHIC IMAGING (ECGI) AND APPLICATION OF ECGI TO STUDY MECHANISMS OF ATRIAL ARRHYTHMIA, POST MYOCARDIAL INFARCTION ELECTROPHYSIOLOGICAL SUBSTRATE, AND VENTRICULAR TACHYCARDIA IN PATIENTS

by

Yong Wang

A dissertation presented to the
Graduate school of Arts and Sciences
of Washington University in
partial fulfillment of the
requirements for the degree
of Doctor of Philosophy

August 2009

Saint Louis, Missouri

Dedication

To my family

For their love and support.

Abstract

ABSTRACT OF THE DISSERTATION

Contributions to the Methodology of Electrocardiographic Imaging (ECGI) and Application of ECGI to Study Mechanisms of Atrial Arrhythmia, Post Myocardial Infarction Electrophysiological Substrate, and Ventricular Tachycardia in Patients

by

Yong Wang

Doctor of Philosophy in Biomedical Engineering

Washington University in St. Louis, 2009

Professor Yoram Rudy, Chair

Electrocardiographic Imaging (ECGI) is a noninvasive imaging modality for cardiac electrophysiology and arrhythmia. ECGI reconstructs epicardial potentials, electrograms and isochrones from body-surface electrocardiograms combined with heart-torso geometry from computed tomography (CT). The application of a new meshless method, the Method of Fundamental Solutions (MFS) is introduced to ECGI with the following major advantages: 1. Elimination of meshing and manual mesh optimization processes, thereby enhancing automation and speeding the ECGI procedure. 2. Elimination of

mesh-induced artifacts. 3. Simpler implementation. These properties of MFS enhance the practical application of ECGI as a clinical diagnostic tool.

The current ECGI mode of operation is offline with generation of epicardial potential maps delayed to data acquisition. A real time ECGI procedure is proposed, by which the epicardial potentials can be reconstructed while the body surface potential data are acquired (< 1msec/frame) during a clinical procedure. This development enables real-time monitoring, diagnosis, and interactive guidance of intervention for arrhythmia therapy.

ECGI is applied to map noninvasively the electrophysiological substrate in eight post-MI patients during sinus rhythm (SR). Contrast-enhanced MRI (ceMRI) is conducted to determine anatomical scar. ECGI imaged regions of electrical scar corresponded closely in location, extent, and morphology to the anatomical scars. In three patients, late diastolic potentials are imaged in the scar epicardial border zone during SR. Scar-related ventricular tachycardia (VT) in two patients are imaged, showing the VT activation sequence in relation to the abnormal electrophysiological substrate. ECGI imaging the substrate in a beat-by-beat fashion could potentially help in noninvasive risk stratification for post-MI arrhythmias and facilitate substrate-based catheter ablation of these arrhythmias.

ECGI is applied to eleven consecutive patients referred for VT catheter ablation procedure. ECGI is performed either before (8 patients) or during (3 patients) the ablation procedure. Blinded ECGI and invasive electrophysiology (EP) study results are compared. Over a wide range of VT types and locations, ECGI results are consistent with EP data regarding localization of the arrhythmia origin (including myocardial depth) and mechanism (focal, reentrant, fascicular). ECGI also provides mechanistic electrophysiological insights, relating arrhythmia patterns to the myocardial substrate. The study shows ECGI has unique potential clinical advantages, especially for hemodynamically intolerant VT or VT that is difficult to induce. Because it provides local cardiac information, ECGI may aid in better understanding of mechanisms of ventricular arrhythmia. Further prospective trials of ECGI with clinical endpoints are warranted.

Many mechanisms for the initiation and perpetuation of atrial fibrillation (AF) have been demonstrated over the last several decades. The tools to study these mechanisms in humans have limitations, the most common being invasiveness of a mapping procedure. In this paper, we present simultaneous noninvasive biatrial epicardial activation sequences of AF in humans, obtained using the Electrocardiographic Imaging (ECGI) system, and analyzed in terms of mechanisms and complexity of activation patterns. We performed ECGI in 36 patients with a diagnosis of AF. To determine ECGI atrial accuracy, atrial pacing from different sites was performed in six patients (37 pacing

events), and ECGI was compared to registered CARTO images. Then, ECGI was performed on all 36 patients during AF and ECGI epicardial maps were analyzed for mechanisms and complexity. ECGI noninvasively imaged the low-amplitude signals of AF in a wide range of patients (97% procedural success). The spatial accuracy in determining initiation sites as simulated by atrial pacing was ~ 6mm. ECGI imaged many activation patterns of AF, most commonly multiple wavelets (92%), with pulmonary vein (69%) and non-pulmonary vein (62%) trigger sites. Rotor activity was seen rarely (15%). AF complexity increased with longer clinical history of AF, though the degree of complexity of nonparoxysmal AF varied and overlapped. ECGI offers a way to identify unique epicardial activation patterns of AF in a patient-specific manner. The results are consistent with contemporary animal models of AF mechanisms and highlight the coexistence of a variety of mechanisms among patients.

Acknowledgements

With a grateful heart, I am writing this acknowledgment. When I was looking back the past seven years, I found that I had been blessed with the best luck of the world and received so much support and help from so many wonderful people.

I have the beginner's luck to start my career under the guidance and mentoring of Dr. Yoram Rudy. He accepted me and guided me through years of adventure on exploring the ECGI world. Without his enlightening guidance, consistent support, and unreserved trust, I would not have been able to overcome the obstacles I encountered, and would not have been able to comprehend and appreciate the beauty of science.

I am lucky that I joined the productive team and have wonderful colleagues. I want to give my special thanks to our inverse group colleagues: Ping Jia, Charu Ramanathan, Raja Ghanem, Paul Kyu, Phillip S. Cuculich, Subham Ghosh, Junjie Zhang and Ramya Vijayakumar. Their expert experience with the technology and the mapping system has been of tremendous help to the completion of the studies. I'd also like to acknowledge all my colleagues in the cell groups: Tom Hund, Greg Faber, Jon Silva, Keith Decker, Tom O'Hara, Leonid Livshitz and Ali Nekouzadeh for creating a very enjoyable, inspiring research environment. Also many thanks to Li Li, Jennifer Godwin-Wyer and Kimberly

Smith for their excellent assistances in various administrative and technical issues.

I am grateful to all the patients who participated in my studies. The experiments could not have been conducted smoothly without their coordination and understanding. Behind every successful experiment, there were many people who helped me to recruit patients and conduct studies. I'd like to say thank you to: Scott Marrus, Ralph J. Damiano, Marci S. Bailey and Timothy Street. Thank you all for your great help!

I am lucky that I have such a supportive thesis committee composing of top scientists on cardiac electrophysiology and engineering: Dr. Igor Efimov, Dr. Mitchell N. Faddis, Dr. Pamela K. Woodard, Dr. Arye Nehorai and Dr. Richard B. Schuessler. I sincerely thank them for their enlightening comments, suggestions and help.

I am lucky that I have a happy family, where I can always find support, understanding, encouragement, and hope. I thank my parents and my in-laws for their love, support, and understanding. I don't know how to express my appreciation to my wife, Qing Wang, for her love, help and sacrifice in the past seven years. I can only say I'm really lucky to marry her. I think I am a really lucky guy. I sincerely appreciate what I have received from all these wonderful people.

为学日益 为道日损

损之又损 以至于无为
无为而无不为

取天下常以无事
及其有事 不足以取天下

《道德经》

In the pursuit of knowledge, every day something is learned.
In the practice of the Tao*, every day some desire is dropped.

Drop and again drop until non-action is achieved.
When nothing is done on purpose, nothing is left undone.

The world is possessed by letting things take their natural courses.
It cannot be mastered by interfering or manipulating.

《Tao De Jing》

* Tao is the essential nature of human being.

Table of Contents

List of Tables

List of Figures

Chapter 1 Introduction

Cardiac electrical activity is a complex process that is both time dependent and spatially distributed throughout the heart. Conventional ECG and multi-electrode body-surface potential mapping (BSPM) only record a very low resolution projection of this activity on the torso surface. Therefore, locations of cardiac events (e.g. activation initiation sites) and spatial details (e.g. number and locations of activation fronts) cannot be determined from such measurements. As a result, invasive electrophysiological mapping from the epicardial and endocardial surfaces of the heart has become an important experimental tool in the study of cardiac excitation. It has also become an essential clinical tool for diagnosis of arrhythmias, guidance of intervention (e.g., ablation) and evaluation of treatment outcome.

Electrocardiographic imaging (ECGI)[1,2] is a novel, noninvasive tool for imaging cardiac arrhythmia and defining electrophysiologic properties. ECGI combines multi-electrode body surface ECG recordings with three-dimensional anatomical heart-torso imaging to reconstruct an epicardial electroanatomical map. ECGI images can be presented as epicardial potential maps, electrograms, isochrones (activation sequences), or repolarization patterns during activation and repolarization of the heart. Unlike invasive electrophysiological mapping, the ECGI technique is completely noninvasive and only requires a single beat to reconstruct the entire epicardial electrical activity. This makes

ECGI a potentially useful tool for noninvasive evaluation of cardiac electrophysiology in patients.

Prior to the recent development of noninvasive ECGI in our laboratory, studies involved invasive cardiac mapping and were, consequently, very limited. With the successful and extensive application and validation of ECGI in animal modes[3-9] and humans studies[2,11-19], we can now begin to study noninvasively the electrophysiology of the human heart in different clinical settings.

1.1 ECGI Theory

The torso volume conductor between the surface of the heart and torso can be treated as a homogenous, passive volume, which greatly simplifies the complex electrocardiography problem into an electrostatic field problem. Because there is no primary electrical source in the volume conductor enclosed by torso surface and epicardial surface, the Laplace equation holds in the volume domain.

The distribution of potentials on the torso can be known through the body surface mapping procedure. The derivative of torso potentials in the normal direction is zero since the normal component of current at the torso surface is zero (the torso is in air-an insulating medium that does not support current flow). However we do not know anything on the epicardial surface, which is the goal of the whole inverse computation in

electrocardiography. This constitutes the following Cauchy problem for Laplace's equation:

$$\nabla^2 u(x) = 0, \quad x \in \Omega \tag{1-1}$$

with the following boundary conditions:

(i) Dirichlet condition: $u(x) = u_T(x), \quad x \in \Gamma_T$ on the torso surface

(ii) Neumann condition: $\frac{\partial u(x)}{\partial n} = c_T(x), \quad x \in \Gamma_T$ on the torso surface

where Ω is the 3D volume domain between the heart's epicardial surface, Γ_E, and the torso surface, Γ_T, The potential distribution on epicardial surface Γ_E is sought. The above system of partial differential equations fully describes the electrostatic field in the electrocardiography inverse problem. There is a unique solution to this Cauchy problem, however the problem is ill-posed.

1.2 Computational Implementation

In the inverse problem of electrocardiography, the goal is to compute the electric potential distribution on the surface of the heart (epicardium) from potential data measured on the torso. The relationship between the potential distributions on the surface of the body and the surface of the heart is mathematically described by the Cauchy problem. The numerical solution for the ECGI inverse computation requires two steps. The first step is the construction of a mathematical expression describing the potential field throughout the torso volume conductor, particularly on the body surface, as a function of epicardial potential data (the forward problem). The second step is the

inversion of that expression to enable the reconstruction of epicardial potentials from the measured torso potential data (the inverse problem).

1.2.1 The Forward Model

To solve the Cauchy problem for Laplace operator in an irregular geometry such as the human heart-torso configuration, it is necessary to utilize numerical methods. There are many kinds of popular numerical methods available: Finite Element Method (FEM), Boundary Element Method (BEM) and so on. Each of these methods has its own advantages and suitable for different kinds of problems.

In the case of computing epicardial surface potential in ECGI, BEM is an excellent choice because only the boundary is discretized into elements (mesh) instead of the whole 3D volume domain, as in FEM (see the following figure for torso mesh and heart surface mesh). Therefore, it involves fewer nodes and mesh connections than does FEM requiring less overhead computationto assemble the mesh, and the mesh can be adapted more easily to different geometries. After applying BEM, the Laplace Equation is discretized into the following form:

$$V_t = A * V_e \tag{1-2}$$

where V_t is the vector of the torso potential, V_e is the vector of the heart surface potential, and A matrix is the transfer matrix between heart and torso that depends only on the geometry.

1.2.2 The Inverse Solution

Although the solution to the Cauchy problem is unique, because the inverse problem is ill-posed, one cannot simply invert the A matrix to compute V_e from V_t. Even low-level noise in the measured data can cause unbounded error in the solution. That is to say, the solution does not depend continuously on the data. Techniques of regularization must therefore be used to minimize the effects of such error by imposing constraints on the solution. Several classes of techniques are available to regularize ill-posed problems. The Tikhonov regularization scheme, which is a type of single parameter minimization method, is used to find the V_e in ECGI.

$$\min_{V_e}\{\|V_t - AV_e\|^2 + t\|V_e\|^2\} \qquad (1\text{-}3)$$

The composite residual and smoothing operator technique (CRESO)[24] is used in the Tikhonov scheme to automatically select the regularization parameter " t ". Temporal and spatial information known *a priori* can also be added into Tikhonov regularization scheme to improve solution accuracy. General Minimal Residual Method (GMRES)[25] is also adopted in our ECGI computation packages as an extension of the minimal residual method (MINRES) from symmetric systems to asymmetric systems.

1.3 Experimental Validation

In the work of previous generations of students in our laboratory, ECGI method was extensively validated using "torso tank" experiment setup[3-9]. The torso-tank experimental setup, developed by Taccardi and co-workers, was used for detailed and rigorous evaluation of our ECGI methodology. This experimental setup consists of a tank in the

shape of a 10-year-old boy's torso filled with an electrolytic solution, with a perfused dog heart (connect to the circulation of a support dog) suspended in the correct anatomical position within the torso volume. The torso tank system consisted of 384 torso surface electrodes and 384 rods projecting radially from the torso surface toward the center of the tank. Each radially projecting rod had an electrode at its tip and multiple electrodes along its length within the torso volume, for a total of 918 rod electrodes. The rods at the level of the heart were pushed in so the tips created an epicardial envelope about 1cm from the epicardial surface.

Based on the torso tank experimental setup, ECGI has been demonstrated to have the capability of reconstructing epicardial potentials, electrograms and isochrones during pacing and determining pacing site locations with better than 10mm accuracy[26,27]. ECGI could reconstruct potential and electrogram characteristics associated with abnormal EP substrates[28]. The pathway and features of reentrant ventricular tachycardia (VT) were faithfully reconstructed using ECGI[8,29]. Repolarization abnormalities were also detected[9].

1.4 ECGI Applications in Human

1.4.1 Body Surface Potential Mapping System

We recently established a new active-electrode mapping system (Active Two System, Biosemi, Netherland), which is a highly integrated system, designed to be a stand-alone and portable unit with data acquisition and data processing capabilities. Noise levels as

low as the thermal noise of the electrode impedance (which is the theoretical minimum) can be achieved by the active design. The electrodes are made from conductive carbon to prevent interference with X-ray fluoroscopy when the system is used in the catheterizaion laboratory during an EP study. These flat electrodes are encapsulated in strips to facilitate application. The Active Two System is fully portable (total weight about 5kg) and operable by a single person. It contains the following components: 1) carbon electrodes in strips 2) A/D converter for 256 channels 3) USB2 receiver 4) high performance laptop with 256 parallel channel data acquisition Labview software 5) battery box with chargers.

1.4.2 Computerized Tomography Imaging

The CT scan is ECG gated at 20% (on) and 70% (off) of the RR intervals. Since the active electrodes are made from X-ray transparent carbon material, CT markers are attached onto each electrode to mark the electrodes location in the CT images. We scan caudal to cranial (foot to head). Most respiratory motion occurs in the lower chest, so patients can hold their breath as long as they can, and then do a slow release. The radiation dose is about 1.8 rad. The slice thickness is 3mm.

1.4.3 Procedure for ECGI Reconstruction

By combining a multi-electrode body surface ECG mapping data with a CT scan of the heart-torso geometry, CADIS (the core ECGI software) can reconstructs an epicardial electro-anatomical map noninvasively. The ECGI images can be presented as epicardial potential maps, electrograms, isochrones or repolarization maps during activation and

repolarization. The complete ECGI procedure is shown in the Figure 1-1. Elastic belts are used to hold the electrodes to the subjects' torso surface. The subject holds breath or keeps shallow breath during the procedure to minimize the affect of respiration.

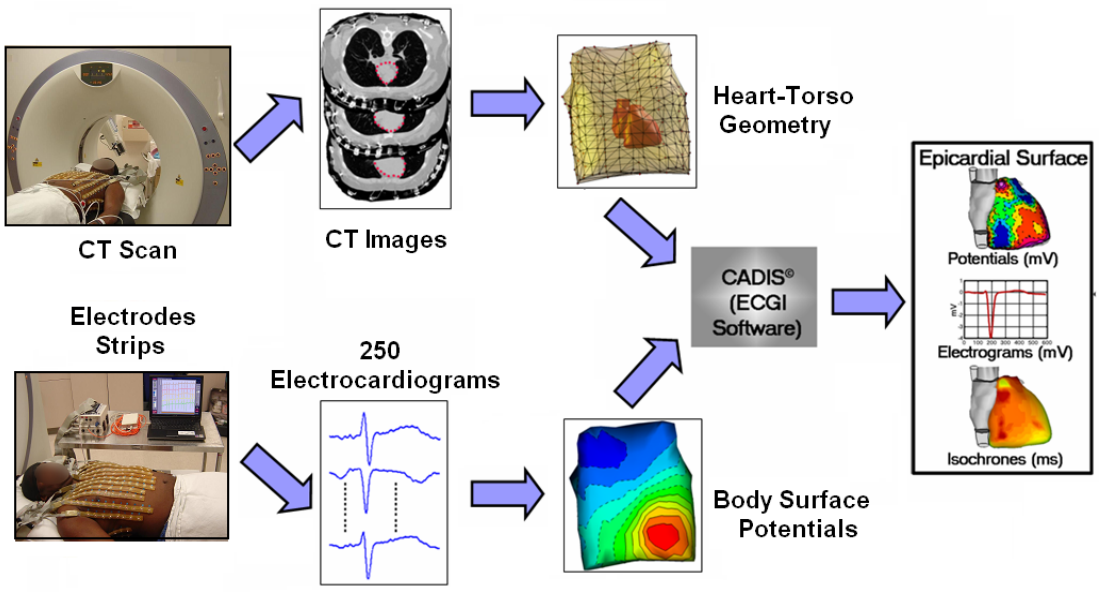

Figure 1 (Figure 1-1): ECGI Procedure.

1.5 Dissertation Objectives and Organization

In this thesis, there are two major objectives related to further development and improvement of the ECGI system: 1)development of a new forward computing model based on meshless numerical method to avoid the limitations of mesh based numerical method (such as BEM, FEM;), 2) design and implement a new ECGI scheme to achieve real time ECGI computation, which can enhance ECGI system's clinical applications. There are three other major objectives related to the clinical evaluation and applications of ECGI to different groups of adult patients: 1) patients with Post-MI, 2) patients with ventricular arrhythmias, and 3) patients with atrial arrhythmias.

The dissertation is organized into following 8 Chapters

Chapter 1: Introduction.

Chapter 2: Application of Method of Fundamental Solutions to Potential-based Inverse Electrocardiography.

Chapter 3: Real Time Electrocardiographic Imaging.

Chapter 4: Characterization of EP substrate in Post-Myocardial Infarction Patients using Noninvasive Electrocardiographic Imaging (ECGI).

Chapter 5: Insights from Noninvasive Electrocardiographic Imaging (ECGI) of Ventricular Arrhythmias in Patients Undergoing Catheter Ablation.

Chapter 6: Characterization of Epicardial Activation in Humans with Diverse AF Patterns using Noninvasive ECG imaging (ECGI).

Chapter 7: Noninvasive Electrocardiographic Imaging of Normal Human Atrial Repolarization, Ventricular Bigeminy, Focal Atrial Tachycardia after Pulmonary Vein Isolation, and Scar-Related Atypical Atrial Flutter.

Chapter 8: Conclusions and Future Work.

Chapter 2 Application of Method of Fundamental Solutions to Potential-based Inverse Electrocardiography

Abstract

Electrocardiographic Imaging (ECGI) is a noninvasive imaging modality for cardiac electrophysiology and arrhythmia. ECGI reconstructs epicardial potentials, electrograms and isochrones from body-surface electrocardiograms combined with heart-torso geometry from computed tomography (CT). The method of choice for computing epicardial potentials has been the boundary element method (BEM) which requires meshing the heart and torso surfaces and optimizing the mesh, a very time-consuming operation that requires manual editing. Moreover, it can introduce mesh-related artifacts in the reconstructed epicardial images. Here we introduce the application of a meshless method, the Method of Fundamental Solutions (MFS) to ECGI. This new approach that does not require meshing is evaluated on data from animal experiments and human studies, and compared to BEM. Results demonstrate similar accuracy, with the following advantages: 1. Elimination of meshing and manual mesh optimization processes, thereby enhancing automation and speeding the ECGI procedure. 2. Elimination of mesh-induced artifacts. 3. Elimination of complex singular integrals that must be carefully computed in BEM. 4. Simpler implementation. These properties of MFS enhance the practical application of ECGI as a clinical diagnostic tool.

2.1 Introduction

Computation of potentials on the surface of the heart from potentials measured on the body surface involves solving Laplace's equation in the source-free volume between the torso and heart surfaces. Several mathematical and computational approaches were introduced to solve this problem, known as the inverse problem of electrocardiography in terms of potentials.[25-28] Other approaches used a bi-domain model-based method to compute activation times (isochrones) on the heart surface.[29-32] Recently, both the potential-based approach (for computing epicardial potentials, electrograms, and isochrones) and the activation-time approach were applied and evaluated in human subjects.[1,10,30-40] Both methods require discretizing the heart and torso surfaces into continuous non-overlapping mesh elements, a procedure called meshing. Meshing is difficult to apply to irregular surfaces[41] and can introduce mesh-related artifacts, especially in the computation of solutions to the ill-posed[42] electrocardiographic problem, if mesh optimization is not carefully done. In our application of inverse electrocardiography, the Boundary Element Method (BEM)[43,44] was used to solve Laplace's equation.[45,46,10,47] In this approach, mesh optimization is the most time-consuming step and requires manual intervention and editing. Importantly, this formulation requires computation of complicated singular integrals that require careful handling.[48,49,50] In addition, BEM often suffers from slow convergence due to the use of low order polynomial approximations.[48,51] These difficulties with the efficient implementation of BEM led us to explore the possibility of applying a meshless method

to inverse electrocardiography, in the hope of overcoming such mesh-related problems.

Meshless methods have been applied successfully in a wide array of engineering and industrial application.[52,53] Inverse electrocardiography is a 3D Cauchy problem for the Laplace operator which has a very well behaved, analytic fundamental solution.[54] This property suggests the Method of Fundamental Solutions (MFS)[55] as the method of choice for this problem among the family of meshless methods.[56]

In this study, we formulate the use of MFS in inverse electrocardiography and evaluate its performance. We test this new method using data from animal experiments[21] and human studies,[10,35] and compare its performance to the BEM-based approach that requires meshing. Human data were processed using the potential-based method with geometrical information (heart-torso geometry) obtained noninvasively using CT imaging. All approaches to the noninvasive reconstruction of cardiac electrical activity can be referred to as cardiac electrophysiological imaging modalities. For clarity, we refer in the paper to the potential-based method employed here as electrocardiographic imaging (ECGI), its MFS version MFS ECGI, and its BEM version BEM ECGI.

2.2 Methods

2.2.1 Formulating the Method of Fundamental Solutions for ECGI

The method of fundamental solutions (MFS) has been used in various mathematical and engineering applications to compute solutions of partial differential equations (PDE).[52,53] MFS approximates the solution of a PDE by a linear combination of fundamental solutions of the governing partial differential operator,[55] which for ECGI is the Laplacian operator ∇^2. The formulation of MFS for a ∇^2 boundary value problem and Cauchy problem is described in the Appendix of this chapter; its implementation in ECGI is described below.

The objective of ECGI is to determine the electric potential on the epicardial surface of the heart noninvasively, from measurements of the electric potential on the torso surface. This constitutes a Cauchy problem for Laplace's equation:[54]

$$\nabla^2 u(x) = 0, \quad x \in \Omega \tag{2-1}$$

with the following boundary conditions:

(iii) Dirichlet condition: $u(x) = u_T(x), \quad x \in \Gamma_T$ on the torso surface

(iv) Neumann condition: $\frac{\partial u(x)}{\partial n} = c_T(x), \quad x \in \Gamma_T$ on the torso surface

where Ω is the 3D volume domain between the heart's epicardial surface Γ_E and the torso surface Γ_T as shown in Figure 2-1. $u(x)$ is the potential at location x; $u_T(x)$ and $c_T(x)$ are the potential and its normal derivative on the torso surface, respectively. The goal of ECGI is to obtain the electric potential on the heart

surface $u_E(x), \quad x \in \Gamma_E$

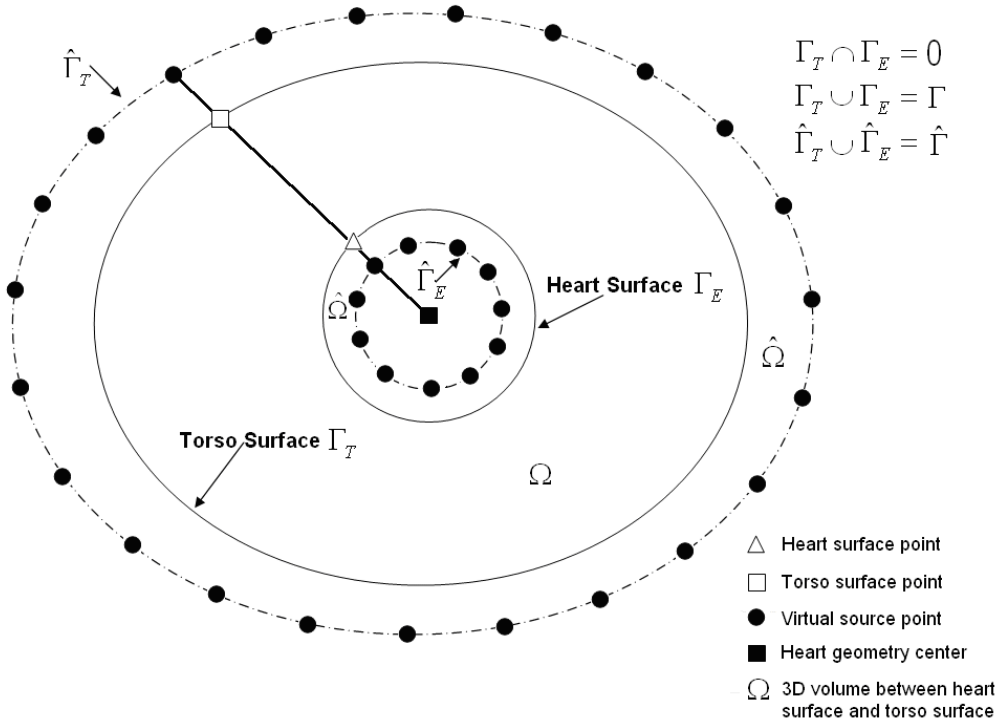

Figure 2 (Figure 2-1): A schematic showing the configuration of fictitious points for a multi-connected domain.

The dashed lines are the auxiliary surfaces that contain the fictitious points (virtual sources) marked by black circles. The filled square is the geometrical center of the "heart", the empty triangle is located on the "heart surface" and the empty square on the "torso surface", the two black circles on their connecting line at the auxiliary surfaces are the corresponding virtual source points.

MFS is an approach for solving numerically Laplace's equation. In MFS, an approximate solution is represented in the form of a linear superposition of source functions (fundamental solutions) located on a set of points (fictitious points, virtual sources) over an auxiliary surface $\hat{\Gamma}$ ($\hat{\Gamma}$ encloses the auxiliary domain $\hat{\Omega}$, which contains the actual

domain Ω as shown in Figure 2-1). As the fundamental solutions satisfy Laplace's equation everywhere except at source points, this representation satisfies Laplace's equation in the domain Ω. In addition, the specified boundary conditions are imposed at a set of boundary points (collocation points) on the domain boundary Γ. Since the fundamental solutions do not have singularities at points on the boundary Γ, standard quadrature rules can be used to approximate the surface potential and its normal gradient when computed on the boundary.[41]

As shown in the Appendix (equations (a21) and (a22)), MFS can be applied to discretize the Dirichlet and Neumann boundary conditions in equation (2-1) as:

Dirichlet condition:

$$a_0 + \sum_{j=1}^{M} a_j f(\|x_k - y_j\|) = u_T(x_k), \quad 1 \le k \le N, \quad x_k \in \Gamma_T, \quad y_j \in \hat{\Gamma} \tag{2-2}$$

Neumann condition:

$$\sum_{j=1}^{M} a_j \frac{\partial f(\|x_k - y_j\|)}{\partial n} = c_T(x_k) = 0, \quad 1 \le k \le N, \quad x_k \in \Gamma_T, \quad y_j \in \hat{\Gamma} \tag{2-3}$$

where $f(r) = \frac{1}{4\pi r}$ is the fundamental solution of Laplace's equation in 3D, $r = \|x - y\|$ is the 3D Euclidean distance between point x and point y, $\hat{n}$ is normal to the torso surface, a_0 is the constant component of $u_T(x)$ and a_j is the coefficient of a virtual source at location y_j. Note that a_0 and a_j have different units in this formulation. The conductivity of the volume is reflected in the coefficient a_j; it does not appear explicitly in the ECGI formulation when the volume of interest is homogenous. M is the

number of fictitious points. N is the number of torso surface points. Γ is the boundary of domain Ω, and $\hat{\Gamma}$ is the auxiliary boundary of the auxiliary domain $\hat{\Omega}$, which contains the domain Ω as shown in Figure 2-1.

Boundary conditions are satisfied on N torso surface points x_k. In equation (2-2) $u_T(x_k)$ is the measured body surface potential at electrode position x_k. In equation (2-3), $c_T(x_k) = 0$ because the torso is in air, an insulating medium that does not support current flow. The locations of the fictitious points y_j are configured based on the particular domain geometry, which in ECGI is a multi-connected surface in 3D, composed of the body surface and heart surface ($\Gamma = \Gamma_T \cup \Gamma_E$). Using a static configuration scheme (see Appendix), the fictitious sources are placed on two auxiliary surfaces ($\hat{\Gamma} = \hat{\Gamma}_T \cup \hat{\Gamma}_E$) which are determined by inflation/deflation of the true surfaces (torso surface and heart surface). Figure 2-1 shows the configuration of the fictitious points in a 2D representation. The fictitious boundary corresponding to the heart surface $\hat{\Gamma}_E$ is obtained by deflating the heart surface by a factor of 0.8 relative to the geometrical center of the heart. The geometrical center of the heart can be found by computing the average coordinate value of all the heart surface nodes. For the torso surface, the fictitious boundary $\hat{\Gamma}_T$ is obtained by inflating the torso surface by a factor of 1.2 relative to the geometrical center of the heart.

Expressing equations (2-2) and (2-3) in matrix form gives:

$$\hat{A}\vec{a} = \vec{b} \tag{2-4}$$

where, $\hat{A} = \begin{pmatrix} 1 & f(\|x_1 - y_1\|) & \cdots & f(\|x_1 - y_M\|) \\ \vdots & \vdots & \cdots & \vdots \\ 1 & f(\|x_N - y_1\|) & \vdots & f(\|x_N - y_M\|) \\ 0 & \dfrac{\partial f(\|x_1 - y_1\|)}{\partial n} & \cdots & \dfrac{\partial f(\|x_1 - y_M\|)}{\partial n} \\ \vdots & \vdots & \cdots & \vdots \\ 0 & \dfrac{\partial f(\|x_N - y_1\|)}{\partial n} & \cdots & \dfrac{\partial f(\|x_N - y_M\|)}{\partial n} \end{pmatrix}$, $\vec{a} = \begin{pmatrix} a_0 \\ a_1 \\ \vdots \\ a_M \end{pmatrix}$, $\vec{b} = \begin{pmatrix} u_T(x_1) \\ \vdots \\ u_T(x_N) \\ 0 \\ \vdots \\ 0 \end{pmatrix}$

Matrix $\hat{A}$ is of dimension $2N \times (M+1)$; $\vec{a}$ and $\vec{b}$ are vectors of dimensions $M+1$ and $2N$ respectively.

This matrix equation can not be solved for $\vec{a}$ without regularizaiton[42], because the matrix $\hat{A}$ is ill-conditioned and the measured body surface potential contains measurement error. The Tikhonov regularization method[42] with CRESO-determined regularization parameter[46] is used to stabilize the inverse procedure and obtain $\vec{a}$, similar to our previous ECGI inverse computations using mesh-based BEM.[4,8,9,21,24,33,57, 1, 47]

Once the coefficient vector $\vec{a}$ is obtained, $u(x)$ can be computed at any location in the domain using:

$$u(x) = a_0 + \sum_{j=1}^{M} a_j f(\|x - y_j\|), \quad x \in \Omega, \quad y_j \in \hat{\Gamma} \tag{2-5}$$

The epicardial potential can then be calculated using:

$$u_E(x) = a_0 + \sum_{j=1}^{M} a_j f(\|x - y_j\|), \quad x \in \Gamma_E, \quad y_j \in \hat{\Gamma} \tag{2-6}$$

Epicardial potentials are calculated using (2-6) on many epicardial nodes; numbers are

provided for each dataset in the Results section. An epicardial potential map, reflecting the spatial distribution of potentials on the epicardial surface, is computed every millisecond during the cardiac circle. The time series of reconstructed epicardial potential maps are then organized by location to provide temporal electrograms for any given point on the epicardium. A reconstructed epicardial electrogram provides the potential variation with time at a given point on the epicardium during the cardiac cycle. Epicardial isochrone maps (a map of the epicardial activation sequence) are computed by taking the time of maximum negative $\frac{du_E}{dt}$ of the temporal electrogram ("intrinsic deflection") at a given location as the time of epicardial activation at that location.

2.2.2 Experimental Methods and Protocols

MFS ECGI reconstructions were performed on data from four studies: (i) Single-site pacing in an isolated canine heart suspended in a human torso-shaped tank; data were obtained during pacing from a right ventricular (RV) anterior epicardial location;[21] (ii) RV endocardial pacing in a patient undergoing bi-ventricular pacing for cardiac resynchronization therapy (CRT); (iii) Simultaneous RV endocardial pacing and left ventricular (LV) epicardial pacing in a patient undergoing bi-ventricular pacing for CRT; (iv) Normal atrial activation in a healthy human subject.[1]

Isolated Canine Hearts Suspended in a Human Torso-Shaped Tank [21]

The performance of MFS in ECGI was evaluated using data from a human torso-shaped

tank.[21] The setup consisted of an isolated canine heart suspended in a homogenous electrolytic medium in the correct anatomical position inside a tank molded in the shape of a ten-year old boy. The tank had 384 surface electrodes recording torso potentials and 242 rods with electrodes at their tips that formed an epicardial recording envelope around the heart. The torso-surface potentials and epicardial potentials were recorded simultaneously. The directly measured epicardial potentials by the rod-tip electrodes served as a "gold standard" for MFS ECGI validation. The torso-surface potentials provided the input data for MFS ECGI noninvasive reconstruction of epicardial potentials, electrograms and isochrones, which were then evaluated by comparison with the directly measured "gold standard". Details were provided in previous ECGI publications. [4,21,24,47]

To simulate focal arrhythmogenic activity, the heart was paced from an anterior epicardial location. The same datasets were used in BEM ECGI and reported in previous publications.[21] Here, these datasets are used to evaluate MFS ECGI and compare its performance to that of BEM ECGI. The pacing protocol also provided a measure of MFS ECGI spatial accuracy (its accuracy in locating the known pacing site). After pacing, a quasi-elliptical region of intense epicardial negativity forms around the pacing site. [4,21,47,58]

Bi-Ventricular Pacing In Human Subjects [1]

We also applied MFS ECGI to clinical data from patients with an implanted bi-ventricular pacing device. For the bi-ventricular pacing data, MFS ECGI accuracy in

locating the pacing sites was evaluated by comparison with the pacing electrodes' positions as determined from CT images. The reconstructed activation pattern was evaluated based on the known patterns of activation generated by pacing.

Data from two heart failure patients undergoing cardiac resynchronization pacing therapy[1] are presented. Subject 1 was paced from a right ventricular (RV) endocardial site, close to the RV apex. Subject 2 was paced simultaneously from an RV endocardial site and from a left ventricular (LV) epicardial site. Body surface potentials were recorded with a 224-channel mapping system using an electrode-vest as previously described.[1] Epicardial geometry and location of the torso electrodes were obtained from CT images of the thorax. The locations of the cardiac pacing leads were also determined from these CT images.[1]

Normal Atrial Activation in a Healthy Human Subject [1]

MFS ECGI was applied to reconstruct atrial activation in a healthy young adult. The same data were used in BEM ECGI and reported in a previous study.[1] The atrial activation pattern was reconstructed from recorded P-wave body surface potential maps with 224 channels, together with a subject-specific torso and atrial geometry obtained using CT. The directly measured normal atrial activation pattern in isolated human hearts (Durrer et. al[59]), was used for qualitative evaluation of the MFS ECGI reconstruction.

Informed consent was obtained according to Institutional Review Board guidelines at University Hospitals of Cleveland, which approved all human studies protocols.

2.2.3 Evaluation Procedures

For the tank-torso protocols, measures in terms of relative error (RE) and correlation coefficients (CC) were computed with respect to the measured data to quantitatively evaluate the accuracy of ECGI; RE and CC were defined previously.[27] RE gives an estimate of the amplitude difference and CC gives an estimate of the similarity of potential patterns or electrogram morphologies between the measured and computed data:

$$RE = \sqrt{\frac{\sum_{i=1}^{L}(V_i^C - V_i^M)^2}{\sum_{i=1}^{L}(V_i^M)^2}}$$

$$CC = \frac{\sum_{i=1}^{L}(V_i^M - \bar{V}^M)(V_i^C - \bar{V}^C)}{\sqrt{\sum_{i=1}^{L}(V_i^M - \bar{V}^M)^2}\sqrt{\sum_{i=1}^{L}(V_i^C - \bar{V}^C)^2}}$$

For potential maps, L is the number of epicardial points at which potentials are measured and computed. V_i^C is the computed potential at epicardial point i, at a given instant of time, and V_i^M is the corresponding measured potential. $\bar{V}^M$ and $\bar{V}^C$ are the *spatial* average of measured and computed potentials respectively, averaged over all L points.

For electrograms, L is the number of time frames for which potential is measured and computed. V_i^C is the computed potential at time i, at a given epicardial location, and V_i^M is the corresponding measured potential. $\overline{V}^M$ and $\overline{V}^C$ are the *temporal* average of measured and computed potentials respectively, averaged over all L times.

In addition to CC and RE, pacing site localization errors (distance between reconstructed and measured locations) were also computed for both torso-tank and human reconstructions. The reconstructed pacing site location was estimated by the center of an ellipse that best fits the quasi-elliptical negative potential region that develops around the pacing site.[4,21,47] The earliest time frame after pacing, for which such pattern was present, was used for this purpose. Pacing sites could also be determined from isochrone maps as the sites of earliest activation.

Qualitative evaluations of ECGI reconstructions are conducted by visual comparison to measured data (torso-tank experiments) and to well established potential, electrogram and isochrone patterns associated with pacing and normal atrial activation (human subjects).

2.3 Results

2.3.1 Single Site Pacing in a Torso-Shaped Tank

Figure 2-2 shows epicardial potential maps for anterior RV pacing, at a time 25 ms after

pacing. There are 240 epicardial nodes, 386 torso nodes and 626 (240+386) virtual source points in this dataset. The top row shows the directly measured epicardial potential maps in four views. The middle and bottom rows show MFS-reconstructed and BEM-reconstructed epicardial potential maps, respectively. The white asterisk in the anterior view marks the pacing site location (top row) and its estimation from the reconstructed epicardial potential maps in the middle and bottom rows. The measured potentials display a central quasi-elliptical negative region (blue) flanked by two positive regions (red, maxima locations are marked by the white plus signs) as expected in the anisotropic myocardium.[21,58] This pattern is captured by both BEM ECGI and MFS ECGI. However, MFS ECGI provides a more accurate potential map pattern than BEM ECGI. MFS ECGI locates the pacing site with an error of 3 mm as compared to a 5 mm error for BEM ECGI. CC (a measure of pattern similarity to the measured potentials) is improved from 0.85 (BEM ECGI) to 0.92 (MFS ECGI); RE (indicative of amplitude accuracy) is improved from 0.97 (BEM ECGI) to 0.47 (MFS ECGI).

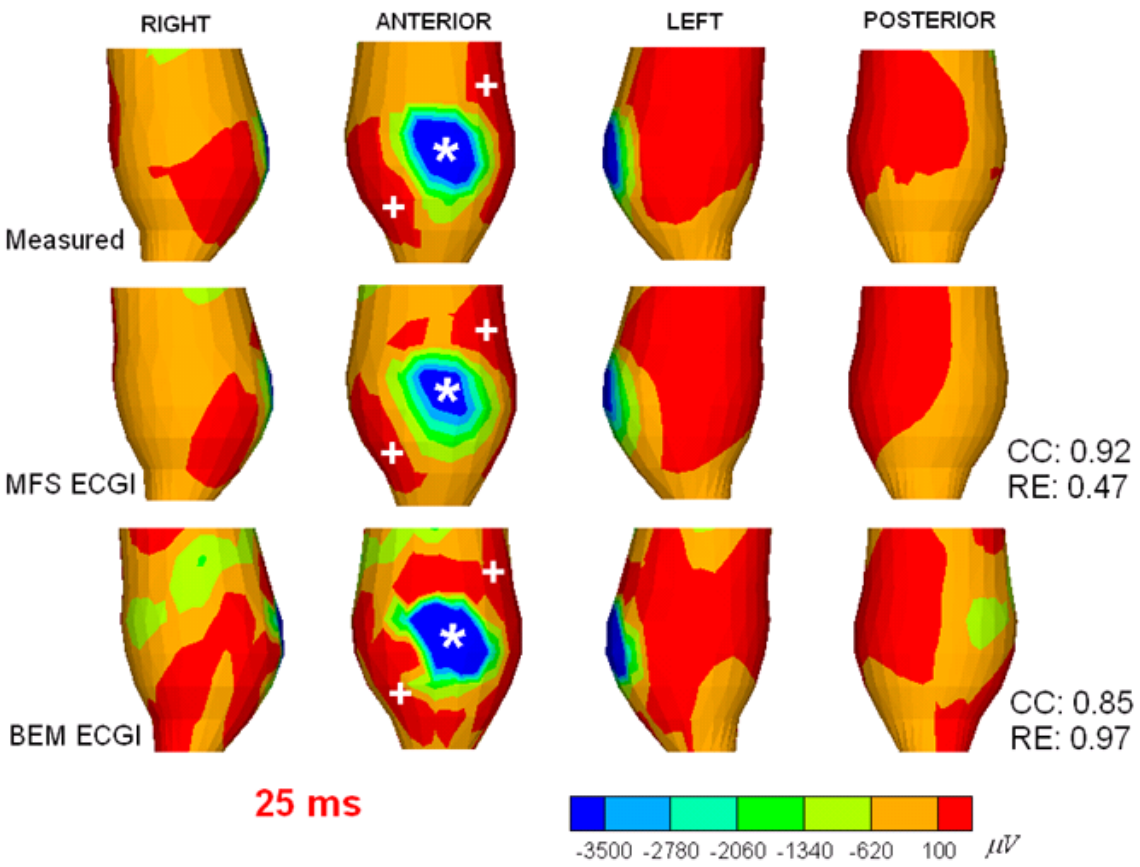

Figure 3 (Figure 2-2): Canine epicardial potential maps 25ms after pacing from a single anterior site (indicated by the asterisk *).

Top row shows the directly measured epicardial potentials (four views) displaying the negative region (dark blue) around the pacing site, and two flanking positive maxima (red). **Middle row** shows the noninvasively reconstructed potentials computed using MFS ECGI; note close similarity of noninvasive and invasive data. **Bottom row** shows the reconstruction using BEM ECGI.

Figure 2-3 shows noninvasively reconstructed epicardial electrograms (format described in figure legend) using MFS ECGI. Figure 2-3A shows four views of the heart surface. Electrograms reconstructed at epicardial sites close to pacing site (sites 1, 2, 3), at intermediate distance from the pacing site (sites 4, 5, 6), and far way from the pacing site

(sites 7, 8, 9) are displayed. In panels B, C, and D, both measured and noninvasively computed electrograms using MFS are displayed. Three main types of waveforms: monophasic negative (B), biphasic (C), and monophasic positive (D), are reconstructed. Notice the close resemblance (high Correlation Coefficient, CC) of the noninvasively reconstructed MFS ECGI electrograms to the measured electrograms. Compared with reconstructed electrograms using BEM ECGI[22], MFS ECGI achieves better accuracy with greatly reduced computation time.

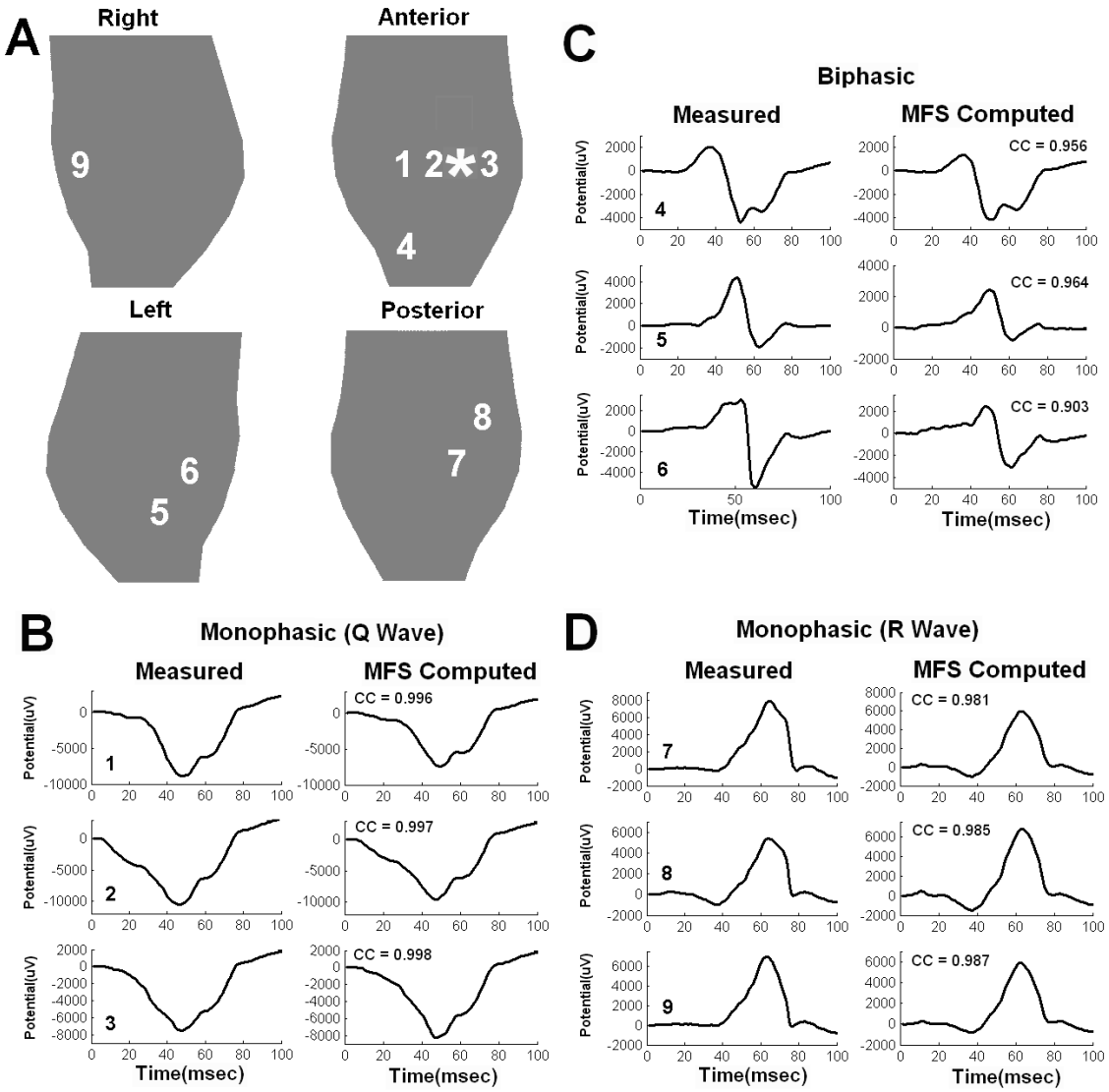

Figure 4 (Figure 2-3): Canine epicardial electrograms (measured and computed using MFS ECGI) from selected locations.

Canine epicardial electrograms (measured and computed using MFS ECGI) from selected locations on the heart surface for pacing from the same single site as in Figure 2 (indicated by the asterisk). **(A)** Four views of epicardial surface. Numbers in boxes identify locations of the electrograms in the other panels. Measured **(left column)** and computed **(right column)** electrograms are compared in B, C and D. Number on the bottom left of each panel identifies the electrogram location (corresponding to numbers in A). **(B)** Monophasic (Q wave) electrograms from sites 1, 2 and 3. **(C)** Biphasic

electrograms from sites 4, 5 and 6. **(D)** Monophasic (R wave) electrograms from sites 7, 8 and 9. CC is the Correlation Coefficient between invasive and noninvasive electrograms, indicating high level of similarity.

Figure 2-4 shows noninvasively reconstructed epicardial isochrones using MFS ECGI and BEM ECGI. Notice that the region of earliest activation (red) is reproduced accurately in the computed isochrones, as is the entire sequence of epicardial activation (CC = 0.78). A similar epicardial isochrone map is reconstructed by BEM ECGI (CC = 0.74). Based on Figure 2-4, it appears that MFS reconstructs smoother isochrones than BEM. A comparison of patterns shows closer similarity of the MFS reconstruction to the measured data, suggesting that the BEM reconstruction is somewhat under-regularized with the chosen CRESO regularization parameter. Similar observations apply to the ECGI reconstructed potential maps in Figure 2-2.

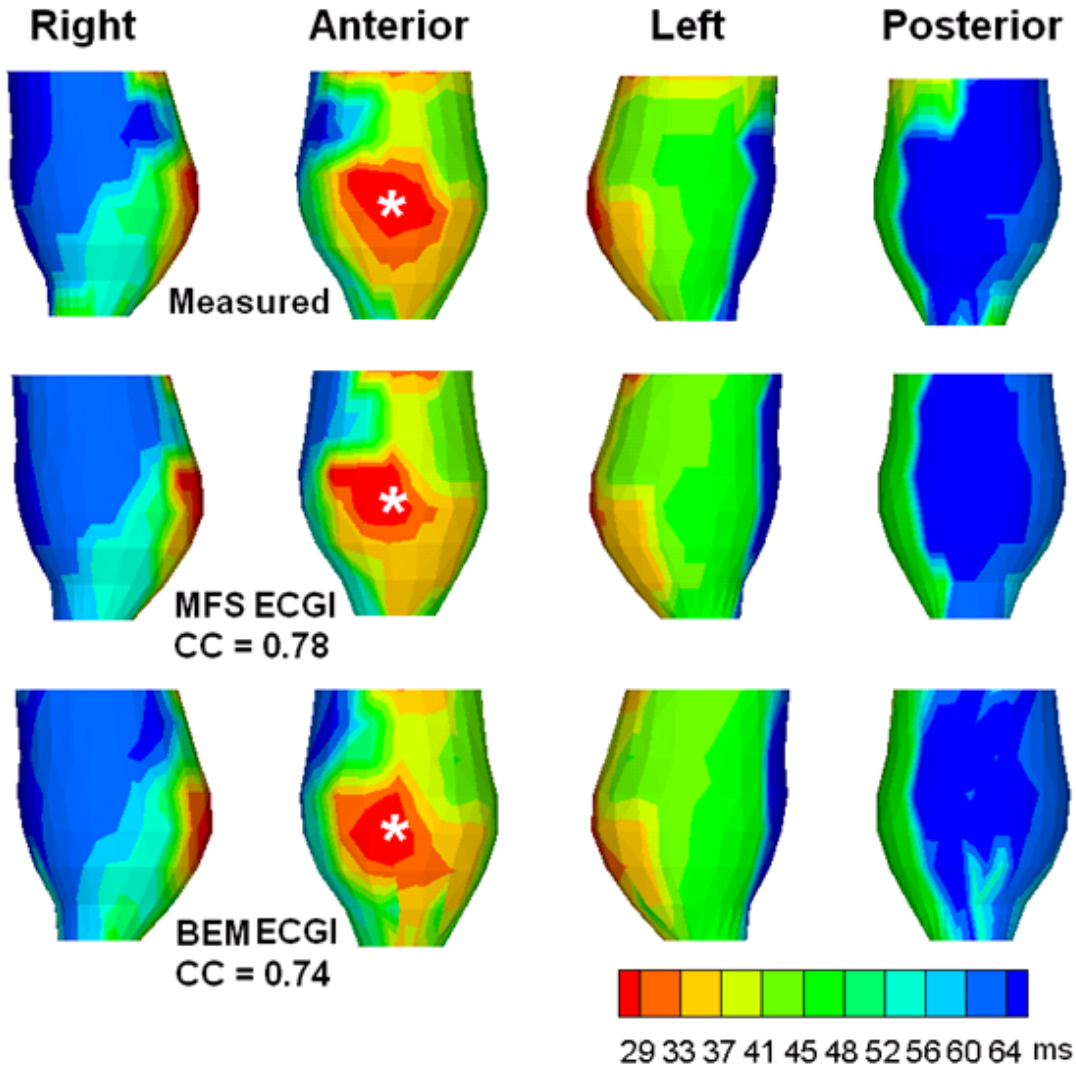

Figure 5 (Figure 2-4): Canine epicardial isochrone map for pacing from the same single site.

Canine epicardial isochrone map for pacing from the same single site as in Figure 2 (indicated by the asterisk). **Top row** shows the directly measured isochrones (four views) displaying the anterior pacing site. **Middle row** shows the noninvasively reconstructed isochrone map computed using MFS ECGI. **Bottom row** shows the noninvasively reconstructed isochrone map computed using BEM ECGI.

2.3.2 RV Endocardial Pacing in a Human Subject

Figure 2-5 compares epicardial potential maps computed with BEM ECGI and MFS

ECGI in a human subject during RV pacing (anterior view). There are 447 epicardial nodes, 115 torso nodes and 562 (447+115) virtual source points in this dataset. The pacing site as determined from CT images is marked by the white asterisk. Three reconstructions are compared: Left, BEM ECGI with an automatically generated mesh; Middle, MFS ECGI; Right, BEM ECGI with a manually optimized mesh. Panel A shows epicardial potential maps during activation, 62 ms after pacing. The negative region (dark blue) generated by BEM ECGI is fragmented, due to meshing artifacts. The three negative regions could be interpreted erroneously as reflecting three pacing sites. MFS ECGI effectively avoids such fragmentation and reconstructs a quasi-elliptical negative region, reflecting the single pacing site. After manual mesh editing, fragmentation of the negative region is eliminated, demonstrating that the fragmentation is mesh related. Panel B of Figure 2-5 shows a reconstructed epicardial potential map for the same protocol during repolarization (205 ms after pacing). As expected during pacing, the negative region of activation in panel A is replaced by a positive region (red). [1,20] Similar to Panel A, fragmentation of the positive region is observed for BEM ECGI, but not for MFS ECGI; it is eliminated from the BEM ECGI reconstruction after manual mesh editing.

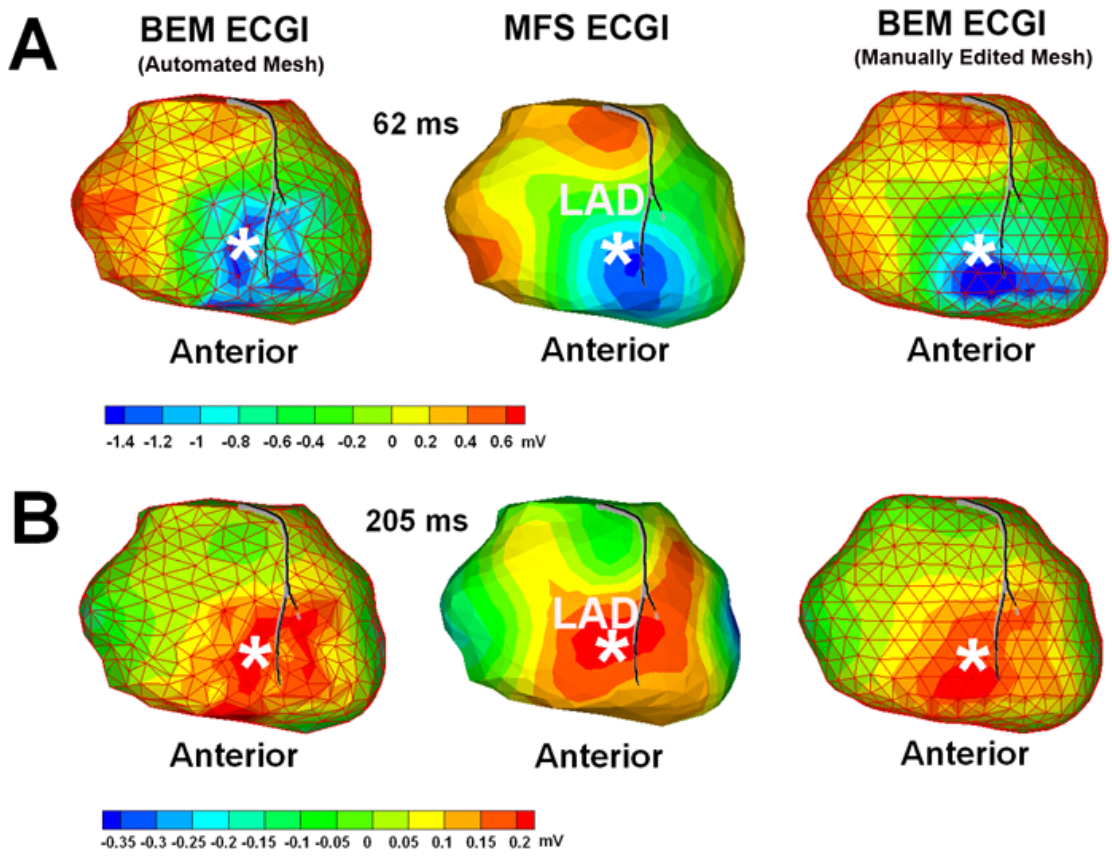

Figure 6 (Figure 2-5): MFS ECGI is free of mesh artifacts

Panel A: Human epicardial potential map (anterior view) 62 ms after pacing from a single RV endocardial site (marked by the asterisk). **Left:** BEM ECGI reconstruction with initial mesh (non-optimized), showing fragmentation of the negative region (blue) caused by meshing artifact. **Middle:** MFS ECGI reconstructs a single continuous minimum (blue) associated with single-site pacing. **Right:** BEM ECGI reconstruction with manually-edited mesh, showing that fragmentation is mesh related. **Panel B:** Human epicardial potential map (anterior view) during repolarization for pacing from the same site (205 ms after pacing).

The error in locating the pacing site is 14mm using BEM ECGI (by fitting an ellipse over

the three negative regions in the automated mesh reconstruction), 8mm using BEM ECGI with the manually optimized mesh, and 5mm using MFS ECGI. In order to improve the BEM ECGI reconstruction result, several manual iterations of mesh editing and optimization were required.

2.3.3 Simultaneous RV Endocardial and LV Epicardial Pacing

Figure 2-6 shows MFS ECGI reconstructions during simultaneous RV endocardial and LV epicardial pacing in a patient undergoing bi-ventricular pacing for CRT. There are 437 epicardial nodes, 189 torso nodes and 626 (437+189) virtual source points in this dataset. Panel A is an epicardial potential map 40 ms after pacing, displayed in three partially overlapping views. The asterisks mark the pacing sites locations determined from CT images. Panel B shows an epicardial isochrone map on the same views. From the isochrone map, it is determined that epicardial activation above the endocardial RV pacing site occurred 25ms later than epicardial activation around the epicardial LV pacing site. Given that pacing from both leads was simultaneous, the delay probably reflects, at least in part, endocardial to epicardial wave front propagation in the RV ventricular wall.

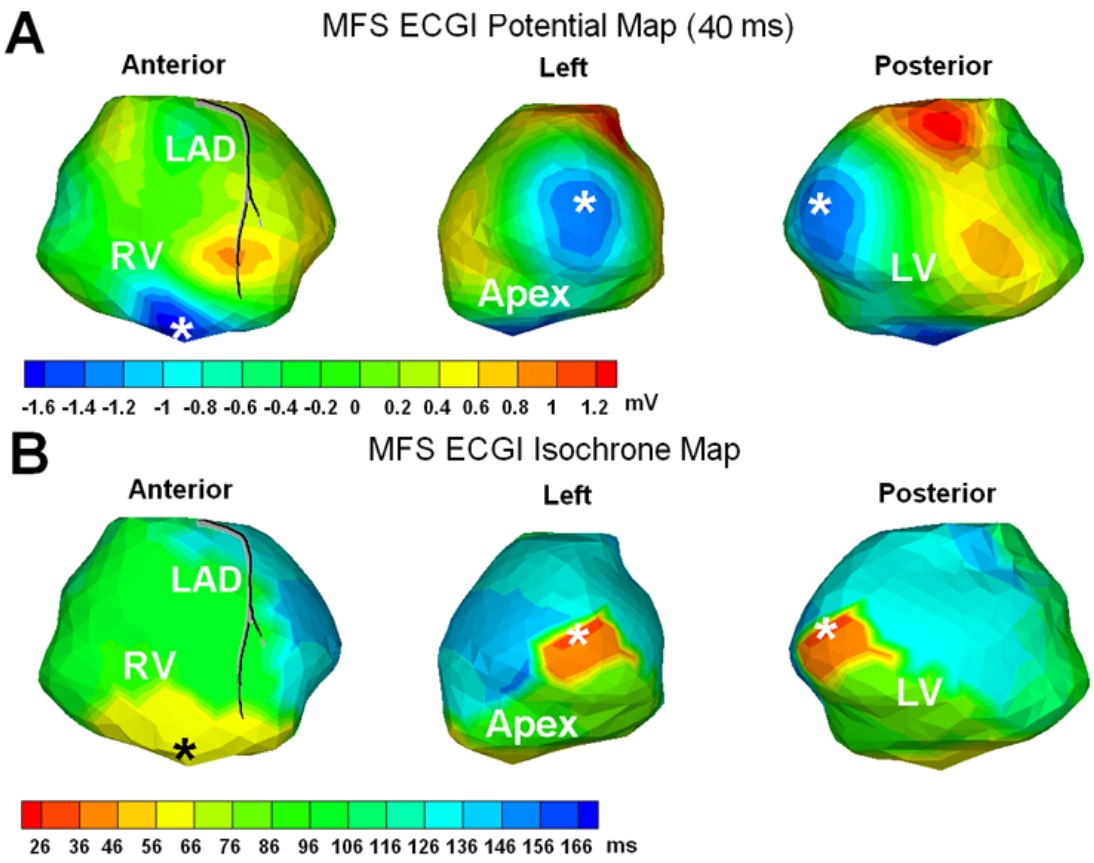

Figure 7 (Figure 2-6): Human epicardial potential map and isochrone map for simultaneous RV and LV pacing

Human epicardial potential map and isochrone map for simultaneous RV and LV pacing (pacing sites marked by the asterisks *; note that the left and back views show the same pacing site). **Panel A** shows the MFS ECGI reconstructed potential map 40ms after pacing (three partially overlapping views).Typical quasi-elliptic negative region (blue) surrounds each pacing site. **Panel B** shows the corresponding MFS ECGI reconstructed isochrone map in the same format.

From both isochrone maps and potential maps the RV pacing site and LV pacing site are located within 5.2mm and 7.4mm, respectively, of their locations as determined from CT. This accuracy is similar to the results of BEM ECGI after several iterations of mesh optimization.

2.3.4 Normal Human Atrial Activation

Figure 2-7 shows normal atrial activation isochrones reconstructed by MFS ECGI for a healthy volunteer. There are 322 atrial epicardial nodes, 228 torso nodes and 550 (322+228) virtual source points in this dataset. Earliest activation starts in the right atrium (RA) between the aorta and superior vena cava (SVC), near the anatomical location of the sinoatrial node (SA node). From the SA node, the impulse propagates radialy to the left atrium (LA) and the rest of the RA (the black arrows show the propagation pathway). The LA appendage (LAA) activates last. The atrial isochrones by MFS ECGI are practically identical to those reconstructed using BEM ECGI[45]. Both reconstructions provide activation patterns that are very consistent with directly measured atrial isochrones in normal isolated human hearts.[59]

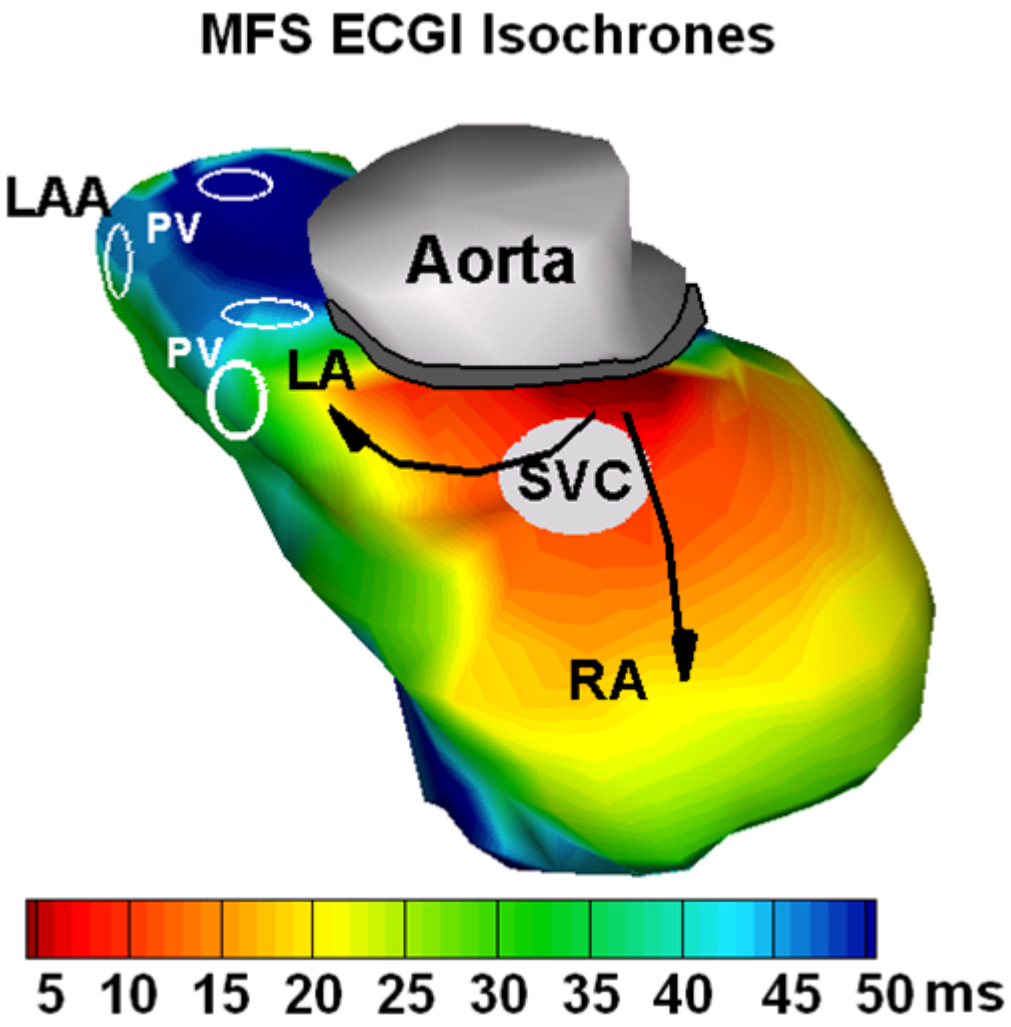

Figure 8 (Figure 2-7) Normal human atrial activation isochrones reconstructed with MFS ECGI.

RA: Right Atrium; LA: Left Atrium; LAA: Left Atrial Appendage; PV: Pulmonary Vein; SVC: Superior Vena Cava. Black arrows indicate direction of activation spread.

2.4 Discussion

In this paper we implement a meshless method, MFS, for noninvasive ECGI and evaluate its accuracy and performance. ECGI is formulated in terms of potentials, computing potentials on the epicardial surface of the heart from electrocardiographic potentials

measured on the body surface.[25-28] The existence of a well-behaved, analytic fundamental solution for the Laplace operator in 3D[54] makes MFS highly suitable for the ECGI application.

Being a potential-based scheme, ECGI reconstructs epicardial potentials, from which electrograms and activation sequences (isochrones) can also be computed. This approach is applicable not only during cardiac activation, but provides images of repolarization as well. [9] A different approach to inverse electrocardiography has been to compute directly the activation sequences on both epicardial and endocardial surfaces of the heart.[29,30,60] The potential-based approach has also been used to reconstruct potentials on the endocardial surface from a non-contact intracavitary catheter.[61-65] It should be noted that while for the potential-based approach optimizing the mesh (a procedure requiring manual editing) is the time-limiting step, for the activation-based approach[30] it is the inverse computation which utilizes a nonlinear-optimization iterative scheme, a complex time consuming process. Mesh related artifacts mainly affect patterns of epicardial potential maps and magnitudes of electrograms in the potential-based ECGI reconstruction. The morphology of electrograms (from which activation times are determined) and activation patterns (isochrones) are minimally affected by mesh structure. This suggests that the activation-time approach that only computes isochrones is less sensitive to mesh properties.

2.4.1 Geometry and Torso Inhomogeneitie

The importance to inverse electrocardiography of geometry accuracy and of conductivity inhomogeneities in the torso volume conductor (due to the lungs and other torso compartments) has been evaluated extensively. [66, 57,67,68] Huiskamp and van Oosterom[66] concluded that a tailored accurate geometry is required for accurate ECGI inverse computation. Other studies[57,67] showed that although the accuracy of reconstruction depends on accurate knowledge of the geometry, small errors in geometry determination (e.g. 1-cm shift error in heart position) can be tolerated by ECGI without major deterioration of reconstruction quality. A study using realistic human anatomy[69] demonstrated that a homogeneous model of the torso produced less accurate epicardial potential magnitudes than an inhomogeneous model, but epicardial potential patterns, electrogram morphologies, isochrones, and locations of pacing sites were reconstructed with comparable accuracy when the torso was assumed homogenous. Independence of epicardial patterns from torso volume-conductor properties was demonstrated experimentally as well.[70] Based on results of these inhomogeneity studies, MFS ECGI is applied and tested here in a homogeneous torso volume-conductor. However, if needed the internal inhomogeneities can be included in BEM ECGI by extending the transfer matrix A to include the boundaries of internal torso compartments.[71] Similar to BEM, the MFS approach can also be extended to a multi-compartment volume-conductor. Malik[72] has shown how MFS can be applied to a multi-dielectric media problem. For such multi-compartment problem additional boundary conditions must be satisfied, namely

continuity of potential and normal component of current at each inter-compartmental interface.[73] Regional formulation of MFS for computation of electric fields was developed in the early 90's [74,75]. Recently a domain decomposition method was combined with MFS for solving the inhomogeneous multi-compartment problems.[76] This approach can be applied to MFS ECGI in cases where the effect of torso inhomogeneities is of interest.

2.4.2 Mesh-Related Considerations

MFS application in ECGI has several advantages over boundary element (BEM) and finite element (FEM) methods [55,77] that require meshing the heart and torso. These advantages result from bypassing the meshing operation in BEM/FEM ECGI. Mesh quality is well known to affect both the time and accuracy of numerical solutions to PDE-based applications.[78] A "bad" mesh structure that contains elements of non-uniform area, non-uniform angle or non-uniform aspect ratio, can introduce serious artifacts in the numerical computation. This is especially true for the ECGI application, because the ill-posed inverse computation[42] that is involved tends to amplify such mesh related numerical errors (Figure 2-5). Non-uniform mesh elements are difficult to avoid in meshing complex surfaces including the heart, especially in the presence of structural disease. Efficient methods for mesh optimization are the topic of ongoing research.[78-80] For ECGI applications, it is difficult to define general criteria for automated optimal mesh generation because the mesh related artifacts are influenced by the ill-posed inverse computation. BEM ECGI usually requires several time-consuming manual iterations for

mesh optimization (we use a constant potential field as a calibration dataset for this purpose). Even after an optimized mesh is constructed, BEM requires manipulation of the 3D surface mesh and computation of a complicated singular surface integral over each mesh element. Being a meshless method, MFS ECGI bypasses these procedures. The reduced complexity of MFS ECGI, its independence of meshing and manual editing (and therefore enhanced suitability for automation) makes this approach particularly suitable for clinical application.

Figure 2-5 demonstrates that fragmentation of reconstructed epicardial potentials is mesh dependent. Several iterations of manual editing improved the mesh and removed fragmentation, resulting in a less fragmented and smoother reconstruction. However, mesh-related artifacts were still present after editing (Figure 2-5, right panel), indicating that even several iterations did not result in an optimal mesh. Based on our experience, obtaining a fully optimized mesh that eliminates all artifacts is a very difficult and time consuming process. MFS ECGI does not require meshing and mesh optimization, avoiding this time consuming manual step that can introduce artifacts in the reconstructed images. It is possible that different regularization schemes[65,81-83] than the ones employed here could provide better accuracy with an unedited mesh, or that better mesh generation algorithms optimized for ECGI could be developed. These possibilities remain to be investigated in future studies. Here, we focus on the possibility of eliminating the meshing step altogether, thereby avoiding mesh related artifacts and the need to compute complex singular integrals

that require special care in BEM.

As shown in equation (2-3), normal vectors are required for the MFS computation. In the results shown here, normal vectors are constructed using the initial unedited mesh, which is generated very quickly by Amira (TGS Template Graphics Software, Inc.) without mesh editing. This may create the impression that MFS is not completely meshfree. The field of meshless approaches is progressing rapidly, including meshless methods for determining normal directions for given surfaces. For example, the Radial Basis Functions (RBF) method[84,85] obtains the 3D surface representation and computes analytically the surface normal/tangent vectors without forming a mesh. Figure 2-8 compares MFS ECGI reconstructions (potential maps and electrograms) with mesh-generated normal vectors and with meshless normal vectors obtained using RBF. Panels A and B show the reconstructed potential maps during depolarization and repolarization, respectivcely. Panel C shows reconstructed electrograms from selected epicardial locations. Both methods produce very similar results. In addition, point-based rendering methods are also emerging very quickly, [86] allowing for direct rendering of the surface without the creation of a polygonal mesh representation.

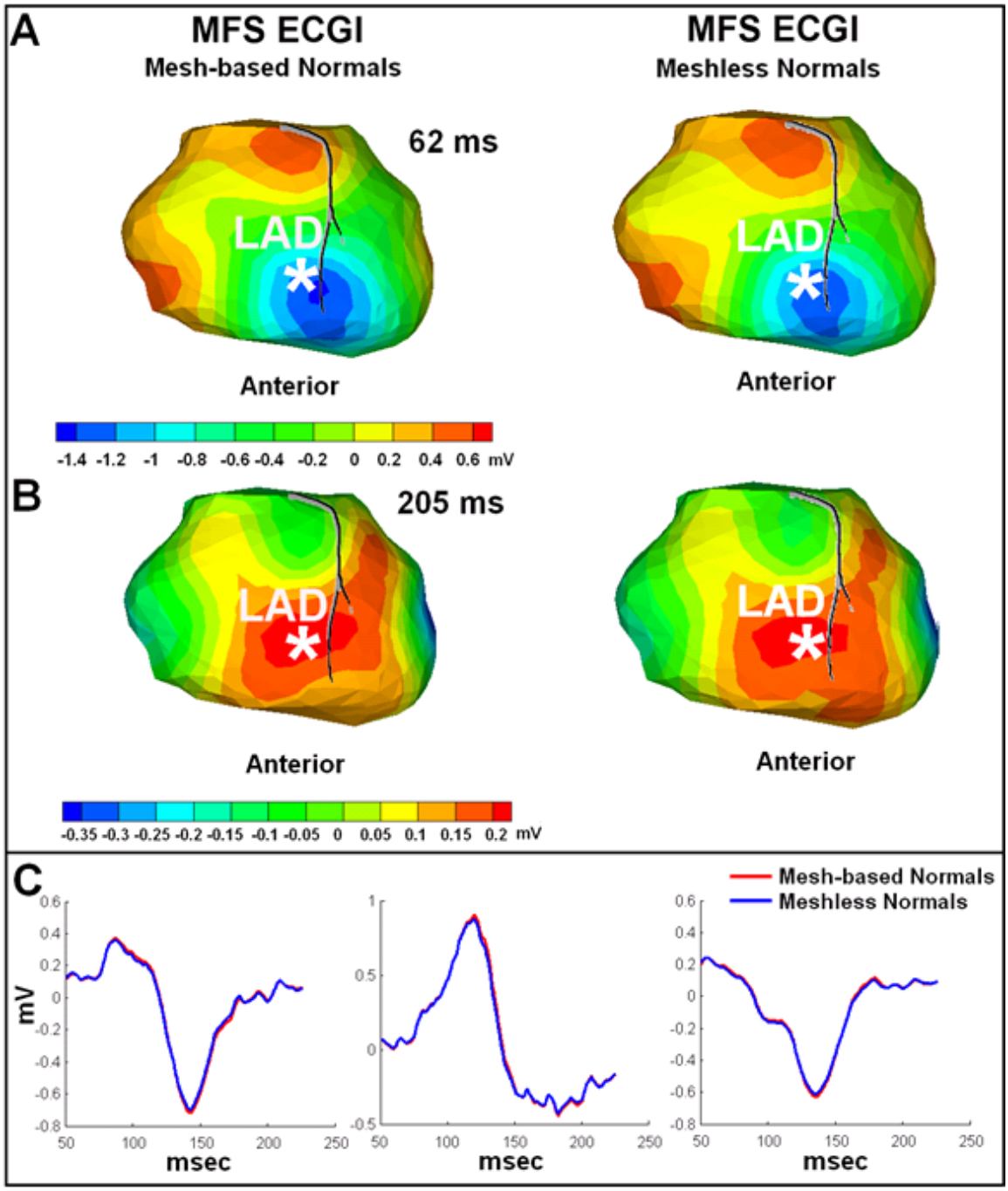

Figure 9 (Figure 2-8): Comparison of MFS ECGI reconstructions with mesh-based and meshless normal vectors.

Panel A: Human epicardial potential map (anterior view) 62 ms after pacing from a single RV endocardial site (marked by the asterisk). **Left:** MFS ECGI reconstruction with normal vectors computed using a mesh. **Right:** MFS ECGI reconstruction with normal vectors computed without a

mesh, using Radial Basis Function (RBF). **Panel B:** Human epicardial potential map (anterior view) during repolarization for pacing from the same site (205 ms after pacing). Same format as Panel A. **Panel C:** Human epicardial electrograms from selected locations on the heart surface for the same pacing dataset. Red traces show the MFS ECGI reconstruction with mesh-based normal vectors. Blue traces show the MFS ECGI reconstruction with meshless normal vectors computed using RBF.

Morphing a template mesh of a stylized heart could be an effective approach for creating a patient-specific mesh in BEM ECGI. However, it requires evaluation in this context. One of the major concerns regarding application of morphing is that many hearts that can benefit from clinical ECGI have pathologies that modify greatly the heart geometry (e.g. dilation, presence of diverticuli or anneurisms). Such localized structural deformations cause large deviations from the anatomy of a template heart. Our laboratory uses Amira to obtain the initial surface mesh for such diseased hearts. The initial mesh requires manual editing to obtain an improved mesh structure for reduction of mesh-related artifacts.

For a given problem, the condition number of the $\hat{A}$ matrix in MFS is usually larger than that of the forward matrix in BEM. For the torso-tank data in this study, the condition number is 2.3516e+014 for BEM, and 9.1934e+016 for MFS; however better accuracy is obtained with MFS. Several studies by others[41,51,87,88] have suggested that the numerical accuracy of MFS is only minimally affected by the condition properties of the matrix.

Recent work by Christiansen and Saranen[89] and Christiansen and Hansen[90] also suggests that the condition number as commonly defined is not an appropriate measure of numerical stability. Better accuracy with a larger condition number was also obtained when a second order BEM scheme was applied in ECGI reconstruction.[91]

A possible advantage of BEM ECGI is that the torso geometry can be constructed with greater precision than that delineated by the electrodes. Consequently, the transfer matrix can be computed with greater accuracy. Such augmentation can not be implemented in MFS ECGI. However, since the zero Neumann condition (no current flow across the torso-air boundary) is valid on the entire torso surface, Neumann conditions at more torso locations (Equation 2-3) can be added in the MFS ECGI formulation (Equation 2-4). We examined the benefit of doing so and results (not shown) show similar or only slightly improved electrograms and potential maps as judged by CC and RE values.

2.4.3 Placement of Virtual Source Points

Implementation of MFS requires choosing a fictitious boundary for placing the virtual source points. There are two widely used approaches for doing so, the dynamic and static methods.[41] In the dynamic configuration, the fictitious boundary is determined together with the solution[92] via a complex, time-consuming nonlinear optimization procedure which does not always guarantee global convergence. In the static configuration, the fictitious boundary is pre-selected corresponding to the real boundary based on some fixed (static)

rules (criteria), for example the inflation-deflation rule used here. For different patients' geometries, the corresponding fictitious boundaries that are generated by the static rule are different. The static method is not the optimal implementation of MFS, but it is very easy to implement and highly suitable for practical engineering applications. Very good accuracy has been obtained using the static method in engineering and industrial applications of MFS,[53] including the application presented here. Although optimal placement of the virtual source points poses a difficulty for MFS implementation at present, much faster and more efficient nonlinear optimization schemes[32] are under development, which will facilitate use of the dynamic method in MFS ECGI.

The "inflation-deflation" procedure used in our reconstructions was designed and tested using data from the human-shaped torso-tank experiments,[21] where directly measured epicardial potentials provided a gold standard for evaluation. Because the heart surface is globally convex, the "inflation-deflation" procedure works well for most heart geometries. In the presence of structural heart disease, the heart surface could contain concave regions. For such geometry, static inflation or deflation relative to a fixed point may place some fictitious points in the domain of interest. In these cases, special care is needed to insure that all fictitious points lie outside the domain of interest. An alternative approach is to employ a more general "inflation-deflation" procedure, which does not inflate or deflate the boundary relative to a fixed point and insures that the virtual source points are placed outside the domain of interest. For example, in the FastRBF toolbox [84,85], inflation and

deflation are achieved by computing isosurfaces based on the distance from the actual boundary, which insures that the fictitious nodes are placed outside the domain for all types of heart geometry. This method is demonstrated in panel A of Figure 2-9 for the complex geometry of the atria in Figure 2-7. A 3D Radial Basis Function (RBF) [84,85] computes a signed distance from the actual object's surface. If the normal direction is inward, points inside the object have positive distances (red) while points outside have negative distances (green-blue). The object's surface is defined as the zero set of the function (yellow). In Panel A, the RBF function grid values are shown on three orthogonal planes: x = 60 (mm), y = 90 (mm), and z = 30 (mm). By setting different RBF values, different inflated (or deflated) surfaces of the atria can be obtained. Panel B of Figure 9 shows an inflated atria surface obtained by selecting RBF = 5(mm). This figure demonstrates that this more general procedure can be used for complex heart geometry such as the atria in this example, or ventricles with irregular geometry due to disease (e.g. diverticuli or aneurisms).

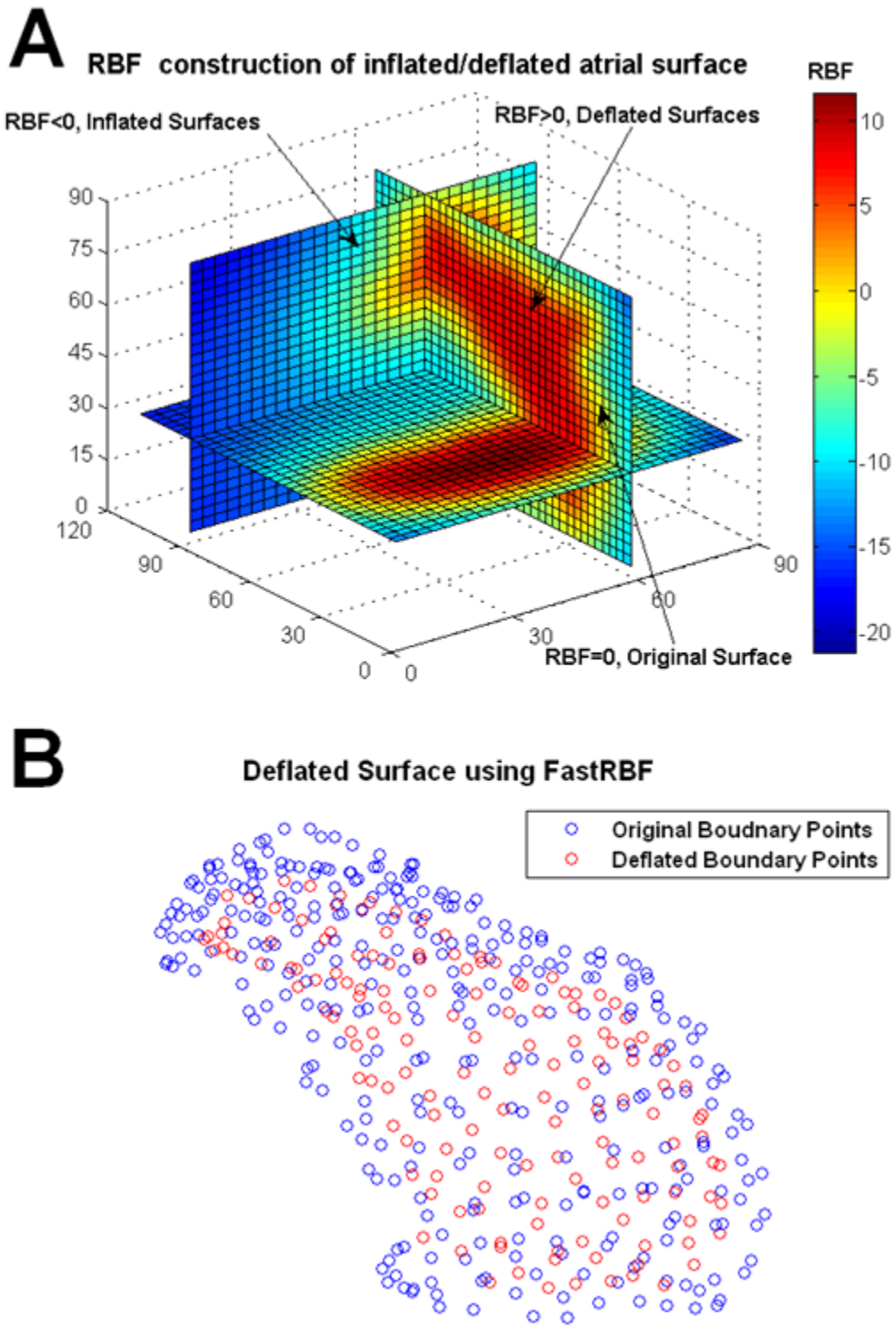

Figure 10 (Figure 2-9): General method to place virtual source points

Panel A: Radial Basis Function (RBF) representation of the atrial surface in Fig. 7 and corresponding

inflated/deflated surfaces. The RBF function grid values are shown on three orthogonal planes: x = 60 (mm), y = 90 (mm), and z = 30 (mm). The original boundary is represented by the isosurface with RBF = 0(mm). Since the positive normal direction is chosen inward, deflated surfaces are represented by isosurfaces with RBF > 0 and inflated surfaces by the isosurfaces with RBF < 0. **Panel B:** A deflated atrial surface obtained by selecting RBF = 5 (mm). Blue circles represent the original boundary points, and red circles represent the deflated surface points; all red circles are enclosed by the 3D surface defined by the blue circles.

Determination of the optimal position of the fictitious nodes relative to the actual boundary is a difficult problem that is the subject of ongoing research[41]. For noise-free boundary conditions, Golberg and Chen[41] have shown that the accuracy of MFS improves when the fictitious nodes are moved far away from the actual boundary. However, for noisy boundary conditions that always exist in actual engineering applications, Mera[93] has found that accuracy deteriorates when the fictitious points are placed too close or too far from the actual boundary. If the fictitious points (singularities) are placed too close to the actual boundary, MFS will have to evaluate nearly-singular matrix elements ($f(r) = \frac{1}{4\pi r}$ and $\frac{\partial f(r)}{\partial n}$) during formation of the matrix $\hat{A}$ (equation (4)). If the fictitious points are placed too far from the actual boundary, the rows in the top half of matrix $\hat{A}$ become very similar to each other, as do the rows in the bottom half; this increases the singularity of the matrix. We used several datasets from the human-shaped torso-tank experiments,[21] to evaluate the dependence of accuracy on the positions of fictitious nodes. The most accurate

reconstructions were obtained for deflating by a factor in the range 0.6 to 0.9 and inflating by a factor in the range 1.1 to 1.5 (within these ranges, accuracy did not depend significantly on the exact parameter value). Based on this empirical observation in a realistic human-shaped heart-torso geometry, we chose 0.8 as the deflating parameter and 1.2 as the inflating parameter for all studies presented here.

With this simple "inflation-deflation" scheme, the number of fictitious points is chosen based on practical considerations to be equal to the number of actual boundary nodes. This is a simple choice employed in this paper, and is not a requirement of the MFS method. Mera[93] has shown that the accuracy of inverse computation using MFS for a backward heat conduction problem improved with increasing number of fictitious nodes. He also found that the accuracy did not improve once the number of fictitious nodes exceeded a certain limit. Since very good reconstruction accuracy was obtained here with the number of fictitious nodes set equal to the number of boundary nodes, we did not attempt to increase this number. It is possible that the number of fictitious nodes could be reduced without significant loss of accuracy as suggested by Mera.[93] Systematic evaluation is needed to determine the optimal number of fictitious points in the context of ECGI.

2.5 Appendix: Formulation of MFS for Laplacian Operator

MFS has evolved from traditional boundary integral methods. Without forming a mesh, MFS uses a set of points to solve numerically partial differential equations. Details of this method can be found in the review article[41]. The following Dirichlet boundary value problem is used to describe the theoretical formulation of MFS for the Laplacian operator:

$$\nabla^2 u(x) = 0, x \in \Omega \tag{a1}$$

$$u(x) = b(x),\ x \in \Gamma,\ \ \Gamma = \partial\Omega \tag{a2}$$

where ∇^2 is the Laplace differential operator with a known fundamental solution $f(r)$ in 3D space. $u(x)$ is a potential function in a source-free domain Ω and $b(x)$ is the Dirichlet boundary condition. According to the definition of fundamental solution,[55] the fundamental solution of the Laplace operator can be obtained by solving the following equation for $f(r)$:

$$\nabla^2 f(r) = \delta(r) \tag{a3}$$

Where $\delta(r)$ is the delta function, $r = \|x - y\|$ is the 3D Euclidean distance between point x and point y, $x, y \in \Omega$. $f(r)$ in two dimensions (2D) and three dimensions (3D) is: [94]

$$f(r)=\begin{cases}-\dfrac{1}{2\pi}\ln r & , \quad 2D \\ \dfrac{1}{4\pi r} & , \quad 3D\end{cases} \tag{a4}$$

Both BEM and MFS use the same Green's function $f(r)=\dfrac{1}{4\pi r}$ in 3D space. However BEM integrates this function locally over elements of the real surface and requires computation of complex singular integrals. By placing the fictitious source points outside the domain of interest, MFS employs global integration and avoids the need to compute complex singular integrals.

The traditional boundary integral approach is to represent the solution $u(x)$ in term of a double layer potential:[48,51]

$$u(x)=\int_{\Gamma}\frac{\partial f(\|x-y\|)}{\partial n}e(y)dy, \quad x\in\Omega, \quad y\in\Gamma \tag{a5}$$

where, n is the outward pointing normal at point y, $e(y)$ is an unknown density function. Equivalently a single layer potential representation of $u(x)$ can be used [48,95]

$$u(x)=\int_{\Gamma} f(\|x-y\|)e(y)dy, \quad x\in\Omega, \quad y\in\Gamma \tag{a6}$$

The source density distribution $e(y)$ can be determined by solving the following equation under the assumption of a double layer:

$$\int_{\Gamma}\frac{\partial f(\|x-y\|)}{\partial n}e(y)dy=b(x), \quad x\in\Gamma, \quad y\in\Gamma \tag{a7}$$

or under the assumption of a single layer:

$$\int_{\Gamma} f(\|x-y\|)e(y)dy=b(x), \quad x\in\Gamma, \quad y\in\Gamma \tag{a8}$$

However, singular integrals are involved in both cases. To alleviate this difficulty, the

following formulation, similar to the single layer potential in (a6), has been used: [92]

$$u(x) = \int_{\hat{\Gamma}} f(\|x - y\|)e(y)dy, \quad x \in \Omega, \quad y \in \hat{\Gamma} \tag{a9}$$

where the auxiliary boundary $\hat{\Gamma}$ is the surface of the auxiliary domain $\hat{\Omega}$ containing the domain Ω (Figure 2-1).

Two different approaches for selecting $\hat{\Gamma}$ and its fictitious source points *y* are described in the literature: [48] static configuration and dynamic configuration. In static configuration, the fictitious boundaries are fixed and pre-selected. The method is easy to implement and use in practical applications. For dynamic configuration, the location of fictitious boundaries is determined together with the solution[92] by a complex, time-consuming nonlinear optimization procedure, which greatly limits its practical application. Since the geometry of the 3D domain between the torso surface and the heart surface is similar for all humans, the static approach is the method of choice for ECGI application.

Because $f(\|x - y\|)$ is the fundamental solution of the Laplace operator [equation (a3)], (a9) satisfies the differential Equation (a1). Therefore we need only to apply the boundary condition (a2):

$$\int_{\hat{\Gamma}} f(\|x - y\|)e(y)dy = b(x), \quad x \in \Gamma, \quad y \in \hat{\Gamma} \tag{a10}$$

where the source density distribution $e(y)$, $y \in \hat{\Gamma}$, is to be determined. Once the source density is determined, equation (a1) subject to (a2) is solved. The analytic integral representation of (a10) implies that there is an infinite number of source density points on $\hat{\Gamma}$. In order to apply numerical methods to the solution, it is necessary to

discretize $e(y)$. Assume $\psi_i(y), i = 1,2,\cdots\infty$ is a complete set of functions on $\hat{\Gamma}$, $e(y)$ can be approximated by:

$$e(y) = \sum_{i=1}^{\infty} c_i \psi_i(y), \quad y \in \hat{\Gamma} \tag{a11}$$

Substituting (a11) into (a10) and satisfying the boundary conditions at the *n* boundary points $x_k \in \Gamma, k = 1,2,\cdots n;$ we have

$$\sum_{i=1}^{\infty} c_i \int_{\hat{\Gamma}} f(\|x_k - y\|)\psi_i(y)dy = b(x_k), \quad 1 \le k \le n, \quad y \in \hat{\Gamma} \tag{a12}$$

Since the fictitious boundary $\hat{\Gamma}$ is located outside the physical domain (Figure 1), the integrand $f(\|x_k - y\|)$ is nonsingular and standard quadrature rules can be applied giving

$$\int_{\hat{\Gamma}} f(\|x_k - y\|)\psi_i(y)dy \approx \sum_{j=1}^{M} w_j f(\|x_k - y_j\|)\psi_i(y_j), \quad y_j \in \hat{\Gamma}, \quad j = 1,2,...,M \tag{a13}$$

where w_j is a weight factor and M is the number of fictitious nodes on the fictitious boundary $\hat{\Gamma}$.[41]

From (a12) and (a13), we obtain:

$$\sum_{i=1}^{\infty} c_i \sum_{j=1}^{M} w_j f(\|x_k - y_j\|)\psi_i(y_j) = \sum_{j=1}^{M} w_j \left[\sum_{i=1}^{\infty} c_i \psi_i(y_j)\right] f(\|x_k - y_j\|) = b(x_k), \quad 1 \le k \le n. \tag{a14}$$

Then:

$$\sum_{j=1}^{M} a_j f(\|x_k - y_j\|) = b(x_k), \quad 1 \le k \le n. \tag{a15}$$

where:

$$a_j = w_j \sum_{i=1}^{\infty} c_i \psi_i(y_j) \tag{a16}$$

For completeness,[87] a constant a_0 is added to (a15):

$$a_0 + \sum_{j=1}^{M} a_j f(\|x_k - y_j\|) = b(x_k), \quad 1 \le k \le n. \tag{a17}$$

After Equation (a17) is solved for a_0 and $a_j (j = 1, 2, \cdots, M)$, the solution to (a1) can be approximated by:

$$u_a(x) = a_0 + \sum_{j=1}^{M} a_j f(\|x - y_j\|), \quad x \in \Omega, \quad y_j \in \hat{\Gamma} \tag{a18}$$

The approximate solution u_a to equation (a1) is represented by a linear combination of fundamental solutions of the governing equation with the singularities $y_j, j = 1, 2, \cdots M$ placed outside the domain of the problem.

MFS is applicable not only to the above boundary value problem, but also to the Cauchy problem[54] that underlies ECGI. In this problem, both Dirichlet and Neumann boundary conditions are given only on portion of the boundary:[54]

$$\nabla^2 u(x) = 0, x \in \Omega \tag{a1}$$

Dirichlet conditions: $$u(x) = b(x), \; x \in \Gamma_1, \quad \Gamma_1 \subset \Gamma = \partial\Omega \tag{a19}$$

Neumann conditions: $$\frac{\partial}{\partial n} u(x) = i(x), \; x \in \Gamma_1, \quad \Gamma_1 \subset \Gamma = \partial\Omega \tag{a20}$$

For the Neumann condition (a20), the gradient at point x is along the outward normal to the boundary at that point. Similar to equation (a17), MFS can be used to discretize the Dirichlet and Neumann boundary conditions (equations (a19) and (a20)) as follows:

$$a_0 + \sum_{j=1}^{M} a_j f(\|x_k - y_j\|) = b(x_k), \quad x_k \in \Gamma_1, \quad k = 1,2,...,n, \quad y_j \in \hat{\Gamma}. \tag{a21}$$

$$\sum_{j=1}^{M} a_j \frac{\partial}{\partial n} f(\|x_k - y_j\|) = i(x_k), \quad x_k \in \Gamma_1, \quad k = 1,2,...,n, \quad y_j \in \hat{\Gamma}. \tag{a22}$$

After solving for the coefficients ($a_0, a_j, j = 1,2,\cdots M$), subject to the boundary conditions (a19) and (a20), the solution to (a1) can be approximated using Equation (a18).

Convergence analysis of MFS for Laplace's equation was conducted by Cheng.[96] When the problem boundary and boundary conditions are smooth functions, MFS converges exponentially to the solution of the problem. This analysis was conducted for 2D; Golberg and Chen[48] provided arguments that similar convergence properties exist in 3D.

Chapter 3 Real Time Electrocardiographic Imaging

Abstract

Electrocardiographic Imaging (ECGI) is a noninvasive modality for computation of cardiac epicardial potentials from measured body surface electrocardiographic potential data. ECGI was extensively validated in animal experiments and recently successfully applied in patients. The current ECGI mode of operation is offline with generation of epicardial potential maps delayed to data acquisition. Here we introduce a real time ECGI procedure, by which the epicardial potentials can be reconstructed while the body surface potential data are acquired (<1msec/frame) during a clinical procedure. This development enables real-time monitoring, diagnosis, and interactive guidance of intervention for arrhythmia therapy.

3.1 Introduction

Electrocardiographic Imaging (ECGI) is a noninvasive modality for imaging cardiac electrophysiological function. The details of the technique were extensively discussed in previous publications.[1-3,8] ECGI has been validated extensively in animal experiments under different physiological and pathological conditions.[6,7,97] Recently, it was also successfully validated and applied in patients.[1,2,11,15,17] In patients, ECGI has demonstrated its potential in the study of mechanisms of cardiac arrhythmias and in providing important information for patient evaluation and guidance of therapy (e.g.,

catheter ablation, pacing for resynchronization therapy in heart failure).

In the current ECGI procedure, a body surface potential map (BSPM) is recorded simultaneously from 256 body surface electrodes and digitized with a sampling frequency of 1kHz. The digitized BSPM data are saved on a hard drive of a computer for later offline inverse computation of epicardial potentials. The ECGI reconstructed epicardial potential data are typically available one day after the clinical procedure. We refer to this procedure as Offline ECGI. If the ECGI inverse computation could be executed as fast as the data acquisition speed (1kHz), which implies reconstruction time for one frame of data < 1ms, the epicardial potential information could be obtained during the BSPM recording, without any delay or data accumulation. We refer to this procedure as Real Time ECGI.

Conducting ECGI in real time can provide the physician with epicardial electrophysiological data during the clinical procedure, thus enabling real-time diagnosis and interactive guidance of intervention. In real-time mode of operation, ECGI could monitor cardiac electrophysiological function continuously, with higher sensitivity and specificity than the body-surface ECG.

In this report, we introduce a new procedure and algorithm that achieve Real Time ECGI. The procedure was tested and compared with Offline ECGI using data from animal

models, from a patient with myocardial infarction, and from a patient with atrial fibrillation.

3.2 Methods

3.2.1 Procedure for Offline ECGI

In offline ECGI, 256 ECG electrodes organized on strips are attached to the torso surface of the patient to record electrocardiographic body surface potential maps (BSPM) during as many cardiac cycles as desired. Following BSPM, a cardiac CT scan is conducted at the same patient posture with the electrodes in place. The heart-torso geometry is labeled and digitized from the CT images, and combined with the BSPM to compute epicardial potentials, electrograms, activation patterns (isochrone maps) and repolarization patterns on the heart surface off-line, following the procedure.

The body surface potential vector Vt can be related to the epicardial potential vector Ve by the transfer matrix A, which encodes the torso-heart geometrical relationship:

$$Vt = A*Ve \tag{3-1}$$

Assume that there are N torso surface electrodes and M epicardial surface sites, then Vt is a $N*1$ vector and Ve is a $M*1$ vector. The Singular Value Decomposition (SVD) of matrix $A \in R^{N*M}$ can be written as[98]:

$$A = U*S*V' = \sum_{i=1}^{P} u_i s_i v_i^{'}, \qquad P = \min(N, M) \tag{3-2}$$

where $U = (u_1, ..., u_P)$ and $V = (v_1, ..., v_P)$ are unitary matrices with orthonormal columns $U'*U = V'*V = I_P$, and $S = diag(s_1, ..., s_P)$ is a diagonal matrix with positive diagonal elements in a non-increasing order. The inversion of matrix A can be expressed as:

$$A^{-1} = V * S^{-1} * U' \tag{3-3}$$

Multiplying equation (3-1) by A^{-1} gives:

$$Ve = V * S^{-1} * U' * Vt \tag{3-4}$$

where $S^{-1} = diag(\frac{1}{s_1}, ..., \frac{1}{s_P})$.

Since the A matrix is ill-conditioned (condition number s_1/s_P is very large), the S^{-1} matrix can not be applied directly to compute A^{-1} and Ve. Instead, the Tikhonov Regularization method[99] is used to regularize the inverse procedure and obtain Ve:

$$\min_{Ve} \left\{ \left\| AVe - Vt \right\|^2 + t \left\| L * Ve \right\|^2 \right\} \tag{3-5}$$

where t is a regularization parameter. Note that this operation depends on Vt, which is different for each time frame during the cardiac cycle. Typically, Ve is computed for each millisecond during the cardiac cycle, and for each time frame operation (3-5) must be repeated. This operation is relatively slow in terms of computational time, precluding real time application of ECGI.

3.2.2 Mathematical Derivation of the Inverse Matrix B

Based on SVD, Tikhonov solution to Equation (3-5) can be written as[98]:

$$Ve = V * \sum_{i=1}^{P} \frac{fi}{si} * U' * Vt \tag{3-6}$$

where f_i $(i = 1, 2, ..., P)$ are called filter factors[98] and have the following form:

$$f_i = s_i^2 / (s_i^2 + t^2) \quad (i = 1, 2, ..., P) \tag{3-7}$$

t is the regularization parameter, which depends on the signal quality (decreases with increasing signal quality). Equation (3-6) indicates that for a selected t value, f_i dampens the contribution from small singular values, which are usually associated with measurement noise in the body surface potential Vt, stabilizing the epicardial potential solution Ve. Based on Equation (3-6), we can define an inverse matrix B as:

$$B = V * \sum_{i=1}^{P} \frac{fi}{si} * U' \tag{3-8}$$

and

$$Ve = B * Vt \tag{3-9}$$

This equation indicates that once the inverse matrix B has been computed, ECGI computation of Ve involves only matrix multiplication, a fast operation that can be achieved in real time.

3.2.3 Numerical Computation of Inverse Matrix B

Equations (3-8) and (3-9) imply that inverse matrix B is in fact the epicardial potential solution for a body surface potential Vt given by the $N * N$ identity matrix I. Therefore, we define N torso potential basis elements as: $Vt_1 = [1, 0, ..., 0]$, $Vt_2 = [0, 1, ..., 0]$, $Vt_N = [0, 0, ..., 1]$; the i_th torso potential basis element $Vt_i = [0, 0, ..., 1(ith), ..., 0]$ is the i_th column of the identity matrix I. Each of the torso

potential basis elements $Vt_i, (i = 1, 2, ..., N)$ can be expressed on the epicardial surface using Tikhonov regularization:

$$Ve_i = Tik(A, t, Vt_i), (i = 1, 2, ..., N) \tag{3-10}$$

where Ve_i are the corresponding epicardial potential basis elements. Obviously, the torso surface potential map can be expressed in terms of the torso potentials basis elements as:

$$Vt = Vt(1) * Vt_1 + Vt(2) * Vt_2 + ... + Vt(N) * Vt_N = \sum_{i=1}^{N} Vt(i) * Vt_i \tag{3-11}$$

Since $Vt = A * Ve$ and Tikhonov regularization are both linear operations, the corresponding epicardial potential can be computed as:

$$\begin{aligned} Ve &= Tik(A, t, Vt) = Tik(A, t, \sum_{i=1}^{N} Vt(i) * Vt_i) \\ &= \sum_{i=1}^{N} Vt(i) * Tik(A, t, Vt_i) = \sum_{i=1}^{N} Vt(i) * Ve_i = B * Vt \end{aligned} \tag{3-12}$$

where B is a $M * N$ matrix with the ith column equal to the Ve_i. Figure 3-1 is a diagrammatic description of this ECGI computational procedure.

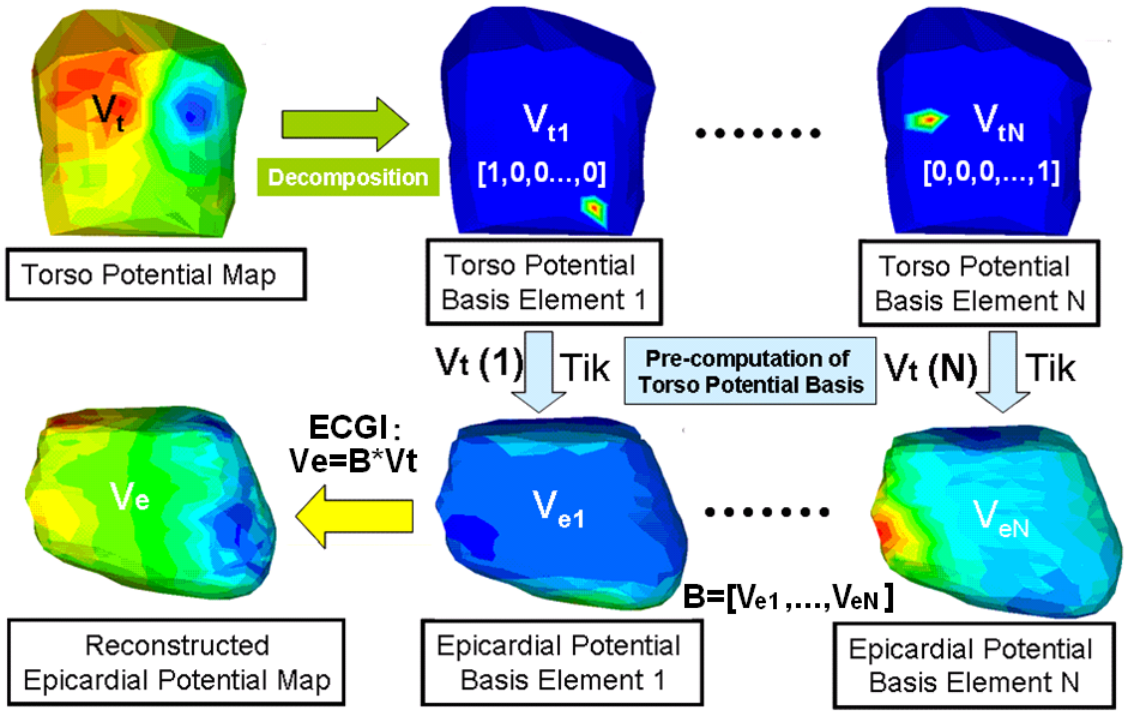

Figure 11 (Figure 3-1): The computation procedure of inverse matrix B and Ve. Tik indicates Tikhonov regularization.

3.2.4 Procedure for Real Time ECGI

Real Time ECGI requires a different protocol than offline ECGI (Figure 3-2). CT scan is conducted *before* any BSPM data are collected. After the CT images are obtained, the heart-torso geometry information is labeled and digitized while the patient with the electrodes attached at the same positions as during CT is transported to the EP procedure room. Scout BSPMs are recorded to evaluate the signal quality in the room based on which electrodes with low Signal to Noise Ratio (SNR) are excluded and an appropriate value for the regularization parameter t is obtained. [100] Based on the geometrical information, transfer matrix A (Equation 1) is computed and saved. From A and t, matrix B is computed following the scheme in the previous section. Once B and t are

available (before the start of the EP procedure), computing Ve involves only matrix multiplication (Equations (9), (12)) and epicardial potentials are computed in real time during the EP procedure. The key to Real Time ECGI is pre-computation of the inverse matrix B, to avoid repetition of operation (5) for every time frame.

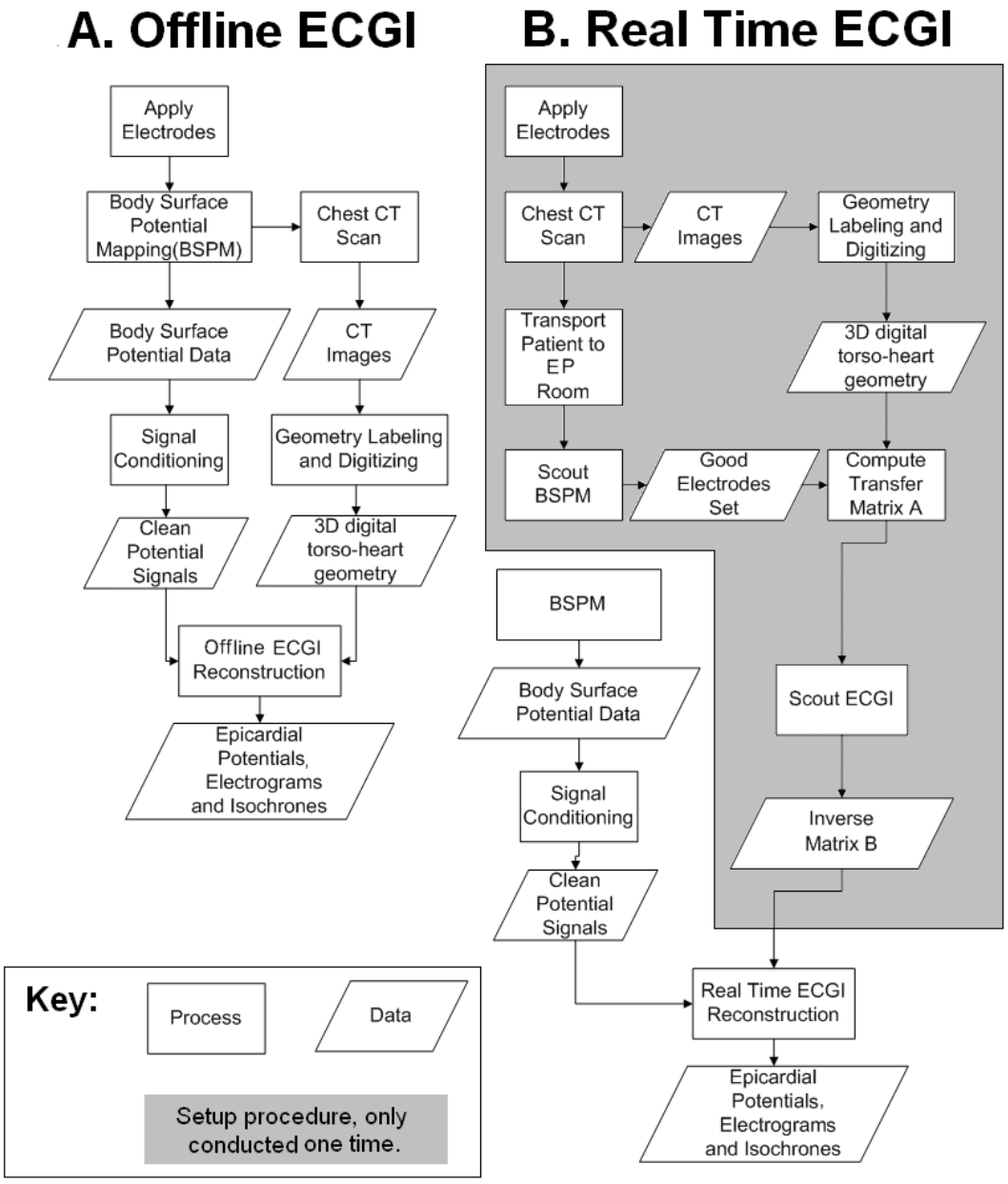

Figure 12 (Figure 3-2): Panel A: Offline ECGI procedure. Panel B: Real time ECGI procedure.

3.2.5 Experimental Methods and Protocols

ECGI is performed on data from three studies: (i) Single-site pacing in an isolated canine heart suspended in a human torso-shaped tank;[4] Data were obtained during pacing from a right ventricular (RV) anterior epicardial location.[101] (ii) Sinus rhythm data from a patient with healed myocardial infarction; (iii) Data from a patient with atrial fibrillation. Real time ECGI is compared to offline ECGI for these representative datasets.

All protocols were approved by the Institutional Review Board at Washington University in St. Louis, and informed consent was obtained from all patients. All the results were generated on a laptop computer with dual core processor (2.33GHz) and 3GB RAM.

3.3 Results

3.3.1 Single Site Pacing in a Human Torso-Shaped Tank

Figure 3-3, panel A shows real time ECGI epicardial potential map at 17ms after the QRS onset. The pacing site (white asterisk) is surrounded by negative potentials (blue). Real time and offline ECGI reconstructed the same epicardial potential maps. However, real time ECGI computes the map in 0.195 ms, about 30 times faster than offline ECGI. Epicardial electrograms from sites b, c (indicated on the epicardial potential map) are shown in Panel B and C respectively. The electrogram from site b, far away from the pacing site, shows a positive R morphology (Panel B).The electrogram c at the pacing

site (Panel C) is a pure negative Q waveform, reflecting an activation front propagating away from the pacing site. Real time ECGI reconstructed the same EGMs as offline ECGI.

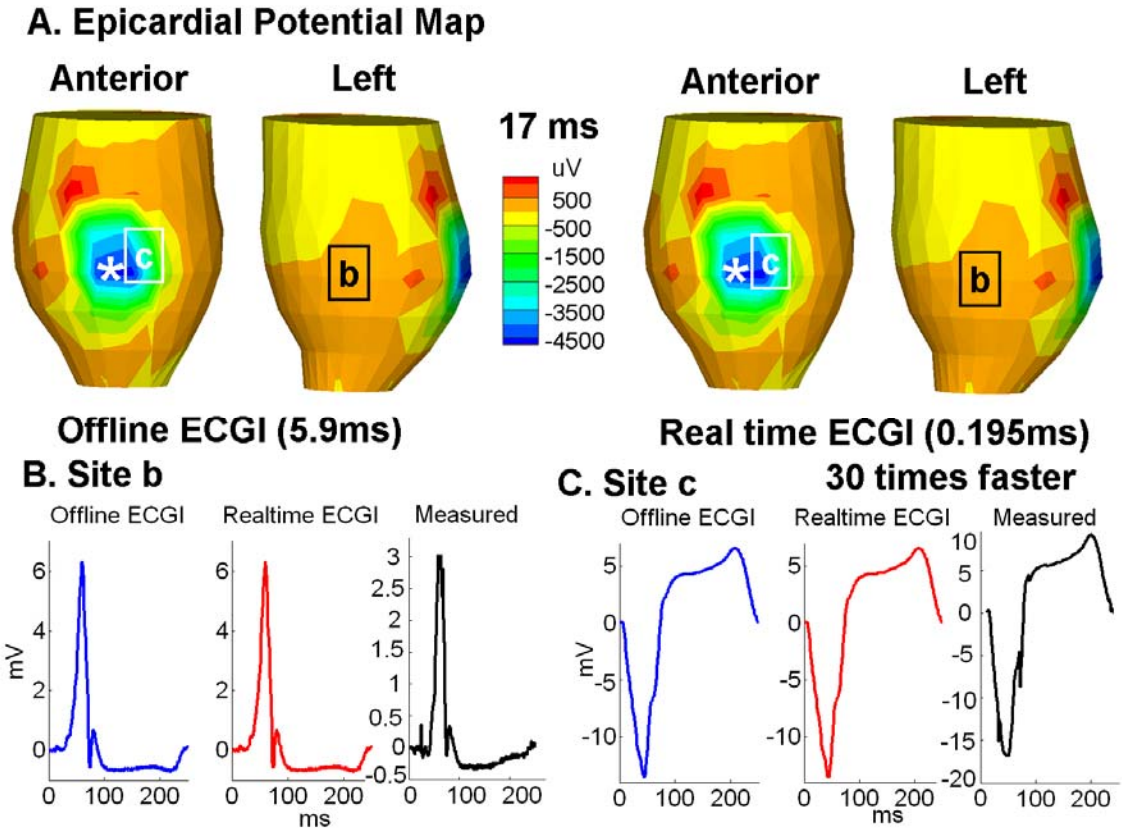

Figure 13 (Figure 3-3): Pacing from anterior RV site (*).

Panel A: Anterior and left views of ECGI reconstructed epicardial potential maps by offline ECGI (left panel) and real time ECGI (right panel). Panels B, C: Selected EGMs (from sites b and c) reconstructed by offline ECGI (blue), real time ECGI (red), and directly measured from the epicardium (black).

In this data set, there are 242 epicardial sites and 384 body surface electrodes, therefore the transfer matrix A is a 384*242 matrix. Different segments (100 frames, 200 frames,

400 frames, 800 frames, 1600 frames and 2000 frames) of body surface data were used to compare the computational efficiency of offline ECGI and real time ECGI. The results are summarized in Table 3-1. Total time refers to total computation time for all frames in a given data segment.

Table 1 (Table 3-1) Computational efficiency comparison for torso-tank data

BSPM segment (ms)	100	200	400	800	1600	2000
Total Time, Offline ECGI (ms)	891	1437	2360	5359	13593	19515
Total Time, Real time ECGI (ms)	32	47	78	157	313	422
Time per Frame, Offline ECGI (ms)	8.91	7.185	5.90	6.6988	8.4956	9.7575
Time per Frame, Real time ECGI (ms)	0.32	0.235	0.195	0.1963	0.1956	0.211

The data in Table 3-1 are visualized in Figure 3-4. The top three panels show that the total computation time of offline ECGI increases exponentially with the segment-length of input data, while the total computation time of real time ECGI increases roughly linearly. For data collected in 2 seconds, it only takes 0.422 seconds for real time ECGI to compute the epicardial potentials, while offline ECGI requires19.515 seconds (a factor of

46). The bottom 3 panels of figure 3-4 show that real time ECGI can execute inverse computation for one frame (1ms data) well within 1ms. This means that following data acquisition and digitization at 1kHz, real time ECGI can generate epicardial potentials for the frame before the next frame is recorded.

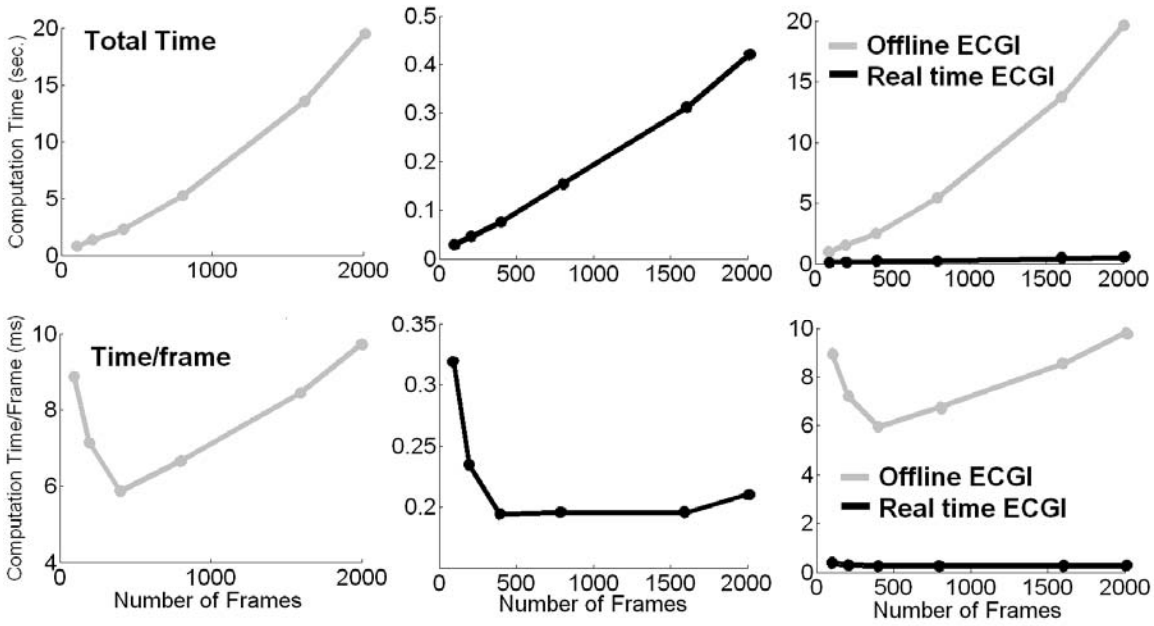

Figure 14 (Figure 3-4): Comparison of computational efficiency of offline and real time ECGI.

Top left: Relationship between total offline ECGI computation time and length of data segment. Top middle: Relationship between total real time ECGI computation time and length of data segment (Note different scale from top left). Top right: comparison of offline and real time ECGI computation times on the same scale. The bottom panels show computation times per single frame (same format as top panels).

For Offline ECGI, matrix decomposition is always performed and is independent of the

BSPM data segment. When the data segment is short (<400ms; <400 frames), most of the computing time is spent on the matrix decomposition. In this situation, the total computing time increases slowly with the segment length, but the computing time per frame decreases. When the data segment is long (>800ms; >800 frames), data manipulation becomes the major computational load. In this situation, the total computing time increases dramatically with segment length. Because the system memory is limited, computing time per frame also increases. This explains the slower initial increase and faster later increase in total time, and the non-monotonic dependence (decrease then increase) of time per frame on the length of the data segment (gray curves in Figure 3-4)

For real time ECGI, because the major computational load is matrix multiplication, total computing time increases linearly with the length of the BSPM data segment before the system memory becomes a "bottleneck" for computing. Computing time per frame becomes essentially constant after initial oscillation, which is probably due to Matlab® management of system memory. When the data segment becomes very long (>1600 ms;1600 frames) relative to available memory, total computing time increases nonlinearly, and computing time per frame increases as well. This is demonstrated by the black curves in the middle panels of Figure 3-4.

3.3.2 Sinus Rhythm Data from a Patient with Healed Myocardial Infarction (MI)

Figure 3-5, panel A shows real time ECGI computed epicardial potential map at 10ms

after the QRS onset during sinus rhythm. Real time ECGI and offline ECGI reconstructed the same epicardial potential maps. Epicardial EGMs from site b, c, d, labeled on the epicardial potential maps, are shown in Panel B, C, and D, respectively. The EGM at site b (Panel B) demonstrates an rS morphology. EGM from left ventricular (LV) site c demonstrates R morphology (Panel C), and EGM from inferior site d demonstrates RS morphology (Panel D). Offline ECGI and real time ECGI reconstructed the EGMs with the same morphologies and magnitudes.

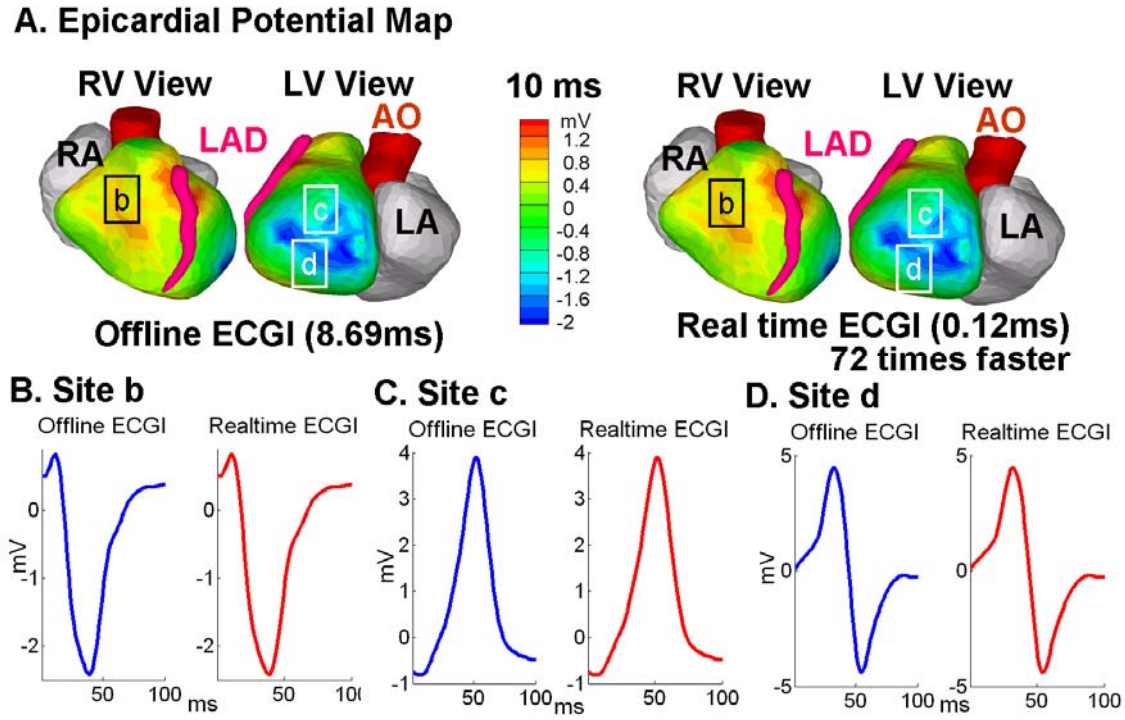

Figure 15 (Figure 3-5): Sinus Rhythm Post-MI.

Panel A: Two views (RV and LV) of ECGI reconstructed epicardial potential maps by offline ECGI (left panel) and real time ECGI (right panel). Selected EGMs (from sites b, c and d) reconstructed by offline ECGI (blue) and real time ECGI (red) are shown in Panel B, C and D.

In this data set, there are 502 epicardial sites and 242 body surface electrodes, therefore the transfer matrix A is a 242*502 matrix. This is a typical size of transfer matrix A in ECGI application. Similar to the data from the Torso-Shaped Tank, different segments (100 frames, 200 frames, 400 frames, 800 frames, 1600 frames and 2000 frames) of body surface data were used to compare the computational efficiency of offline ECGI and real time ECGI. The results are summarized in Table 3-2.

Table 2 (Table 3-2) Computational efficiency comparison for SR data in a healed MI patient

BSPM segment (ms)	100	200	400	800	1600	2000
Total Time, Offline ECGI (ms)	453	719	1563	4187	13906	20078
Total Time, Real time ECGI (ms)	15	31	63	94	187	234
Time per Frame, Offline ECGI (ms)	4.53	3.595	3.9075	5.2337	8.6913	10.039
Time per Frame, Real time ECGI (ms)	0.15	0.1550	0.1575	0.1175	0.1167	0.1170

The data in Table 3-2 are visualized in Figure 3-6. Similar observation can be made as in the Torso-Shaped Tank data. Real time ECGI reconstructs one frame of epicardial potential (1ms data) well within 1ms, which is far beyond the capability of offline ECGI.

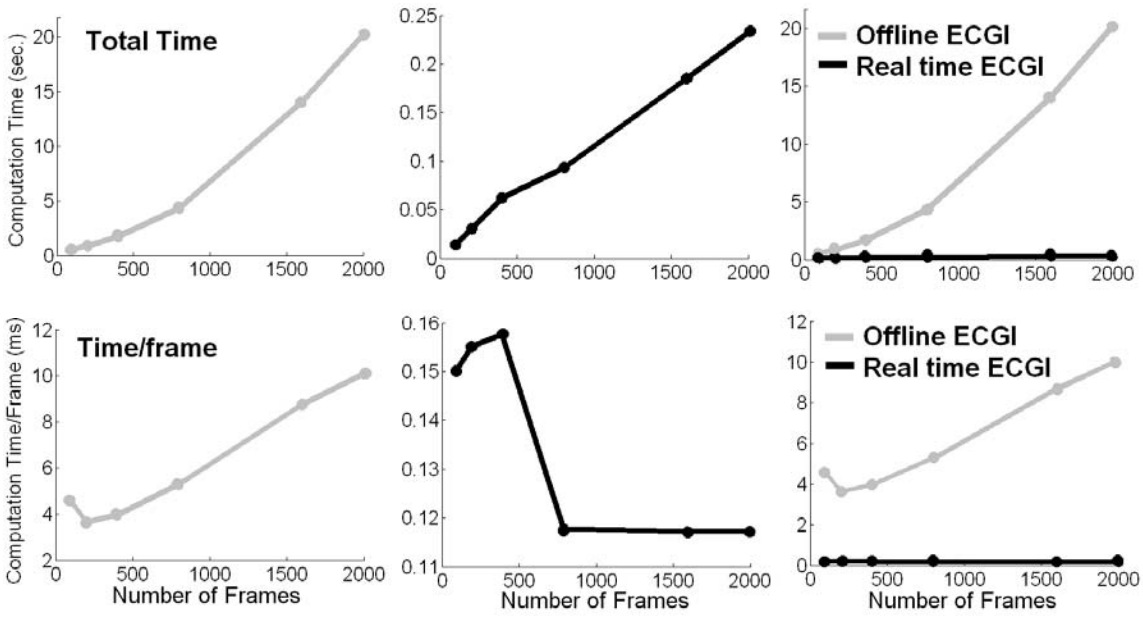

Figure 16 (Figure 3-6): Comparison of computational efficiency of offline and real time ECGI.

Same format as Figure 3-4.

3.3.3 Data from a patient with Atrial Fibrillation

Figure 3-7, Panel A shows real time ECGI computed epicardial potential map at 142 ms from start of the recording. Both right atrium (RA) and left atrium (LA) are shown in the map. Real time ECGI and offline ECGI reconstructed the same epicardial potential maps. Epicardial electrograms from site b, c and d, labeled on the epicardial potential maps, are shown in Panel B, C and D, respectively. EGM b close to the left superior pulmonary vein (Panel B) is fragmented with high frequency components. EGM c from a right superior pulmonary vein site is more regular with almost no high frequency fractionation (Panel C). EGM d from a RA free wall site is of regular morphology with no fractionation (Panel D). This progression indicates a gradient in the degree of

fractionation from LA to RA. Offline ECGI (blue) and real time ECGI (red) reconstructed the same EGMs.

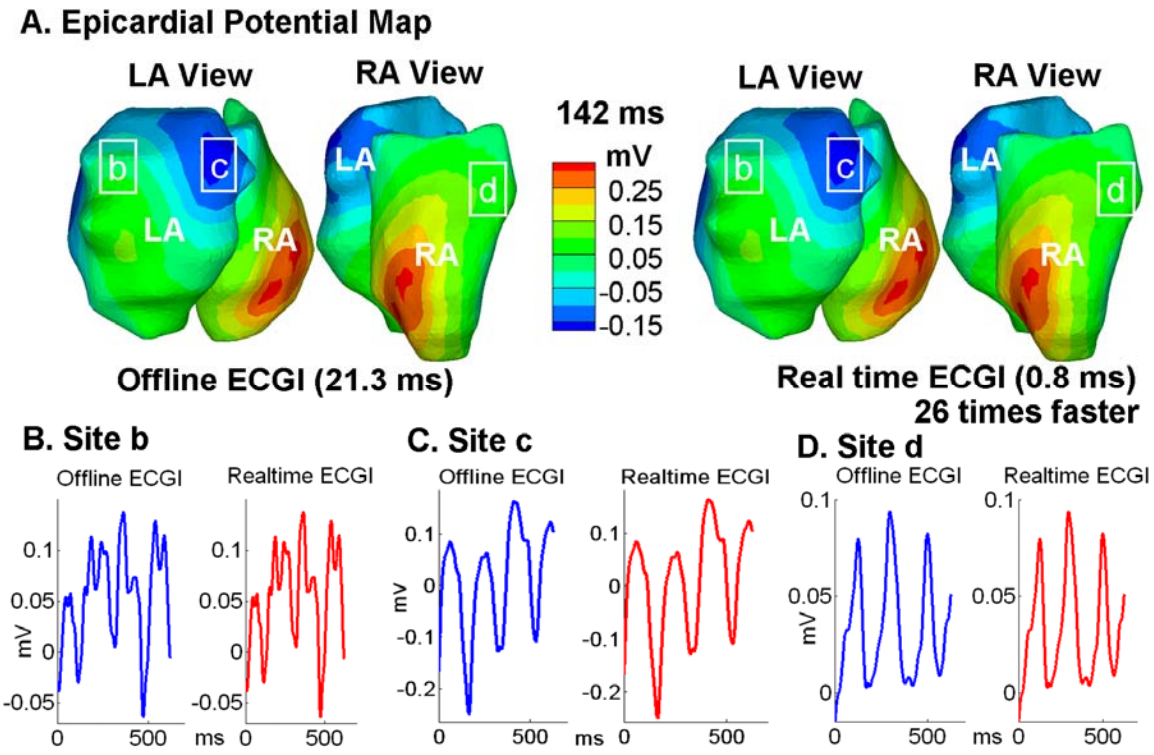

Figure 17 (Figure 3-7): Atrial fibrillation data

Panel A: Two views (LA and RA) of ECGI reconstructed epicardial potential maps by offline ECGI (left panel) and real time ECGI (right panel). Selected EGMs (from sites b, c and d) reconstructed by offline ECGI (blue) and real time ECGI (red) are shown in Panels B, C and D.

In this data set, there are 4004 epicardial sites and 217 body surface electrodes, therefore the transfer matrix A is a 217*4004 matrix. This is a high resolution transfer matrix A in ECGI application. Similar to the data from the Torso-Shaped Tank, different segments (100 frames, 200 frames, 400 frames, 800 frames, 1600 frames and 2000 frames) of body

surface data were used to compare the computational efficiency of offline ECGI and real time ECGI. The results are summarized in Table 3-3.

Table 3 (Table 3-3) Computational efficiency comparison for atrial fibrillation data

BSPM segment (ms)	100	200	400	800	1600	2000
Total Time, Offline ECGI (ms)	2234	3438	6234	13281	34078	46703
Total Time, Real time ECGI (ms)	79	171	328	656	1312	1640
Time per Frame, Offline ECGI (ms)	22.34	17.19	15.585	16.5225	21.2987	23.3515
Time per Frame, Real time ECGI (ms)	0.79	0.855	0.820	0.820	0.820	0.820

The data in Table 3-3 are visualized in Figure 3-8, showing similar behavior to the two previous examples. Real time ECGI reconstructs one frame of epicardial potential (1ms data) within 1ms (0.82ms) and therefore in real time. However, compared to the two previous examples, the computation time per frame is increased. This is mainly due to the high density of epicardial sites (4004 sites). This very high resolution was chosen to challenge real time ECGI for evaluation purpose; it is more than needed in clinical applications. For the same resolution, offline ECGI computed 1ms of data in 21.3 ms, far beyond what is required for real time application.

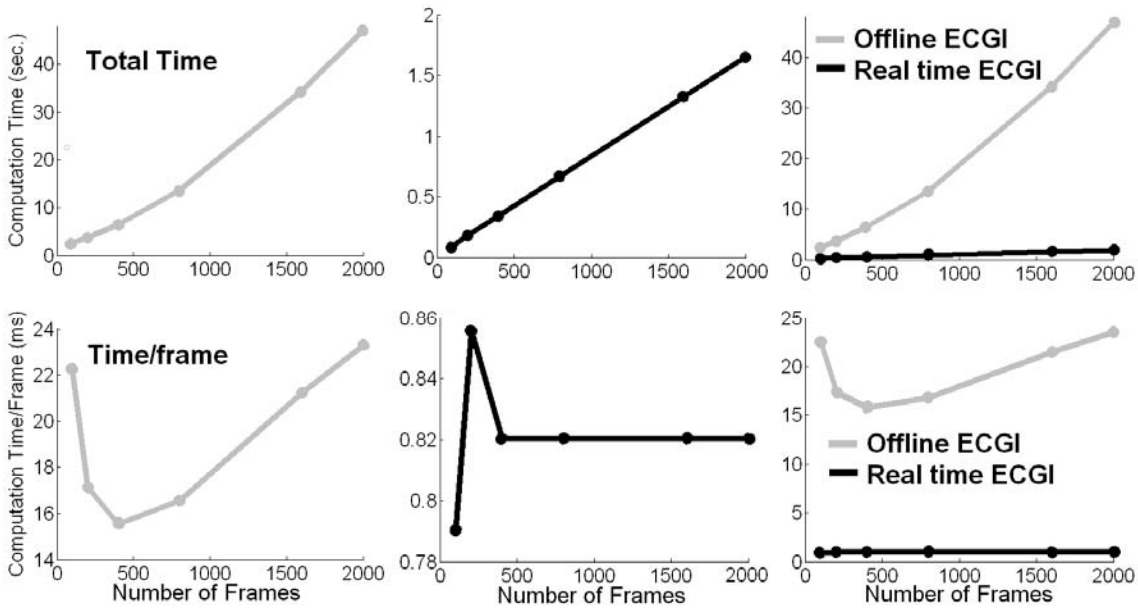

Figure 18 (Figure 3-8): Comparison of computational efficiency of offline and real time ECGI. Same format as Figure 3-4.

3.4 Discussion

The Real Time ECGI introduced in this manuscript can reconstruct epicardial potentials from BSPM recordings during data acquisition without delay. In addition to the obvious importance of real-time performance during clinical intervention (catheter ablation, application of pacing electrodes, drug delivery), it enables the use of ECGI in long-term monitoring of cardiac patients. This is particularly useful in patients with dynamically changing arrhythmias such as atrial fibrillation, unstable or polymorphic ventricular tachycardia, etc.

The approach described in this paper is a computational framework that does not depend

on the specific type of numerical methods used in ECGI. Boundary Element Method (BEM) was used to construct the transfer matrix A for the data from the torso-tank experiments and from the post-MI patient. The Method of Fundamental Solution (MFS) [102], a mesh-free numerical method, was adapted for ECGI previously. Here, we applied MFS instead of BEM in real time ECGI of the atrial fibrillation data. Similarly, other types of numerical methods such as the Finite Element Method (FEM), or Radial Basis Function (RBF) method[85] can also be used in the Real Time ECGI framework as proposed.

The key to Real Time ECGI is the pre-computation of inverse matrix B. The computation of matrix B is conducted during the downtime before the start of the clinical procedure or a research protocol. Once the B matrix is available, the ECGI inverse computation becomes a process of matrix multiplication. Although all the examples described in this manuscript use Matlab® to conduct the matrix multiplication, computation of matrix B can be integrated into the data acquisition software or output to a custom designed computation hardware to provide even faster matrix multiplication.

The real time ECGI procedure proposed in this paper requires that the regularization method is a linear process and does not depend on the BSPM data recorded during the procedure. Therefore, only direct regularization methods such as Tikhonov regularization can be employed in the framework of real time ECGI. Non-stationary iterative

regularization methods, such as GMRes [101] and other Krylov-Subspace based iteration methods, depend on the BSPM data for convergence and are not suitable for real- time ECGI.

The examples described in this manuscript employed the Tikhonov method with pre-calculated CRESO[103] regularization parameter t. The t value depends on the BSPM signal quality. High quality signals (high signal/noise ratio) require only a small t, while lower quality signals require a larger t and greater regularization. The data acquisition environment affects the signal quality during the study. We determine an optimal t-value before the procedure by conducting pilot recordings in the same environment where the procedure will be conducted.

Chapter 4 Characterization of EP substrate in Post-Myocardial Infarction Patients using Noninvasive Electrocardiographic Imaging (ECGI)

Abstract

Post-myocardial infarction (MI) scar-related arrhythmias are a life threatening rhythm disorder. However, our ability to map and ablate these arrhythmias is limited by current invasive mapping techniques. In this study, we applied a novel imaging modality for cardiac electrophysiology and arrhythmia (Electrocardiographic Imaging, ECGI) to map noninvasively the electrophysiological substrate in eight post-MI patients during sinus rhythm (SR). Contrast-enhanced MRI (ceMRI) was conducted to determine anatomical scar. ECGI imaged regions of low potentials with long duration, fractionated electrograms that corresponded closely in location, extent, and morphology to the anatomical scars. In three patients, late diastolic potentials were imaged in the scar epicardial border zone during SR. We also imaged scar-related ventricular tachycardia (VT) in two patients, showing the VT activation sequence in relation to the abnormal electrophysiological substrate. ECGI can noninvasively image the altered electrophysiological substrate properties of a post-MI scar and map the activation patterns during SR and VT in a beat-by-beat fashion. Imaging the substrate could potentially help in noninvasive risk stratification for post-MI arrhythmias and facilitate substrate-based catheter ablation of these arrhythmias.

4.1 Introduction

Scar-related arrhythmias are the most common cause of sudden cardiac death. Intraoperative mapping techniques have identified the border zone between scarred and normal myocardium as the predominant substrate for development of ventricular tachycardia (VT) in post-MI patients.[104,105] In patchy and nonuniform border zone, electrically active myocardial tissue is interspersed within fibrous scar tissue. This creates local mismatches of electrical properties that lower the safety factor for conduction and result in substrate for reentrant VT.[106-108] Identification and characterization of such arrhythmogenic substrates before an arrhythmia occurs could reduce the risk of sudden death by indicating the need for device, drug, or ablation therapy.

Current noninvasive methods for characterizing abnormal substrates rely on the 12-lead ECG[109-112] in combination with other imaging modalities such as computed tomography (CT), magnetic resonance imaging (MRI), nuclear imaging, and positron emission tomography (PET) [113-116] However, these methods cannot provide detailed electrophysiologic (EP) information about the cardiac substrate. Body surface potential mapping has been used to estimate the location of abnormal EP substrate.[109-111,117] However, this approach is limited by low specificity and challenges with interpretation of low amplitude signals measured far from the heart.[112] Invasive EP mapping techniques have become an important tool for characterizing the scar substrate and for guiding

catheter ablation of VT.[118-122] So far, invasive substrate mapping during sinus rhythm is mostly conducted on the endocardial surface using intracardiac catheters. Because not all VTs originate from the endocardium and may involve epicardial components of the reentry circuit,[123,124] a percutaneous subxyphoid puncture technique has been developed, permitting mapping and ablation on the epicardial surface.[125] This technique is invasive and carries risk.[125] An accurate, noninvasive EP imaging tool would be helpful to delineate the location and extent of the scar substrate during sinus rhythm and characterize its electrophysiologic properties.

Experimental and clinical studies have shown that abnormal electrical properties associated with a scar substrate are reflected in specific characteristics of cardiac potential distributions and electrograms. [126-129] Canine studies in a 5-day old infarct showed low-level fractionated electrograms in the infarct substrate, which correlated with slow, discontinuous conduction; a property that supports arrhythmogenicity [130]. Low-amplitude potentials, broad fractionated electrograms, and delayed activation were recorded from a human infarcted papillary muscle[107] and during invasive mapping in post-MI patients with history of VT.[131-134] Our laboratory has demonstrated the ability of a new noninvasive EP imaging modality (Electrocardiographic Imaging, ECGI) to reconstruct, from body surface potentials, such characteristics of epicardial potentials and electrograms over the scar region in animal (canine) experiments[8,23,24,97] In this study, we use ECGI to reconstruct such electrical properties and to characterize the

electrophysiological substrates in patients with structurally abnormal myocardium (healed MI). Through image-fusion techniques, we combine the ECGI electrophysiological images with delayed-contrast MRI anatomic images and correlate electrophysiological properties with structural scar information.

4.2 Methods

Eight patients included in this study had histories of myocardial infarction (>=3 months). All protocols were approved by the Human Research Protection Office at Washington University in St. Louis, and informed consent was obtained.

ECGI methodology was described previously [1]. 256 carbon electrodes were applied to the patient's torso and connected to a portable mapping system (BioSemi, Netherlands). After CT markers were attached to each electrode, the patients underwent thoracic non-contrast gated CT imaging (70% of R-R interval) with an axial resolution of 1mm. The 256 electrodes were kept in the same position during ECGI data acquisition as in the CT scanner. Ventricular epicardial surface geometry and body surface electrode positions were labeled and digitized from the CT images. 256 channels of body surface potentials (BSP) were sampled at 1-ms intervals during the cardiac cycle, and the data were saved on a laptop computer. The ECGI procedure is summarized in Figure 4-1.

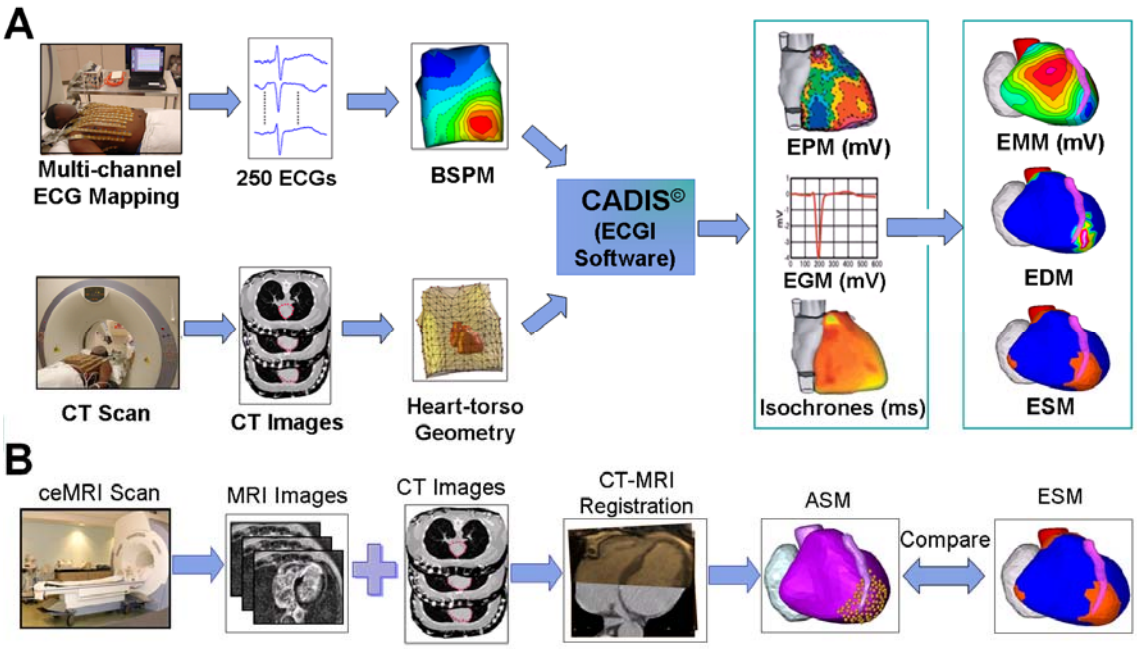

Figure 19 (Figure 4-1): Study procedure

Panel A: The ECGI Procedure. 256 carbon electrodes are applied to the subject's torso to measure 256 ECGs. The subject then undergoes a thoracic CT scan, which provides epicardial surface geometry and torso-electrode positions in the same reference frame. The potential and geometry data are processed mathematically to obtain noninvasive ECGI epicardial images that include EPM, EGM, activation and repolarization sequences. From these data, EMM, EDM and ESM are constructed.

Panel B: Comparing the EP scar to the anatomical scar. To image the anatomical scar, contrast enhanced MRI images are obtained from six patients without implanted devices, and SPECT images are obtained from the other two. CT and MRI images are co-registered to construct the ASM, which is compared to the ESM. EDM = EGM Deflection Maps (number of deflections per EGM during SR); EPM = Epicardial Potential Maps; EMM = EGM Magnitude Maps (peak-to-peak EGM QRS magnitude during SR); ESM= EP Scar Map (based on EMM and/or EDM); AI = Activation Isochrones; ASM = Anatomical Scar Map (from contrast-enhanced MRI).

The BSP and torso-heart geometrical relationship were combined by ECGI algorithms to noninvasively construct epicardial potential maps, electrograms (EGM), activation sequences (isochrones) and repolarization patterns[1]. ECGI is constructed on a beat-by-beat basis and does not require accumulating data from many identical beats (as required with the "roving-probe" approach of catheter mapping). Activation times were determined by the maximal negative slope of the epicardial electrograms and used to construct isochrone maps. Lines of block (LOB) were determined if local activation times differed by more than 50ms. Slow conduction is represented by crowded isochrones. Activation movies for consecutive beats were also constructed by animating the activation wavefront on the epicardial surface. For each frame of ECGI data, a corresponding frame depicting the three dimensional spatial locations of activation sites was generated. The activation wavefront connecting these sites was displayed as a red line on a blue epicardial surface. Once all time frames were processed in this fashion, an activation movie was generated to display propagation of the wavefront. Repolarization data (T wave) was excluded between consecutive beats of VT.

Gadolinium-enhanced cardiac magnetic resonance (MR) scans were conducted on 6 of the patients to obtain images of the infarct anatomical substrate. MRI was performed on a 1.5T MR system (Sonata: Siemens Medical Solutions, Malvern, PA) with maximum gradient capabilities (40 mT/meter gradient strength: 200 mT/meter/sec slew rate). The

study was ECG-gated. After obtaining scout true Fast Imaging with Steady Precession (FISP) images to determine the short and long axis views of the heart, 0.2 mmol/Kg gadolinium-based MR contrast agent (Optimark; TycoHealthcare, Mallinckrodt, St. Louis, MO) was injected at 1 cc/sec via a compatible power injector. After a 10-minute delay, two-dimensional T1-weighted inversion recovery segmented fast gradient recalled echo images (repetition time 8 ms, echo time 4 ms, flip angle 30 degrees, segments 13, field-of-view 300-380 mm, matrix 256 x 172, triggered every 2 heartbeats) were obtained. Images were obtained in the short axis plane of the heart from the base of the left ventricle to the apex. Images were obtained contiguously every 8 mm. To determine the appropriate inversion recovery time, a scout sequence was run after the gadolinium injection and just prior to the 10-minute delayed acquisition, allowing the operator to select inversion recovery time to best null the myocardium. The infarct regions were labeled and digitized as anatomical scar substrate. Registration between the MR and CT images was established based on the normalized mutual information. For two patients, nuclear single photon emission computed tomography (SPECT) data were collected retrospectively for qualitative comparison and analysis. The anatomic scar imaging and the ECGI scar imaging were performed independently to eliminate bias.

4.3 Results

4.3.1 Patient #1,#2, and #3: Characteristics of Post-MI Electrical Substrate

ECGI-imaged electrical characteristics of the epicardial substrate and MR-imaged

anatomical scar for Patient 1 are shown in Figure 4-2. In Panel A, isochrone map shows earliest activation at the superior RV (white asterisk), propagating towards inferior RV and LV (white arrows). One wavefront encounters a long LOB along the septum, as shown by left anterior descending coronary artery (LAD). The other wavefront propagates slowly and counterclockwise around the LOB, activating the LV in a typical left bundle branch block (LBBB) pattern. Magnitude map shows the epicardial distribution of EGM magnitude ("voltage map"). The lowest magnitude region (blue) is located at the apical LV, near the distal LAD. The boundaries of the low magnitude region coincide with the LOB in the isochrone map. Deflection map shows the epicardial distribution of EGM fractionation. The most fragmented EGMs are located at the apical LV region. EP scar map labels the electrical scar in red by thresholding magnitude map (smaller than 30% of maximum EGM). Four selected EGMs (a-d) from a non-scar region and four selected EGMs (e-h) from the scar region are shown (note different voltage scale), demonstrating much smaller magnitudes and high degree of fragmentation. In Panel B, the anatomical scar is labeled from registered MR-CT images using yellow markers. The anatomical scar map correlates well with the EP scar map of panel A in terms of location, size and morphology of the scar.

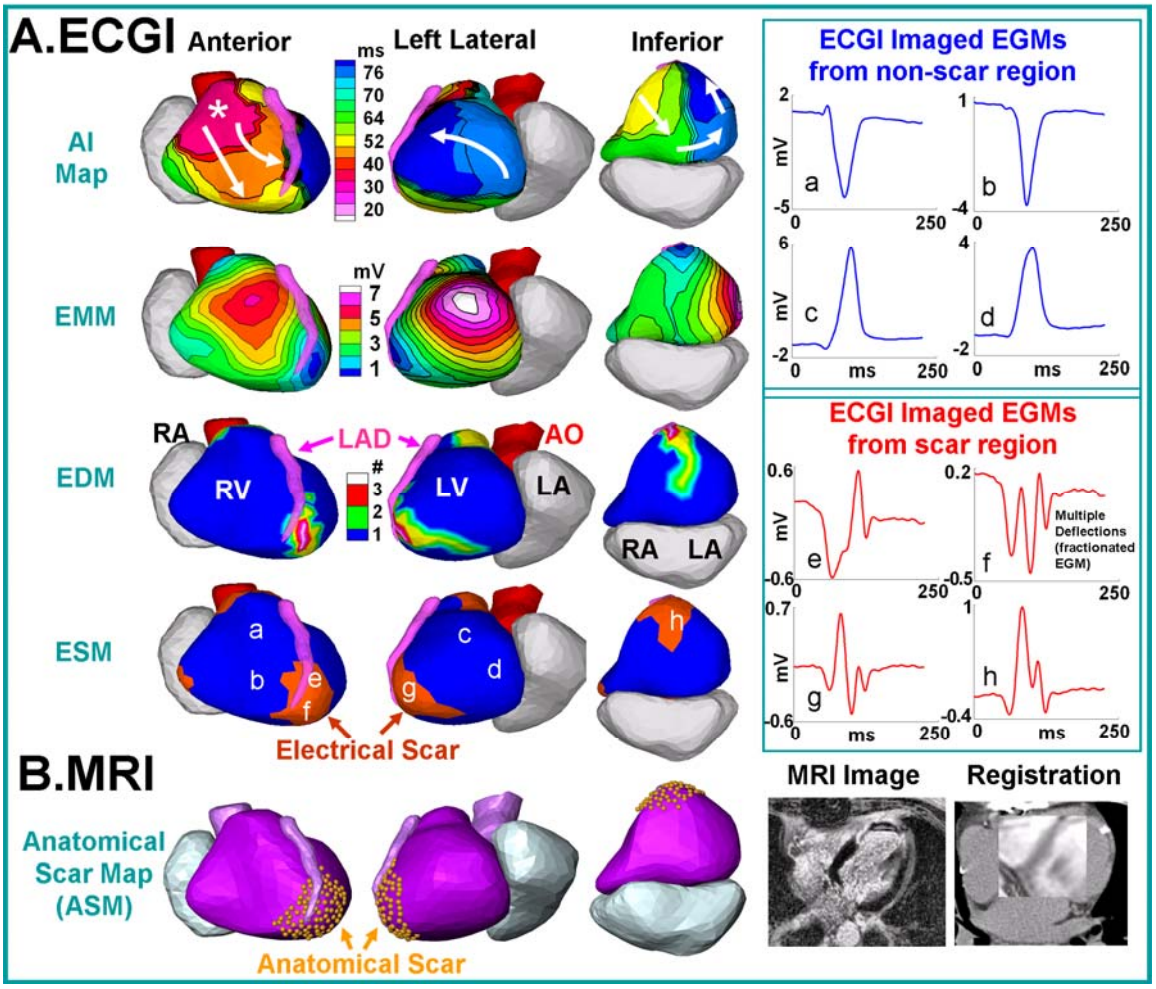

Figure 20 (Figure 4-2): ECGI images for patient 1

Panel A: ECGI AI map, EMM, EDM and ESM in three views. White asterisk in AI map shows the RV breakthrough site and white arrows show direction of wavefront propagation. Eight selected EGMs from non-scar region of ESM (blue) and from scar region (red) are shown on the right. **Panel B:** ASM in the same three views based on MRI-CT registered images. MRI image and CT-MRI registration results are shown on the right.

ECGI data for Patient 2 are shown in Figure 4-3. In Panel A, the isochrone map shows a normal sinus rhythm (SR) epicardial activation sequence. A region in the inferior view of

isochrone map demonstrates earlier activation than the normal RV breakthrough, (pink) which suggests diastolic activities within an inferior scar. Magnitude map shows low magnitude regions (blue) over inferior, superior, and apical regions of the heart. The low amplitude region at the inferior base coincides with the LOB in the inferior isochrone map. Deflection map shows regions of highly fragmented EGMs on the inferior surface of the heart. EP scar map labels the electrical scar (red). Six selected EGMs (a-f) from the scar region are depicted, showing low magnitudes and fractionation. Two selected EGMs (g-h) from the non-scar region are also shown, with much larger magnitude without fragmentation. In Panel B, the anatomical scar is labeled using yellow markers. Because the slice thickness (8mm) of the MR scan is larger than that of the CT (1mm), the superior basal scar is not captured by MRI. The location of the electrical scar (EP scar map) and anatomical scar (anatomical scar map) are well correlated, but the electrical scar is somewhat larger than the anatomical scar, suggesting the presence of an electrophysiological border zone.

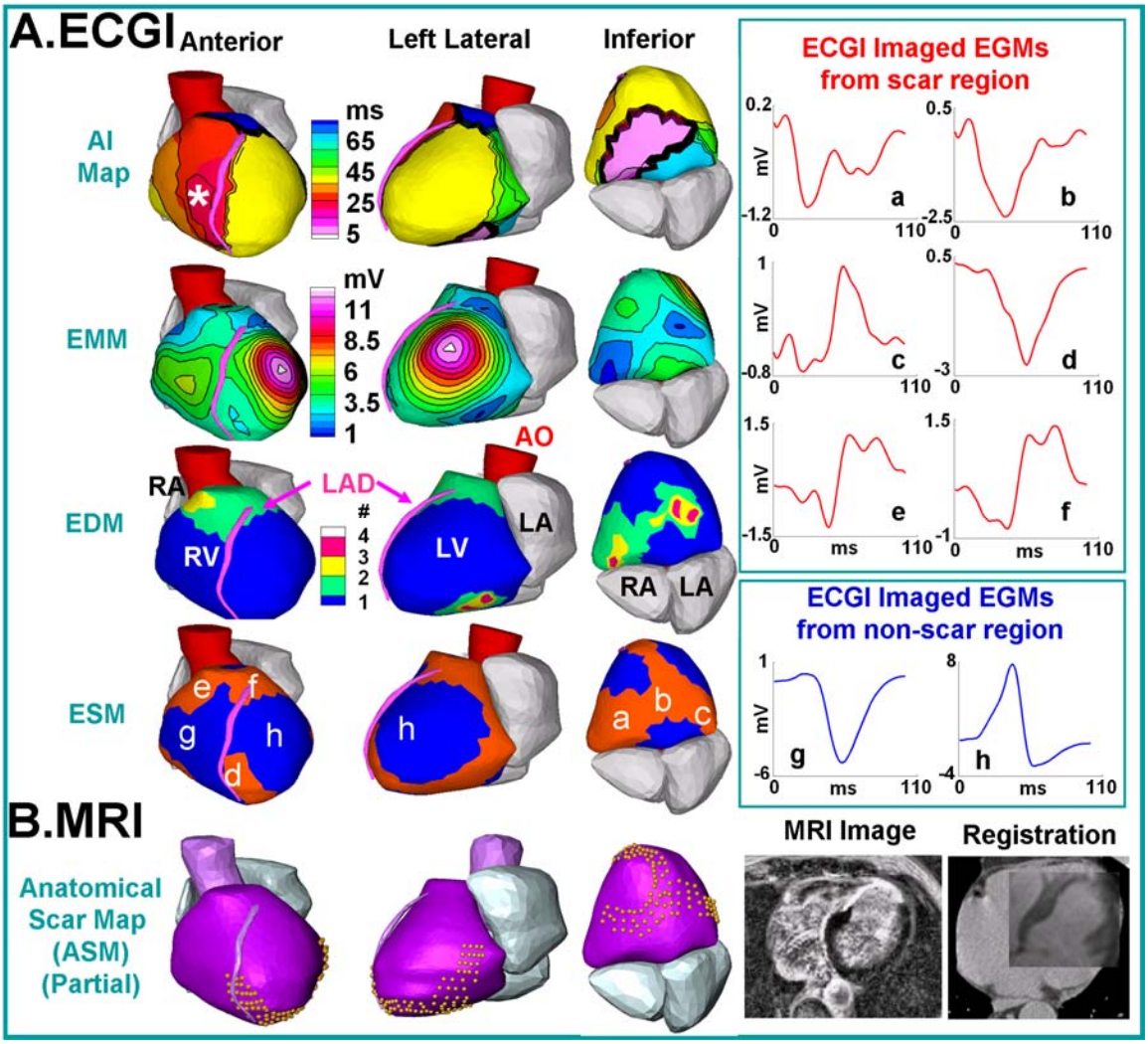

Figure 21 (Figure 4-3): ECGI images for patient 2

Panel A: ECGI AI map, EMM, EDM and ESM in three views. White asterisk in the AI map shows the RV breakthrough site. Eight selected EGMs from non-scar region of ESM (blue) and from scar region (red) are shown on the right. **Panel B**: ASM in the same three views based on CT-MRI images. MRI image and CT-MRI registration results are shown on the right.

ECGI data for Patient 3 are shown in Panel A and B of Figure 4-4. In Panel A, the isochrone map shows a normal sinus rhythm epicardial activation sequence. The RV

breakthrough site is labeled by a white asterisk and lateral LV is activated last (light blue). Similar to the patient 2, the scar region in the inferior view of isochrone map shows earlier activation than the normal RV breakthrough, suggesting the diastolic activities within the scar. Magnitude map shows low potential regions (blue) over inferior, right lateral, and mid-LV part of the heart. Similar to patient 2, the low potential region at the inferior base (site d, e and f) coincides with the LOB in the inferior isochrone map. EP scar map labels the electrical scar (red). Four selected EGMs (c-f) from the scar region are depicted in red, showing low magnitudes and fractionation. Two selected EGMs (a-b) from the non-scar region are depicted in blue, showing much larger magnitude without fragmentation. In Panel B, parts of the anatomical scar are labeled using yellow markers from MR images, after they are registered to CT images.

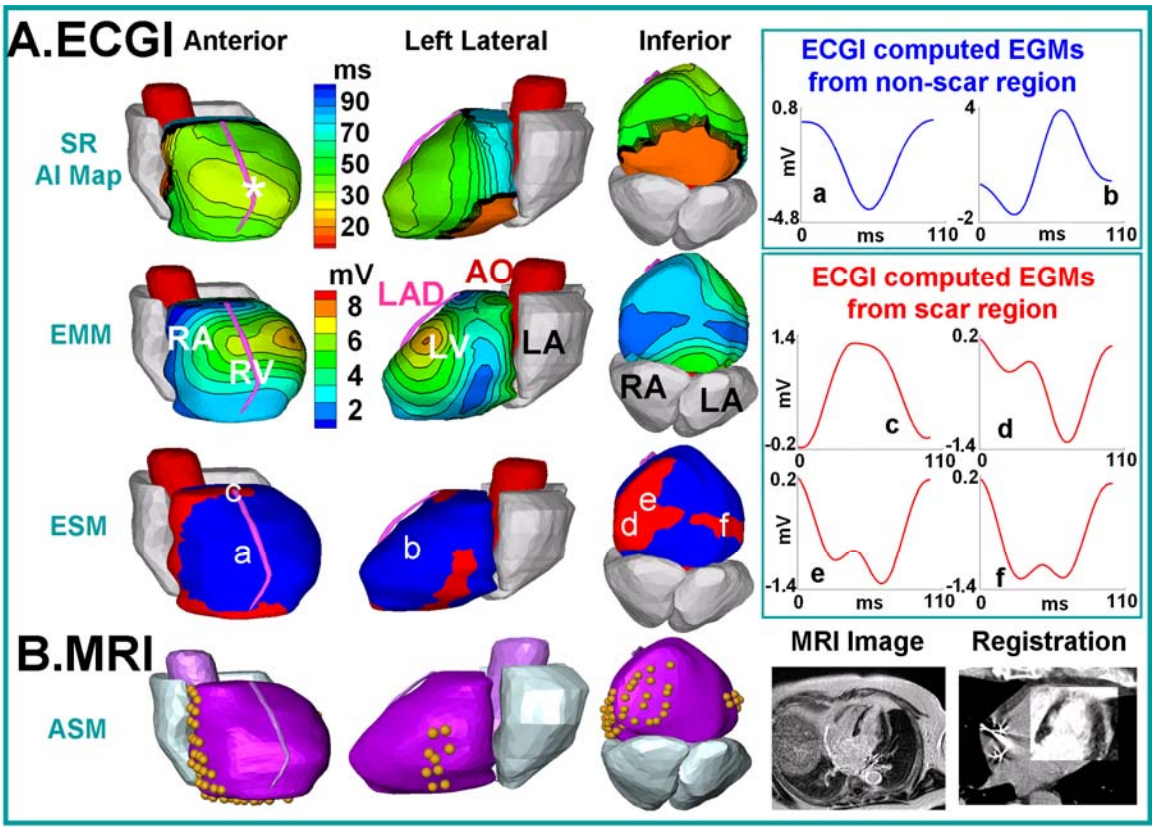

Figure 22 (Figure 4-4): ECGI images for patient 3

ECGI AI map during SR, EMM and ESM are shown in three partially overlapping views. In the SR AI map, the RV breakthrough site is labeled by white asterisk. Six selected EGMs from non-scar region of ESM (blue) and from scar region (red) are shown on the right. Panel B shows the ASM in the same three views based on CT-MRI images. A typical contrast-enhanced MR image and CT-MRI registration result are shown on the right.

4.2.2 Patient #4, #5 and #6: Diastolic Late Potentials Post-MI

Diastolic late potentials were observed in three of the patients (patient #4, #5 and #6). ECGI images for Patient 4 are shown in Figure 4-5. The EP scar map and magnitude map show a large scar along the LAD anteriorly and the posterior descending artery (PDA)

inferiorly (in red). Deflection map shows fragmented EGMs in the inferior basal region, where diastolic late potentials are also imaged (black boxes on EGMs). In order to exclude baseline fluctuations, which may appear as late potentials, non-scar EGMs a and b are plotted together with scar EGM e for magnitude comparison. Although the QRS peak-to-peak magnitude of the non-scar EGM is 4.5 times larger than that of the scar EGM, the late potentials in the scar EGM are 3.5 times larger than the baseline fluctuations in the non-scar EGM, which confirms their physiological origin. In all three patients, late potentials occurred in the area of greatest fractionation.

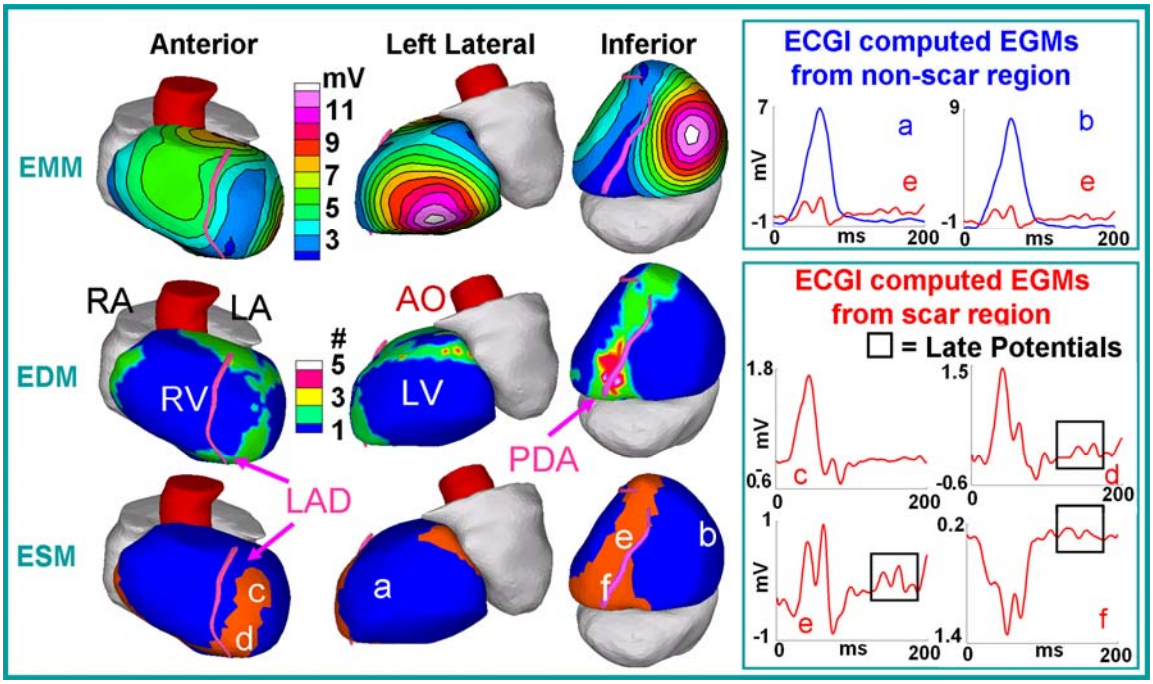

Figure 23 (Figure 4-5): ECGI images for patient 4

ECGI EMM, EDM and ESM are shown in three views. Six selected EGMs from the non-scar region (blue, top) and from the scar region (red, bottom) are shown on the right. Scar EGM e (red) is also shown in the top panel together with non-scar EGMs a and b for magnitude comparison.

ECGI images for Patient 5 are shown in Figure 4-6. Similar with Patient 4, EP scar map and magnitude map show a large scar along the LAD anteriorly and the PDA inferiorly (in red). Deflection map shows fragmented EGMs in the right inferior and apical region, where diastolic late potentials are also imaged (black box on EGMs). The non-scar EGMs a, b, and c are plotted together with scar EGM i for magnitude and morphology comparison. Note absence of diastolic deflections ("late potentials") in the non-scar EGMs. Movies of ECGI-imaged epicardial activation during systole and diastole (Movie 1) are available in the attached CD.

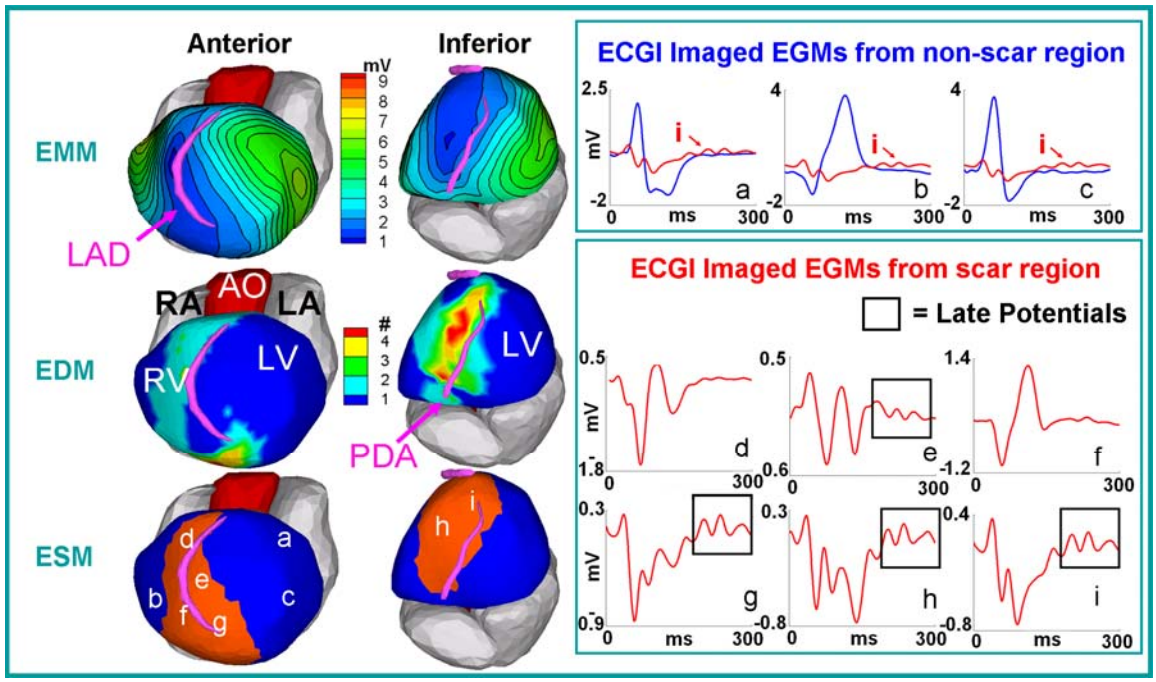

Figure 24 (Figure 4-6): ECGI images for patient 5

ECGI EMM, EDM and ESM are shown in anterior and inferior views. Nine selected EGMs from the non-scar region (blue, top) and from the scar region (red, bottom) are shown on the right. Scar EGM i (red) is also shown in the top panels together with non-scar EGMs a, b, and c for magnitude and morphology comparison. Movies of the ECGI-imaged epicardial activation during systole and diastole

are available in the attached CD.

ECGI images for Patient 6 are shown in Figure 4-7. The isochrone map shows a normal RV breakthrough (white asterisk). EP scar map and magnitude map show a large apical/LV scar; another smaller scar is located at the superior region (site c) close to the aorta (AO) (labeled red in EP scar map). The borders of the scars correspond to lines of block and slow conduction in isochrone map. Diastolic late potentials are imaged in the region close to sites c and e (black box on EGMs). The non-scar EGMs a, and b are plotted together with scar EGM c for magnitude comparison. Minimal baseline fluctuations are observed in the non-scar EGMs (a, b), supporting physiological origin of diastolic late deflections in scar EGMs (c and e).

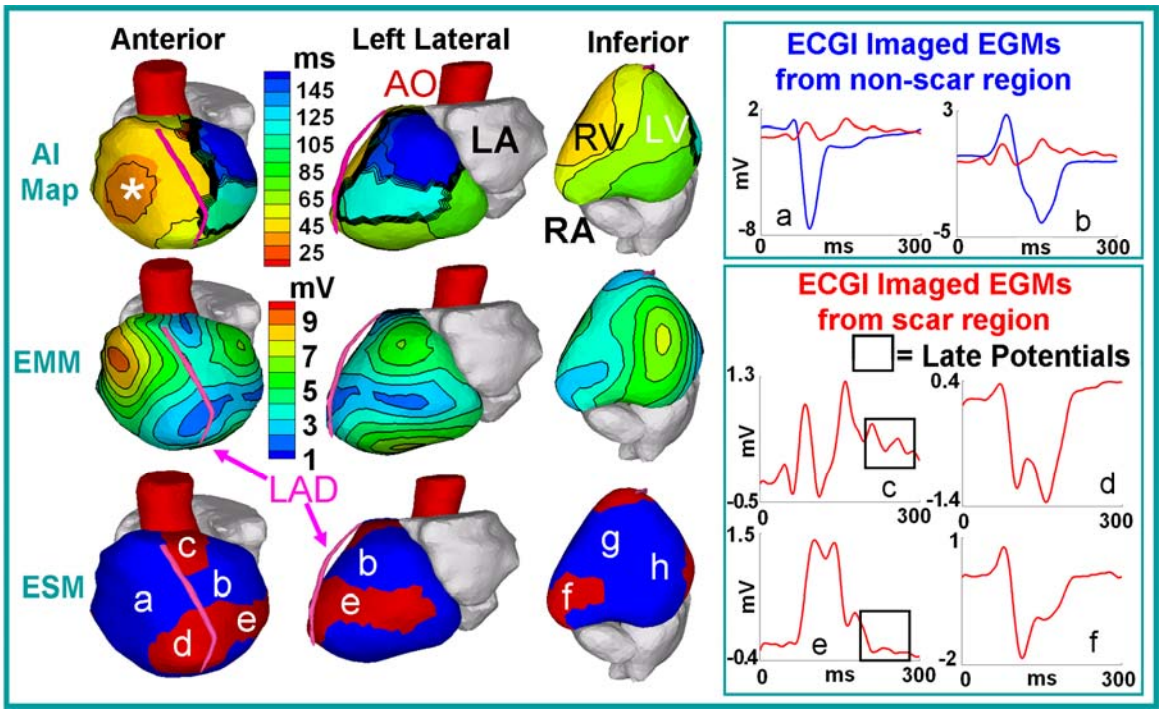

Figure 25 (Figure 4-7): ECGI images for patient 6

ECGI AI map, EMM and ESM are shown in three partially overlapping views. The normal RV

breakthrough during SR is labeled by a white asterisk. Six selected EGMs from the non-scar region (blue) and from the scar region (red) are shown on the right. Scar EGM c is also shown together with non-scar EGMs a and b for magnitude and morphology comparison.

4.2.3 Patient #7 and #8: VT associated with Post-MI Scar

VT was recorded in patients #7 and #8. ECGI images for Patient 7 are shown in Figure 4-8. Isochrone map during SR shows a slow conduction line along the LAD, which coincides with the boundary of the low potential region in anterior RV. The LV activates before the RV, generating an RBBB pattern. EP scar map and magnitude map show a large anterior RV scar, labeled as S2 in EP scar map. Another smaller scar is located at the LV basal region (S1). Two scar-related reentry circuits are present in the VT isochrone map; one is formed around the S1 scar (white arrows), and the second (black arrows) around the S2 scar. By sharing a common central pathway (blue arrows), the two pathways form a double-loop activation pattern during VT.

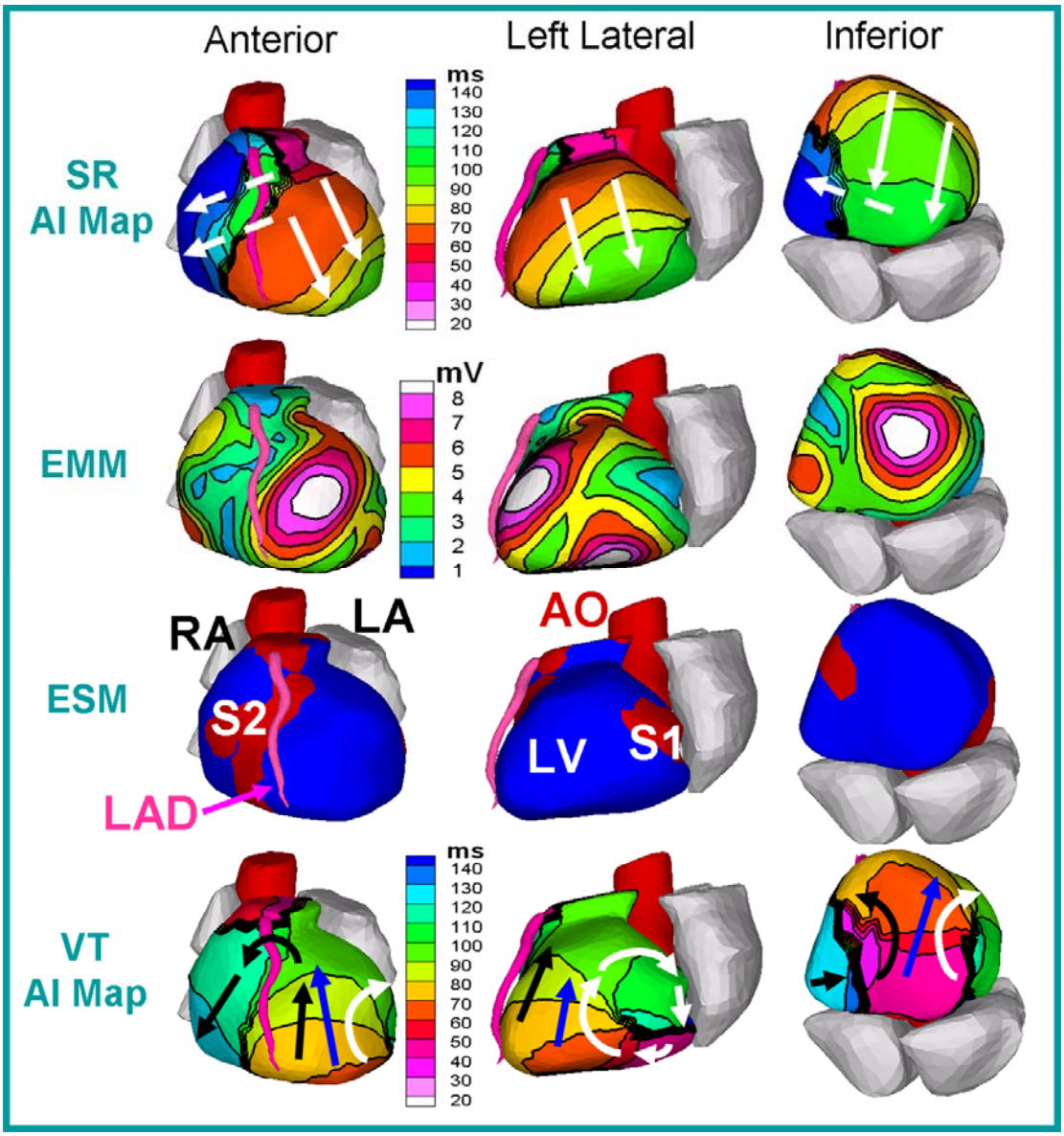

Figure 26 (Figure 4-8): ECGI images for patient 7

ECGI AI map during SR (top row) and VT (bottom row), EMM and ESM are shown in three views. In the SR AI map, direction of epicardial wavefront propagation is labeled by white arrows. White dashed arrows indicate slow conduction. In the VT AI map, two reentry circuits are shown. The white arrows show a reentry pathway around scar S1, and the black arrows show a second reentry pathway around scar S2. Blue arrows show the common central pathway shared by the two reentry circuits.

The origin of each ECGI-imaged VT beat was the inferior base of the heart. Propagation pattern of the VT consisted of two wavefronts, one (white arrows) propagates clockwise, with a high degree of curvature, to the base of lateral LV and encounters an inferior line of block at the edge of the S1 scar. The other (black arrows) propagates superiorly toward the base and makes a slow counter-clockwise turn around a line of block near the septum to RV, around the S2 scar. The latest activation during VT is at the lateral base of the RV. This second loop connects with the first wavefront at the inferior base, where the next wavefront begins. Movies of the epicardial activation are available in the attached CD (Movie 2), showing a short period of earliest activation near the borderzone of the scar S1. The subsequent VT beat begins near this borderzone site.

ECGI images for Patient 8 are shown in Figure 4-9. The isochrone map during SR shows a normal RV breakthrough site (white asterisk) and a normal epicardial activation pattern. EP scar map and magnitude map show a left inferior scar in the left lateral view. The boundary of the scar coincides with slow conduction lines in both the SR isochrone map and the VT isochrone map. During VT, the LV epicardial activation front begins at the lateral apex (white circle), and moves around the scar (curved black arrows). Ventricular activation occurs in a right bundle branch block (RBBB) pattern, which is typical for LV tachycardia.

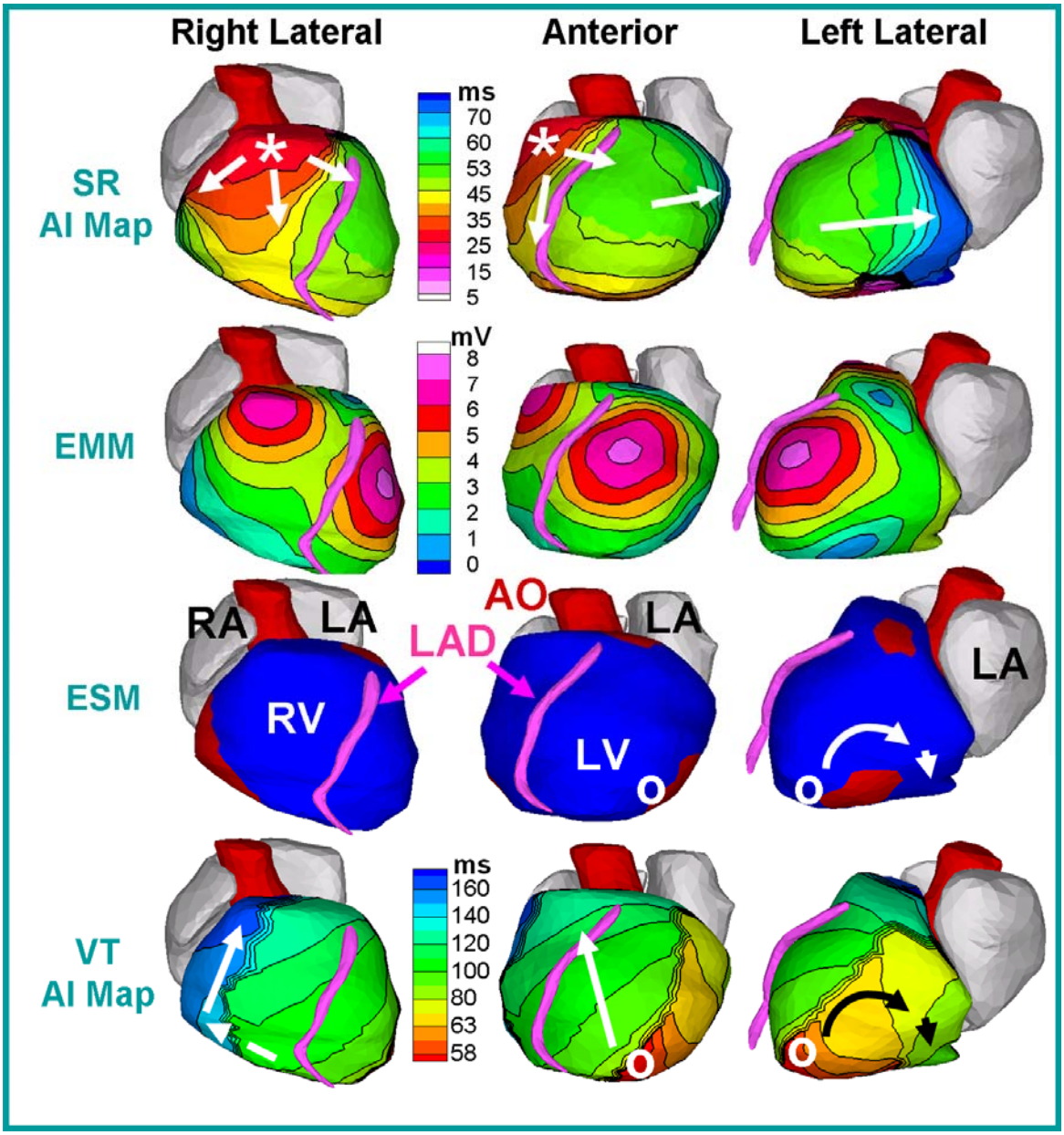

Figure 27 (Figure 4-9): ECGI images for patient 8

ECGI AI map during SR (top) and VT (bottom), EMM and ESM are shown in three views. In the SR AI map, the RV breakthrough site is labeled by a white asterisk and the direction of epicardial activation is shown by white arrows. In the VT AI map and ESM, the earliest epicardial breakthrough site is labeled by a white circle, and the following epicardial activation direction is shown by black arrows.

4.4 Discussion

In this study, we report eight cases of post-MI patients imaged noninvasively with ECGI. We demonstrate that ECGI can noninvasively image the electrophysiological properties of MI epicardial substrate during sinus rhythm. From these data, quantitative measures can be derived, including voltage magnitudes and number of deflections of epicardial electrograms. All ECGI data are generated within a single sinus beat, an advantage over catheter mapping which requires assembling data from many identical beats.

Contrast-enhanced magnetic resonance imaging (ceMRI) with a gadolinium-based contrast agent has been used for anatomical imaging of MI. In one study, infarct surface area and mass, measured by ceMRI, were better than LV ejection fraction at identifying of patients who are prone to VT after a myocardial infarct.[114] Here, we show that ECGI can noninvasively image a post-MI “electrophysiological scar” (ESM) that corresponds very closely to the epicardial aspect of the anatomical scar in terms of location and size. This finding suggests that ECGI could be employed as a low-cost, noninvasive imaging modality to image the epicardial morphology of MI scars without using a contrast agent. The information on the epicardial extent of the electrophysiological scar could be incorporated as one parameter in a method of risk stratification for VT. In patients with implanted devices, in which MRI can not be employed, ECGI could constitute an alternative noninvasive modality for imaging the scar substrate.

Previous studies have shown that fractionated, low-magnitude electrograms are commonly found in the post-MI region.[130] It is well-accepted that fractionated electrograms in healed infarct reflect slow, non-uniform and discontinuous conduction.[130, 135] The anatomical substrate of a patchy scar contains islands of surviving myocardial fibers separated by inexcitable scar tissue. This provides an electrophysiological substrate that supports asymmetrical electrical loading on a propagating action potential, a property that favors formation of unidirectional block.[108] The combination of unidirectional block and slow conduction is highly arrhythmogenic, providing conditions for reentrant VT.[108] Consistent with previous invasive studies [130] [135], the ECGI noninvasive epicardial electrograms from the scar are fragmentated (deflection map), of small magnitude (magnitude map) and prolonged duration, reflecting the substrate properties described above. These electrogram properties (low magnitude, long duration, fractionation) could be considered, together with the extent of the abnormal electrophysiological region, in risk-stratification for VT. [136]

Catheter ablation of VT is associated with a limited success rate, and is generally limited to patients with hemodynamically stable VT. Catheter-based substrate mapping during sinus rhythm based on electrogram properties (magnitude and morphology) has been used to characterize the substrate for VT and guide a substrate-based ablation procedure. ECGI could provide similar information noninvasively.

Signal-averaged electrocardiograms of low amplitude and high frequency have been recorded from the body surface in post-MI patients at the end of the QRS complex.[137,138] These late potentials are thought to originate from the infarct border zone and correspond to fragmented electrograms recorded directly from the heart.[139,140] In three of our patients (#4, #5, and #6), late diastolic potentials were imaged on the epicardial surface of the heart during sinus rhythm. This activity usually starts around 160ms after the QRS onset on the reconstructed epicardial electrogram, consistent with invasive mapping.[140] The late potentials are located in a region of the epicardial border zone with higher degree of electrogram fragmentation, consistent with previous direct recordings[139,140]; they likely reflect slow conduction along viable myocardial fibers in the border zone.

In this study, hemodynamically stable VT was captured in two patients (#7 and #8). In both patients, ECGI-imaged reentry circuits were closely related to the electrophysiological scar. These data are consistent with a recently published animal study,[116] in which epicardial reentrant VTs were induced in a post-MI swine model. In this model, the isthmus of the reentrant circuit was confined to a region of viable myocardium surrounded by the scar tissue. From our study, ECGI-imaged activation sequence during the VT, together with the imaged electrophysiological substrate during SR, could provide useful information for guiding catheter ablation of these VTs. For example, patient #7 had a corridor of viable tissue between two scar regions, and the VT

beats originated in this channel. Ciaccio et al [141,142] showed in infarcted canine (invasive direct epicardial mapping) and human hearts (endocardial mapping) that the scar-related reentry isthmus (common central pathway) could be localized from the SR activation map. They defined the longest-duration activation pathway by tracing the activation sequence from the latest to the earliest activation region. This "primary path" was in accord with propagation within the isthmus during VT, and our ECGI-derived common central pathway during sinus rhythm and VT in Figure 4-8 agrees with those findings. Similar results were found for patient #8, where the scar-dependent reentry pathway during VT corresponds to the pathway of the longest conduction during SR. The VT's imaged here were well-tolerated and stable, which comprise a small fraction of all VT patients. However, the consistency between the ECGI results (in patients #7 and #8) and Ciaccio's findings suggest that ECGI could be employed to locate noninvasively the VT isthmus by analyzing the epicardial activation map during SR, thereby guiding and facilitating VT ablation without the need to induce a stable arrhythmia.

As discussed in previous publications [1], isochrone maps are useful in displaying the activation sequence as color-coded images for periodic and stable rhythms. For complicated and dynamic changing rhythms, such as atrial fibrillation or polymorphic VT, analysis of several sequential isochrone maps is required to describe the activation pattern. In this study, we constructed dynamic continuous activation movies that helped greatly in this regard. The activation movie captured the origin and entire activation pattern of a

long, dynamically changing rhythm. This is particularly useful during a clinical on-site application. With recent developments, ECGI can be generated in real-time during the clinical intervention.

Several limitations of the study should be recognized. At this stage of development, ECGI images are limited to the epicardium. Intraoperative epicardial mapping and endocardial mapping suggest epicardial location of the arrhythmia substrate in up to 33% of patients[124,143]. Epicardial location has been suggested as one reason for failure of endocardial catheter ablation.[144-146]. This realization of epicardial involvement and the need to differentiate between endocardial and epicardial circuits, has led to development of a technique for epicardial mapping and ablation through subxyphoid approach.[125,147]. However, if needed, ECGI could be combined with catheter endocardial mapping to provide information on both surfaces of the heart.

The extent of the ECGI-determined electrophysiological scar depended on the threshold chosen for scar EGM magnitude (30% or smaller than the maximum EGM magnitude in non-scar regions). With this choice, the electrophysiological scars and ceMRI-imaged anatomical scars were highly correlated in our patient population. It will require a much larger-scale study to establish a magnitude criterion with high level of statistical significance, possibly with different magnitudes in different regions of the heart. As shown here, using multiple criteria (EGMs magnitude, duration, and fractionation)

increases the accuracy of scar determination (in patient #1 and #2 adding fractionation as a criterion prevented over-estimation of the scar size). It should be added that slice thickness of the MRI images was relatively coarse compared to the CT images (1mm) and did not always capture the anatomical scar with the same resolution, especially in very inferior and very superior regions.

Finally, the number of the patients included in the study is relatively small. At this stage, ECGI is still a novel research tool, which precludes its application in large-scale multicenter clinical studies. In particular, our results suggest that ECGI could be used for arrhythmia risk stratification based on electrophysiological properties of the scar (low potentials, degree of EGMs fractionation) that reflect “patchiness” and heterogeneity of the infarct substrate. This observation needs to be validated in a large study, where quantitative statistical correlation between risk and these properties can be established.

4.5 Legends for the Video files

Movie 1 (Patient #5): Epicardial activation during systole and diastole. Blue area denotes low voltage region (scar). Top left: two electrograms from normal myocardium (blue, yellow) and from scar (red, cyan). Top right shows the scar electrogram on an expanded scale. LP = late potentials. Note that diastolic activity is in the scar region.

Movie 2 (Patient #7): Epicardial activation during stable slow VT. Blue area denotes low voltage region (scar). See text in paper for detailed description.

Chapter 5 Insights from Noninvasive Electrocardiographic Imaging (ECGI) of Ventricular Arrhythmias in Patients Undergoing Catheter Ablation

Abstract

Ventricular tachycardia (VT) is a common cause of sudden cardiac death. Advances in knowledge of VT mechanisms and invasive mapping techniques have facilitated the ability to treat VT with radiofrequency catheter ablation, but significant limitations persist. We report our experience with a noninvasive electroanatomic mapping system (Electrocardiographic Imaging, ECGI) before and during VT ablation procedures. Eleven consecutive patients referred for VT catheter ablation procedure were included. ECGI was performed either before (8 patients) or during (3 patients) the ablation procedure. Blinded ECGI and invasive electrophysiology (EP) study results were compared. All ECGI procedures yielded high-resolution images of epicardial activity. Over a wide range of VT types and locations, ECGI results were consistent with EP data regarding localization of the arrhythmia origin (including myocardial depth) and mechanism (focal, reentrant, fascicular). ECGI also provided mechanistic electrophysiological insights, relating arrhythmia patterns to the myocardial substrate. ECGI is feasible and reliable to perform in the study of ventricular arrhythmias both before and during an ablation procedure. ECGI has unique potential clinical advantages, especially for hemodynamically intolerant VT or VT that is difficult to induce. Because it provides

local cardiac information, ECGI may aid in better understanding of mechanisms of ventricular arrhythmia. Further prospective trials of ECGI with clinical endpoints are warranted.

5.1 Introduction

Ventricular tachycardia (VT) is a common cause of sudden cardiac death(SCD)[148-150]. While implantable cardiac defibrillators are used to abort SCD[151], they do not treat the underlying disease. Understanding mechanisms of VT has led to their treatment with radiofrequency catheter ablation[152-155]. Innovative imaging modalities have facilitated ablation procedures, improving success and safety. Nevertheless, success rates are variable, and morbidity and mortality related to these lengthy procedures are significant.

There are limitations to current VT ablation procedures. First, the point-by-point roving-probe method for electrical mapping is time-consuming and requires a sustained, hemodynamically-tolerated monomorphic VT. Conversely, hemodynamically intolerant VT does not allow for detailed mapping. Third, particularly for VT arising from the RV outflow tract, sedation for the ablation procedure often renders the VT noninducible[156]. Fourth, there are limitations in identifying and ablating atypical endocardial sites, such as the coronary cusps of the aorta[157]. Finally, there are specific challenges in identifying and ablating nonendocardial reentry circuits or focal sources, frequently seen in patients with nonischemic cardiomyopathies[147,158]

Thus, the ability to noninvasively image the initiation, propagation and other characteristics of VT during a single beat has potential clinical benefit. Here, we present observations from using a noninvasive electroanatomic mapping method, Electrocardiographic Imaging (ECGI), in a series of patients undergoing catheter ablation for various forms of VT.

5.2 Methods

Eleven consecutive patients referred for catheter ablation for sustained symptomatic VT were included in this study. All protocols were approved by the Human Research Protection Office (HRPO) at Washington University in St. Louis, and informed consent was obtained.

ECGI methodology was described in detail [1,2]. 256 carbon electrodes on strips were applied to patient's torso surface. Small CT markers were attached to each electrode. All strips were connected to a portable mapping system (BioSemi, Netherlands). After electrodes application, patients underwent thoracic noncontrast gated CT with axial resolution of 3mm. Scans were gated at 70% of the R-R interval (ventricular diastole). For patients who had continued ECGI mapping during a subsequent EP study, the 256 carbon electrodes were kept in the same position. Patient-specific ventricular epicardial surface geometry and body surface electrode positions were labeled and digitized from

CT images.

The 256 channels of body surface potentials (BSP) were sampled at 1-ms intervals during the cardiac cycle, and the data were saved on a laptop computer. BSP were acquired during sinus rhythm, VT, and programmed electrical stimulation, when available.

The BSP and geometrical information (torso-heart geometrical relationship) were combined by ECGI algorithms to noninvasively construct epicardial electrograms, activation sequences (isochrones), potential maps, and repolarization patterns [1,2]. ECGI is constructed on a beat-by-beat basis and does not require accumulating data from many identical beats. Activation times were determined by the maximal negative slope of the epicardial electrograms. Activation movies for several consecutive beats were also constructed by animating the activation wave front on the patient-specific CT-derived epicardial surface. Based on the isochrone map, lines or regions of block were inferred if activation times in adjacent area differed by more than 50ms. Slow conduction is represented by crowded isochrones.

ECGI was performed prior to the ablation procedure (8 patients) when the patients demonstrated spontaneous ventricular rhythms. Otherwise, ECGI was used during the ablation procedure (3 patients). The results of ECGI were processed independently from the results of the EP study. Additionally, EP operators did not have access to ECGI results

prior to the procedure. Additional cardiac images, such as three-dimensional electroanatomic maps, gadolinium-enhanced cardiac MRI and single-photon emission computed tomography (SPECT), were obtained retrospectively, when available, for each patient. Pertinent medical records for patients in this study are summarized in Table 5-1.

Table 4 (Table 5-1) Clinical background

	Age Gender	**Clincial Presentation**	**LV Ejection Fraction**	**Ventricular Substrate**	**VT Morphology**	**Antiarrhythmic Medication**
RV 1	48 years Female	Symptomatic nonsustained VT at rest and after exertion.	42%	Nonischemic cardiomyopathy	LBBB pattern Right Inferior (V3)	None
RV 2	42 years Male	Symptomatic nonsustained VT at rest.	70%	Normal	LBBB pattern Inferior	Beta-blocker
RV 3	58 years Female	Symptomatic sustained VT at rest.	65%	Normal	LBBB pattern Right Inferior (V3-V4)	Beta-blocker
RV 4	21 years Male	Symptomatic nonsustained VT at rest.	58%	Normal	LBBB pattern Right Inferior (V3)	Beta-blocker
RV 5	76 years Male	Recurrent admissions for sustained VT during recovery portion of exercise stress test.	35%	Previous anterior myocardial infarction	RBBB pattern Left Inferior (V2)	Beta-blocker
LV 1	63 years Female	Symptomatic sustained slow VT at rest, poorly tolerating multiple antiarrhythmic drugs	10%	Nonischemic cardiomyopathy	RBBB pattern, Right Superior	Amiodarone, Mexiletine, Beta-blocker
LV 2	59 years Male	Minimally symptomatic sustained slow VT	40%	Previous inferior myocardial infarction	RBBB pattern, Left Superior	Beta-blocker
LV 3 LV 6	45 years Male	Recurring syncope and sustained VT at rest.	55%	Cardiac sarcoid	RBBB pattern, Right Superior	Amiodarone, Beta-blocker

LV 4	35 years Male	Symptomatic sustained VT who had undergone prior EPS with slow pathway modification.	70%	Normal	RBBB pattern, Left Superior	Calcium-channel blocker
LV 5	53 years Female	Symptomatic sustained VT at rest.	65%	Normal	RBBB pattern, Left Superior	Amiodarone

5.3 Results

Eleven ECGI procedures were performed on 10 patients (mean age 50 years, range 21 – 76 years). One patient required a second (epicardial) ablation procedure eight months later and underwent ECGI before both procedures. All ECGI procedures were completed successfully and yielded high-resolution images. There were no major equipment failures or adverse patient events related to ECGI image acquisition.

Tachycardia characteristics obtained during the EP study, including conventional 12-lead ECG morphology, cycle length, and information regarding induction, testing and ablation of the tachycardia are detailed in Table 5-2. In total, 4 patients had a focal source in the right ventricular outflow tract (RVOT), 1 patient had a focal source in the left coronary cusp of the aorta, 1 patient had a focal nonendocardial source in the apical lateral left ventricle, 2 patients had reentry around myocardial scars, 2 patients had intrafascicular reentry (fascicular VT), and 1 patient had focal epicardial VT related to advanced cardiac sarcoid disease.

Table 5 (Table 5-2) Tachycardia characteristics

	Timing of ECGI	VT Morphology	VT Induction	Primary VT Cycle Length	Diagnostic Maneuvers	Procedural Endpoint	Conclusion of EPS	Follow Up
RV1	Before EPS	LBBB pattern Right Inferior (V3)	Spontaneous and isoproterenol induced VPD's	N/A	• Activation Map: left coronary cusp, 15 ms preQRS.	RF application eliminated ventricular ectopy. Noninducible at conclusion.	Left coronary cusp origin	No recurrance
RV2	Before EPS	LBBB pattern Inferior (V3)	Spontaneous and isoproterenol induced VPD's	N/A	• Pace Map: 12/12 match, mid-septal RVOT. • Activation Map: mid-septal RVOT, 19 ms preQRS.	RF application eliminated ventricular ectopy. Noninducible at conclusion.	Mid-septal RVOT	No recurrance
RV3	Before EPS	LBBB pattern Right Inferior (V3-V4)	Spontaneous and isoproterenol induced VPD's	N/A	• Activation Map: midseptal RVOT, 30 ms preQRS. • Pace Map: 12/12 match, midseptal RVOT	RF application eliminated ventricular ectopy. Noninducible at conclusion.	Mid-septal RVOT	No recurrance
RV4	Before EPS	LBBB pattern Inferior (V3, V4)	Spontaneous and isoproterenol induced VPD's	N/A	• Pace Map: 12/12 match posterior right RVOT	RF application eliminated ventricular ectopy. Noninducible at conclusion.	Posterior right RVOT	No recurrance
RV5	Before EPS	LBBB pattern Left Inferior (V2)	No inducible arrhythmia during EPS.	N/A	N/A	N/A	N/A	Received ICD

LV1	During EPS	VT1 & 2: RBBB pattern, Right Superior	Double ventricular extrastimuli yielded sustained, tolerated VT	390 ms (VT2 at 490 ms)	• Activation Map: Earliest activation anterolateral apex, local electrogram, 21ms preQRS. • Pace Map: 12/12 match anterolateral apex • Entrainment: PPI-TCL = 74ms	Multiple endocardial RF applications failed to alter the tachycardia.	Not likely to be reentrant. Epicardial or midmyocardial origin.	Underwent heart transplant for refractory heart failure and intractable VT.
LV2	Before EPS	VT1 & 2: RBBB pattern, Left Superior	Spontaneous, sustained tolerated accelerated idioventricular rhtyhm	627ms (VT2 at 641ms)	• Voltage Map: inferobasal septal scar • Activation Map: earliest activation inferobasal septum, border zone, 67ms preQRS. Highly fractionated signal. • Entrainment: concealed, PPI-TCL = 13 ms	RF applications altered, then terminated the tachycardia. Noninducible at conclusion.	Reentrant. Inferobasal septal scar border azone.	ICD implant No recurrance
LV3	Before EPS	VT1: RBBB pattern, Right Superior VT2: RBBB pattern, Right Inferior	Spontaneous, tolerated nonsustained VT	463 ms (VT2 at 500ms)	• Activation Map: earliest activation inferolateral apical. Two distinct exit sites corresponding to two VT morphologies. 0-10ms pre QRS.	RF applications eliminated the nonsustained tachycardia. Noninducible at conclusion.	Likely reentrant Two exit sites from an inferolateral apical scar.	ICD implant. 8 months later, VT recurred (see LV6)
LV4	During	RBBB	Single LV	317 ms	• Activation Map:	RF applications	Left posterior	No

	EPS	pattern, Left Superior	ventricular extrastimuli induced sustained tolerated VT		earliest midinferior septum, 30ms pre-QRS fascicular potential.	eliminated the sustained tachycardia. Noninducible at conclusion.	fascicular VT	recurrance
LV5	During EPS	RBBB pattern, Left Superior (V3)	With isoproterenol, nonsustained VT	344 ms	• Pace Map: 10-11/12 match mid-apical septum	No ablation performed due to patient anxiety and adverse reaction to isoproterenol.	Likely left posterior fascicular VT	Treated with CCB
LV6	Before EPS	RBBB pattern, Right Inferior	Spontaneous, tolerated, nonsustained VT	1177ms	• Epicardial access • Activation Map: Earliest activation anterolateral basal. 0-10 ms preQRS • Pace Map: 12/12	RF applications after pericardial insufflation eliminated the nonsustained tachycardia. Noninducible at conclusion.	Focal or microreentrant Epicardial origin	Underwent heart transplant for refractory heart failure. Explant confirmed cardiac sarcoid.

Based on the results of prior studies, we used ECGI to identify characteristics of each tachycardia based on single-beat analysis of isochrone, potential, local electrogram, and wavefront propagation information. A three-step process was used to determine each patient's unique tachycardia properties:

- Step 1: Localize the origin with isochrone and potential maps
- Step 2: Determine mechanism by observing three-dimensional propagation pattern

- Step 3: Determine myocardial depth by using local electrograms (pure Q wave for epicardial sources, rS complex for intramural or endocardial sources)

Detailed results of ECGI are presented below, organized by location and mechanism of the clinical VT. A summary schematic of the locations of the various VT's and a comparison of ECGI observations and EP study results are shown in Figure 5-1 and Table 5-3.

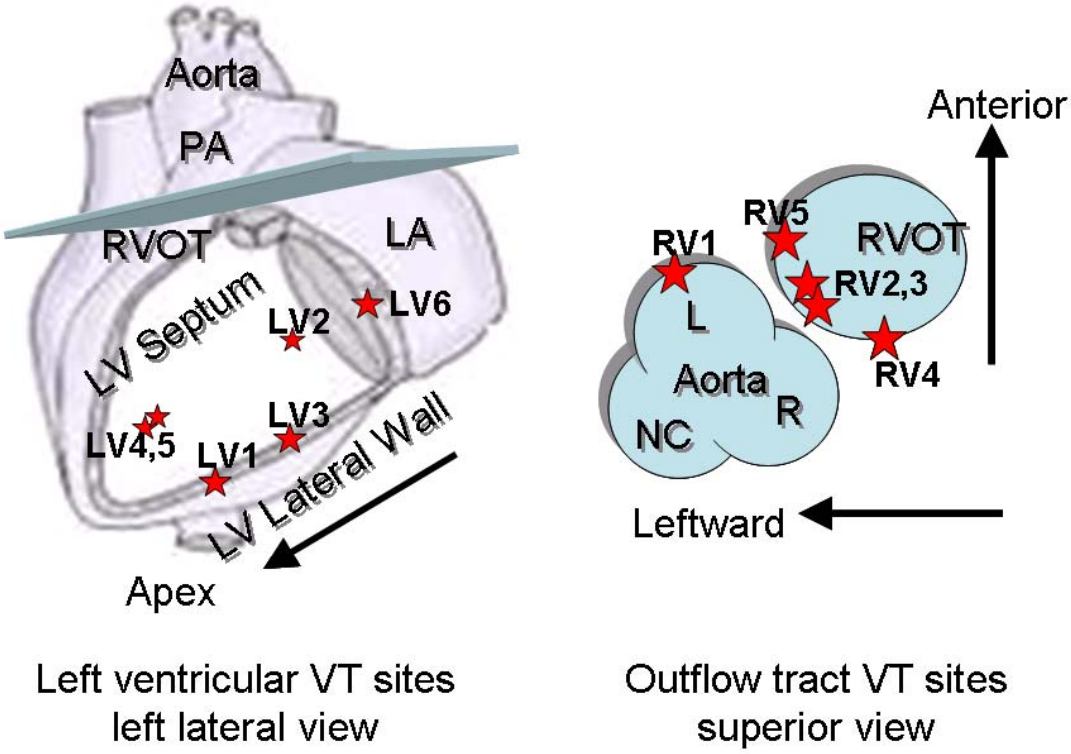

Figure 28 (Figure 5-1): Sites of origin of the ventricular tachycardias included in this study.

ECGI characteristics of VT localization, propagation and local electrogram compared with the conclusion of the EP study are shown in Table 5-3. LA= Left Atrium, RVOT = Right Ventricle Outflow Tract, PA= Pulmonary Artery, L=Left, R=Right, NC=Noncoronary Cusps of the Aorta;

Table 6 (Table 5-3) ECGI observations and tachycardia characteristics

Patient	ECGI Localization	ECGI Propagation	ECGI Local Electrogram	Conclusion of EP Study
RV1	Left coronary cusp	Radial		Focal, left coronary cusp origin
RV2	Mid-septal RVOT	Radial		Focal, mid-septal RVOT
RV3	Mid-septal RVOT	Radial		Focal, mid-septal RVOT
RV4	Posterior right RVOT	Radial		Focal, posterior right RVOT
RV5	Anterior left RVOT	Radial		N/A
LV1	Apical lateral LV	Radial	Q wave	Focal, apical lateral LV Epicardial or midmyocardial origin
LV2	Inferior basal LV	Spiral wavefront High degree of curvature Anatomic line of block Presystolic activation	Low amplitude, fractionated	Reentrant. Inferior basal LV septal scar
LV3	Two sites: 1) Inferior lateral LV 2) Apical lateral LV	Spiral wavefront High degree of curvature Anatomic line of block Presystolic activation	Q wave and rS complex Low amplitude, fractionated	Likely reentrant Two exit sites from inferior lateral apical scar
LV4	Large area apical LV	Radial	rS complex	Left posterior fascicular
LV5	Large area apical LV	Radial	Q wave	Likely left posterior fascicular
LV6	Anterior basal LV	Radial	Q wave	Focal, anterior basal LV Epicardial origin

5.3.1 Left Bundle Branch Block (LBBB) pattern VT (RVOT tachycardia)

Five patients (RV1 to RV5, mean age 49 years, range 21-76 years) underwent EP study with the presumptive diagnosis of symptomatic RVOT tachycardia based on conventional 12-lead ECG analysis and normal cardiac function from prior imaging. None of the patients met diagnostic criteria for arrhythmogenic right ventricular cardiomyopathy. Of four catheter-mapped tachycardias (RV1 to RV4), two had mid-septal RVOT origins, one had posterior right origin and one had a left coronary aortic cusp origin (Figure 5-1). The four ablations were deemed successful based on the absence of the PVC morphology after ablation and the absence of symptoms in follow-up clinic visits.

The three-step process of ECGI analysis is demonstrated using Figure 5-2A, which displays ECGI isochrone and potential maps of a premature ventricular beat from a patient with a mid-septal RVOT source (RV2).

- Step 1: Localization—Isochrone map identifies an area in the septal RVOT as the earliest activation (white asterisk). Consistently, the potential map shows an intense local minimum; (dark blue, indicating initiation of wave front) at the same location.
- Step 2: Propagation—Propagation pattern is away from this location in a radial fashion, consistent with a focal mechanism.

- Step 3: Myocardial Depth—Local electrogram at this location shows a small r wave followed by a deep S wave, consistent with an endocardial origin (not shown).

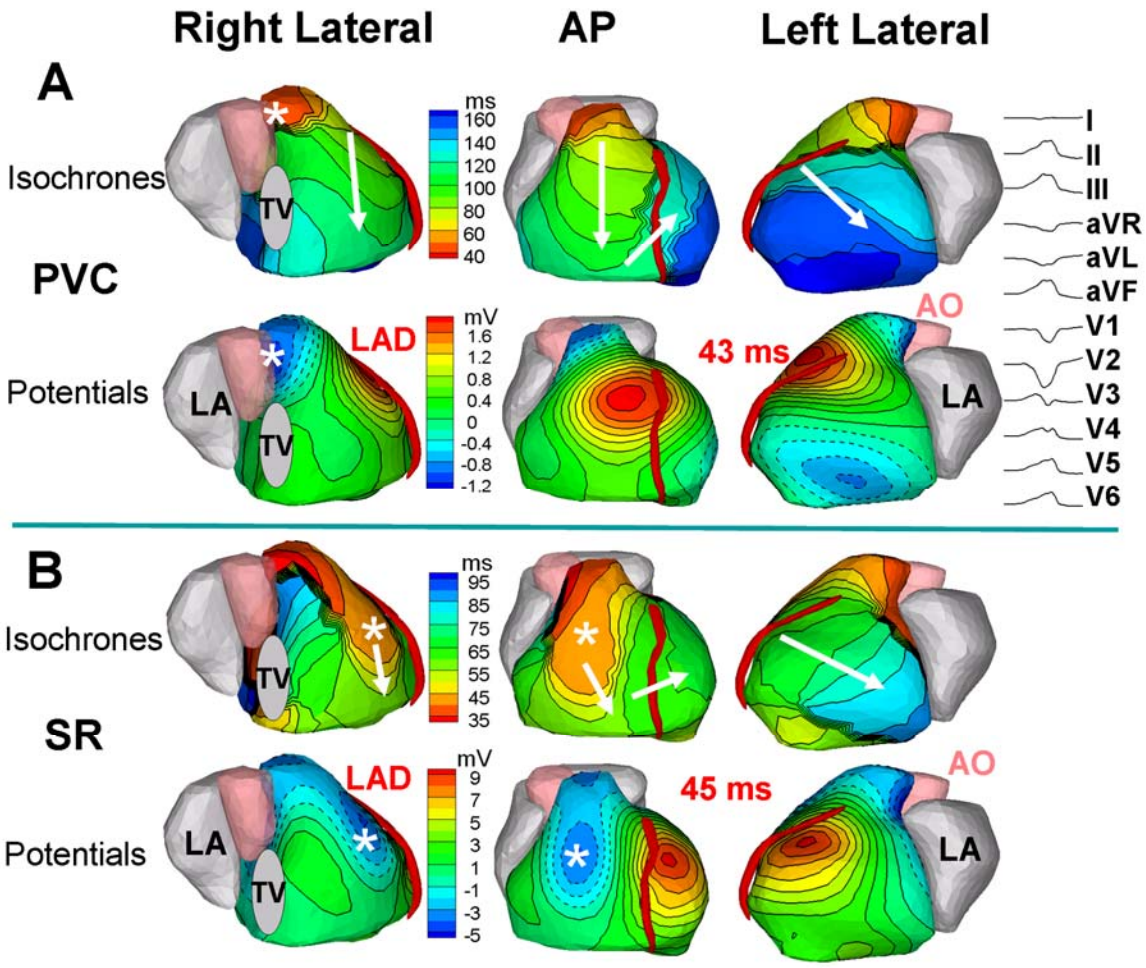

Figure 29 (Figure 5-2): ECGI of a mid-septal RVOT tachycardia, (RV2)

Panel A: isochrone map (upper row) and potential map (lower row, 43 ms from the onset of QRS) during a spontaneous PVC beat in three views (AP=Anteroposterior). White asterisk indicates the ECGI determined mid-septal RVOT VT origin. White arrows indicate the direction of activation wavefront propagation. The conventional 12-lead ECG for the PVC is shown on the right. Panel B shows isochrone map (upper row) and potential map (lower row, 45 ms from the onset of QRS) for a

sinus beat in three views. White asterisk indicates the RV epicardial breakthrough site. AO = Aorta, LAD = Left Anterior Descending Coronary Artery, LA = Left Atrium, TV = Tricuspid Valve, MV = Mitral Valve, RA = Right Atrium.

The noninvasive ECGI images were confirmed during the ablation procedure, where invasive activation mapping of the PVCs identified earliest activation in the mid-septal RVOT with a perfect pace map match. Radiofrequency ablation at this location eliminated the ventricular ectopy.

For comparison, ECGI images are shown during sinus rhythm in Figure 5-2B. The earliest epicardial breakthrough in the anterior RV is marked by the white asterisk. The wavefront propagates from RV to LV with some slowing of conduction (crowded isochrones) across the anterior septum. The latest activation region is the lateral LV. The epicardial potential map for the same sinus beat shows an intense negative potential minimum around the breakthrough site, typical of sinus rhythm pattern.[2]

Similar data are presented for other patients with LBBB-VT. All five LBBB-VTs originated in the outflow tracts, as shown in Figure 5-1.

Several similarities exist among this group of LBBB-VT patients, namely the propagation pattern and presumed mechanism. Uniformly, the ECGI-derived activation sequence for

the VT (during a PVC) begins in the right ventricle and proceeds along the anterior RV from base to apex. Using Figure 5-2A as an example, the wavefront encounters a line of slow conduction at the ventricular septum, as shown by the crowded isochrones near the labeled left anterior descending artery (LAD). Activation of the left ventricle proceeds apex to base, with the basal lateral LV the last area to activate. This pattern of activation can be considered a “signature” of LBBB-VT ventricular activation.

The second similarity of these LBBB outflow tract tachycardias is the observed mechanism. These tachycardias generally have a focal, rather than reentrant, mechanism. With the ECGI map, a focal mechanism can be inferred by an area of early intense negative potential at the same site as isochronal initiation with a radial activation wavefront. All five ECGI images of outflow tract tachycardia suggested focal mechanisms.

The largest variations among the group were in the exact locations of the tachycardia initiation sites. Importantly, the exact location and orientation of VT activation could not be determined from the conventional 12-lead ECG. For example, two patients with mid-septal RVOT origins (RV2 and RV3) had very similar ECGI images (Figure 5-2 and Figure 5-4), but significant differences on the conventional 12-lead ECG. The ECG in Figure 5-2 shows a pure inferior activation pattern with an isoelectric signal in lead I.

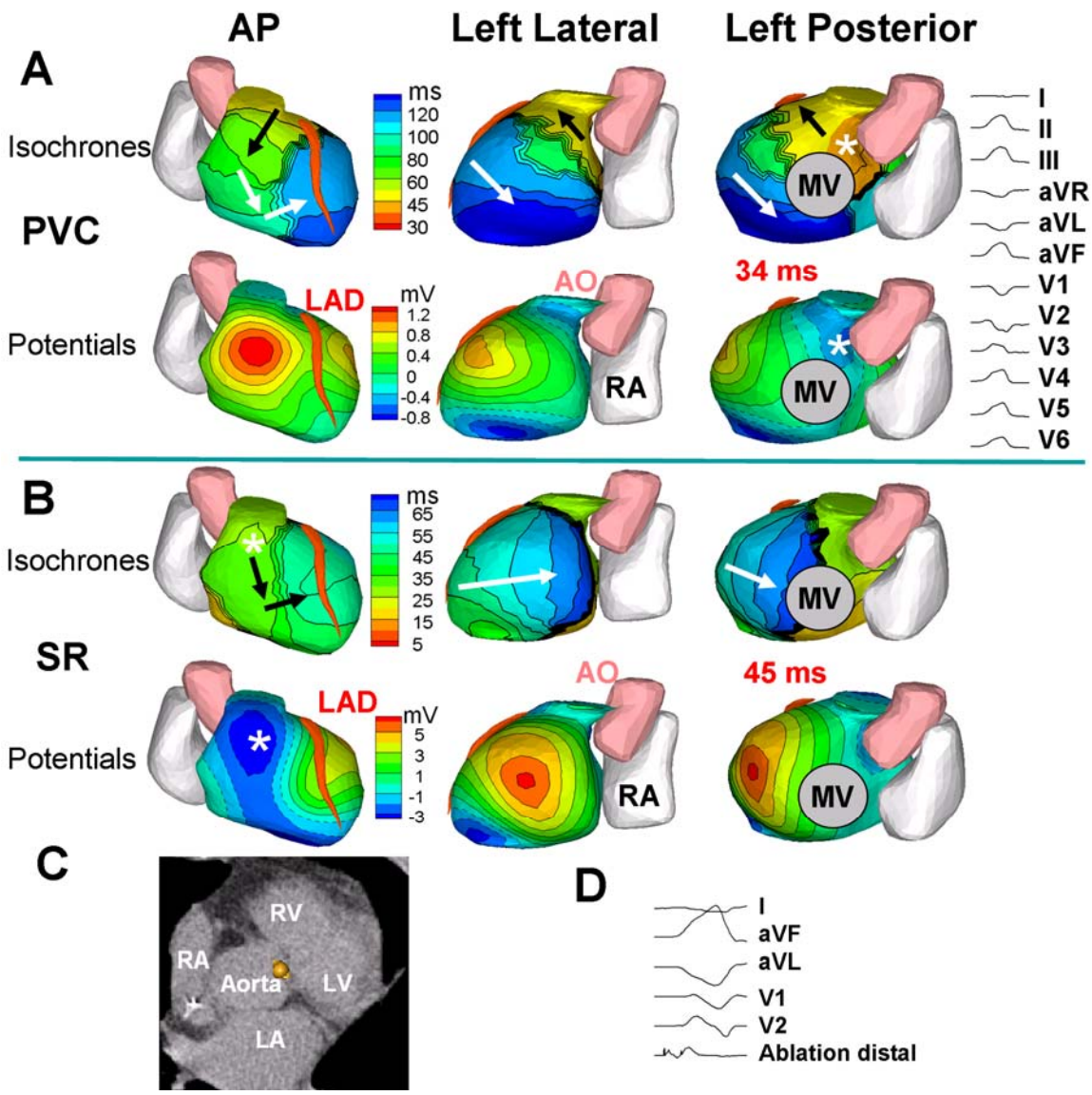

Figure 30 (Figure 5-3): ECGI of tachycardia originating in the left coronary aortic cusp, (RV1)

Panel A: Isochrone map (upper row) and potential map, (lower row, 34 ms from the onset of QRS) for a PVC beat in three views. White asterisk indicates the ECGI determined RVOT VT origin. Arrows indicate the activation wavefront propagation direction. The conventional 12-lead ECG from a PVC is shown on the right. Panel B shows the isochrone map (upper row) and potential map (lower row, 45 ms from the onset of QRS) for a sinus beat. White asterisk indicates RV epicardial breakthrough. Arrows show the sinus activation propagation sequence. Panel C shows a CT cross

section image; yellow dot indicates the ECGI determined VT origin. Panel D shows the surface ECG of a PVC during the EP study and (bottom) the electrogram recorded with ablation catheter at the site of the left coronary aortic cusp.

Spontaneous PVCs from Patient RV1 had the most leftward origin of early isochrone and negative potential. Figure 5-3 shows the corresponding ECGI results to highlight the area of focal initiation (white asterisks in panel A) that begins at the base of the left side of the aorta, near the left coronary cusp. The propagation pattern continues superiorly and rightward towards the anterior RV (white arrows) and then across the septum in a typical LBBB pattern. When superimposed onto the CT scan obtained during ECGI, the origin of the VT is found to be in the left coronary cusp of the aorta, which concurs with the findings of the EP study. Of note, despite published data for interpreting the ECG for left-sided outflow VT [159], the conventional 12-lead ECG in this case does not readily identify the correct location of the VT.

Figure 5-4 (RV3) has a markedly positive signal in lead I, suggesting a more leftward activation pattern. The difference in surface ECG morphology can be accounted for by different cardiac geometries relative to the body-surface leads. In this case, the surface ECG suggests different locations for the arrhythmias foci, but ECGI, which takes into account the specific patient anatomy, shows otherwise. This ECGI finding was supported by catheter mapping.

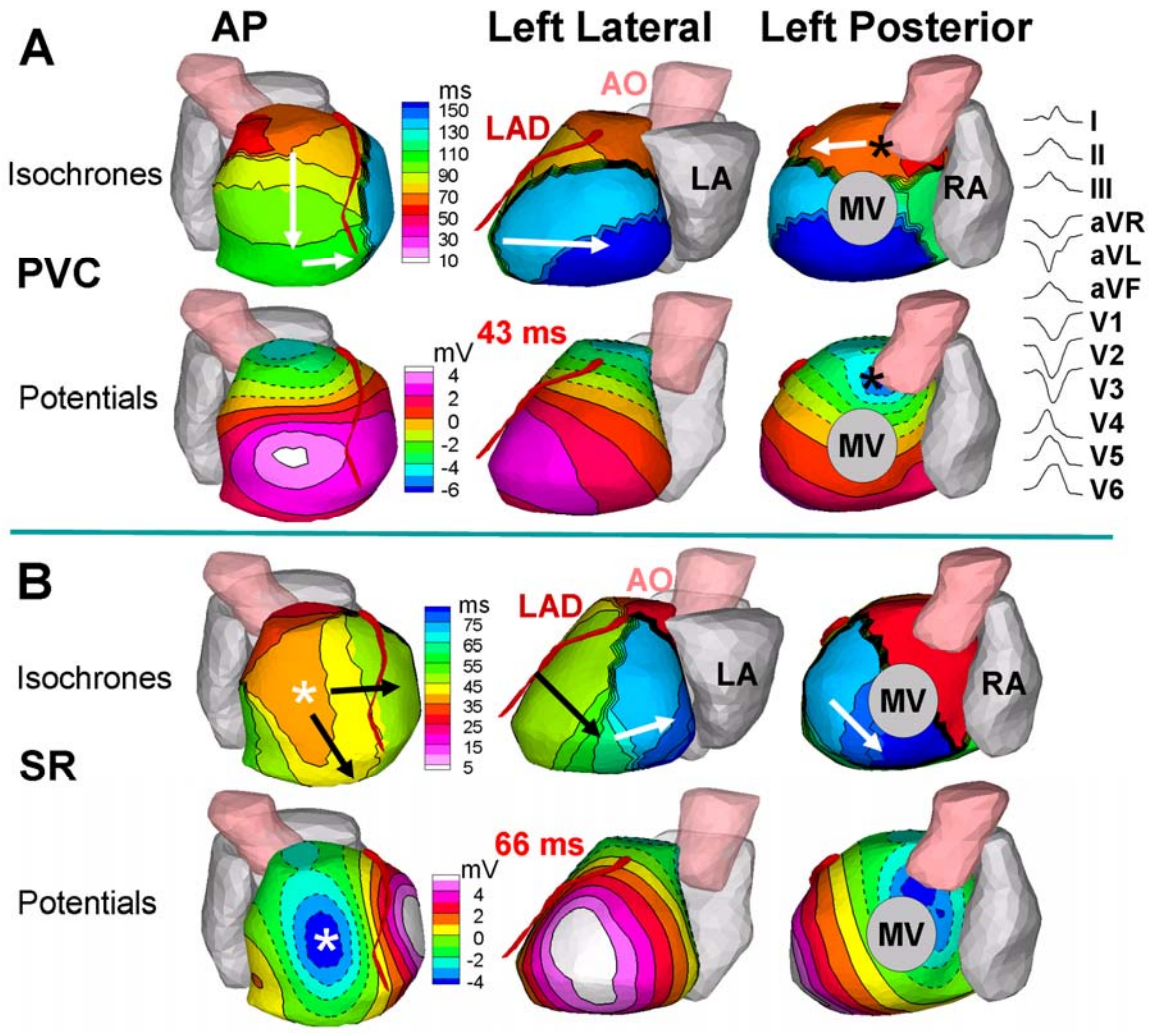

Figure 31 (Figure 5-4): ECGI of a mid-septal RVOT tachycardia, (RV3)

Panel A: isochrone map (upper row) and potential map (lower row, 43 ms from the onset of QRS) for a PVC beat in three views. Black asterisk indicates the ECGI determined RVOT VT origin. Arrows indicate the activation wavefront propagation direction. The conventional 12-lead ECG during PVC is shown on the right. Panel B shows the isochrone map (upper row) and potential map (lower row, 66 ms from the onset of QRS) for a sinus beat. White asterisk indicates RV epicardial breakthrough; arrows show direction of wave front propagation.

Two additional patients had sites of origin in the anterior left and posterior right RVOT,

respectively (Figures 5-5 and 5-6). The overall activation pattern for both patients was consistent with the “signature” LBBB pattern. The area of earliest activation on these isochrone maps varied when compared to the mid-septal RVOT location. For Figure 5-5 (RV4), with a posterior right origin, the earliest isochrone and negative potential were in the most posterior portion of the RVOT. Interestingly, the earliest propagation pattern included a portion of the anterior LV as well as the RV. The area of slowed conduction in this patient was displaced apically and laterally from the septum, but the overall LBBB signature pattern was preserved. The early anterior LV activation may account for the decreased terminal leftward forces on the conventional 12-lead ECG.

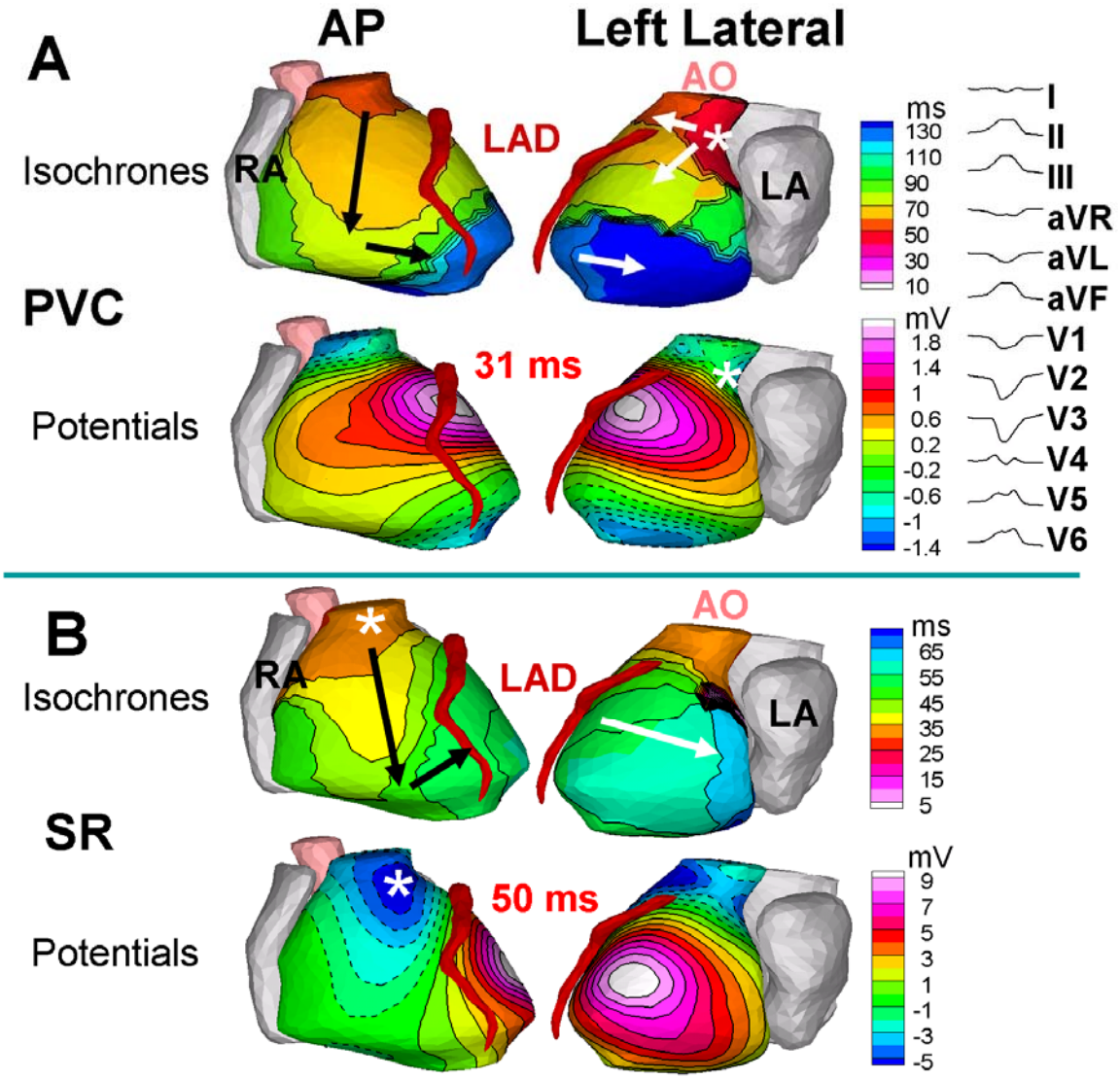

Figure 32 (Figure 5-5): ECGI of a posterior right RVOT tachycardia, (RV4)

Panel A: Isochrone map (upper row) and potential map (lower row, 31 ms from the onset of QRS) for a PVC beat in two views. White asterisk indicates the ECGI determined RVOT VT origin. Arrows show the activation wavefront propagation direction. The conventional 12-lead ECG during the PVC is shown on the right. Panel B shows the isochrone map (upper row) and potential map (lower row, 50 ms from the onset of QRS) for a sinus beat in two views. White asterisk indicates RV epicardial breakthrough. The arrows show direction of wave front propagation.

For Figure 5-6 (RV5), demonstrates an anterior left origin with the earliest isochrone and negative potential occurring more anteriorly in the RVOT. The activation pattern advanced quickly and preferentially down the anterior right ventricle, without early LV activation.

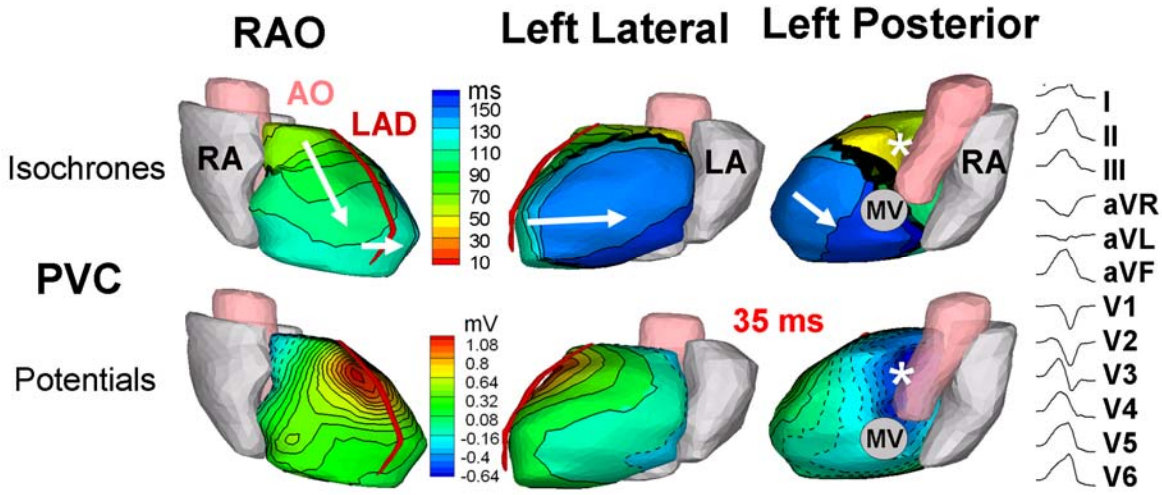

Figure 33 (Figure 5-6): ECGI of an anterior left RVOT tachycardia, (RV5)

The isochrone map (upper row) and potential map (lower row, 35 ms from the onset of QRS) for a PVC beat in three views. White asterisk indicates the ECGI determined RVOT VT origin. The white arrows show the direction of the activation wavefront propagation. The conventional 12-lead ECG during the PVC is shown on the right.

5.3.2 Right Bundle Branch Block (RBBB) pattern VT (LV tachycardia)

Five patients underwent six ablation procedures with a presumptive diagnosis of VT originating in the LV based on conventional 12-lead ECG analysis and cardiac imaging (LV1-LV6, mean age 51 years, range 35-63). ECGI was performed before the EP

procedure for three patients and during the EP procedure for the other three patients.

In total, two patients had reentry around a myocardial scar, two patients had intrafascicular reentry (fascicular VT), one patient had a focal VT of intramural origin, and one patient had a focal epicardial VT related to advanced cardiac sarcoid disease.

In all six patients, ECGI accurately localized the VT (Figure 5-1). Unlike RVOT tachycardia with a “signature” LBBB pattern and a consistent focal propagation pattern, tachycardias from the LV had different activation patterns, reflecting the variety of origins and mechanisms of LV-VT (Table 5-3). Pertinent illustrative examples are described below, using the three-step process of localization, propagation and myocardial depth to characterize each tachycardia.

Patient LV1 had a nonischemic cardiomyopathy and at the end of her EP study, she was deemed to have a nonendocardial focal VT at the apical-lateral LV. ECGI results during the EP study are shown in Figure 5-7. Double ventricular extrastimuli induced hemodynamically tolerated VT at a cycle length of 390ms. Isochrone maps of the RV pacing train, premature ventricular stimuli, and first beat of induced VT are shown in Figures 5-7A, 5-7B, and 5-7C, respectively.

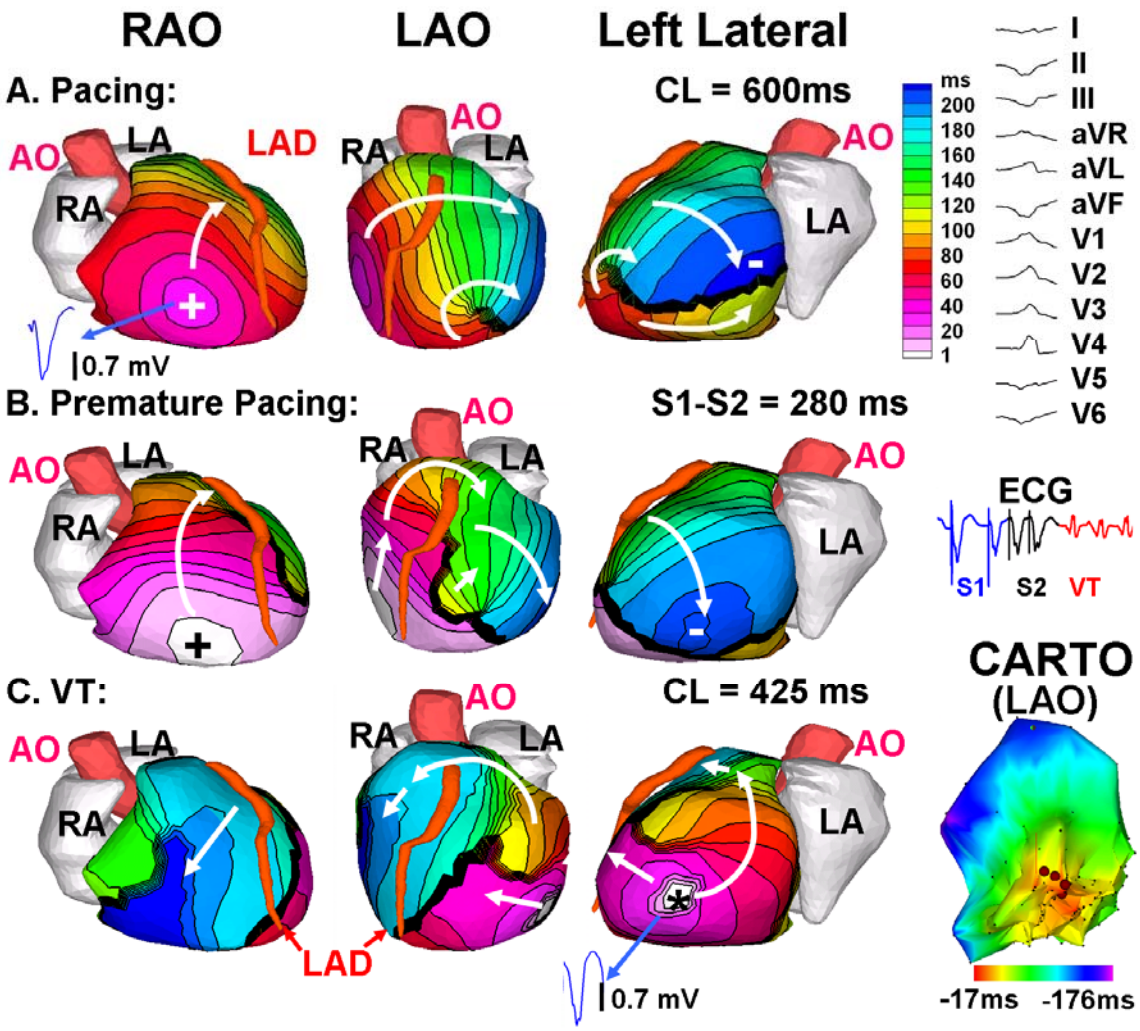

Figure 34 (Figure 5-7): ECGI of a focal ventricular tachycardia induced by programmed electrical stimulation, (LV1)

Panel A: Epicardial activation sequence during drivetrain (S1) pacing at cycle length of 600ms.(RAO = right anterior oblique, LAO=left anterior oblique). White arrows show direction of wavefront propagation. Thick black line indicates conduction block. Earliest epicardial activation site is marked by + and corresponds to the underlying endocardial pacing site. ECGI epicardial electrogram from this site is shown (blue arrow) with rS complex consistent with endocardial activation. The conventional 12-lead ECG during VT is shown on the right. Panel B: Premature (S2) pacing at 280ms coupling interval from the same pacing site. The major wave front is forced to pivot around the extended line of

block. There is some fusion with an intramural trans-septal front (small white arrow). Panel C: VT; earliest epicardial activation site is marked by asterisk. ECGI electrogram from the VT origin site is shown (blue arrow), with a pure Q wave, suggestive of an epicardial origin. A body surface ECG is shown on the right of Panel B. All S1 beats (blue) are similar, as are the two S2 beats (black) and all VT beats (red). Invasive LV endocardial activation map of the VT in LAO projection is in Panel C, right (red is early). ECGI epicardial activation movies are in the attached CD (LV1).

With drive train pacing (S1, Figure 5-7A), the earliest epicardial activation starts from the pacing site (white +) near the RV apex and propagates both superiorly and inferiorly towards the left ventricle. ECGI epicardial electrogram from the site of earliest epicardial activation shows rS morphology, consistent with endocardial initiation of the paced beats.

The epicardial activation sequence during premature ventricular extrastimuli (S2) from the same site is shown in Figure 5-7B. The premature beat retains a similar overall activation pattern to drive train pacing, with two distinct differences. First, the line of block is elongated over the anterior septum towards the base of the heart (LAO view), demonstrating its functional nature. Second, in the LV the line of block shifts inferiorly and the latest activation region (white -) is delayed and shifted apically (left lateral view).

Figure 5-7C shows epicardial activation during the first beat of induced VT. The earliest epicardial activation (black star in left lateral view) occurs at the latest activation region

of the previous S2 paced beat, suggesting triggered activity as the mechanism. The activation wavefronts propagate towards both the apex and the base (white arrows). The activation wavefront that propagates towards the apex encounters a line of block. The activation wavefront that propagates towards the base turns around the line of block and propagates toward the RV. The electrogram from the earliest epicardial site is a pure Q wave, indicating an epicardial origin of the VT [34]. ECGI epicardial activation movies are in the attached CD (LV1).

A three-dimensional endocardial map was created during the procedure, showing the earliest activation in a large area in the anterolateral apex (Figure 5-7D). At the conclusion of the procedure, it was deemed that the likely mechanism was focal, and that the endocardium was not the site of origin. These conclusions are consistent with the ECGI images and electrograms.

Patients LV2 and LV3 were found to have reentrant VT around areas of myocardial scar during EP study. ECGI results for patient LV2 are shown in Figure 5-8. This patient had an extensive inferoseptal scar from a prior inferior wall myocardial infarction (SPECT image in Figure 5-8C) and presented with slow hemodynamically tolerated VT. As shown by ECG lead V2 (inset), sinus capture (SC) beats occasionally interrupted the VT rhythm. ECGI images of an SC beat and a VT beat are shown in panels A and B, respectively.

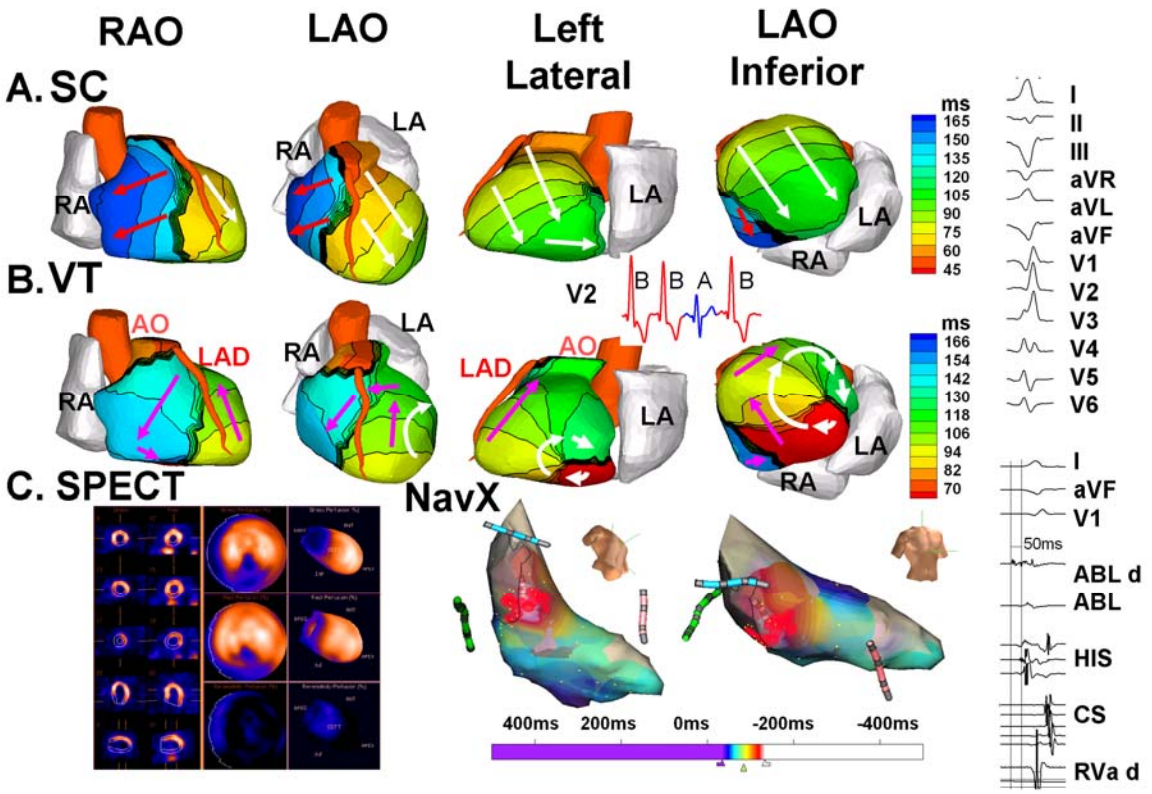

Figure 35 (Figure 5-8): ECGI of reentrant VT from inferobasal scar, (LV2)

Panel A: Four views of activation sequence during a sinus capture (SC) beat (labeled A, blue on the V2 ECG). Arrows indicate direction of the activation wavefronts. Panel B: Activation sequence during VT beats (labeled B, red on the V2 ECG). White arrows indicate a clockwise lateral loop (left lateral and LAO inferior views); Pink arrows show propagation into the RV in a counter-clockwise fashion. Panel C: Left: SPECT images showing a scar at the inferobasal LV region (blue). Right: NavX invasive endocardial map of VT activation (red early, blue late). ECGI epicardial activation movies, including early activation of a region near the inferior scar border, are in the attached CD (LV2). The conventional 12-lead ECG during VT and the ablation-catheter signals are shown on the right side of the figure.

The origin of each ECGI-imaged VT beat was the inferior base of the heart (red, LAO and left lateral views). The propagation pattern of the VT consisted of two wave fronts. One (white arrows) propagated clockwise, with a high degree of curvature, toward the base of lateral LV, where it encountered an inferior line of block. The other (pink arrows) propagated superiorly toward the base where it made a slow counter-clockwise turn around a line of block near the septum to RV. The latest activation during VT was at the lateral base of the RV. This second wavefront connected with the first wavefront at the inferior base, where the next wavefront begins. In this region of the inferobasal septum, ECGI reconstructs low-amplitude, highly fractionated electrograms, consistent with a scar (data not shown). Movies of the epicardial activation are available in the attached CD (LV2), showing a short period of earliest activation near the border zone of the scar. The subsequent VT beat begins near this border zone site. During the ablation procedure, a voltage map confirmed the inferobasal septal scar (Figure 5-8C). A limited invasive activation map during the slow VT showed the earliest activation in the scar border zone in the inferobasal septum, with the earliest electrogram signal >50 ms before the surface QRS (Right side of Figure 5-8).

A second scar-based reentrant VT is shown in Figure 5-9. This patient presented with syncope and sustained VT on ambulatory monitoring. A gadolinium-enhanced MRI revealed patchy myocardial and subepicardial enhancement in the lateral LV, consistent with a focal myocarditis or cardiac sarcoid. ECGI during VT identified two distinct areas

of early epicardial activation (white asterisks, Figure 5-9A), which differed slightly from beat to beat (T1, T2, T3). The propagation pattern varied somewhat based on the relative contribution of the two sources, but the images in Figure 5-9 show that for all beats the wavefront turns clockwise and propagates to the LV lateral base with a high degree of curvature, where it reaches a line of block in the inferolateral base. A fusion beat is also shown (SF) with a combination of normal anterior RV activation and abnormal inferolateral VT activation. Movies of the epicardial activation are available in the attached CD (LV3).

Electrogram analysis showed both pure Q wave and rS pattern during VT, consistent with both epicardial and endocardial involvement. Figure 5-9B shows a peak-to-peak amplitude “substrate map” of ECGI epicardial electrograms obtained during the SF beat. The mid-lateral LV has a region of low amplitude (blue), which corresponds closely to the MRI scar images. The activation sequence is superimposed on the substrate map, demonstrating its relationship to the scar substrate (blue). During the ablation procedure, pre-ablation activation mapping detected an earliest endocardial activation site in the inferolateral LV, which corresponds to the earliest region of epicardial activation mapped by ECGI.

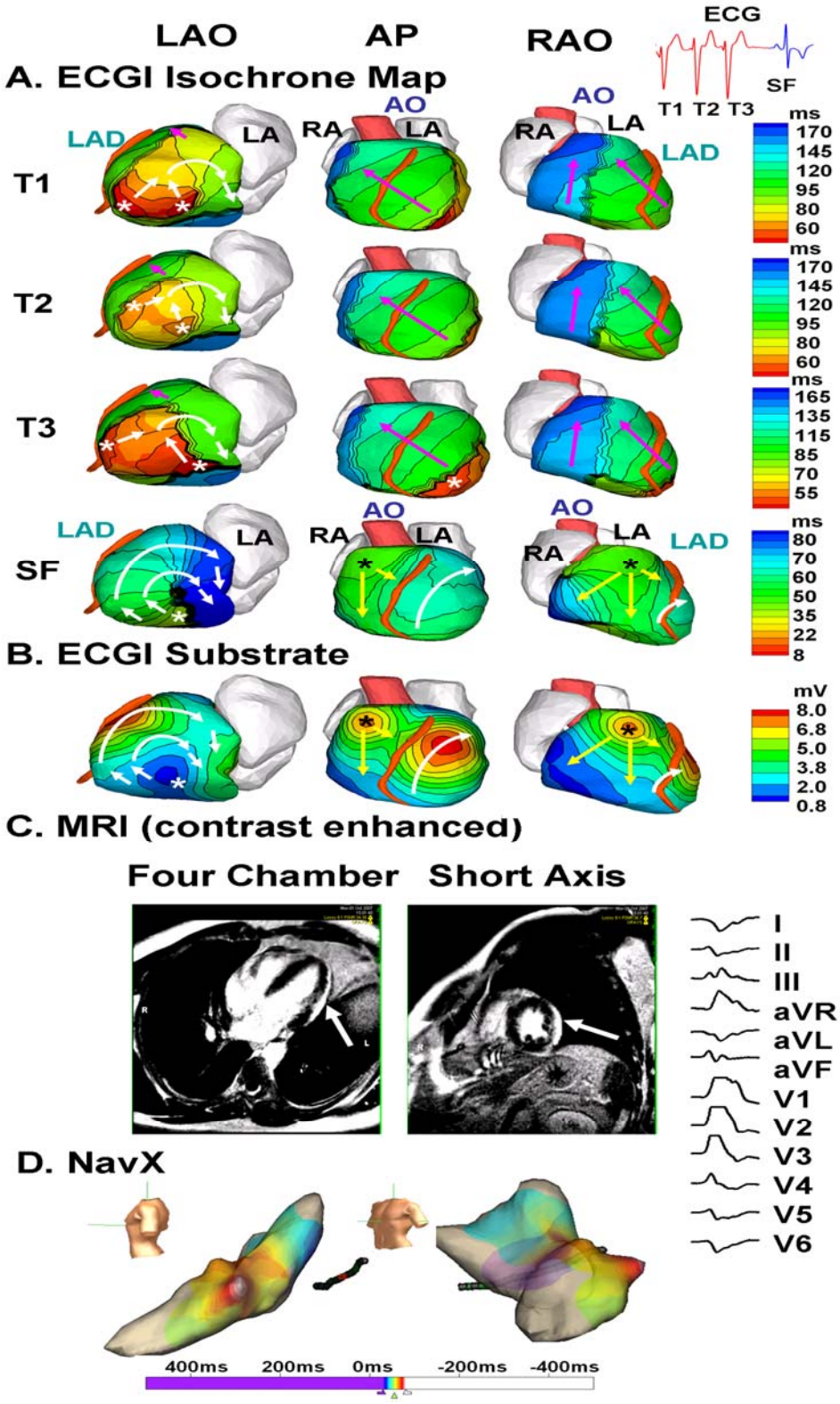

Figure 36 (Figure 5-9): ECGI of a reentrant VT in lateral VT (lateral wall infiltrative cardiomyopathy), (LV3)

Panel A. Activation patterns for three consecutive VT beats (T1, T2, T3) and one fusion beat of sinus

and VT activation (SF) in three views. The displayed beats are marked by T1, T2, T3 and SF on one surface ECG. Asterisks mark earliest epicardial activation sites and arrows the propagation direction of the activation wave front. For the VT beats, white arrows show the clockwise rotating wave fronts and pink arrows show a second wavefront that activates the RV. The black asterisk and yellow arrows in SF1 map show normal RV breakthrough site and activation, which fuses with VT activation (white asterisk and arrows). ECGI epicardial activation movies are available in the attached CD. Panel B. Substrate map during a sinus beat, created using peak-to-peak magnitude of ECGI epicardial electrograms (low potentials are blue; scale in mV). Arrows indicating the activation pattern are superimposed, demonstrating how the wavefront relates to the underlying scar substrate. Panel C. Contrast-enhanced (gadolinium) MRI images in two views. The LV mid-lateral scar appears bright (arrows). Panel D. NavX map of endocardial activation during VT; regions of earliest activation are red. The conventional 12-lead ECG of the VT is shown on the right.

Two patients in the study had fascicular VT (LV4 and LV5), thought to be a microreentrant circuit involving the distal Purkinje network. ECGI activation sequences for these patients are shown in Figure 5-10 and Figure 5-11. In Figure 5-10A, the VT earliest epicardial activation is over a large area at the apex. A broad wavefront propagates towards the LV base. One segment rotates clockwise to the lateral base. A second segment propagates inferiorly toward the posterior base (inferior view) and after a long conduction delay activates the RV and propagates superiorly towards the base of the heart. This is consistent with the RBBB pattern seen on the conventional 12-lead ECG.

The ECGI local electrogram at the apex (blue arrow) clearly shows rS morphology, identifying an endocardial or intramural origin of VT. Movies of ECGI-imaged epicardial activation are available in the attached CD (LV4).

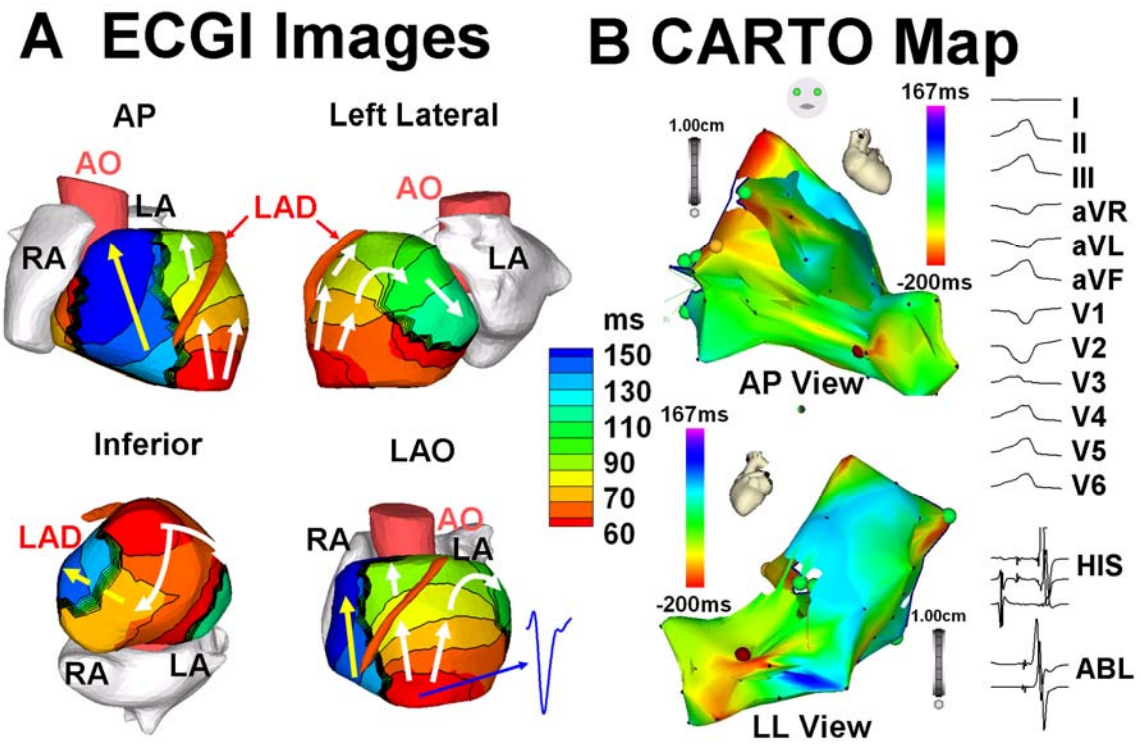

Figure 37 (Figure 5-10): ECGI of left posterior fascicular VT, (LV4).

Panel A: Four views of the activation sequence during VT. White arrows indicate the activation pathways during the first 120 ms. Yellow arrows indicate the activation sequence of anterior-lateral RV after a long conduction delay. Epicardial electrogram with rS morphology at apex (blue arrow) indicates endocardial or deep intramural origin of the VT. ECGI epicardial activation movies are in the attached CD. Panel B: Endocardial CARTO activation maps in AP and left-lateral views demonstrate successful ablation at an endocardial site (red sphere) that corresponds to the ECGI-imaged site of earliest epicardial activation. The conventional 12-lead ECG and catheter recordings during the induced VT are shown on the right.

During the EP study, activation mapping revealed the earliest activation at the mid-to-apical inferior septum, where a fascicular potential was recorded (Figure 5-10B). This apical septal site is consistent with the ECGI epicardial activation maps.

Results from the second fascicular VT (LV5) can be found in Figure 5-11. The conventional 12-lead ECG showed monomorphic VT and clinically, despite extensive mapping, the procedure was ultimately abandoned due to the inability to obtain a perfect pacemap match. Interestingly, ECGI demonstrated both morphology and magnitude differences between beats of VT. This is highlighted in the isochrone maps. Between VT morphologies, there are similar slow conduction lines, lines of block, and general patterns of propagation. However, the most distinct difference between different beats is the location of the earliest activation site (asterisk). Movies of ECGI-imaged epicardial activation are available in the attached CD (LV5). ECGI of the pacemap "target" VT was considerably different than the other imaged VT beats, which helps explain the inability to successfully ablate the VT.

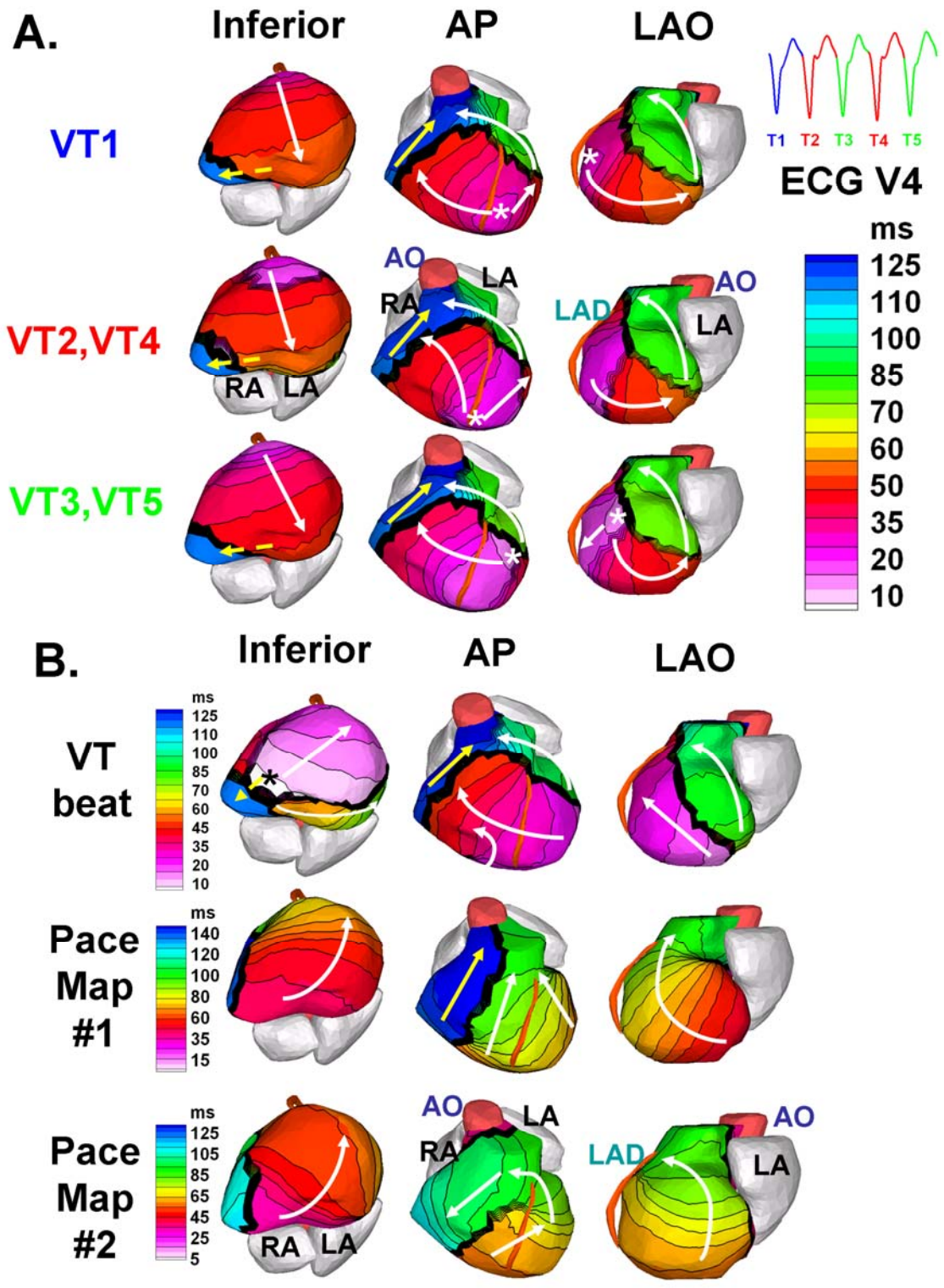

Figure 38 (Figure 5-11): Patient LV5.

Panel A: Three morphologies of VT within five consecutive beats. Each row shows the ECGI

activation map for one VT morphology. The five consecutive VT beats in lead V4 are color coded based on the morphology. White arrows indicate the direction of the activation wavefronts. Yellow arrows indicate slow conduction and late RV activation. Asterisk marks the earliest activation site for the beat. ECGI epicardial activation movies are in the attached CD. Panel B: ECGI maps of epicardial activation during the “target” pacemap VT beat (top row) and two unsuccessful pacemap locations near the left posterior fascicle in the middle and bottom rows.

Finally, patient LV3 presented eight months after his first endocardial ablation with frequent nonsustained VT and worsening heart failure symptoms. His cardiac function had deteriorated over time. On conventional 12-lead ECG, he had three distinct morphologies of VT. His predominant arrhythmia had characteristics consistent with an epicardial location, and an epicardial ablation was performed. ECGI images are shown in Figure 5-12.

Isochrone map and potential map show earliest activation during VT in the anterolateral base (Figure 5-12A). The propagation pattern is radial from a central focus, and the local electrogram is pure Q wave, consistent with an epicardial source. Electroanatomic mapping of the epicardial surface during VT (Figure 5-12B) was entirely consistent with the noninvasive ECGI findings.

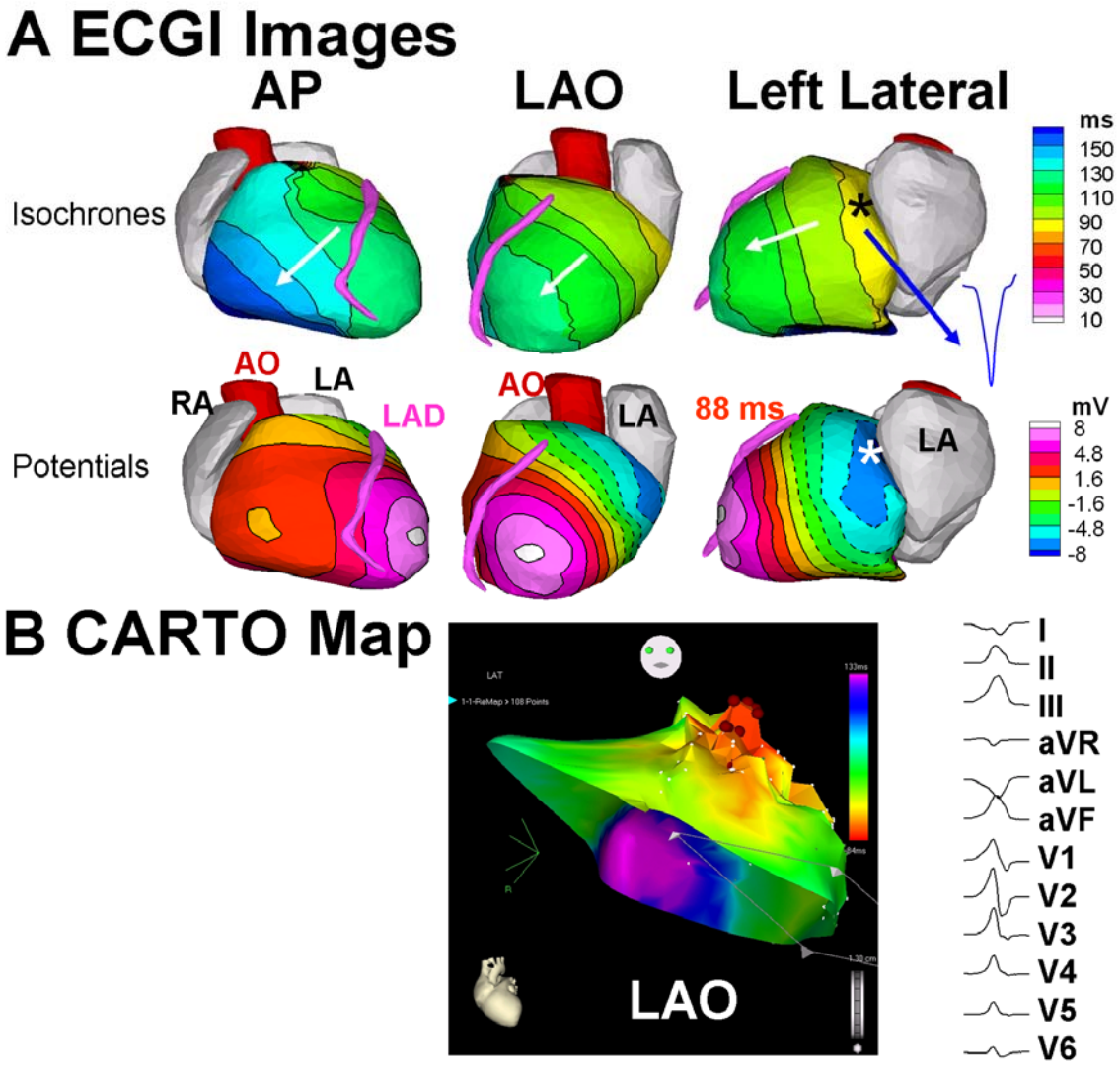

Figure 39 (Figure 5-12): ECGI of anterior basal focal VT, (LV6)

Panel A. Isochrone map (upper row) and potential map (lower row, 88 ms from the onset of QRS) during VT beat in three views. Asterisk indicates the ECGI determined VT origin. White arrows indicate the direction of activation wavefront propagation. Epicardial electrogram with Q wave at the earliest activation region is shown in blue. Panel B. Epicardial electroanatomical map (CARTO) is shown in LAO projection, with early activation at the anterolateral base (red). The conventional 12-lead ECG during a VT beat is shown on the right.

5.4 Discussion

This paper reports the first findings from a noninvasive three-dimensional electroanatomic mapping system, ECGI, in a series of patients undergoing catheter ablation for a broad range of ventricular tachycardia types. A number of general conclusions regarding ECGI performance in this study should be mentioned. First, ECGI proved to be a reliable and versatile system, with 100% imaging success rate when performed either before or during an EP study. Second, despite a wide range of VT locations and mechanisms included in this study, ECGI results were consistent with the conclusions of the ablation procedures in all cases. Third, based on comparison with three-dimensional catheter mapping, when available, ECGI provided high local spatial resolution. This property overcomes a limitation of the body surface ECG, which provides only global information. For example, despite a monomorphic appearance of the conventional 12-lead ECG during VT in patient LV3, there are differences in local activation between beats, with a shift of initial activation sites (Figure 5-9).

The combination of three aspects of ECGI results could accurately characterize each tachycardia: localization, propagation and electrogram characteristics. With these three data elements, one can construct ECGI criteria to differentiate between focal mechanisms (local initiation; radial propagation pattern) and reentrant mechanisms (spiral wavefront with high degree of curvature; usually associated with an anatomic or functional line of block and / or an underlying scar; early activation in the scar region).

The ability of ECGI to obtain information on local epicardial activation and its progression on a beat-by-beat basis can provide important insights into VT mechanisms. An interesting example of focal tachycardia is the VT induced by programmed stimulation (LV1, nonischemic cardiomyopathy; Figure 4). At baseline pacing (CL=600ms), an inferior (anatomical) line of block was present on lateral LV. During premature pacing (S1-S2=280ms), this line of block was functionally extended, forcing the activation front to pivot around it with high curvature, thereby prolonging activation time (relative to the time of pacing stimulus) and shifting latest activation to a location near the center of the anatomical block. The next beat is the first VT beat. It is coupled to the S2 premature beat and starts from the location of its latest activation. The delayed late activation by S2 promotes recovery and capture of adjacent ventricular regions by the VT excitation. Taken together, these properties are consistent with triggered activity as the mechanism of VT initiation.

Physiological insights can also be obtained for reentrant VTs. The examples in this study include the relationship and anchoring to a myocardial scar, early activation in the scar, and exit sites at the scar border form which the rotating wave front emerges. From the clinical perspective, this information can assist in guiding ablation. It should be mentioned that frequently the ECGI-imaged activation wave front sequence did not cover the entire tachycardia cycle length. This can be accounted for by intramural activation

(ECGI is limited to the epicardium) and/or slow discontinuous conduction inside the scar (reflected in early activation detected by ECGI at the scar border zone).

The results of this study suggest possible clinical usefulness for ECGI. Potential clinical advantages include: 1) the ability to map the entire heart in a single beat, including areas of presystolic activation and areas of scar; 2) the ability to map prior to an ablation procedure (catheter or surgical), without the antiarrhythmic effects of sedation; 3) identification of alternate non-RVOT sites of VT in patients with outflow tract tachycardias, such as the example above from the left coronary cusp; 4) identification of epicardial origin of VT based on electrogram morphology (Q wave vs. rS pattern), which allows for a more appropriate individualized ablation strategy, such as early epicardial access; 5) ability to image noninvasively the electrical substrate over time, which can be applied in follow up evaluations of therapy or progression of disease. A randomized trial would be needed, however, before one can conclude that the use of ECGI translates into faster, safer and more successful procedures.

An obvious limitation of all ECGI studies at this translational stage is a limit on the number of subjects. This is dictated by the unavailability of ECGI systems for multi-site studies, by the need for careful processing and detailed analysis of data on a case by case basis, and by the still experimental stage of this new approach. In this pilot VT study, we present examples of different types of tachycardia and examine the ability of ECGI to

provide mechanistic insights. A detailed description of mechanisms and further evaluation of the clinical application of ECGI in VT patients will require a multi-center study in much larger groups of subjects in each VT category.

5.5 Legends for the Video files

LV1.wmv: Patient (LV1), Epicardial Focal VT; The first two beats are S1 paced beats, followed by two S2 paced beats and two VT beats.

LV2.wmv: Patient (LV2), Scar-related Reentry VT; The first two beats and last beat are VTs, the third beat is sinus capture (SC) beat.

LV3.wmv: Patient (LV3), Scar-related Reentry VT; The first three beats are VT beats, the last beat is the sinus fusion beat.

LV4.wmv: Patient (LV4), Fascicular VT; Two beats of epicardial activation during VT are shown.

LV5.wmv: Patient (LV5), Fascicular VT; Eight beats of epicardial activation during VT are shown.

Chapter 6 Characterization of Epicardial Activation in Humans with Diverse AF Patterns using Noninvasive ECG imaging (ECGI)

Abstract

Many mechanisms for the initiation and perpetuation of atrial fibrillation (AF) have been demonstrated over the last several decades. The tools to study these mechanisms in humans have limitations, the most common being invasiveness of a mapping procedure. In this paper, we present simultaneous noninvasive biatrial epicardial activation sequences of AF in humans, obtained using the Electrocardiographic Imaging (ECGI) system, and analyzed in terms of mechanisms and complexity of activation patterns. We performed ECGI in 36 patients with a diagnosis of AF. To determine ECGI atrial accuracy, atrial pacing from different sites was performed in six patients (37 pacing events), and ECGI was compared to registered CARTO images. Then, ECGI was performed on all 36 patients during AF and ECGI epicardial maps were analyzed for mechanisms and complexity. ECGI noninvasively imaged the low-amplitude signals of AF in a wide range of patients (97% procedural success). The spatial accuracy in determining initiation sites as simulated by atrial pacing was ~ 6mm. ECGI imaged many activation patterns of AF, most commonly multiple wavelets (92%), with pulmonary vein (69%) and non-pulmonary vein (62%) focal source sites. Rotor activity was seen rarely (15%). AF complexity increased with longer clinical history of AF, though the degree of complexity of nonparoxysmal AF varied and overlapped. ECGI offers a way to identify

unique epicardial activation patterns of AF in a patient-specific manner. The results are consistent with contemporary animal models of AF mechanisms and highlight the coexistence of a variety of mechanisms among patients.

6.1 Introduction

Atrial fibrillation (AF) is the most common cardiac arrhythmia, accountable for increased risks of stroke, heart failure, and all-cause mortality[160,161]. It is responsible for nearly one-third of all hospital admissions with a cardiac rhythm abnormality[162]. Published guidelines have provided a standardized approach toward treating AF[163]. In general, patients are clustered into groups based on the clinical duration and frequency of recurrence of AF (paroxysmal, persistent, longstanding persistent, permanent). While this approach has served clinicians well, it does not take into account the various mechanisms of the arrhythmia.

Lessons from numerous models of AF have brought about conflicting results regarding a single unifying mechanism. Common theories include the “multiple wavelet” hypothesis[164], the “mother rotor/fibrillatory conduction” hypothesis[165], and the “pulmonary vein/focal source” hypothesis[166]. Additional contributions from the autonomic nervous system likely play a key role in AF as well[167]. Mechanisms of initiation and perpetuation of AF continue to be the subject of on-going intense investigation.[168-175]

Toward improving the treatment of AF, it is incumbant to understand the underlying mechanism in each individual patient. Indeed, the HRS/EHRA/ECAS 2007 Expert Consensus Statement on the Surgical and Catheter Treatment of Atrial Fibrillation summarizes the state of our knowledge by stating, "Although much has been learned about the mechanisms of AF, they remain incompletely understood. Because of this, it is not possible to precisely tailor an ablation strategy to a particular AF mechanism."[176]

Currently, there is a paucity of simultaneous atrial mapping data during AF in patients. In this paper, we present simulatneous noninvasive biatrial epicardial activation sequences of AF for a wide range of AF phenotypes. The maps were obtained using the noninvasive Electrocardiographic Imaging (ECGI)[1] system and analyzed in terms of mechanisms and complexity of activation patterns.

6.2 Methods

Thirty-six subjects included in this study had histories of atrial arrhythmias and were referred from the electrophysiology and cardiothoracic surgery services. Subjects were identified in both the inpatient and outpatient settings. All protocols were approved by the Institutional Review Board at Washington University in St. Louis, and informed consent was obtained from all patients.

ECGI System

ECGI methodology was described previously in detail[1,2]. 256 carbon electrodes organized on strips were applied to patient's torso surface. Small CT markers were attached to the back side of each carbon electrode. All carbon electrode strips were connected to a portable mapping system (Active 2 system, BioSemi, Netherlands). After the electrodes were applied, the patients underwent thoracic noncontrast gated CT imaging with an axial resolution of 3mm. Scans were gated at 20% of the R-R interval (atrial diastole) if in sinus rhythm. When the ECGI was performed during an EP study or pulmonary vein isolation procedure, the carbon electrodes were kept in the same position as during the preprocedural CT. Atrial epicardial surface geometry and body surface electrode positions were labeled and digitized from CT images.

The 256 channels of body surface potentials (BSP) were sampled at 1-ms intervals during the cardiac cycle, and the data were saved on a laptop computer. BSP were acquired during sinus rhythm or atrial arrhythmias. During the EP study, BSP were acquired during atrial pacing from various locations and during atrial tachycardias. Several minutes of data were recorded from each patient. The QRST complex was excluded from the reconstruction and analysis of atrial arrhythmias.

The BSP and geometrical information (torso-heart geometrical relationship) were

combined by ECGI algorithms to noninvasively construct epicardial potential maps, electrograms, activation sequences (isochrones) and repolarization patterns. ECGI has been extensively validated in animal models[3-9,91,177] and human studies.[1,2,10,12-18,33,34,102,178,179] ECGI is constructed on a beat-by-beat basis and does not require accumulating data from many identical beats. Activation times were determined by the maximal negative slope of the epicardial electrograms. Activation movies for several consecutive beats were also constructed by animating the activation wave front on the patient-specific CT-derived epicardial surface. Activation movies are created from several recordings for each patient. All the activation movies from different recordings are analyzed. Lines or regions of block were determined if activation times across local areas differed by more than 50ms. Slow conduction is represented by crowded isochrones.

Clinical Classification of AF

AF was classified based on standard criteria of AF duration. Paroxysmal AF is defined as recurrent AF lasting less than 7 days and terminating spontaneously. Persistent AF is defined by episodes longer than 7 days in duration or that requirement for electrical or pharmacologic cardioversion. Long-standing persistent AF is defined as longer than one year in duration.

Simulation of Focal Atrial Activation with Pacing during Biatrial ECGI Mapping

ECGI was performed on six patients in sinus rhythm undergoing pulmonary vein isolation procedures. ECGI was obtained during pacing from various sites in the left and right atria to simulate focal initiation sites. Anatomic locations of the pacing sites were recorded onto an endocardial electroanatomic map (CARTO, Biosense-Webster) or regionalized to the specific structure being paced. ECGI reconstructions of the paced P waves were analyzed to determine the location of pacing site based on earliest isochronal activation, location of a local potential minimum during depolarization and corresponding potential maximum during repolarization. Examples are shown in Figure 1. When possible, the three-dimensional distance from the ECGI-imaged site to the recorded anatomic site from a registered electroanatomic map was measured (Amira 4.1, Visage Imaging).

Analysis of Atrial Arrhythmias

Static isochrone maps of the atrial activation sequence were constructed for patients in sinus rhythm and organized atrial arrhythmias. For patients in AF, activation movies of AF were constructed during long RR intervals (500 to 1000ms) by animating the activation wavefront on the CT epicardial surface using one millisecond incremental time intervals. Detailed visual analysis of at least five atrial fibrillation movies for each patient (500-1000 ms per movie) was performed. The number of observed simultaneous wavelets participating in AF ("number of wavelets"), the locations of spontaneous atrial

depolarization sites, and number of such sites that initiated new wavefronts ("number of focal sources") were recorded. To minimize nonphysiologic error, the definition of a "focal source" required a local cycle length of at least 100ms and had to be observed at least twice in a movie segment. To quantify the complexity of an individual's AF, a "complexity index" was calculated as the arithmetic sum of the mean number of wavelets and the mean number of focal sources. A complexity index of 1 represents the simplest AF, with higher numbers representing more complex AF.

Continuous variables, such as number of wavelets or focal sources, were analyzed using a Student's t-test. When patients were grouped according to their clinical history (paroxysmal, persistent, long-standing persisitent), an analysis of variance (ANOVA) test was used to determine differences between the three groups.

Patient Selection

The pertinent clinical characteristics of the thirty-six patients are summarized in Table 6-1 and Table 6-2. Twenty of the thirty-six patients were ECGI-imaged during atrial fibrillation. Six patients referred for AF were found by ECGI to have other atrial arrhythmias (atypical atrial flutter (4), atrial tachycardia (2)). Fifteen patients were imaged during sinus rhythm. Using clinical criteria, eleven of the thirty-six patients were classified as paroxysmal (31%), nineteen as persistent (53%), and six (16%) as long-standing persistent. This was a heterogeneous group with respect to age (31 to 76

years), duration of AF (1 month to 30 years), and left atrial size (3.5 to 5.7 cm).

Overall, ECGI yielded interpretable images in 35 of 36 patients (97%). One patient without interpretable ECGI was diagnosed with atrial flutter from a pacemaker interrogation and did not have any discernable atrial activity on her standard 12-lead ECG. She had undergone a prior Cox-maze procedure and mitral valve replacement. In all patients, ECGI was well-tolerated without any adverse events related to the imaging.

Table 7 (Table 6-1) Clinical Characteristics

	Number (%)	Mean (Range)
Age		55.4 years (31-76 years)
Gender		
Male	24 (67%)	
Female	12 (33%)	
Race		
Caucasian	33 (91%)	
Black	2 (6%)	
Other	1 (3%)	
Years since diagnosis of AF		8.3 years (0.2 to 30 years)
Clinical classification of AF		
Paroxysmal	11 (31%)	
Persistent	19 (53%)	
Longstanding Persistent	6 (17%)	
Left atrial dimension		4.4 cm (3.5 to 5.7 cm)
Mitral regurgitation		0.86 (0[none] to 3[severe])
Clinical History		
CHF	2 (6%)	
HTN	14 (39%)	
DM	2 (6%)	
CVA/TIA	4 (11%)	
Antiarrhythmic medication	36 (100%)	
Immediate family history of AF	6 (17%)	

Seven patients had a prior pulmonary vein isolation procedure (2 persistent, 5 long-standing persistent). At the time of ECGI, five of the seven were in AF, one was in atrial tachycardia and one was in atypical atrial flutter. Two patients had a prior Cox-Maze procedure; one was imaged in atypical atrial flutter while the other was imaged during AF. One patient had a suspected atrial tachycardia based on ambulatory monitoring but had only isolated premature atrial beats during EP study. One patient with a prior Fontan corrective surgery had an atypical atrial flutter and had undergone two prior right atrial radiofrequency ablation procedures. One patient was imaged during an ablation procedure for idiopathic VT and developed AF during induced VT.

Table 8 (Table 6-2) Detailed Patient AF characteristics

Patient #	Clinical Group	Mapped Rhythm	# Wavelets	# Focal sources	Complexity Index	Prior Procedures
11	Paroxysmal	Sinus	NA	NA		
15	Paroxysmal	Sinus	NA	NA		
16	Paroxysmal	Sinus	NA	NA		
20	Paroxysmal	Sinus	NA	NA		
22	Paroxysmal	Sinus, PAC	NA	NA		
26	Paroxysmal	Sinus	NA	NA		
23	Paroxysmal	AF	1	0	1	
19	Paroxysmal	Sinus, AF	1	1	2	
27	Paroxysmal	Sinus, AF	1.5	2	3.5	
33	Paroxysmal	Sinus, AT, AF	1	1	2	
35	Paroxysmal	Sinus, AT, AF	1	1	2	
8	Persistent	Sinus	NA	NA		
24	Persistent	Sinus	NA	NA		
25	Persistent	Sinus	NA	NA		
6	Persistent	Sinus	NA	NA		
1	Persistent	AF	2	4	6	
3	Persistent	AF	1	1	2	

4	Persistent	AF	1.5	3	4.5	
10	Persistent	AF	1.5	1	2.5	
13	Persistent	AF	2.5	4	6.5	
14	Persistent	AF	1.5	2	3.5	
17	Persistent	AF	2.5	3	5.5	
18	Persistent	AF	1.5	2	3.5	
7	Persistent	AF	2.5	3	5.5	
34	Persistent	AF	2.5	2	4.5	
32	Persistent	AF	4	3	7	Prior Maze
29	Persistent	AF	2	2	4	Prior PVI
30	Persistent	AF/AFL	2	2	4	Prior PVI
28	Persistent	AF/AFL	2	1	3	Fontan
21	Longstanding Persistent	AFL	NA	NA		Prior Maze
2	Longstanding Persistent	AF	2	3	5	Prior PVI
5	Longstanding Persistent	AF	3	6	9	Prior PVI
12	Longstanding Persistent	AF	2	3	5	Prior PVI
31	Longstanding Persistent	AF	3	3	6	Prior PVI
9	Longstanding Persistent	AT	3	1	4	Prior PVI

6.3 Results

Simulation of Focal Atrial Activation with Pacing

In six patients, ECGI was performed during pulmonary vein isolation procedures with atrial pacing from various atrial locations. A total of thirty-seven paced events were recorded in all four pulmonary veins (PV), posterior left atrium, mitral valve isthmus, coronary sinus, atrial septum, sinus node and atrial appendages. The cardiac structure being paced was correctly identified by ECGI in all 37 pacing events (100% accuracy).

Twelve pacing events were recorded on endocardial electroanatomic maps and merged with the epicardial atrial shell derived from the ECGI-CT image. ECGI-determined pacing locations were accurate within a mean 6.3 ± 3.9 mm (Figure 6-1).

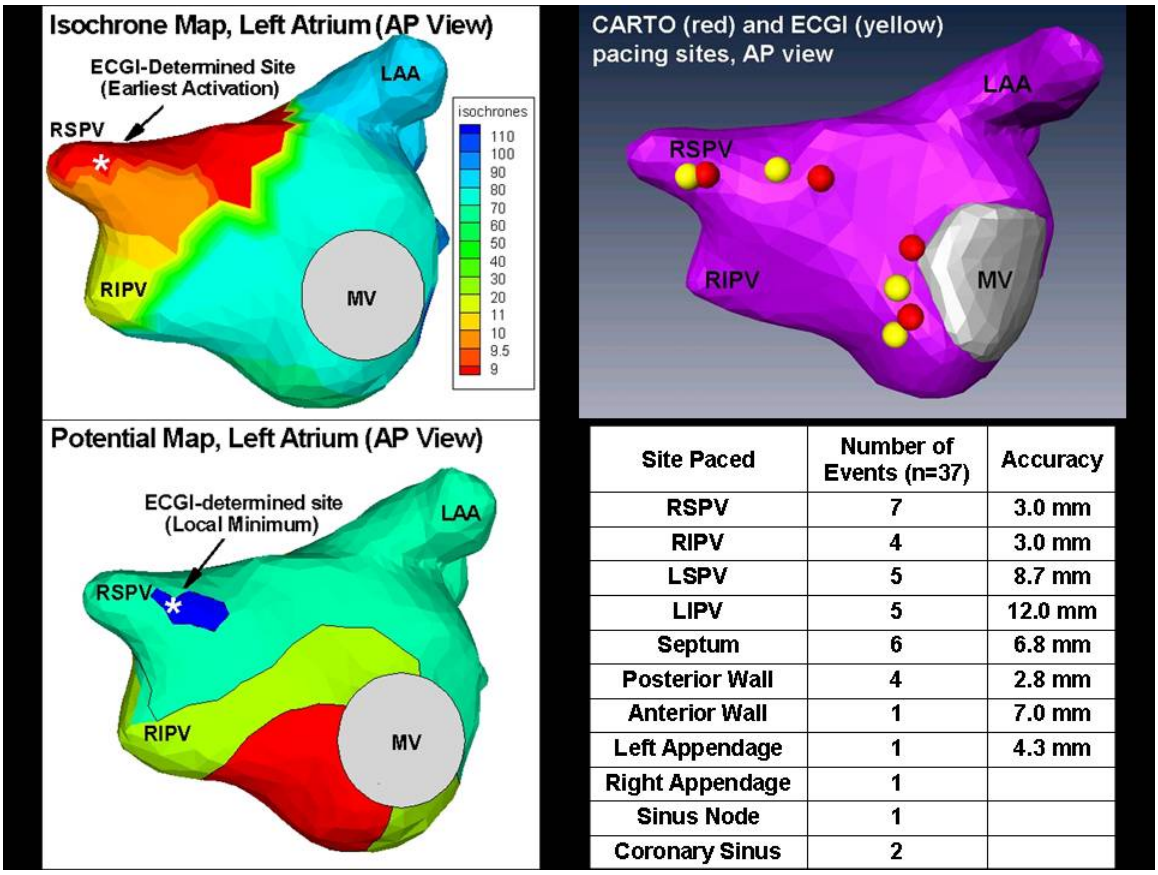

Site Paced	Number of Events (n=37)	Accuracy
RSPV	7	3.0 mm
RIPV	4	3.0 mm
LSPV	5	8.7 mm
LIPV	5	12.0 mm
Septum	6	6.8 mm
Posterior Wall	4	2.8 mm
Anterior Wall	1	7.0 mm
Left Appendage	1	4.3 mm
Right Appendage	1	
Sinus Node	1	
Coronary Sinus	2	

Figure 40 (Figure 6-1) Evaluation of ECGI Accuracy in Locating Atrial Initiation Sites

Simulated by Pacing. TOP LEFT: Isochronal map of the left atrium in Anteroposterior (AP) view with white star indicating the earliest activation as imaged by ECGI. BOTTOM LEFT: Potential map of the left atrium (AP view) locating the local minimum (blue region, white star). TOP RIGHT: Merged 3-D CARTO left atrial image with ECGI image, in the AP view. Pacing sites marked from CARTO in the RSPV and various points on the intraatrial septum are recorded in red, with ECGI-predicted sites marked in yellow. BOTTOM RIGHT: Detailed information regarding the specific sites included in the atrial pacing simulation and the distance between CARTO and ECGI-imaged points. RSPV = Right

Superior Pulmonary Vein; RIPV = Right Inferior Pulmonary Vein; LAA = Left Atrial Appendage; MV = Mitral Valve.

Analysis of Atrial Arrhythmias

When atrial arrhythmias were imaged, many activation patterns were observed. For most patients (24/26, 92%), multiple simultaneous wavelets were visible on the atrial epicardium. Rarely (2/26, 8%), the predominant mechanism was one single wave macroreentry, involving both atria. Rotor activity was less common (4/26, 15%) than multiple wavelets and was observed in the posterior left atrium, posterolateral and anterolateral right atrium. Rotors rarely sustained more than one full rotation before breaking into several less organized wavelets. In six patients with a clinical diagnosis of AF, ECGI determined the actual mechanism to be occult atypical atrial flutter (4/26, 15%) and atrial tachycardia (2/26, 8%) based on the regularity and reproducibility of the atrial activation pattern.

Spontaneous, focal, radial epicardial activation occuring near the pulmonary veins (PV) (18/26, 69%) or from non-PV sites (16/26, 62%) were commonly seen in addition to the multiple wavelets. Non-PV spontaneous activation sites were predominately left atrial posterior wall, coronary sinus, lateral right atrium, or vena cava. By convention, we refer to these location as “focal source sites,” though their role in intiating AF was not studied.

Examples of several of the observed activation patterns are shown in Figures 2-7 and In the attached CD Movies 1-6. With simpler forms of AF, an isochrone map can represent the pattern of AF. However, for most patients, the patterns of atrial activation involve several wavelets with frequent wavebreaks and shifting pivots, making isochrones less robust. We refer the reader to the movies in the attached CD for dynamic activation movies of AF. Figures 2 and 3 (and corresponding Movies 1 and 2 in the attached CD) show examples of PV focal source sites in the left inferior and left superior PV (LIPV and LSPV, respectively) during AF. Movie 3 in the attached CD demonstrates a PV focal source site in the right inferior PV (RIPV) during AF. Figure 4 (and Movie 4 in the attached CD) shows one example of a focal source site and rotor activity at the anterolateral right atrium during AF. Figure 5 (and Movie 5 in the attached CD) demonstrates the less common phenomenon of single wave macroreentry underlying paroxymal nonsustained AF in a young patient with a structurally normal heart. Figures 6 and 7 (and Movie 6 in the attached CD) is a representative example of a more complex AF pattern with several simultaneous wavelets and partial rotor activity in the left atrial posterior wall and right atrium. PV-focal source activities are also observed. Figure 6 demonstrates the combination of PV-focal source activity and wavelet pattern. Figure 7 shows a complex multiple wavelet pattern during the same AF.

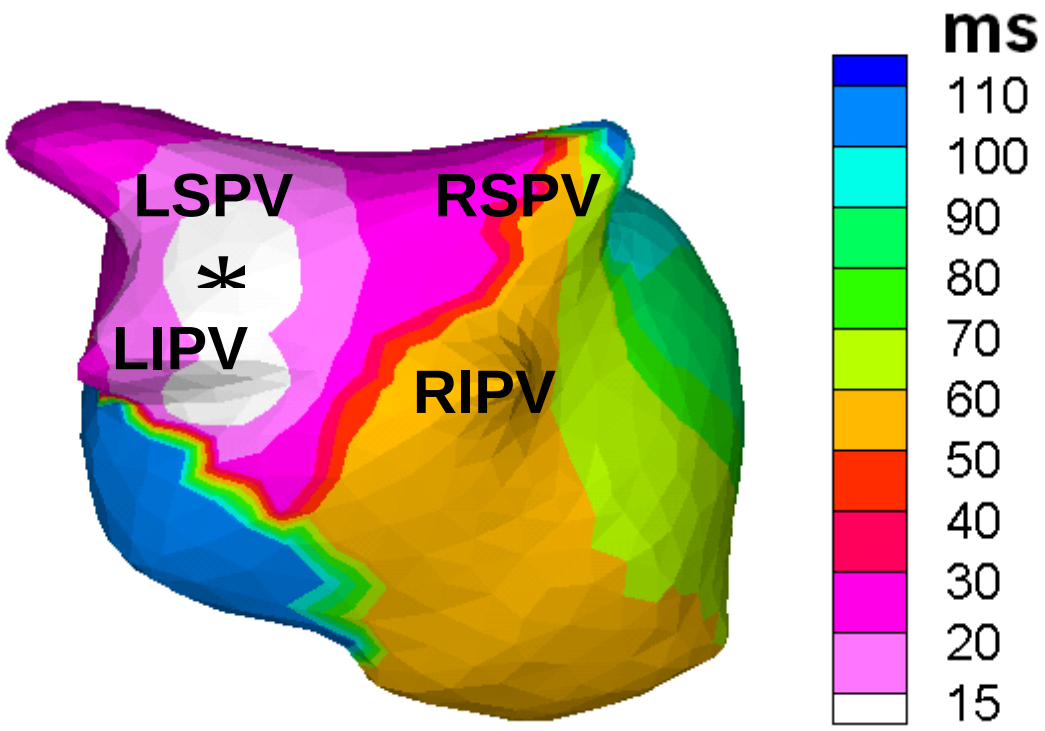

Figure 41 (Figure 6-2) Example of LIPV focal source.

ECGI isochrone map of both atria in the PA view during ~100 ms of AF demonstrates the initiation of atrial depolarization from the LIPV (white) with radial spread. Slow conduction (crowded isochrones) is seen near the right pulmonary veins, and a line of block is seen inferiorly beneath the LIPV (red to blue). A corresponding activation movie is in the attached CD (Movie 1). LSPV = Left Superior Pulmonary Vein; LIPV = Left Inferior Pulmonary Vein.

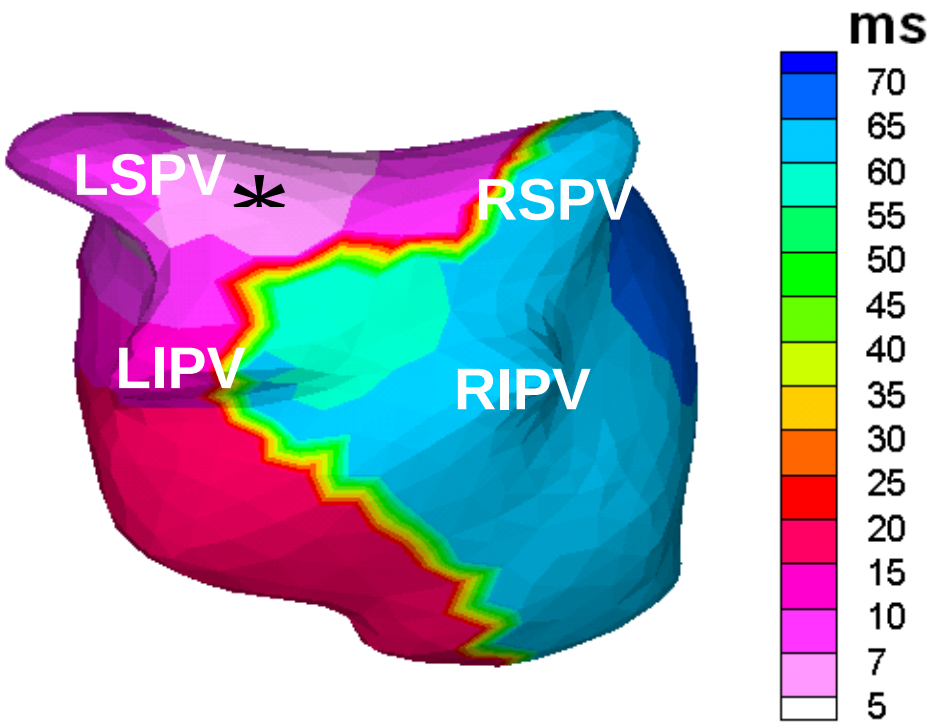

Figure 42 (Figure 6-3) Example of a LSPV focal source

ECGI isochrone map of both atria in the PA view during ~70 ms of AF demonstrates the initiation of atrial depolarization from the superior aspect of the LSPV (light pink). Slow conduction (crowded isochrones) is seen across the left atrial posterior wall. A corresponding movie is in the attached CD (Movie 2).

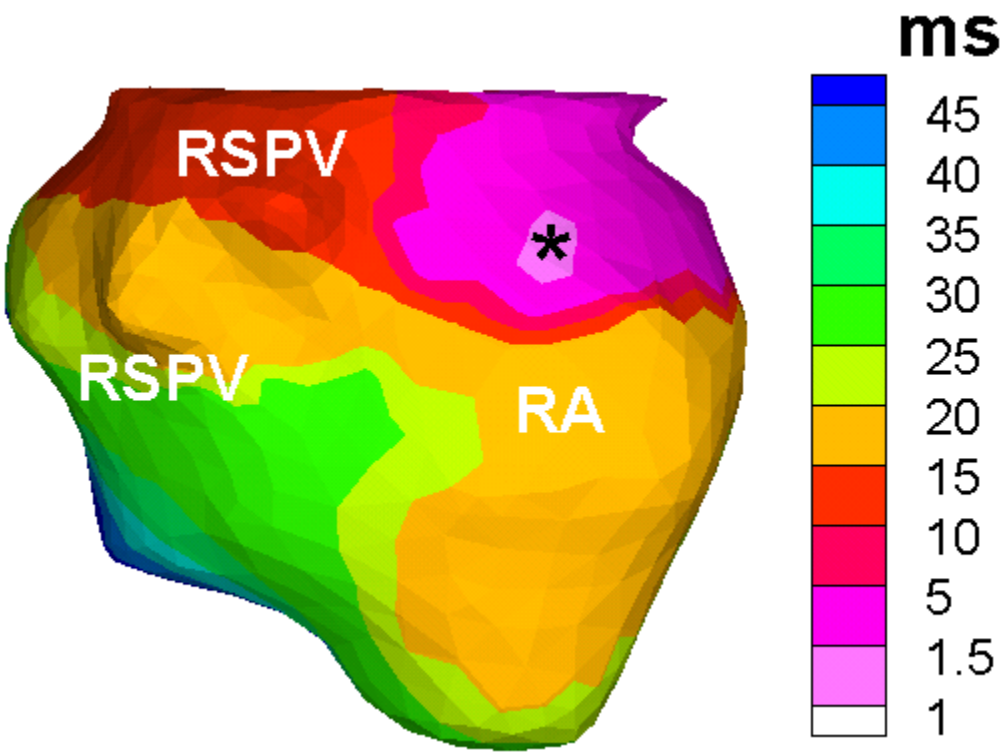

Figure 43 (Figure 6-4) Example of a right atrial focal source

Isochrone map of both atria in a right lateral view during atrial fibrillation demonstrates a pattern of local spontaneous depolarization in the anterolateral right atrium with a counterclockwise rotor-like pattern of activation. A corresponding movie is in the attached CD, demonstrating this pattern repeating three times (Movie 4).

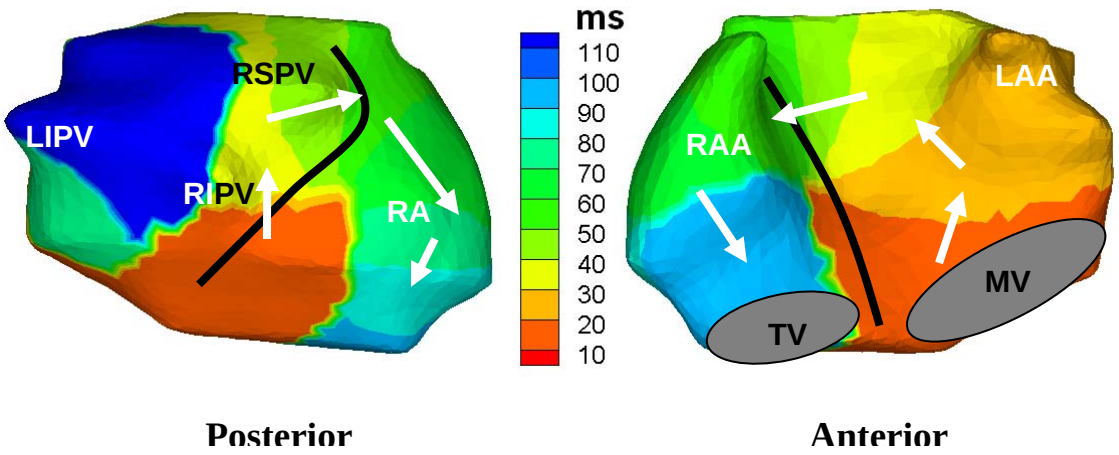

Figure 44 (Figure 6-5) Example of single wave biatrial reentry

ECGI isochrone map of both atria in the right posterior view (left) and anterior view (right) during ~100 ms of atrial fibrillation demonstrates a single spiral wave. The broad, sweeping activation wavefront involves both atria and propagates in a counterclockwise fashion (seen best in anterior view, right panel). Black line marks the inter-atrial septum. An activation movie of four continuous beats can be found in the attached CD (Movie 5).

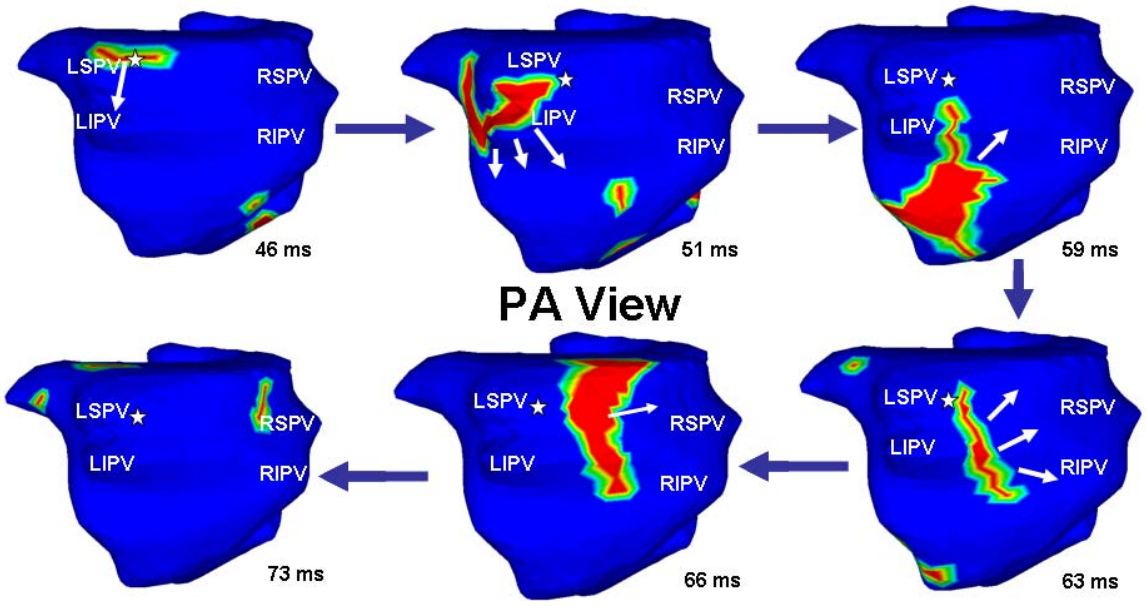

Figure 45(Figure 6-6) Example of combination pattern with PV focal source and single wavelet

Activation (from 46 ms to 73 ms) of both atria in the PA view is shown. Atria surface is shown in blue. Activation wavelets are shown in red (boundaries highlighted green). White arrows indicate the propagation direction of the wavelet. The white star denotes a pivot point of wavelet rotation. At 46ms, a focal source emerges from LSPV and focal sources a wave of radial activation (51ms). The emerging wavelet pivots around an area in the LA posterior wall (59-63ms) (star) and then propagates towards the right PVs (63-73ms). (from Movie 6 in attached CD)

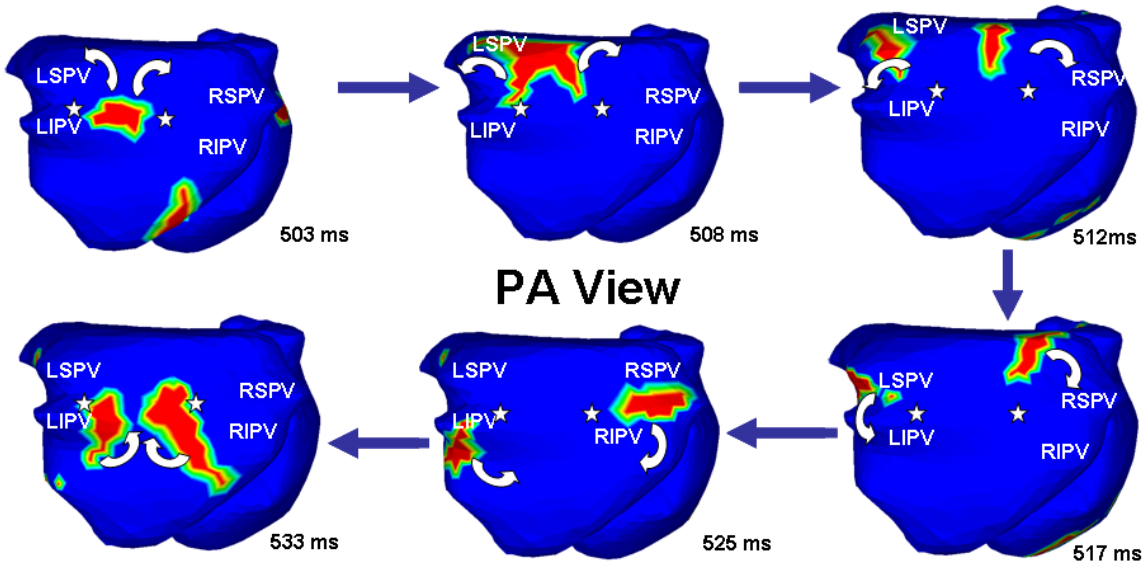

Figure 46 (Figure 6-7) Example of multiple wavelets pattern

Activation (from 503 ms to 533 ms) of both atria in the PA view is shown. Atria surface is shown in blue. Activation wavelets are shown in red (boundaries highlighted green). White arrows indicate the propagation direction of wavelets. The white stars denote the pivot points around which the wavelets turn. Single wavelet at 503ms breaks into two wavelets on the posterior LA wall (508-525ms) and propagates around two pivot points (stars). At 533ms, the two wavelets coalesce and terminate. (from Movie 6 in attached CD).

Analysis of AF Complexity

Of the twenty-six patients who were imaged during an atrial arrhythmia, there were significant differences in the complexity of the arrhythmia based on the standard clinical grouping (paroxysmal, persistent, long-standing persistent). AF complexity was determined by the mean number of simultaneous wavelets and focal source sites.

Patients classified as having paroxysmal AF had fewer wavelets (mean 1.1) during AF

than patients with persistent AF (2.2 wavelets, $p = 0.017$) or long-standing persistent (2.6 wavelets, $p < 0.005$) AF. In aggregate, the three groups were significantly different with regard to number of wavelets (ANOVA $p = 0.011$, see Figure 8 Panel A).

Similarly, patients with paroxysmal AF had fewer focal source sites (mean 1.0 focal sources) than patients with persistent (2.3 focal sources, $p = 0.034$) or long-standing persistent (3.2 focal sources, $p = 0.034$) AF. Compared among the three groups, each group was significantly different (ANOVA $p = 0.031$, Figure 8 Panel A).

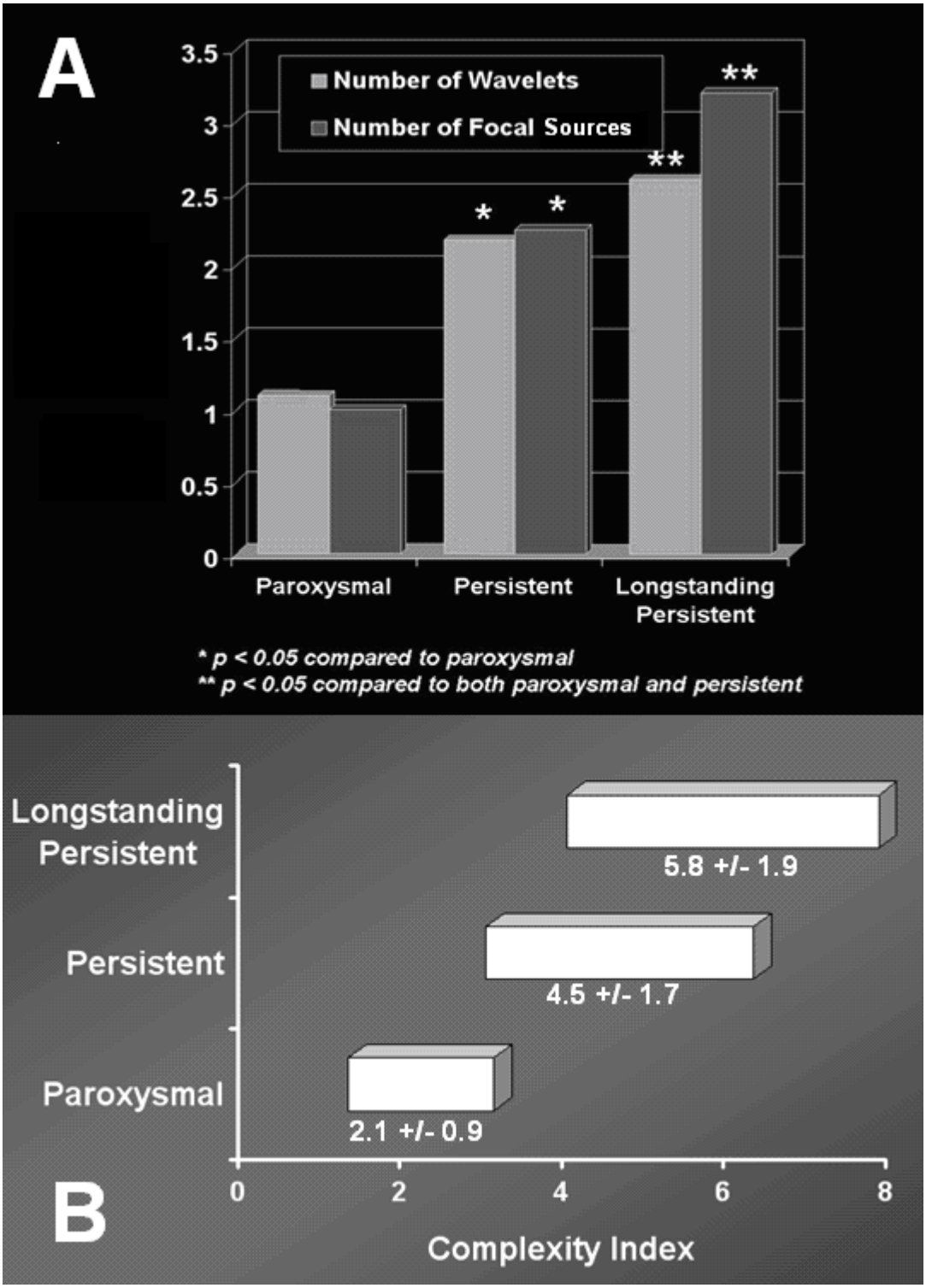

Figure 47(Figure 6-8) Complexity Analysis

Panel A: Increasing complexity of atrial fibrillation stratified by clinical classification of paroxysmal, perisistent and long-standing persistent AF. (ANOVA for wavelet, p = 0.011; focal focal sources, p =

0.031) **Panel B.** Complexity Index for paroxysmal, persistent and longstanding persistent AF groups. Complexity Index is the sum of the mean number of wavelets and number of focal source sites for each patient. A Complexity Index of 1 is the minimum, and represents the “simplest” AF. The Complexity Index increases with the duration of AF. There is overlap between the persistent and longstanding persistent groups.

Within the group of patients with paroxysmal AF, there was considerable homogeneity and simplicity with regards to the number of wavelets and focal sources. Using the sum of the mean number of wavelets and focal sources as a “complexity index,” patients with paroxysmal AF had values that ranged from 1 to 3.5, with a mean of 1.9 (see Figure 8 Panel B). In general, paroxysmal AF patients had fewer than 3 wavelets with 0-2 focal focal sources.

In contrast, patients with persistent AF demonstrated heterogeneity with regards to these parameters. Patients in this group had one to four simultaneous wavelets and one to four focal focal sources visible during AF. The complexity index ranged from 2 to 7, with a mean of 4.4. At the extremes, the “simplest” AF pattern among the patients with persistent AF (Patient 3) had a single wavelet from a single driver in the right atrium (complexity index of 2). The most complex AF pattern in this group (Patient 13) had an average of four wavelets and at least three identifiable focal source sites contributing to AF.

The patients with long-standing persistent AF had the most complex AF patterns. One patient in this group (Patient 5) who had undergone several prior catheter ablations, exhibited the most complex AF pattern of the entire cohort, with a mean of three wavelets arising from a total of six identifiable focal source sites (two pulmonary veins, coronary sinus, right atrium, and two sites in the posterior left atrial wall). Graphically (Figure 8 Panel B), the persistent and long-standing persistent groups demonstrated overlap with regards to the complexity index, while the paroxysmal group did not.

6.4 Discussion

AF is characterized by a dynamically changing activation sequence.[180,181] This hallmark of AF poses a severe limitation on point-by-point catheter mapping of AF, which requires a stable, monomorphic arrhythmia. Simultaneous recording from many electrodes over a relatively long duration is required to accurately map AF. Invasive multi-channel mapping studies were conducted on both epicardial and endocardial atrial surfaces in animals[182-190]. These studies have been invaluable and provided the basis for much of our understanding of AF mechanisms. However, many aspects of animal models of AF are different from properties of human AF, including the ion-channel profiles of atrial cells, the atrial anatomical substrates, and the modification of these properties by remodeling processes over time. Because of these differences and to characterize human AF, intra-operative multi-channel epicardial mapping studies were performed in patients.

Observations from direct epicardial recordings[34,191-193] have been instrumental to the characterization of AF in humans. These landmark observations were limited, however, by access to only certain parts of the atria, relatively short time periods for recording data in a patient with an open chest, and the influence of general anesthesia on autonomic tone. Also, in most studies, mapping was confined to regions of the atrial epicardium with limited spatial resolution. In other studies, invasive endocardial mapping of AF was performed using multi-channel catheter (basket or balloon) arrays in the left and right atria[194-198], as well as the pulmonary veins[199]. The catheter approach limited mapping to the endocardial surfaces of the atria. Although this approach is less invasive than surgical mapping, it still involves effects of sedation, and the intra-atrial presence of the array greatly limits mapping time. The mapping resolution is also compromised by the limited number of recording electrodes. Due to its invasive nature, this approach is not suitable for conducting repeated mapping protocols in longitudinal studies of atrial electrophysiology over time. Several AF mechanisms have been proposed based on the animal studies and limited number of human studies mentioned above. They include the mother rotor/fibrillatory conduction [168,200-202], the pulmonary vein/focal mechanism[166], and the multiple wavelet mechanism[164]. Studies have also suggested involvement of the autonomic nervous system in human AF[167].

The present study applies ECGI as a noninvasive mapping tool for studying mechanisms of human AF. ECGI can map the epicardial activation pattern of AF on both atria with

relatively high spatial resolution. There is no surgery, sedation or invasive intervention involved in ECGI mapping, therefore the AF pattern can be observed in "real-world" conditions, over long periods of time (minutes to hours). Due to its noninvasive nature, ECGI can be repeatedly conducted on the same patient to provide longitudinal information on the evolution of the atrial electrophysiological substrate over time. ECGI has been validated extensively in animal and human studies in normal hearts and a variety of pathological conditions[1-10,12-18,33,34,91,102,177-179]The pacing data presented here determine ECGI's atrial accuracy at 6mm and is comparable to previously published data from ventricular reconstructions[3,10,91]. This study is the first to report detailed, three-dimensional noninvasive imaging of bi-atrial epicardial activation patterns during AF in humans. Major findings include: 1) ECGI is feasible with low amplitude fibrillatory atrial signals; 2) many various epicardial activation patterns are observed over a population, but specific, and often reproducible, activation patterns can be identified in individual patients; 3) the most common activation pattern was multiple concurrent wavelets with simultaneous spontaneously depolarizing (focal source) sites from areas near the pulmonary veins and other sites within both atria; 4) complexity of AF increased with longer clinical duration of AF, though; 5) among non-paroxysmal AF, the clinical distinction of "long-standing" did not seem to differentiate complexity.

The data presented here are consistent in many ways with the contemporary animal models of AF mechanisms[182-190] and highlight the coexistence of a variety of mechanisms

as previously reported in animals and humans[34,191-193]. ECGI offers a way to identify unique atrial activation patterns in a patient-specific manner. Observed epicardial activation patterns were often, though not always, repeated in each patient, which suggests a possible clinical application for patient-specific therapy. Because it is noninvasive, ECGI can be applied to large populations. Considering that ECGI is a new method, still in its translational phase and requiring careful analysis of extremely large amount of data for each recorded AF, the study population of 36 patients is rather large. It is an appropriately heterogeneous cohort for characterizing the wide spectrum of AF patterns, which was the aim of the study. Prospectively-designed studies using ECGI in specific subgroups of patients may better characterize the most common underlying mechanisms of AF.

Clinically, ECGI provides a noninvasive way to define a patient's individual electrical phenotype, which could lead to a tailored treatment plan. For example, if we can visualize electrically important areas before an ablation procedure, such as a right atrial focal source site, it may guide the procedure. Our observation that patients with paroxysmal AF have "simpler" forms of AF is likely an important reason for the greater success rates of catheter ablation in this patient group. More interesting, however, is the range of complexity in patients with nonparoxysmal AF, with some patients having a simpler pattern, like paroxysmal AF, and others a much more complex pattern. This may

help explain the wide range of reported success with catheter ablation in patients with nonparoxysmal AF. Additionally, our data showed overlap in AF complexity between persistent and longstanding persistent groups. ECGI may have a role in identifying the longstanding persistent AF patients who would be more likely to benefit from an ablation procedure. Conversely, ECGI may identify patients who are unlikely to benefit from a catheter or surgical ablation due to extensive scarring[17] and complex atrial activation patterns that may be difficult to treat with current strategies. Finally, ECGI offers potential to noninvasively follow therapy (electrical or pharmacological) outcome over time, and better understand why AF recurs in some patients.

Several key limitations are worth noting. First, ECGI reconstructs potentials on the epicardial surface of the atria. While the atria are generally thin, evolving evidence suggests at least a modest difference between local endocardial and epicardial activation[191].The observation that we describe as a “focal source” may well be the epicardial breakthrough of intramural activation. In the future, simultaneous endocardial and ECGI epicardial mapping may further elucidate the role of intramural activity and effects of fiber orientation and tissue anisotropy in AF. Second, the ill-posed nature of the mathematical formulation of ECGI limits its spatial resolution. Therefore, ECGI images cannot differentiate micro-reentry from focal source activity. Third, this first ECGI AF study was aimed at obtaining comparative data from a wide range of phenotypes, with patients form all clinical classification groups of AF. Future studies will focus on each

subgroup with greater detail. Moreover, the study included patients who had prior catheter or surgical procedures. While this type of AF may not be naturally occurring, it is certainly of clinical relevance. Finally, a limitation for ECGI is the inherent AF signal quality, which is often of low amplitude on the body surface. By considering at least five AF activation movies (ranging from 500-1000 ms each) for each patient and limiting the definition of “focal source” to a cycle length of at least 100ms, nonphysiologic artifacts were minimized.

6.5 Conclusions

ECGI can noninvasively image the low-amplitude signals of AF in a wide range of patients. The spatial accuracy of determining initiation sites (as simulated by atrial pacing) is ~ 6mm. In our patient population, ECGI imaged many mechanisms of atrial fibrillation, most commonly multiple wavelets (92%), with pulmonary vein (69%) and non-pulmonary vein (62%) focal source sites. Rotor activity was seen rarely (15%). Not surprisingly, AF complexity increased with longer clinical history of AF, though the degree of complexity of nonparoxysmal AF varied and overlapped. Looking forward, ECGI may be used scientifically as an additional tool to study the various mechanisms of AF in subgroups of patients and clinically to provide mechanistic-based diagnosis and individualized treatment plans.

6.6 Legends for the Video files

With simpler forms of AF, an isochrone map can represent the overall pattern of AF. However, for most patients, the patterns of atrial activation involve several wavelets with frequent wavebreaks and shifting pivots, making isochrones less robust. The following movies in the attached CD highlight various epicardial activation patterns observed during AF.

Movie 1 (with Figure 6-2 in text). Example of a left inferior pulmonary vein (LIPV) focal source. Activation movie in the PA view during ~100 ms of atrial fibrillation demonstrates the initiation of a focal atrial depolarization from the LIPV with radial spread. Slow conduction is seen near the right pulmonary veins, and a line of block is seen inferiorly beneath the RIPV.

Movie 2 (with Figure 6-3 in text)**.** Example of a left superior pulmonary vein (LSPV) focal source. Activation movie in the PA view during ~70 ms of atrial fibrillation demonstrates the initiation of a focal atrial depolarization from the LSPV with radial spread. Slow conduction is seen across the left atrial posterior wall.

Movie 3. Example of a right inferior pulmonary vein (RIPV) focal source. Activation

movie in the PA view during ~30 ms of atrial fibrillation demonstrates the initiation of focal atrial depolarization from the RIPV with radial spread.

Movie 4 (with Figure 6-4 in text). Example of a non-PV right atrial focal source, triggering rotor activity in a patient with persistent AF. Activation movie of both atria in a right lateral view during AF demonstrates a repeating pattern of local spontaneous depolarization (focal source) in the anterolateral right atrium.

Movie 5 (with Figure 6-5 in text). Example of single wave biatrial reentry pattern in a patient with paroxysmal AF. Activation movie of both atria in the right posterior view during ~600 ms of AF demonstrates a single wave without an obvious focal source. This movie is presented in a translucent view, allowing the reader to visualize the wavefront on the posterior wall (brighter color) as well as the distant anterior structures (faded color). The broad, sweeping activation wavefront propagates in both atria in a counter-clockwise fashion.

Movie 6 (with Figures 6-6 and 6-7 in text). Example of complex patterns in a patient with persistent AF with rotor activity. Activation movie of both atria in the PA view shows ~ 1000 ms of AF. Multiple simultaneous mechanisms are seen, including multiple wavelets and partial rotors with distinct locations of wave break on the posterior left atrium and right atrium.

Chapter 7 Noninvasive Electrocardiographic Imaging of Normal Human Atrial Repolarization, Ventricular Bigeminy, Focal Atrial Tachycardia after Pulmonary Vein Isolation, and Scar-Related Atypical Atrial Flutter

7.1 Noninvasive Electrocardiographic Imaging of Normal Human Atrial Repolarization

Knowledge of normal atrial activation and repolarization patterns provides an important baseline for understanding atrial arrhythmias. We recently published images of normal atrial activation under complete physiological conditions, using a novel noninvasive imaging modality developed in our laboratory, called Electrocardiographic Imaging (ECGI).[1] 256 carbon electrodes organized in strips are applied to the patient's torso surface to obtain body surface potentials (BSP) and the patient undergoes thoracic noncontrast gated CT with the electrodes in place. The BSP and anatomical information from the CT scan (torso-heart geometrical relationship) are combined mathematically by ECGI algorithms to noninvasively construct epicardial potential maps, electrograms and activation sequences (isochrones) and repolarization patterns.[2] Here we provide images of normal atrial repolarization obtained from a 49-year-old male with normal atrial activity. The figure shows ECGI images of atrial surface potentials at two instances

during depolarization (left panel, 18ms and 36ms from onset of P wave) and repolarization (right panel, 105ms and 123ms from onset of P wave); arrows show propagation of zero potential lines, ＋ is potential maximum, － is potential minimum. The sequence of repolarization (white arrows) is determined by and follows the sequence of depolarization (black arrows), unlike the ventricles where the repolarization sequence is determined by local repolarization properties.[2] A close similarity between potential patterns during depolarization and repolarization is evident in the image and is consistent with previous invasive mapping in canine experiments.[203] The patterns are almost identical, except that the polarity is reversed. This indicates that the repolarization sequence follows the depolarization sequence, because differences in action potential durations across the atria are much smaller than differences in atrial activation times, as expected in the absence of a specialized conduction system involvement. LA: left atria; RA: right atria; SVC: superior vena cava; IVC: inferior vena cava; PV: pulmonary veins (denoted by the four black circles).

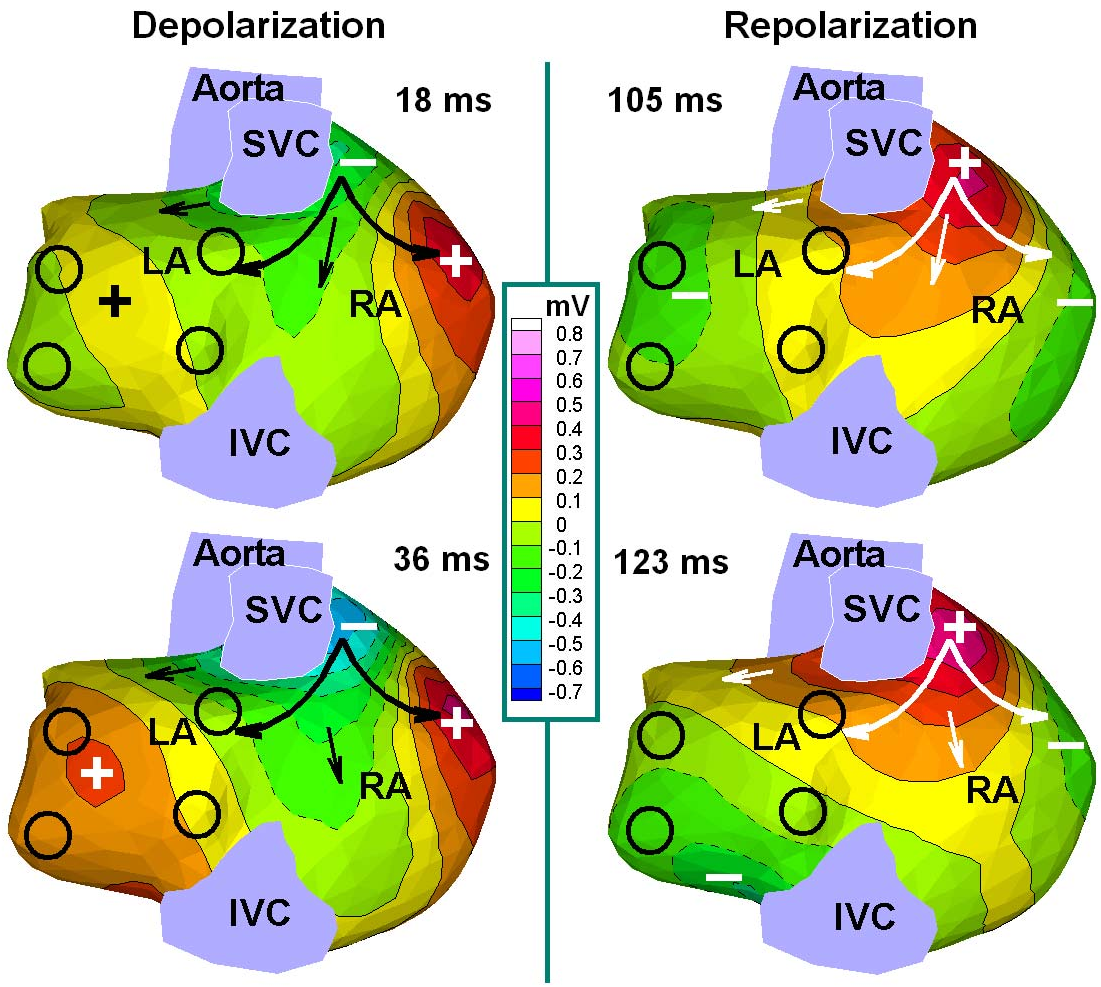

Figure 48 (Figure 7-1): Normal human atrial repolarization (see text for details)

7.2 Noninvasive Electrocardiographic Imaging of Focal Atrial Tachycardia after Pulmonary Vein Isolation

Electrocardiographic imaging (ECGI) is a novel, noninvasive tool for imaging cardiac arrhythmia and defining electrophysiologic properties.[1,35] ECGI combines multi-electrode body surface ECG recordings with three-dimensional anatomical heart-torso imaging to reconstruct an epicardial electroanatomical map. ECGI-reconstructed data can be

presented as epicardial potential maps, electrograms, or isochrones during activation and repolarization. The ECGI procedure has been extensively tested and validated in experimental preparations with normal and abnormal canine hearts[4,5,8,9,21,23,24,204]. Recently, ECGI has been validated in humans[1,10,33-35]. To date, we have presented human ECGI studies of normal activation and repolarization [1,35], right and left bundle branch block [1,10], various pacing protocols [1,10,33], atrial flutter [1], native sinus rhythm and bi-ventricular pacing for cardiac resynchronization (CRT) in heart failure patients [10], and focal ventricular tachycardia [34].

This report describes the first case in which ECGI was applied in a patient with a focal atrial tachycardia. In particular, ECGI accurately located the earliest site of activation in an atrium which had previously undergone two percutaneous pulmonary vein isolation procedures. The tachyarrhythmia was successfully terminated with RF ablation in the ECGI-determined location.

7.2.1 Case Report

A fifty-five year old caucasian female with a history of two prior pulmonary vein isolation procedures for long standing atrial fibrillation was evaluated for increasing palpitations and an episode of near syncope. She had a history of rheumatic mitral valve disease and had undergone a percutaneous valvuloplasty nine years prior. Since her valvuloplasty, she had an average of two admissions each year for symptomatic atrial

fibrillation. She was cardioverted each time and, in addition to her oral anticoagulation, she was tried on a number of antiarrhythmic medications without sustained success. She underwent percutaneous pulmonary vein isolation procedures fourteen and six months prior to this admission. Low voltage electrograms were recorded throughout the left atrium during the first and second procedures. Transthoracic and transesophageal echocardiography demonstrated marked left atrial enlargement (~5.6 cm), mild mitral stenosis (mean gradient = 6-8 mmHg) and mild-to-moderate mitral regurgitation.

When she presented with recurring palpitations after the 2nd pulmonary vein isolation procedure, an ECG revealed an ectopic atrial tachycardia with a rate of 136bpm. Neither sotalol nor dofetilide suppressed the arrhythmia. The decision was made to attempt an ablation procedure. Prior to the procedure, ECGI was performed to noninvasively localize the source of tachycardia.

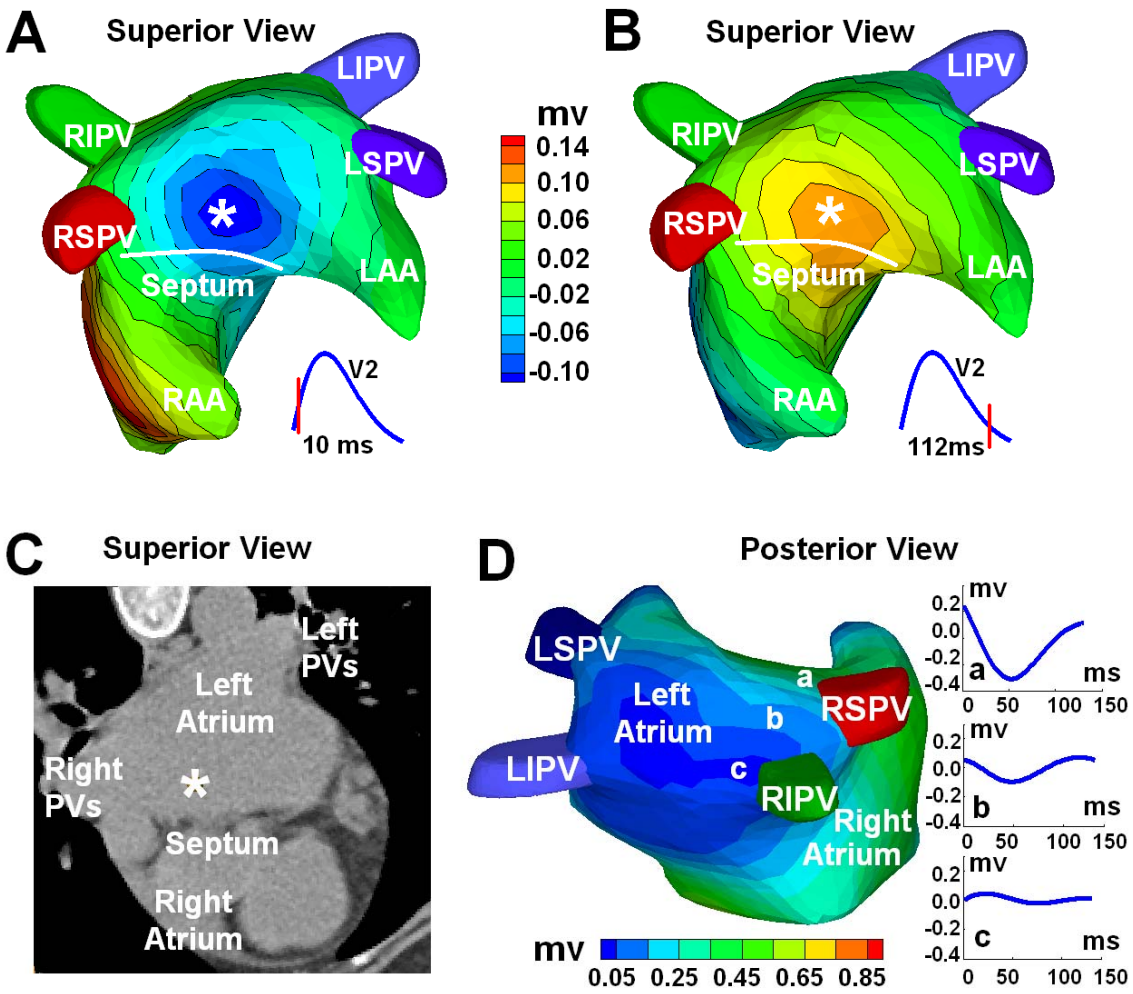

Figure 49 (Figure 7-2): ECGI three-dimensional voltage and electrogram maps

Panel A and B show atrial epicardial potential maps at 10 ms and 112 ms after the onset of the surface P wave. Panel A captures the epicardial breakthrough pattern during activation, and Panel B shows the repolarization pattern with reverse polarity. The white asterisk indicates the site of earliest activation as predicted by ECGI. Panel C shows the ECGI-determined earliest activation site (white asterisk) on a CT image of the atria. Panel D is an electrogram magnitude map (peak-to-peak) reconstructed by ECGI (posterior view). The dark blue represents a region of low magnitude electrograms, indicating a scar region. Three electrograms selected from a non-scar region (a) and from the scar region (b, c) are shown. Location of low magnitude electrograms is consistent with prior pulmonary vein isolations and

left atrial substrate modification. RIPV = right inferior pulmonary vein; LIPV = left inferior pulmonary vein; RSPV = right superior pulmonary vein; LSPV = left superior pulmonary vein; LAA = left atrial appendage; RAA = right atrial appendage;

ECGI-reconstructed atrial epicardial surface voltage maps were produced for a single P-wave extracted during the tachycardia (Figure 7-2). At the onset of the surface P wave, an epicardial breakthrough (local potential minimum) was imaged on the left atrium, near the atrial septum (Figure 7-2A). During the end of the surface P wave, a repolarization pattern with reverse polarity (local potential maximum) appeared at the same site (Figure 7-2B). These observations strongly suggested the existence of an activation source at the breakthrough site. These findings were consistent for several ECGI imaged P waves during the tachycardia. Panel C superimposes the site of the breakthrough on a CT image. As shown, the earliest site of activation determined by ECGI was located on the roof of the left atrium, between the right superior pulmonary vein and the atrial septum (Figure 7-2C).

Additionally, ECGI-reconstructed atrial epicardial potential maps were organized by location to provide temporal electrograms for any given site on the atrial epicardium. A three-dimensional map encoding electrogram magnitudes is shown in Figure 7-2D. Very low magnitude electrograms were reconstructed on the posterior left atrium, especially around the pulmonary veins, consistent with scar from the patient's previous pulmonary

vein isolation procedures. For reference, ECGI-imaged atrial electrogram magnitudes in normal subjects range from 0.6mV to 1mV. Low voltages were also observed on the posterior wall of the left atrium. This probably reflects the patient's underlying disease and the effects of the two prior ablation procedures. Diffuse low voltage was observed during the initial study prior to the pulmonary vein isolation. The prior procedures induced wide circumferential ablation that contained much of the posterior wall, linear lesions connecting the superior veins and inferior veins, and ablation of residual potentials recorded on the posterior wall by a lasso catheter. During the ECGI study, potentials neither could be identified within the pulmonary veins nor the antra around the orifices, suggesting successful prior pulmonary vein isolation procedures. This was consistent with recordings made by a lasso catheter during the study.

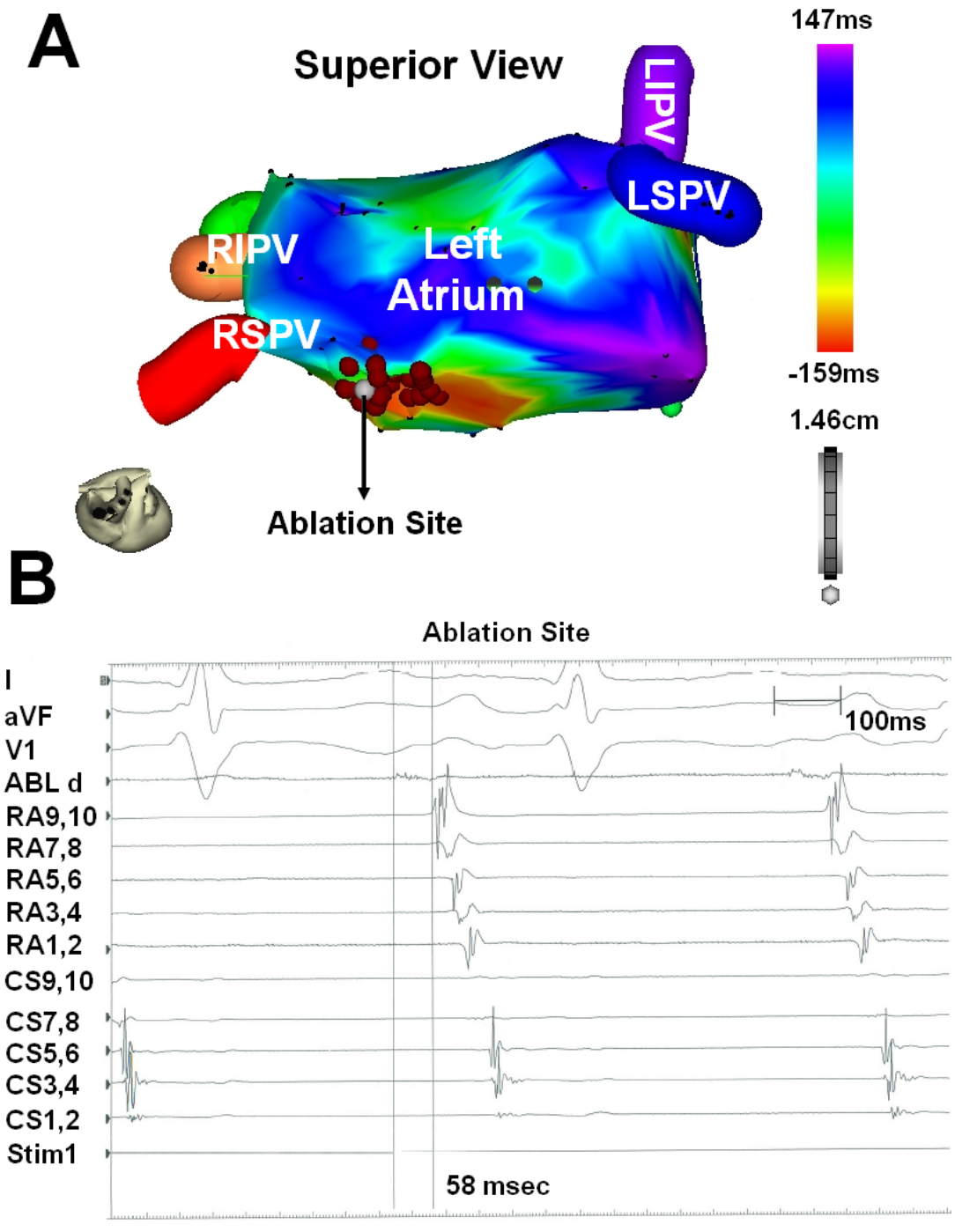

Figure 50 (Figure 7-3) Electroanatomic isochrone map and multichannel intracardiac electrograms.

Panel A is the left atrial electroanatomic isochrone map. The white marker (arrow) identifies the ablation site that successfully terminated the atrial tachycardia. The red markers are sites where RF

energy was applied circumferentially around the site of earliest activation. Panel B is the multichannel endocardial electrogram recording prior to successful ablation, with the ablation catheter at the superior left atrium, near the activation site predicted by ECGI. Surface leads I, aVF, and V1 are followed by intracardiac recordings from the ablation catheter, a decapolar catheter located on the lateral wall of the right atrium, and a decapolar catheter positioned in the coronary sinus (proximal to distal).The ablation catheter measured spontaneous diastolic potentials 58 msec prior to the onset of the surface P wave.

At the onset of the EP study that followed the ECGI procedure, the patient was in an atrial tachycardia with a cycle length of 540ms. Using a lasso catheter, all four pulmonary veins were determined to be electrically isolated. Right and left atrial electroanatomic catheter mapping identified a focal tachycardia originating from the superior left atrium, between the right superior pulmonary vein and the atrial septum (Figure 7-3). Figure 7-3A is a catheter electroanatomic isochrone map (CARTO) constructed in the electrophysiology laboratory during mapping and ablation of the tachycardia. The site of earliest activation is indicated by the white dot. RF energy was applied at this site and circumferentially around this site as indicated by the red markers. Diastolic potentials were recorded 58ms before the onset of the surface P-wave near the ECGI-predicted site (Figure 7-3B). The tachycardia was terminated with application of RF energy to this location, and the tachycardia did not recur with administration of isoproterenol. The patient concluded the study in sinus rhythm.

7.2.2 Conclusion

This report describes a clinical application of the ECGI noninvasive electrical imaging system as an adjunctive technology to accurately identify the specific origin of a focal left atrial tachycardia and atrial electrophysiological substrate prior to catheter ablation. This case has several points of interest. Atrial tachycardias are relatively common in patients with atrial fibrillation who have undergone isolation of the pulmonary veins and often require additional mapping and ablation. Localization of an atrial tachycardia by analysis of the standard 12 lead ECG is difficult because the P-wave morphology can be affected by the T-wave. Moreover, the criteria for interpretation of P-wave morphology recorded on a standard lead ECG[205] may not be valid in patients with diseased atria who have undergone circumferential pulmonary vein isolation combined with ablation of fragmented potentials. In the case under discussion, ECGI correctly located the arrhythmic focus to the roof of the left atrium, between the right superior pulmonary vein and atrial septum. Because the CT scan was not registered to the CARTO electroanatomic image, a precise quantitative measure of localization accuracy could not be obtained. ECGI also identified areas of low voltage on the posterior wall of the left atrium that were attributable to the patient's prior ablation procedures and underlying atrial myopathy. The feasibility of assessing PV isolation noninvasively using ECGI will be further tested in a larger study. Despite an abnormal left atrial substrate with extensive scar tissue, ECGI was accurate in its localization of the focus of the tachycardia. Although further

work remains to prove its clinical utility in large groups of patients, ECGI offers promise for improved noninvasive analysis of the origin and mechanisms of atrial arrhythmias.

7.3 Noninvasive Electrocardiographic Imaging of Scar-Related Atypical Atrial Flutter

7.3.1 Introduction

Atrial arrhythmias, including atrial fibrillation, atrial flutter and other types of atrial tachycardia are common in humans. For instance, atrial fibrillation affects 0.5-1% of the general population, and more than 6% of people over 80 years old.[206] Knowledge of electrophysiological properties of the underlying atrial substrate can improve diagnosis and treatment of these arrhythmias. However, until recently a noninvasive method for imaging cardiac electrophysiology and arrhythmias has not been available. Electrocardiographic Imaging (ECGI) was developed for this purpose.[1,35] ECGI reconstructs an epicardial electro-anatomical map noninvasively by combining a 250-electrode body surface ECG with CT scan of the heart-torso geometry. The ECGI images can be presented as epicardial potential maps, electrograms, isochrones or repolarization maps during activation and repolarization.[1,35] ECGI was systematically tested and validated experimentally in normal and abnormal canine hearts.[5,8,9,23,24] In these experimental settings, torso potentials (the ECGI input) and epicardial potentials (the ECGI output) were measured simultaneously and at high spatial and temporal resolution. The directly measured epicardial potentials provided the ideal “gold standard”

for validation of the noninvasive ECGI reconstructions; We evaluated and validated the performance of ECGI under many different conditions, including ECGI of myocardial scars[23,24] and reentry circuits[8,24], the electrophysiological elements imaged in this report. Recently, ECGI has also been successfully applied and validated in human subjects, including comparison to intra-operative multi-electrode mapping during surgery[33], determination of ECGI accuracy in locating focal sites of initial activation in humans by comparison to known locations of pacing electrodes in various RV and LV positions[1,10], comparison to catheter-based localization of focal VT[34] and determination of the origin of human atrial tachycardia [207] In this case report, we describe the atrial substrate and arrhythmia mechanism of atypical atrial flutter in a patient who previously underwent catheter ablations for atrial fibrillation.

7.3.2 Patient History

The patient is a 48-year-old male with a two-year history of paroxysmal atrial fibrillation, unresponsive to multiple drug therapy. When not in atrial fibrillation, the patient had marked bradycardia, suggestive of sinus node dysfunction. He underwent catheter-based pulmonary vein (PV) isolation. After his first catheter ablation, the patient developed atypical atrial flutter. During this tachycardia, he had ventricular rates of 130 to 140 beats per minute. The patient's negative F-waves on Lead I were consistent with a left atrial (LA) origin of this tachycardia. Four months after the first ablation, he underwent a second procedure which revealed an inducible tricuspid isthmus-dependent atrial flutter

and inducible LA reentry. The PVs were re-isolated and complete electrical isolation was documented. Additional ablations were made in the left side of the mitral isthmus, on the LA roof, and on the right side of the tricuspid IVC isthmus. Atrial flutter was not inducible following these ablations. Three months after the second ablation, the patient redeveloped persistent atypical atrial flutter. He was referred for a surgical COX-MAZE procedure after unsuccessful cardioversion.

7.3.3 Methods

Body-surface ECG data were recorded for 5 minutes from 250 carbon electrodes mounted in strips. ECGI reconstructions were performed during beats with relatively long RR interval for which the atrial F wave was not masked by the QRS, and also for a 10 seconds ECG segment from which the QRST was removed. [208] Following the QRST removal, the ECG had a typical sawtooth morphology, and the ECGI-reconstructed atrial activation sequence was repetitious and consistent with only minor variations between cycles.

7.3.4 Results

One day before the COX-MAZE procedure, ECGI was performed. Based on the magnitudes of the ECGI reconstructed epicardial electrograms, the atrial tissue was classified in terms of its electrophysiological properties. ECGI images showed low potential regions (electrogram magnitude <0.5mV peak to peak; Figure 7-4A) around

each of the PVs and in the left atrial appendage (LAA) region. At surgery, scar tissue was observed around the PVs and on the LAA (Figure 7-4B), which corresponded well with the low voltage regions imaged by ECGI. Figure 7-4C shows two selected ECGI electrograms, one from the scar region (b) and one from a region remote to the scar (a).

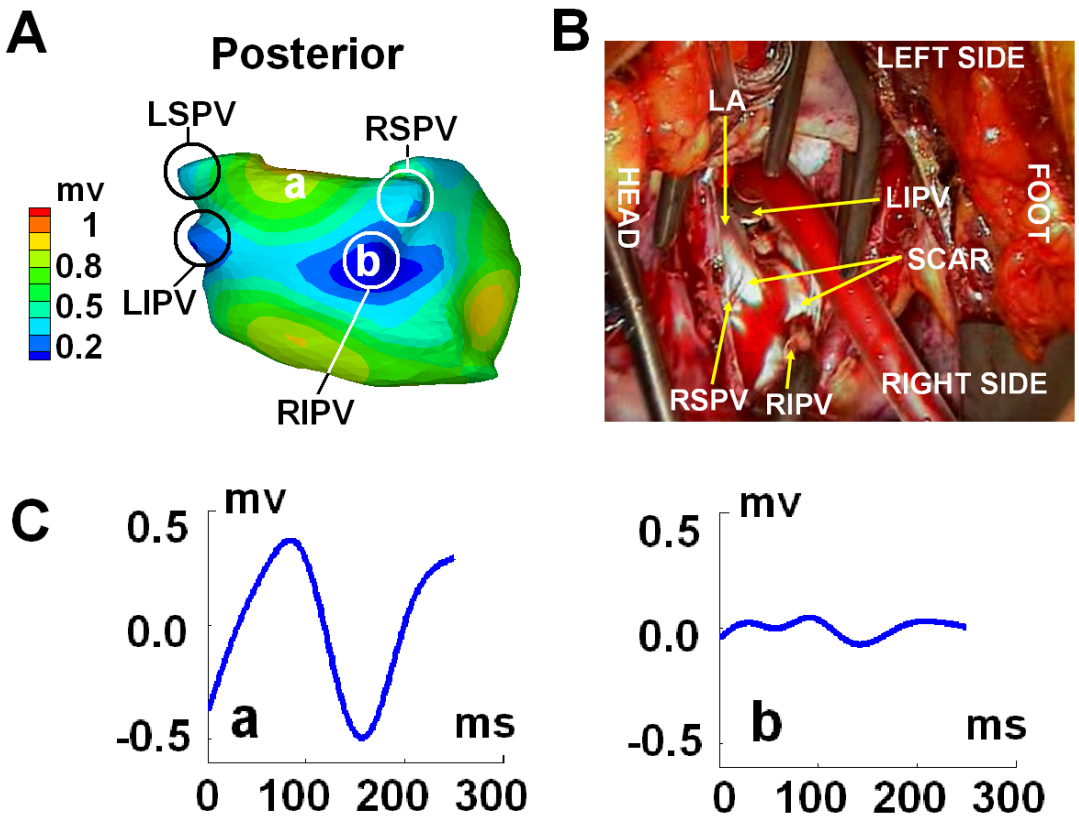

Figure 51 (Figure 7-4): ECGI magnitude map

Panel A: ECGI epicardial electrogram magnitude map (posterior view). Small magnitude regions (<0.5mV; shown in blue) indicate scar. Panel B: photograph extracted from the video recorded during the Cox-Maze procedure; Tissue appearing white is the scar. Panel C: Two selected ECGI-reconstructed epicardial electrograms from different sites on the epicardial surface: (a) remote to the scar; (b) within the scar （locations are marked in panel A） LIPV = Left Inferior Pulmonary

Vein, LSPV = Left Superior Pulmonary Vein, RIPV = Right Inferior Pulmonary Vein, RSPV = Right Superior Pulmonary Vein, LAA = Left Atrial Appendage, RAA = Right Atrial Appendage

ECGI-imaged activation sequence for one flutter cycle is shown in Figure 7-5. The reentry circuit driving the atypical flutter was mainly confined to the left atrium (LA). The circuit is depicted by the solid black and white arrows in the four panels of Figure 7-5. Earliest activation occurred at the LA inferior region below the left inferior PV (LIPV) (site 1). The activation front propagated posteriorly towards the right atrium (site 2) as indicated by the solid white arrows in Panel A and B. It could not propagate superiorly due to a line of block connecting the two inferior PVs (thick black line), associated with the posterior scar from the previous catheter ablations. This line of block extended to the anterior LA (Panel C). After about 50ms delay due to slow conduction at the border of the low potential region near the two right PVs (white arrow, Panel B), the activation wavefront turned around the line of block into the previously unexcited superior region (site 3). The reentrant wavefront continued to propagate towards the roof of the LA (site 4). From the LA roof, the wavefront propagated to anterior site 7, both directly and via the left atrial appendage (LAA) (site 6) (Panels C and D), and continued to the inferior mitral valve region (MV; site 8). It passed the MV isthmus, completing the reentry circuit (Panels C and D). The next flutter cycle started again from site 1. A secondary wavefront emerged from the reentry circuit and propagated mainly in the right atrium (RA) (dashed black arrows in Panels B, C and D). It descended from the roof of

the LA (site 4) to the inferior portion of RA free wall (site 5). There was a long line of functional block between site 2 and site 5 (thick black line in Panel B) due to refractoriness.

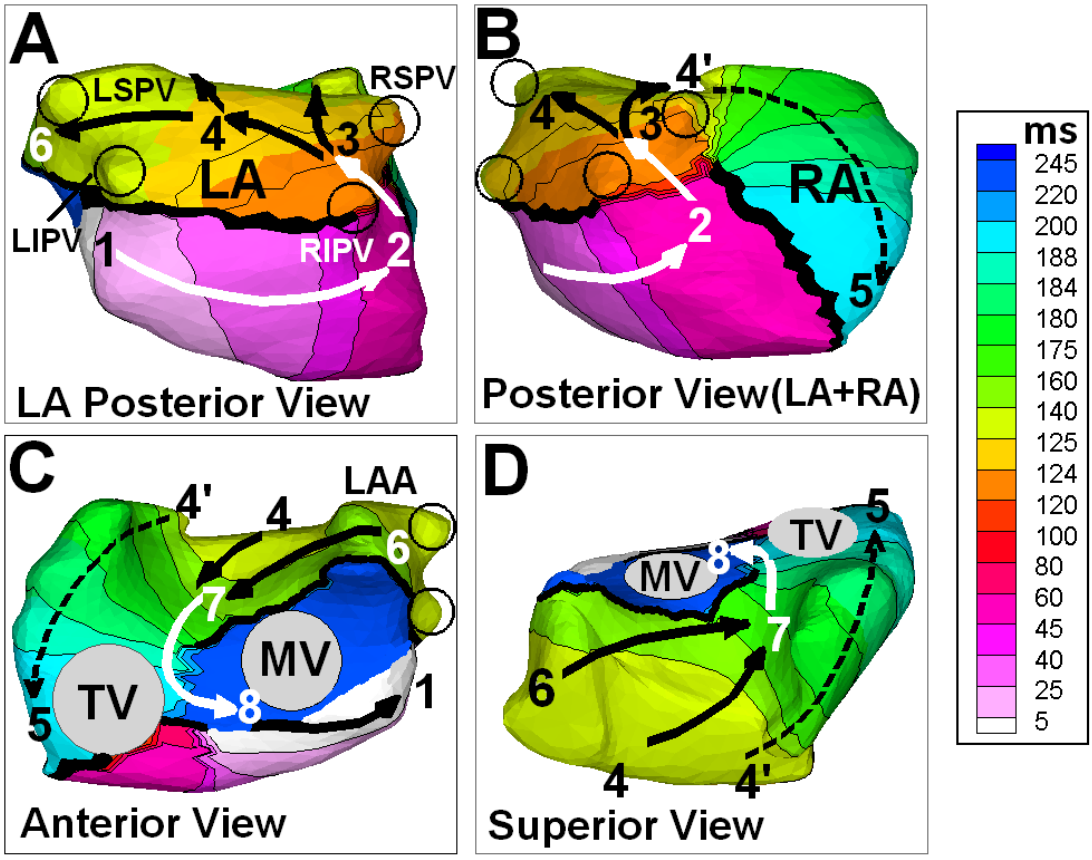

Figure 52 (Figure 7-5): ECGI reconstructed isochrone map of the flutter cycle.

Solid arrows show the reentry circuit. Dashed arrows show a secondary front emanated from the main reentry circuit. The sequence of reentry is 1→2→3→4→(6)→7→8→1. Black circles show locations of the four pulmonary veins. RA = Right Atrium, LA = Left Atrium, MV = Mitral Valve, TV = Tricuspid Valve. LIPV = Left Inferior Pulmonary Vein, LSPV = Left Superior Pulmonary Vein, RIPV = Right Inferior Pulmonary Vein, RSPV = Right Superior Pulmonary Vein, LAA = Left Atrial Appendage.

7.3.5 Summary

We report the first application of ECGI in a patient with atypical atrial flutter that developed after catheter ablation for PV isolation. ECGI detected and mapped regions of low voltages that coincided with scar tissue around the pulmonary veins from the previous catheter ablation procedures, as verified during a COX-MAZE surgical procedure. The flutter reentry circuit was constrained by the scar and mainly confined to the LA. The mitral isthmus between the coronary sinus and the PVs participated in the reentry circuit. ECGI also imaged a region of low potentials on the let atrial appendage (LAA), which is uncommon. Typically, the left atrial appendage (LAA) is a region of highest voltage, as measured by endocardial mapping. During the COX-MAZE procedure it was observed that the LAA is extensively scarred (due to the underlying disease, not prior ablation), consistent with the ECGI reconstruction of low voltages in this region. The case reported in this manuscript was unique from the ECGI perspective, because prior to the COX-MAZE procedure the diagnosis was atrial fibrillation. ECGI constructed a monomorphic stable reentrant activation pattern that was repeated for many beats, indicating anatomical rather than functional reentry. Both ECGI reconstruction of low potentials and direct observation during surgery consistently identified an extensive scar around which the ECGI reconstructed isochrones formed the reentry circuit; the scar provided the anatomical substrate that stabilized the reentry. The repeatability of the reentry pattern over many beats demonstrates the consistency of ECGI methodology. It should be recognized that ECGI generates the entire activation map during a single beat

and is therefore well suited to detect beat-to-beat changes during an arrhythmia. In contrast, catheter mapping (e.g. CARTO) is conducted point-by-point in a roving-prove fashion and requires data from many beats to construct an activation map. As such, it cannot provide data for comparison to ECGI in most cases. Following the COX-MAZE procedure, the patient returned to normal sinus rhythm.

7.4 Noninvasive Electrocardiographic Imaging of Ventricular Bigeminy in a Human Subject

Ventricular bigeminy refers to the appearance of paired different ventricular complexes in the body surface ECG (Figure 7-6, lead V2, inset in Panel A). From this ECG morphology it is inferred that bigeminy is generated by interaction between an extrasystolic beat and a regular periodic ventricular beat.[209] The regular beat is typically generated by sinus rhythm, but could also be a paced rhythm. The mechanism of ventricular bigeminy was mainly inferred based on analysis of body surface ECG signals.[209,210] However, the ECG measures the reflection of cardiac electrical activation at a limited number of points, on the body surface, remote from the heart. It does not provide detailed information about cardiac activation patterns, data that are necessary for understanding the mechanism of ventricular bigeminy. Here we apply noninvasive Electrocardiographic Imaging (ECGI)[1] to image ventricular epicardial activation during bigeminy in a patient with atrial fibrillation, who underwent AV node ablation and an implanted pacemaker in the right ventricular (RV) apex (asterisk in anterior view). ECGI is a functional imaging modality that combines 250 body-surface ECGs with thoracic CT.

[1,35] Using inverse reconstruction algorithms, ECGI generates electroanatomical maps on the epicardial surface of the heart noninvasively. Following extensive validation, it has been applied in human subjects with various cardiac electrophysiological conditions.[10,33,34,207] Panel A of Figure 7-6 shows the sequence of ventricular activation during bigeminy. The top row demonstrates the regular paced beat with wavefront propagation from the pacing site to the rest of the heart over 160 ms duration due to slow activation in the absence of conduction system participation. The bottom row shows activation during the following beat, with wavefront propagating from an LV ectopic initiation site (triangle in posterior view) to complete ventricular activation in 130 ms. The interaction between the extrasystolic beat and the paced beat generates the bigeminy. Occasionally, we captured and imaged fusion between the paced rhythm and the extrasystole. Such fusion beats are shown in Panel B of Figure 7-6. In the top row, the initiation of paced activation precedes that of extrasystolic activation by 15 ms. This closely coupled biventricular activation increases electrical synchronization and reduces the QRS duration to 100ms. In the bottom row, the sequence is reversed and the extrasystole initiation precedes the paced beat by 10 ms with fusion beats of similar duration but different morphology. These first ECGI images of bigeminy in a human subject provide detailed epicardial activation sequences, confirming its origin in the interaction between an extrasystolic beat and a regular periodic beat.

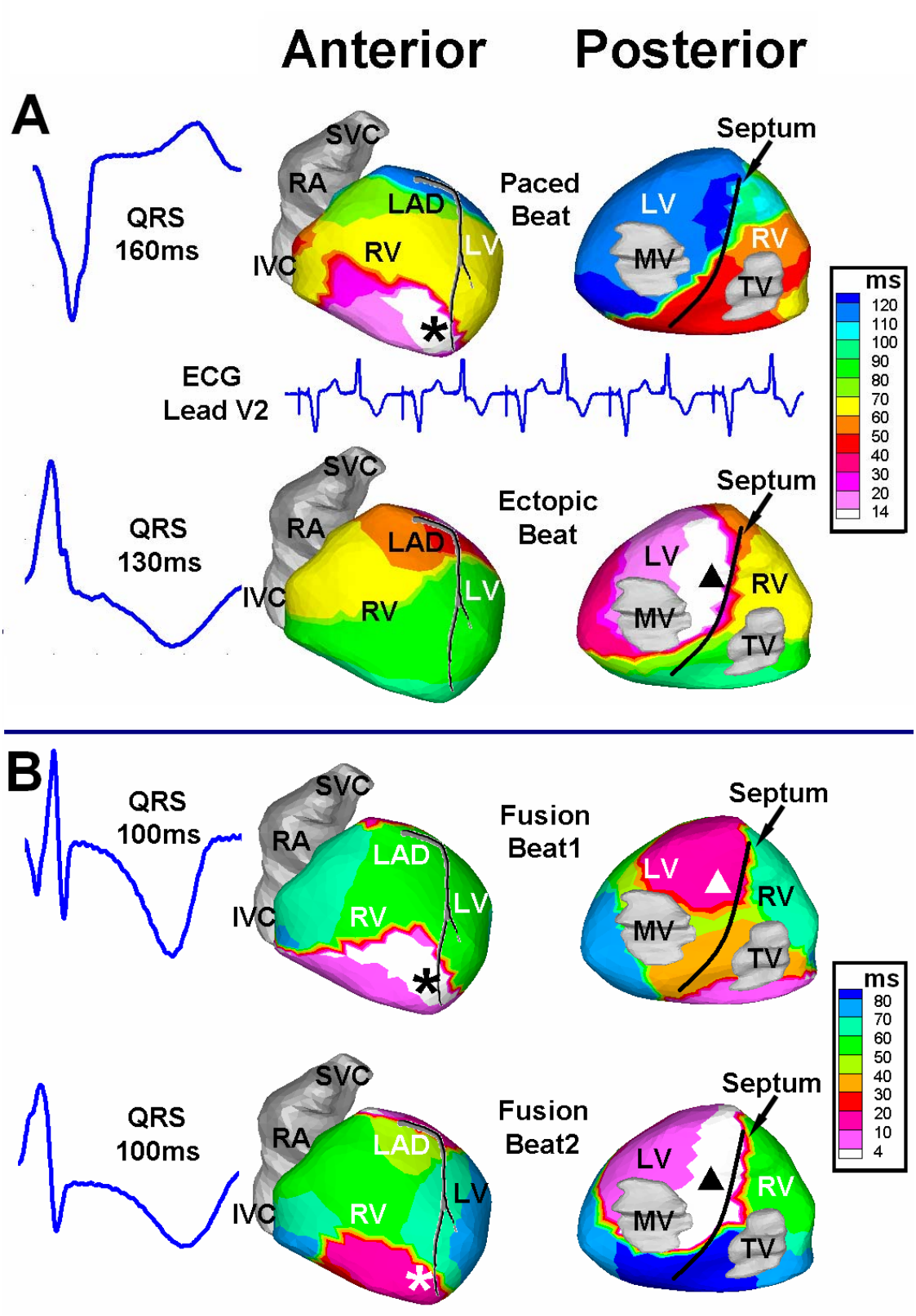

Figure 53 (Figure 7-6) ECGI reconstructed isochrone map

Panel A: The ventricular activation sequence during bigeminy. Top row shows activation sequence for a paced beat from a pacemaker lead located at right ventricular (RV) apex (black asterisk) in the anterior and posterior views (with atria removed). Bottom row shows activation during an extrasystolic beat from a left ventricular (LV) ectopic site (triangle). Panel B: Ventricular activation sequence during two different fusion beats between the paced beat and extrasystolic beat. In the top row, the onset of paced activation precedes that of extrasystolic activation by 15 ms. In the bottom row, the extrasystole onset precedes the paced beat by 10 ms. RA = Right Atrium; SVC=Superior Vena Cava; IVC = Inferior Vena Cava; MV = Mitral Valve; TV = Tricuspid Valve; The solid black line in the posterior view indicates septum location.

Chapter 8 Conclusions and Future Work

8.1 Conclusions

Cardiac arrhythmias continue to be a leading cause of death and disability. Despite this alarming fact, a noninvasive imaging modality (analogous to CT or MRI) for cardiac electrophysiology and arrhythmia has not been available for clinical diagnosis and guidance of therapy. Importantly, such an imaging modality is also greatly needed for the study of arrhythmia mechanisms in humans, where the arrhythmic substrate and disease processes differ considerably from those in experimental animal models. In Dr. Yoram Rudy's Laboratory, we have developed, implemented, and validated a novel noninvasive imaging modality (Electrocardiographic Imaging, ECGI) and demonstrated its successful application in humans. ECGI reconstructs epicardial potentials, electrograms and isochrones from body-surface electrocardiograms combined with heart-torso geometry from computed tomography (CT). The studies presented in this dissertation focused on the continued development of ECGI methodology and clinical applications in different group of adult patients.

By introducing the application of a meshless method, the Method of Fundamental Solutions (MFS), to ECGI, the time-consuming meshing operation involved in the boundary element method (BEM) is eliminated, and the mesh-related artifacts in the

BEM reconstructed epicardial images are avoided. Our studies demonstrate that the MFS method has similar accuracy but simpler implementation due to the elimination of complex singular integrals involved in BEM. These properties of MFS can enhance the practical application of ECGI as a clinical diagnostic tool. We have also proposed a Real Time ECGI procedure, in which ECGI inverse computation could be executed as fast as the BSP data acquisition speed. In Real Time ECGI mode, the epicardial potential information could be obtained during the BSPM recording, without any delay or data accumulation. Real Time ECGI can provide epicardial electrophysiological data during the clinical procedure, thus enabling interactive guidance of intervention.

ECGI has been successfully applied in patients with post-myocardial infarction, ventricular arrhythmias, and atrial arrhythmias. In these human studies, ECGI has demonstrated its ability to (1) noninvasively characterize the electrophysiological substrate within one recorded beat; (2) noninvasively image the complicated ventricular and atrial arrhythmias in a beat to beat fashion and provide insight to explain underlying mechanisms, especially for patients who have dynamically changing conditions and can not be easily mapped using currently available mapping tools; (3) noninvasively provide location information about the origin of focal arrhythmias and facilitate ablations; (4) provide noninvasive electrophysiology information for patient-specific treatment plans. Our studies demonstrate that ECGI has great potential to be applied in both clinical practice to facilitate the treatment of cardiac arrhythmias and scientific research to better

understand the underlying mechanism of disease.

8.2 Future Work

Although ECGI has been improved dramatically and been successfully applied in many different clinical settings over years, there is still room to enhance the ECGI system in the following aspects: (1) a better and more automatic segmentation algorithm can enhance the clinical application of ECGI; (2) a better user-interface, providing multiple choices for inverse computation including regularization method and inverse parameters, can make ECGI system easier to use; (3) better integration with other imaging modalities such as MRI will enhance ECGI's visualization capability and provide fused anatomical-electrophysiological information; (4) integration with invasive mapping systems such as CARTO, Navx etc. will provide comprehensive electrophysiological information (both epicardial and endocardial mapping data); (5) better consideration of inhomogeneous volume conductor will improve the accuracy of ECGI. With the development of computational power and signal processing techniques, all these technique improvement will be achieved.

ECGI has been extensively tested and validated over the last decades. Our studies with relatively small numbers of subjects have clearly demonstrated ECGI's capabilities and potentials to provide important information and play unique roles in both clinical practice

and basic electrophysiological research. In the next phase of ECGI application, better designed prospective studies should be conducted to evaluate ECGI's performance in guiding clinical practice in a more direct way. In these studies, ECGI results will not only be used to confirm data obtained from other imaging or mapping tools, but also be considered as important independent information to influence clinical interactions and decisions. Clinical trials with large numbers of subjects should also be conducted to evaluate ECGI's clinical usefulness.

References

1. Ramanathan C, Ghanem RN, Jia P, Ryu K, Rudy Y. Noninvasive electrocardiographic imaging for cardiac electrophysiology and arrhythmia. *Nat Med*. 2004;10:422-8.
2. Ramanathan C, Jia P, Ghanem R, Ryu K, Rudy Y. Activation and repolarization of the normal human heart under complete physiological conditions. *Proc Natl Acad Sci U S A*. 2006;103:6309-14.
3. Oster HS, Taccardi B, Lux RL, Ershler PR, Rudy Y. Noninvasive electrocardiographic imaging: reconstruction of epicardial potentials, electrograms, and isochrones and localization of single and multiple electrocardiac events. *Circulation*. 1997;96:1012-24.
4. Oster HS, Taccardi B, Lux RL, Ershler PR, Rudy Y. Electrocardiographic imaging: Noninvasive characterization of intramural myocardial activation from inverse-reconstructed epicardial potentials and electrograms. *Circulation*. 1998;97:1496-507.
5. Burnes JE, Ghanem RN, Waldo AL, Rudy Y. Imaging dispersion of myocardial repolarization, I: comparison of body-surface and epicardial measures. *Circulation*. 2001;104:1299-305.
6. Burnes JE, Taccardi B, Ershler PR, Rudy Y. Noninvasive electrocardiogram imaging of substrate and intramural ventricular tachycardia in infarcted hearts. *J Am Coll Cardiol*. 2001;38:2071-8.
7. Burnes JE, Taccardi B, MacLeod RS, Rudy Y. Noninvasive ECG imaging of electrophysiologically abnormal substrates in infarcted hearts : A model study. *Circulation*. 2000;101:533-40.
8. Burnes JE, Taccardi B, Rudy Y. A noninvasive imaging modality for cardiac arrhythmias. *Circulation*. 2000;102:2152-8.
9. Ghanem RN, Burnes JE, Waldo AL, Rudy Y. Imaging dispersion of myocardial repolarization, II: noninvasive reconstruction of epicardial measures. *Circulation*. 2001;104:1306-12.
10. Jia P, Ramanathan C, Ghanem RN, Ryu K, Varma N, Rudy Y. Electrocardiographic imaging of cardiac resynchronization therapy in heart failure: observation of variable electrophysiologic responses. *Heart Rhythm*. 2006;3:296-310.
11. Ghosh S, Avari JN, Rhee EK, Woodard PK, Rudy Y. Noninvasive Electrocardiographic Imaging (ECGI) of a univentricular heart with Wolff-Parkinson-White syndrome. *Heart Rhythm*. 2008.
12. Ghosh S, Avari JN, Rhee EK, Woodard PK, Rudy Y. Noninvasive electrocardiographic imaging (ECGI) of epicardial activation before and after catheter ablation of the accessory pathway in a patient with Ebstein anomaly. *Heart Rhythm*. 2008;5:857-60.
13. Ghosh S, Avari JN, Rhee EK, Woodard PK, Rudy Y. Hypertrophic cardiomyopathy with preexcitation: insights from noninvasive electrocardiographic imaging (ECGI) and catheter mapping. *J Cardiovasc Electrophysiol*. 2008;19:1215-7.
14. Ghosh S, Rhee EK, Avari JN, Woodard PK, Rudy Y. Cardiac memory in patients with Wolff-Parkinson-White syndrome: noninvasive imaging of activation and repolarization before and after catheter ablation. *Circulation*. 2008;118:907-15.
15. Wang Y, Cuculich PS, Woodard PK, Lindsay BD, Rudy Y. Focal atrial tachycardia after

pulmonary vein isolation: noninvasive mapping with electrocardiographic imaging (ECGI). *Heart Rhythm*. 2007;4:1081-4.

16. Wang Y, Li L, Cuculich PS, Rudy Y. Electrocardiographic Imaging of Ventricular Bigeminy in a Human Subject. *Circ Arrhythm Electrophysiol*. 2008;1:74-75.
17. Wang Y, Schuessler RB, Damiano RJ, Woodard PK, Rudy Y. Noninvasive electrocardiographic imaging (ECGI) of scar-related atypical atrial flutter. *Heart Rhythm*. 2007;4:1565-7.
18. Wang Y, Rudy Y. Electrocardiographic imaging of normal human atrial repolarization. *Heart Rhythm*. 2009;6:582-3.
19. Colli-Franzone P, Guerri L, Taccardi B, Viganotti C. Finite element approximation of regularized solutions of the inverse potential problem of electrocardiography and applications to experimental data. *Calcolo*. 1985;22:91-186.
20. Ramanathan C, Jia P, Ghanem R, Calvetti D, Rudy Y. Noninvasive electrocardiographic imaging (ECGI): application of the generalized minimal residual (GMRes) method. *Annals of Biomedical Engineering*. 2003;31:981-94.
21. Oster HS, Taccardi B, Lux RL, Ershler PR, Rudy Y. Noninvasive electrocardiographic imaging: reconstruction of epicardial potentials, electrograms, and isochrones and localization of single and multiple electrocardiac events. *Circulation*. 1997;96:1012-1024.
22. Oster HS, Taccardi B, Lux RL, Ershler PR, Rudy Y. Noninvasive electrocardiographic imaging: Noninvasive characterization of intramural myocardial activation from inverse-reconstructed epicardial potentials and electrograms. *Circulation*. 1998;97:1496-1507.
23. Burnes JE, Taccardi B, MacLeod RS, Rudy Y. Noninvasive ECG imaging of electrophysiologically abnormal substrates in infarcted hearts: A model study. *Circulation*. 2000;101:533-40.
24. Burnes JE, Taccardi B, E. PR, Rudy Y. Noninvasive electrocardiogram imaging of substrate and intramural ventricular tachycardia in infarcted hearts. *Journal of the American College of Cardiology*. 2001;38:2071-8.
25. Barr RC, Spach MS. Inverse solutions directly in terms of potentials. In: Nelson CV, Geselowitz DB, eds. *The Theoretical Basis of Electrocardiography*. Oxford: Clarendon Press; 1976:294-304.
26. Franzone P, Taccardi B, Viganotti C. An approach to inverse calculation of epicardial potentials from body surface maps. *Adv Cardiol*. 1978;21:50-4.
27. Rudy Y, Messinger-Rapport BJ. The inverse problem in electrocardiography: solutions in terms of epicardial potentials. *Crit Rev Biomed Eng*. 1988;16:215-68.
28. Yamashita Y. Inverse solution in electrocadiography: determining epicardial from body surface maps by using the finite element method. *Jpn Circ J*. 1981;45:1312-1322.
29. Huiskamp G, Greensite F. A new method for myocardial activation imaging. *IEEE Trans Biomed Eng*. 1997;44:433-46.
30. Modre R, Tilg B, Fischer G, Wach P. Noninvasive myocardial activation time imaging: a novel inverse algorithm applied to clinical ECG mapping data. *IEEE Trans Biomed Eng*. 2002;49:1153-61.
31. Modre R, Tilg B, Fischer G, Hanser F, Messnarz B, Seger M, Hintringer F, Roithinger FX. Ventricular surface activation time imaging from electrocardiogram mapping data. *Med Biol Eng*

Comput. 2004;42:146-50.

32. Fischer G, Pfeifer B, Seger M, Hintermuller C, Hanser F, Modre R, Tilg B, Trieb T, Kremser C, Roithinger FX, Hintringer F. Computationally efficient noninvasive cardiac activation time imaging. *Methods Inf Med*. 2005;44:674-86.
33. Ghanem RN, Jia P, Ramanathan C, Ryu K, Markowitz A, Rudy Y. Noninvasive electrocardiographic imaging (ECGI): comparison to intraoperative mapping in patients. *Heart Rhythm*. 2005;2:339-54.
34. Intini A, Goldstein RN, Jia P, Ramanathan C, Ryu K, Giannattasio B, Gilkeson R, Stambler BS, Brugada P, Stevenson WG, Rudy Y, Waldo AL. Electrocardiographic imaging (ECGI), a novel diagnostic modality used for mapping of focal left ventricular tachycardia in a young athlete. *Heart Rhythm*. 2005;2:1250-2.
35. Ramanathan C, Jia P, Ghanem RN, Ryu K, Rudy Y. Activation and repolarization of the normal human heart under complete physiological conditions. *Proc. Natl. Acad. Sci., U.S.A. (PANS)*. 2006;In Press.
36. Tilg B, Hanser F, Modre-Osprian R, Fischer G, Messnarz B, Berger T, Hintringer F, Pachinger O, Roithinger FX. Clinical ECG mapping and imaging of cardiac electrical excitation. *J Electrocardiol*. 2002;35 Suppl:81-7.
37. Tilg B, Fischer G, Modre R, Hanser F, Messnarz B, Schocke M, Kremser C, Berger T, Hintringer F, Roithinger FX. Model-based imaging of cardiac electrical excitation in humans. *IEEE Trans Med Imaging*. 2002;21:1031-9.
38. Modre R, Tilg B, Fischer G, Hanser F, Messnarz B, Seger M, Schocke MF, Berger T, Hintringer F, Roithinger FX. Atrial noninvasive activation mapping of paced rhythm data. *J Cardiovasc Electrophysiol*. 2003;14:712-9.
39. Messnarz B, Tilg B, Modre R, Fischer G, Hanser F. A new spatiotemporal regularization approach for reconstruction of cardiac transmembrane potential patterns. *IEEE Trans Biomed Eng*. 2004;51:273-81.
40. Tilg B, Fischer G, Modre R, Hanser F, Messnarz B, Roithinger FX. Electrocardiographic imaging of atrial and ventricular electrical activation. *Med Image Anal*. 2003;7:391-8.
41. Golberg MA, Chen CS. The method of fundamental solutions for potential, Helmholtz and diffusion problems. In: Golberg MA, ed. *Boundary Integral Methods - Numerical and Mathematical Aspects*. Southampton-Boston: Computational Mechanics Publications; 1998:103-176.
42. Tikhonov AN, Arsenin VY. *Solution of Ill-Posed Problems*. Washington DC: VH Winston & Sons; 1977.
43. Beer G, Watson JO. *Introduction to Finite and Boundary Element Methods for Engineers*. West Sussex: Wiley; 1992.
44. Brebbia CA, Telles JCF, Wrobel LC. *Boundary element techniques: Theory and applications in engineering*. Berlin, Germany: Springer Verlag; 1984.
45. Barr RC, Spach MS. Inverse calculation of QRS-T epicardial potentials from body surface potential distributions for normal and ectopic beats in the intact dog. *Circ Res*. 1978;42:661-75.
46. Colli-Franzone P, Guerri L, Tentoni S, Viganotti C, Baruffi S, Spaggiari S, Taccardi B.

Mathematical procedure for solving the inverse problem of electrocardiography. *Math Biosci*. 1985;77:353-396.

47. Rudy Y, Burnes JE. Noninvasive electrocardiographic imaging (ECGI). *Annals of Noninvasive electrocardiol.* 1999;4:340-359.
48. Golberg MA, Chen CS. *Discrete Projection Methods for Integral Equations*. Southampton: Computational Mechanics Publications; 1996.
49. Atkinson KE, Chien D. Piecewise Polynomial collocation for boundary integral equations. *SIAM Journal on Scientific and Statistical Computing.* 1985;76:651-681.
50. Sauter SA, Krapp A. On the effect of numerical integration in the Galerkin boundary element method. *Numerische Mathematik*. 1996;74:337-360.
51. Patridge PW, Brebbia CA, Wrobel LC. *The Dual Reciprocity Boundary Element Method*. Southampton-Boston: Computational Mechanics Publications; 1992.
52. Fairweather G, Johnston RL. The method of fundamental solutions for problems in fluid flow. *Appl. Math. Modeling*. 1984;8:265-270.
53. Hon YC, Wei T. A fundamental solution method for inverse heat conduction problem. *Engineering Analysis with Boundary Elements*. 2004;28:489-495.
54. Hon YC, Wei T. Solving Cauchy problems of elliptic equations by the method of fundamental solutions. In: Kassab A, Brebbia CA, Divo E, Poljak D, eds. *Boundary Elements XXVII*. Southampton-Boston: WIT press; 2005:57-65.
55. Fairweather G, Karageorghis A. The method of fundamental solutions for elliptic boundary value problems. *Adv Comput Math.* 1998;9:69-95.
56. Belytschko T, Krongauz Y, Organ D, Fleming M, Krysl P. Meshless methods: An overview and recent developments. *Comput. Method. Appl. Mech. Eng.* 1996;139:3-47.
57. Messinger-Rapport BJ, Rudy Y. Noninvasive recovery of epicardial potentials in a realistic heart-torso geometry. Normal sinus rhythm. *Circ Res*. 1990;66:1023-39.
58. Taccardi B, Macchi E, Lux R, Ershler P, Spaggiari S, Baruffi S, Vyhmeister Y. Effect of myocardial fiber direction on epicardial potentials. *Circulation*. 1994;90:3076-3090.
59. Durrer D, van Dam RT, Freud GE, Janse MJ, Meijler FL, Arzbaecher RC. Total excitation of the isolated human heart. *Circulation*. 1970;41:899-912.
60. Huiskamp G, van Oosterom A. The depolarization sequence of the human heart surface computed from measured body surface potentials. *IEEE Trans Biomed Eng*. 1988;35:1047-58.
61. Khoury DS, Taccardi B, Lux RL, Ershler PR, Rudy Y. Reconstruction of endocardial potentials and activation sequences from intracavitary probe measurements. Localization of pacing sites and effects of myocardial structure. *Circulation.* 1995;91:845-63.
62. Khoury DS, Berrier KL, Badruddin SM, Zoghbi WA. Three-dimensional electrophysiological imaging of the intact canine left ventricle using a noncontact multielectrode cavitary probe: study of sinus, paced, and spontaneous premature beats. *Circulation*. 1998;97:399-409.
63. Jia P, Punske B, Taccardi B, Rudy Y. Electrophysiologic endocardial mapping from a noncontact nonexpandable catheter: a validation study of a geometry-based concept. *Journal of Cardiovascular Electrophysiology*. 2000;11:1238-51.
64. Yue AM, Franz MR, Roberts PR, Morgan JM. Global endocardial electrical restitution in human

right and left ventricles determined by noncontact mapping. *J Am Coll Cardiol*. 2005;46:1067-75.

65. Berrier KL, Sorensen DC, Khoury DS. Solving the inverse problem of electrocardiography using a Duncan and Horn formulation of the Kalman filter. *IEEE Trans Biomed Eng*. 2004;51:507-15.
66. Huiskamp G, van Oosterom A. Tailored versus realistic geometry in the inverse problem of electrocardiography. *IEEE Trans Biomed Eng*. 1989;36:827-35.
67. Huiskamp GJ, van Oosterom A. Heart position and orientation in forward and inverse electrocardiography. *Med Biol Eng Comput*. 1992;30:613-20.
68. Cheng LK, Bodley JM, Pullan AJ. Effects of experimental and modeling errors on electrocardiographic inverse formulations. *IEEE Trans Biomed Eng*. 2003;50:23-32.
69. Ramanathan C, Rudy Y. Electrocardiographic imaging: II. Effect of torso inhomogeneities on noninvasive reconstruction of epicardial potentials, electrograms, and isochrones. *Journal of Cardiovascular Electrophysiology*. 2001;12:241-52.
70. Green LS, Taccardi B, Ershler PR, Lux RL. Epicardial potential mapping. Effects of conducting media on isopotential and isochrone distributions. *Circulation*. 1991;84:2513-21.
71. Ramanathan C, Rudy Y. Electrocardiographic imaging: I. Effect of torso inhomogeneities on body surface electrocardiographic potentials. *Journal of Cardiovascular Electrophysiology*. 2001;12:229-40.
72. Malik NH. A review of the charge simulation method and its applications. *IEEE Transactions on Electrical Insulation*. 1989;24:3-20.
73. Plonsey R, Barr RC. *Bioelectricity : a quantitative approach*. New York: Plenum Press; 1988.
74. Blaszczyk A, Steinbigler H. Region-oriented charge simulation. *IEEE Transaction on magnetics*. 1994;30:2924-2927.
75. Blaszczyk A. Formulations based on region-oriented charge simulation for electromagnetics. *IEEE Transaction on magnetics*. 2000;36:701-704.
76. Berger JR, Karageorghis A. The method of fundamental solutions for heat conduction in layered materials. *International Journal for Numerical Methods in Engineering*. 1999;45:1681-1694.
77. Taden A, Godinho L, Chen CS. Performance of the BEM, MFS and RBF collocation method in a 2.5 wave propagation analysis. In: Kassab A, Brebbia CA, Divo E, Poljak D, eds. *Boundary Elements XXVII*. Southampton-Boston: WIT press; 2005:143-153.
78. Batdorf M, Freitag LA, Ollivier-Gooch C. Computational Study of the Effect of Unstructured Mesh Quality on Solution Efficiency. *Proc. 13th AIAA Computational Fluid Dynamics Conf.* 1997:1888.
79. Brewer M, Diachin L, Leurent T, Melander D. The Mesquite Mesh Quality Improvement Toolkit. *Proceedings, 12th International Meshing Roundtable*. 2003:239-250.
80. Freitag L, Leurent T, Knupp P, Melander D. MESQUITE Design: Issues in the Development of a Mesh Quality Improvement Toolkit. *Proceedings of the 8th Intl. Conference on Numerical Grid Generation in Computational Field Simulations*. 2002:159-168.
81. Brooks DH, Ahmad GF, MacLeod RS, Maratos GM. Inverse electrocardiography by simultaneous imposition of multiple constraints. *IEEE Trans Biomed Eng*. 1999;46:3-18.
82. Ghodrati A, Brooks DH, Tadmor G, Punske B, MacLeod RS. Wavefront-based inverse electrocardiography using an evolving curve state vector and phenomenological propagation and

potential models. *International Journal of Bioelectromagnetism*. 2005;7:210-213.

83. Greensite F. The temporal prior in bioelectromagnetic source imaging problems. *IEEE Trans Biomed Eng*. 2003;50:1152-9.

84. Carr JC, Beatson RK, Cherrie JB, Mitchell TJ, Fright WR, McCallum BC, Evans TR. Reconstruction and Representation of 3D Objects with Radial Basis Functions. *Proceedings of the 28th annual conference on Computer graphics and interactive techniques*. 2001:67-76.

85. Carr JC, Fright WR, Beatson RK. Surface interpolation with radial basis functions for medical imaging. *IEEE Trans Med Imaging*. 1997;16:96-107.

86. Sainz M, Pajarola R. Point-Based Rendering Techniques. *Computers & Graphics*. 2004;28:869-879.

87. Bogomolny A. Fundamental solutions method for elliptic boundary value problems. *SIAM Journal on Numerical Analysis*. 1985;22:644-669.

88. Golberg MA, Chen CS, Karur SR. Improved multiquadric approximation for partial differential equations. *Engin. Anal. with Bound. Elem.* 1996;18:9-17.

89. Christiansen S, Sararen J. The conditioning of some numerical methods for first kind integral equations. *Journal of Computational and Applied Mathematics*. 1996;67:43-58.

90. Christiansen S, Hansen PC. The effective condition number applied to error analysis of certain boundary collocation methods. *Journal of Computational and Applied Mathematics*. 1994;54:15-36.

91. Ghosh S, Rudy Y. Accuracy of quadratic versus linear interpolation in noninvasive Electrocardiographic Imaging (ECGI). *Ann Biomed Eng*. 2005;33:1187-201.

92. Karageorghis A, Fairweather G. The method of fundamental solutions for the numerical solution of the biharmonic equation. *Journal of Computational Physics*. 1987;69:435-459.

93. Mera NS. The method of fundamental solutions for the backward heat conduction problem. *Inverse Problems in Science and Engineering*. 2005;13:65-78.

94. Kythe PK. *Fundamental Solutions for Differential Operators and Applications*. Boston-Basel-Berlin: Birkhauser; 1996.

95. Chen Y, Atkinson K. Solving a Single Layer Integral Equation on Surface in R3. *SIAM J. Num. Anal., Reports on Computational Mathematics #51*. 1994.

96. Cheng RSC. *Deta-Trigonometric and Spline Methods using the Single-Layer Potential Representation*. Ph.D. dissertation: University of Maryland; 1987.

97. Jia P, Punske B, Taccardi B, Rudy Y. Endocardial mapping of electrophysiologically abnormal substrates and cardiac arrhythmias using a noncontact nonexpandable catheter. *J Cardiovasc Electrophysiol*. 2002;13:888-95.

98. Hansen PC. The L-curve and its use in the numerical treatment of inverse problems. In: Johnston P, ed. *Computational Inverse Problems in Electrocardiology*. Southampton: WIT Press; 2001:119-142.

99. Tikhonov AN, Arsenin VY. *Solution of Ill-posed Problems*. Washington DC: VH Winston & Sons; 1977.

100. Rudy Y, Oster HS. The electrocardiographic inverse problem. *Crit Rev Biomed Eng*. 1992;20:25-45.

101. Ramanathan C, Jia P, Ghanem R, Calvetti D, Rudy Y. Noninvasive electrocardiographic imaging (ECGI): application of the generalized minimal residual (GMRes) method. *Ann Biomed Eng*. 2003;31:981-94.
102. Wang Y, Rudy Y. Application of the method of fundamental solutions to potential-based inverse electrocardiography. *Ann Biomed Eng*. 2006;34:1272-88.
103. Colli-Franzone P, Guerri L, Tentoni S, Viganotti C, Baruffi S, Spaggiari S, Taccardi B. A mathematical procedure for solving the inverse problem of electrocardiography. *Math. Biosci.* 1985;77:353-396.
104. Guiraudon GM, Thakur RK, Klein GJ, Yee R, Guiraudon CM, Sharma A. Encircling endocardial cryoablation for ventricular tachycardia after myocardial infarction: experience with 33 patients. *Am Heart J*. 1994;128:982-9.
105. Ostermeyer J, Breithardt G, Borggrefe M, Godehardt E, Seipel L, Bircks W. Surgical treatment of ventricular tachycardias. Complete versus partial encircling endocardial ventriculotomy. *J Thorac Cardiovasc Surg*. 1984;87:517-25.
106. de Bakker JM, van Capelle FJ, Janse MJ, Wilde AA, Coronel R, Becker AE, Dingemans KP, van Hemel NM, Hauer RN. Reentry as a cause of ventricular tachycardia in patients with chronic ischemic heart disease: electrophysiologic and anatomic correlation. *Circulation.* 1988;77:589-606.
107. de Bakker JM, van Capelle FJ, Janse MJ, Tasseron S, Vermeulen JT, de Jonge N, Lahpor JR. Slow conduction in the infarcted human heart. 'Zigzag' course of activation. *Circulation*. 1993;88:915-26.
108. Kleber AG, Rudy Y. Basic mechanisms of cardiac impulse propagation and associated arrhythmias. *Physiol Rev*. 2004;84:431-88.
109. Kuchar DL, Thorburn CW, Sammel NL. Late potentials detected after myocardial infarction: natural history and prognostic significance. *Circulation*. 1986;74:1280-9.
110. Oikarinen L, Viitasalo M, Korhonen P, Vaananen H, Hanninen H, Montonen J, Makijarvi M, Katila T, Toivonen L. Postmyocardial infarction patients susceptible to ventricular tachycardia show increased T wave dispersion independent of delayed ventricular conduction. *J Cardiovasc Electrophysiol*. 2001;12:1115-20.
111. Perkiomaki JS, Koistinen MJ, Yli-Mayry S, Huikuri HV. Dispersion of QT interval in patients with and without susceptibility to ventricular tachyarrhythmias after previous myocardial infarction. *J Am Coll Cardiol.* 1995;26:174-9.
112. Zabel M, Klingenheben T, Franz MR, Hohnloser SH. Assessment of QT dispersion for prediction of mortality or arrhythmic events after myocardial infarction: results of a prospective, long-term follow-up study. *Circulation*. 1998;97:2543-50.
113. Mahnken AH, Koos R, Katoh M, Wildberger JE, Spuentrup E, Buecker A, Gunther RW, Kuhl HP. Assessment of myocardial viability in reperfused acute myocardial infarction using 16-slice computed tomography in comparison to magnetic resonance imaging. *J Am Coll Cardiol*. 2005;45:2042-7.
114. Bello D, Fieno DS, Kim RJ, Pereles FS, Passman R, Song G, Kadish AH, Goldberger JJ. Infarct morphology identifies patients with substrate for sustained ventricular tachycardia. *J Am Coll*

Cardiol. 2005;45:1104-8.

115. Fahmy TS, Wazni OM, Jaber WA, Walimbe V, Di Biase L, Elayi CS, DiFilippo FP, Young RB, Patel D, Riedlbauchova L, Corrado A, Burkhardt JD, Schweikert RA, Arruda M, Natale A. Integration of positron emission tomography/computed tomography with electroanatomical mapping: a novel approach for ablation of scar-related ventricular tachycardia. *Heart Rhythm*. 2008;5:1538-45.
116. Ashikaga H, Sasano T, Dong J, Zviman MM, Evers R, Hopenfeld B, Castro V, Helm RH, Dickfeld T, Nazarian S, Donahue JK, Berger RD, Calkins H, Abraham MR, Marban E, Lardo AC, McVeigh ER, Halperin HR. Magnetic resonance-based anatomical analysis of scar-related ventricular tachycardia: implications for catheter ablation. *Circ Res*. 2007;101:939-47.
117. Maynard SJ, Menown IB, Manoharan G, Allen J, Mc CAJ, Adgey AA. Body surface mapping improves early diagnosis of acute myocardial infarction in patients with chest pain and left bundle branch block. *Heart*. 2003;89:998-1002.
118. Verma A, Marrouche NF, Schweikert RA, Saliba W, Wazni O, Cummings J, Abdul-Karim A, Bhargava M, Burkhardt JD, Kilicaslan F, Martin DO, Natale A. Relationship between successful ablation sites and the scar border zone defined by substrate mapping for ventricular tachycardia post-myocardial infarction. *J Cardiovasc Electrophysiol*. 2005;16:465-71.
119. Zeppenfeld K, Kies P, Wijffels MC, Bootsma M, van Erven L, Schalij MJ. Identification of successful catheter ablation sites in patients with ventricular tachycardia based on electrogram characteristics during sinus rhythm. *Heart Rhythm*. 2005;2:940-50.
120. Voss F, Steen H, Bauer A, Giannitsis E, Katus HA, Becker R. Determination of myocardial infarct size by noncontact mapping. *Heart Rhythm*. 2008;5:308-14.
121. Reek S, Geller JC, Mittag A, Grothues F, Hess A, Kaulisch T, Klein HU. Noncontact mapping of ventricular tachycardia in a closed-chest animal model of chronic myocardial infarction. *Pacing Clin Electrophysiol*. 2003;26:2253-63.
122. Jacobson JT, Afonso VX, Eisenman G, Schultz JR, Lazar S, Michele JJ, Josephson ME, Callans DJ. Characterization of the infarct substrate and ventricular tachycardia circuits with noncontact unipolar mapping in a porcine model of myocardial infarction. *Heart Rhythm*. 2006;3:189-97.
123. Harris L, Downar E, Mickleborough L, Shaikh N, Parson I. Activation sequence of ventricular tachycardia: endocardial and epicardial mapping studies in the human ventricle. *J Am Coll Cardiol*. 1987;10:1040-7.
124. Kaltenbrunner W, Cardinal R, Dubuc M, Shenasa M, Nadeau R, Tremblay G, Vermeulen M, Savard P, Page PL. Epicardial and endocardial mapping of ventricular tachycardia in patients with myocardial infarction. Is the origin of the tachycardia always subendocardially localized? *Circulation*. 1991;84:1058-71.
125. Sosa E, Scanavacca M, d'Avila A, Pilleggi F. A new technique to perform epicardial mapping in the electrophysiology laboratory. *J Cardiovasc Electrophysiol*. 1996;7:531-6.
126. Laxer C, Ideker RE, Pilkington TC. The use of unipolar epicardial QRS potentials to estimate myocardial infarction. *IEEE Transactions on Biomedical Engineering*. 1985;32:64-67.
127. de Bakker JM, Coronel R, Tasseron S, Wilde AA, Opthof T, Janse MJ, van Capelle FJ, Becker AE, Jambroes G. Ventricular tachycardia in the infarcted, Langendorff-perfused human heart: role of

the arrangement of surviving cardiac fibers. *Journal of the American College of Cardiology*. 1990;15:1594-607.

128. Watabe S, Taccardi B, Lux RL, Ershler PR. Effect of nontransmural necrosis on epicardial potential fields. Correlation with fiber direction. *Circulation*. 1990;82:2115-27.
129. Wrobleski D, Houghtaling C, Josephson ME, Ruskin JN, Reddy VY. Use of electrogram characteristics during sinus rhythm to delineate the endocardial scar in a porcine model of healed myocardial infarction. *J Cardiovasc Electrophysiol*. 2003;14:524-9.
130. Gardner PI, Ursell PC, Fenoglio JJ, Jr., Wit AL. Electrophysiologic and anatomic basis for fractionated electrograms recorded from healed myocardial infarcts. *Circulation*. 1985;72:596-611.
131. Klein H, Karp RB, Kouchoukos NT, Zorn GL, Jr., James TN, Waldo AL. Intraoperative electrophysiologic mapping of the ventricles during sinus rhythm in patients with a previous myocardial infarction. Identification of the electrophysiologic substrate of ventricular arrhythmias. *Circulation*. 1982;66:847-53.
132. Kienzle MG, Miller J, Falcone RA, Harken A, Josephson ME. Intraoperative endocardial mapping during sinus rhythm: relationship to site of origin of ventricular tachycardia. *Circulation*. 1984;70:957-65.
133. Cassidy DM, Vassallo JA, Miller JM, Poll DS, Buxton AE, Marchlinski FE, Josephson ME. Endocardial catheter mapping in patients in sinus rhythm: relationship to underlying heart disease and ventricular arrhythmias. *Circulation*. 1986;73:645-52.
134. Bogun F, Krishnan S, Siddiqui M, Good E, Marine JE, Schuger C, Oral H, Chugh A, Pelosi F, Morady F. Electrogram characteristics in postinfarction ventricular tachycardia: effect of infarct age. *J Am Coll Cardiol*. 2005;46:667-74.
135. Josephson ME, Wit AL. Fractionated electrical activity and continuous electrical activity: fact or artifact? *Circulation*. 1984;70:529-32.
136. Josephson ME, Horowitz LN, Spielman SR, Greenspan AM. Electrophysiologic and hemodynamic studies in patients resuscitated from cardiac arrest. *Am J Cardiol*. 1980;46:948-55.
137. Simson MB. Use of signals in the terminal QRS complex to identify patients with ventricular tachycardia after myocardial infarction. *Circulation*. 1981;64:235-42.
138. Denes P, Santarelli P, Hauser RG, Uretz EF. Quantitative analysis of the high-frequency components of the terminal portion of the body surface QRS in normal subjects and in patients with ventricular tachycardia. *Circulation*. 1983;67:1129-38.
139. Berbari EJ, Scherlag BJ, Hope RR, Lazzara R. Recording from the body surface of arrhythmogenic ventricular activity during the S-T segment. *Am J Cardiol*. 1978;41:697-702.
140. Simson MB, Untereker WJ, Spielman SR, Horowitz LN, Marcus NH, Falcone RA, Harken AH, Josephson ME. Relation between late potentials on the body surface and directly recorded fragmented electrograms in patients with ventricular tachycardia. *Am J Cardiol*. 1983;51:105-12.
141. Ciaccio EJ, Chow AW, Davies DW, Wit AL, Peters NS. Localization of the isthmus in reentrant circuits by analysis of electrograms derived from clinical noncontact mapping during sinus rhythm and ventricular tachycardia. *J Cardiovasc Electrophysiol*. 2004;15:27-36.
142. Ciaccio EJ, Tosti AC, Scheinman MM. Relationship between sinus rhythm activation and the

reentrant ventricular tachycardia isthmus. *Circulation*. 2001;104:613-9.

143. Littmann L, Svenson RH, Gallagher JJ, Selle JG, Zimmern SH, Fedor JM, Colavita PG. Functional role of the epicardium in postinfarction ventricular tachycardia. Observations derived from computerized epicardial activation mapping, entrainment, and epicardial laser photoablation. *Circulation*. 1991;83:1577-91.
144. Blanchard SM, Walcott GP, Wharton JM, Ideker RE. Why is catheter ablation less successful than surgery for treating ventricular tachycardia that results from coronary artery disease? *Pacing Clin Electrophysiol*. 1994;17:2315-35.
145. Gonska BD, Cao K, Schaumann A, Dorszewski A, von zur Muhlen F, Kreuzer H. Catheter ablation of ventricular tachycardia in 136 patients with coronary artery disease: results and long-term follow-up. *J Am Coll Cardiol*. 1994;24:1506-14.
146. Morady F, Harvey M, Kalbfleisch SJ, el-Atassi R, Calkins H, Langberg JJ. Radiofrequency catheter ablation of ventricular tachycardia in patients with coronary artery disease. *Circulation*. 1993;87:363-72.
147. Sosa E, Scanavacca M, d'Avila A, Oliveira F, Ramires JA. Nonsurgical transthoracic epicardial catheter ablation to treat recurrent ventricular tachycardia occurring late after myocardial infarction. *J Am Coll Cardiol*. 2000;35:1442-9.
148. Moss AJ, Hall WJ, Cannom DS, Daubert JP, Higgins SL, Klein H, Levine JH, Saksena S, Waldo AL, Wilber D, Brown MW, Heo M. Improved survival with an implanted defibrillator in patients with coronary disease at high risk for ventricular arrhythmia. Multicenter Automatic Defibrillator Implantation Trial Investigators. *N Engl J Med*. 1996;335:1933-40.
149. A comparison of antiarrhythmic-drug therapy with implantable defibrillators in patients resuscitated from near-fatal ventricular arrhythmias. The Antiarrhythmics versus Implantable Defibrillators (AVID) Investigators. *N Engl J Med*. 1997;337:1576-83.
150. Buxton AE, Lee KL, Fisher JD, Josephson ME, Prystowsky EN, Hafley G. A randomized study of the prevention of sudden death in patients with coronary artery disease. Multicenter Unsustained Tachycardia Trial Investigators. *N Engl J Med*. 1999;341:1882-90.
151. Zipes DP, Camm AJ, Borggrefe M, Buxton AE, Chaitman B, Fromer M, Gregoratos G, Klein G, Moss AJ, Myerburg RJ, Priori SG, Quinones MA, Roden DM, Silka MJ, Tracy C, Smith SC, Jr., Jacobs AK, Adams CD, Antman EM, Anderson JL, Hunt SA, Halperin JL, Nishimura R, Ornato JP, Page RL, Riegel B, Blanc JJ, Budaj A, Dean V, Deckers JW, Despres C, Dickstein K, Lekakis J, McGregor K, Metra M, Morais J, Osterspey A, Tamargo JL, Zamorano JL. ACC/AHA/ESC 2006 guidelines for management of patients with ventricular arrhythmias and the prevention of sudden cardiac death: a report of the American College of Cardiology/American Heart Association Task Force and the European Society of Cardiology Committee for Practice Guidelines (Writing Committee to Develop Guidelines for Management of Patients With Ventricular Arrhythmias and the Prevention of Sudden Cardiac Death). *J Am Coll Cardiol*. 2006;48:e247-346.
152. Marchlinski FE, Callans DJ, Gottlieb CD, Zado E. Linear ablation lesions for control of unmappable ventricular tachycardia in patients with ischemic and nonischemic cardiomyopathy. *Circulation*. 2000;101:1288-96.
153. Arenal A, Glez-Torrecilla E, Ortiz M, Villacastin J, Fdez-Portales J, Sousa E, del Castillo S, Perez

de Isla L, Jimenez J, Almendral J. Ablation of electrograms with an isolated, delayed component as treatment of unmappable monomorphic ventricular tachycardias in patients with structural heart disease. *J Am Coll Cardiol*. 2003;41:81-92.

154. Stevenson WG. Catheter ablation of monomorphic ventricular tachycardia. *Curr Opin Cardiol*. 2005;20:42-7.
155. Reddy VY, Reynolds MR, Neuzil P, Richardson AW, Taborsky M, Jongnarangsin K, Kralovec S, Sediva L, Ruskin JN, Josephson ME. Prophylactic catheter ablation for the prevention of defibrillator therapy. *N Engl J Med*. 2007;357:2657-65.
156. Joshi S, Wilber DJ. Ablation of idiopathic right ventricular outflow tract tachycardia: current perspectives. *J Cardiovasc Electrophysiol*. 2005;16 Suppl 1:S52-8.
157. Bala R, Marchlinski FE. Electrocardiographic recognition and ablation of outflow tract ventricular tachycardia. *Heart Rhythm*. 2007;4:366-70.
158. Soejima K, Stevenson WG, Sapp JL, Selwyn AP, Couper G, Epstein LM. Endocardial and epicardial radiofrequency ablation of ventricular tachycardia associated with dilated cardiomyopathy: the importance of low-voltage scars. *J Am Coll Cardiol*. 2004;43:1834-42.
159. Dixit S, Gerstenfeld EP, Lin D, Callans DJ, Hsia HH, Nayak HM, Zado E, Marchlinski FE. Identification of distinct electrocardiographic patterns from the basal left ventricle: distinguishing medial and lateral sites of origin in patients with idiopathic ventricular tachycardia. *Heart Rhythm*. 2005;2:485-91.
160. Risk factors for stroke and efficacy of antithrombotic therapy in atrial fibrillation. Analysis of pooled data from five randomized controlled trials. *Arch Intern Med*. 1994;154:1449-57.
161. Stewart S, Hart CL, Hole DJ, McMurray JJ. A population-based study of the long-term risks associated with atrial fibrillation: 20-year follow-up of the Renfrew/Paisley study. *Am J Med*. 2002;113:359-64.
162. Wattigney WA, Mensah GA, Croft JB. Increasing trends in hospitalization for atrial fibrillation in the United States, 1985 through 1999: implications for primary prevention. *Circulation*. 2003;108:711-6.
163. Fuster V, Ryden LE, Cannom DS, Crijns HJ, Curtis AB, Ellenbogen KA, Halperin JL, Le Heuzey JY, Kay GN, Lowe JE, Olsson SB, Prystowsky EN, Tamargo JL, Wann S, Smith SC, Jr., Jacobs AK, Adams CD, Anderson JL, Antman EM, Hunt SA, Nishimura R, Ornato JP, Page RL, Riegel B, Priori SG, Blanc JJ, Budaj A, Camm AJ, Dean V, Deckers JW, Despres C, Dickstein K, Lekakis J, McGregor K, Metra M, Morais J, Osterspey A, Zamorano JL. ACC/AHA/ESC 2006 Guidelines for the Management of Patients with Atrial Fibrillation: a report of the American College of Cardiology/American Heart Association Task Force on Practice Guidelines and the European Society of Cardiology Committee for Practice Guidelines (Writing Committee to Revise the 2001 Guidelines for the Management of Patients With Atrial Fibrillation): developed in collaboration with the European Heart Rhythm Association and the Heart Rhythm Society. *Circulation*. 2006;114:e257-354.
164. Moe GK, Rheinboldt WC, Abildskov JA. A Computer Model of Atrial Fibrillation. *Am Heart J*. 1964;67:200-20.
165. Jalife J, Berenfeld O, Skanes A, Mandapati R. Mechanisms of atrial fibrillation: mother rotors or

multiple daughter wavelets, or both? *J Cardiovasc Electrophysiol*. 1998;9:S2-12.

166. Haissaguerre M, Jais P, Shah DC, Takahashi A, Hocini M, Quiniou G, Garrigue S, Le Mouroux A, Le Metayer P, Clementy J. Spontaneous initiation of atrial fibrillation by ectopic beats originating in the pulmonary veins. *N Engl J Med*. 1998;339:659-66.
167. Hou Y, Scherlag BJ, Lin J, Zhang Y, Lu Z, Truong K, Patterson E, Lazzara R, Jackman WM, Po SS. Ganglionated plexi modulate extrinsic cardiac autonomic nerve input: effects on sinus rate, atrioventricular conduction, refractoriness, and inducibility of atrial fibrillation. *J Am Coll Cardiol*. 2007;50:61-8.
168. Jalife J, Berenfeld O, Mansour M. Mother rotors and fibrillatory conduction: a mechanism of atrial fibrillation. *Cardiovasc Res*. 2002;54:204-16.
169. Shiroshita-Takeshita A, Brundel BJ, Nattel S. Atrial fibrillation: basic mechanisms, remodeling and triggers. *J Interv Card Electrophysiol*. 2005;13:181-93.
170. Chen YJ, Chen SA. Electrophysiology of pulmonary veins. *J Cardiovasc Electrophysiol*. 2006;17:220-4.
171. Everett THt, Olgin JE. Basic mechanisms of atrial fibrillation. *Cardiol Clin*. 2004;22:9-20.
172. Allessie M, Ausma J, Schotten U. Electrical, contractile and structural remodeling during atrial fibrillation. *Cardiovasc Res*. 2002;54:230-46.
173. Dobrev D, Friedrich A, Voigt N, Jost N, Wettwer E, Christ T, Knaut M, Ravens U. The G protein-gated potassium current I(K,ACh) is constitutively active in patients with chronic atrial fibrillation. *Circulation*. 2005;112:3697-706.
174. Everett THt, Wilson EE, Verheule S, Guerra JM, Foreman S, Olgin JE. Structural atrial remodeling alters the substrate and spatiotemporal organization of atrial fibrillation: a comparison in canine models of structural and electrical atrial remodeling. *Am J Physiol Heart Circ Physiol*. 2006;291:H2911-23.
175. Nattel S. New ideas about atrial fibrillation 50 years on. *Nature*. 2002;415:219-26.
176. Calkins H, Brugada J, Packer DL, Cappato R, Chen SA, Crijns HJ, Damiano RJ, Jr., Davies DW, Haines DE, Haissaguerre M, Iesaka Y, Jackman W, Jais P, Kottkamp H, Kuck KH, Lindsay BD, Marchlinski FE, McCarthy PM, Mont JL, Morady F, Nademanee K, Natale A, Pappone C, Prystowsky E, Raviele A, Ruskin JN, Shemin RJ. HRS/EHRA/ECAS expert Consensus Statement on catheter and surgical ablation of atrial fibrillation: recommendations for personnel, policy, procedures and follow-up. A report of the Heart Rhythm Society (HRS) Task Force on catheter and surgical ablation of atrial fibrillation. *Heart Rhythm*. 2007;4:816-61.
177. Wang Y, Rudy Y. Meshless methods in potential inverse electrocardiography. *Conf Proc IEEE Eng Med Biol Soc*. 2006;1:2558-9.
178. Ghosh S, Rudy Y. Application of L1-norm regularization to epicardial potential solution of the inverse electrocardiography problem. *Ann Biomed Eng*. 2009;37:902-12.
179. Ghosh S, Avari JN, Rhee EK, Woodard PK, Rudy Y. Noninvasive electrocardiographic imaging (ECGI) of a univentricular heart with Wolff-Parkinson-White syndrome. *Heart Rhythm*. 2008;5:605-8.
180. Lewis T, Meakins J, White PD. The excitatory process in the dog's heart. Part I: The Auricles. *Phil Trans Roy Soc B*. 1914;205.

181. Puech P, Esclavissat M, Sodi-Pallares D, Cisneros F. Normal auricular activation in the dog's heart. *Am Heart J*. 1954;47:174-91.
182. Allessie MA, Lammers W, Bonte F, Hollen J. In: *Cardiac Electrophysiology and Arrhythhmias.* Orlando, FL:: Grune and Stratton; 1985:265-275.
183. Schuessler RB, Kawamoto T, Hand DE, Mitsuno M, Bromberg BI, Cox JL, Boineau JP. Simultaneous epicardial and endocardial activation sequence mapping in the isolated canine right atrium. *Circulation.* 1993;88:250-63.
184. Kumagai K, Uno K, Khrestian C, Waldo AL. Single site radiofrequency catheter ablation of atrial fibrillation: studies guided by simultaneous multisite mapping in the canine sterile pericarditis model. *J Am Coll Cardiol*. 2000;36:917-23.
185. Sih HJ, Zipes DP, Berbari EJ, Adams DE, Olgin JE. Differences in organization between acute and chronic atrial fibrillation in dogs. *J Am Coll Cardiol*. 2000;36:924-31.
186. Derakhchan K, Li D, Courtemanche M, Smith B, Brouillette J, Page PL, Nattel S. Method for simultaneous epicardial and endocardial mapping of in vivo canine heart: application to atrial conduction properties and arrhythmia mechanisms. *J Cardiovasc Electrophysiol*. 2001;12:548-55.
187. Mansour M, Mandapati R, Berenfeld O, Chen J, Samie FH, Jalife J. Left-to-right gradient of atrial frequencies during acute atrial fibrillation in the isolated sheep heart. *Circulation.* 2001;103:2631-6.
188. Sun H, Velipasaoglu EO, Wu DE, Kopelen HA, Zoghbi WA, Spencer WH, 3rd, Khoury DS. Simultaneous multisite mapping of the right and the left atrial septum in the canine intact beating heart. *Circulation.* 1999;100:312-9.
189. Kumagai K, Khrestian C, Waldo AL. Simultaneous multisite mapping studies during induced atrial fibrillation in the sterile pericarditis model. Insights into the mechanism of its maintenance. *Circulation.* 1997;95:511-21.
190. Kadish A, Hauck J, Pederson B, Beatty G, Gornick C. Mapping of atrial activation with a noncontact, multielectrode catheter in dogs. *Circulation.* 1999;99:1906-13.
191. Cox JL, Canavan TE, Schuessler RB, Cain ME, Lindsay BD, Stone C, Smith PK, Corr PB, Boineau JP. The surgical treatment of atrial fibrillation. II. Intraoperative electrophysiologic mapping and description of the electrophysiologic basis of atrial flutter and atrial fibrillation. *J Thorac Cardiovasc Surg*. 1991;101:406-26.
192. Ferguson TB, Jr., Schuessler RB, Hand DE, Boineau JP, Cox JL. Lessons learned from computerized mapping of the atrium. Surgery for atrial fibrillation and atrial flutter. *J Electrocardiol*. 1993;26 Suppl:210-9.
193. Sahadevan J, Ryu K, Peltz L, Khrestian CM, Stewart RW, Markowitz AH, Waldo AL. Epicardial mapping of chronic atrial fibrillation in patients: preliminary observations. *Circulation*. 2004;110:3293-9.
194. Saksena S, Giorgberidze I, Mehra R, Hill M, Prakash A, Krol RB, Mathew P. Electrophysiology and endocardial mapping of induced atrial fibrillation in patients with spontaneous atrial fibrillation. *Am J Cardiol*. 1999;83:187-93.
195. Schilling RJ, Kadish AH, Peters NS, Goldberger J, Davies DW. Endocardial mapping of atrial fibrillation in the human right atrium using a non-contact catheter. *Eur Heart J*. 2000;21:550-64.

196. Markides V, Schilling RJ, Ho SY, Chow AW, Davies DW, Peters NS. Characterization of left atrial activation in the intact human heart. *Circulation*. 2003;107:733-9.
197. Earley MJ, Abrams DJ, Sporton SC, Schilling RJ. Validation of the noncontact mapping system in the left atrium during permanent atrial fibrillation and sinus rhythm. *J Am Coll Cardiol*. 2006;48:485-91.
198. Takahashi Y, Hocini M, O'Neill MD, Sanders P, Rotter M, Rostock T, Jonsson A, Sacher F, Clementy J, Jais P, Haissaguerre M. Sites of focal atrial activity characterized by endocardial mapping during atrial fibrillation. *J Am Coll Cardiol*. 2006;47:2005-12.
199. De Ponti R, Tritto M, Lanzotti ME, Spadacini G, Marazzi R, Moretti P, Salerno-Uriarte JA. Computerized high-density mapping of the pulmonary veins: new insights into their electrical activation in patients with atrial fibrillation. *Europace*. 2004;6:97-108.
200. Waldo AL. Mechanisms of atrial fibrillation. *J Cardiovasc Electrophysiol*. 2003;14:S267-74.
201. Jalife J. Rotors and spiral waves in atrial fibrillation. *J Cardiovasc Electrophysiol*. 2003;14:776-80.
202. Jalife J. Experimental and clinical AF mechanisms: bridging the divide. *J Interv Card Electrophysiol*. 2003;9:85-92.
203. Spach MS, King TD, Barr RC, Boaz DE, Morrow MN, Herman-Giddens S. Electrical potential distribution surrounding the atria during depolarization and repolarization in the dog. *Circ Res*. 1969;24:857-73.
204. Oster HS, Taccardi B, Lux RL, Ershler PR, Rudy Y. Electrocardiographic imaging: noninvasive localization of pacing sites simulating ectopic foci. *Circulation*. 1994;90:I-437.
205. Kistler PM, Roberts-Thomson KC, Haqqani HM, Fynn SP, Singarayar S, Vohra JK, Morton JB, Sparks PB, Kalman JM. P-wave morphology in focal atrial tachycardia: development of an algorithm to predict the anatomic site of origin. *J Am Coll Cardiol*. 2006;48:1010-7.
206. Fuster V, Ryden LE, Asinger RW, Cannom DS, Crijns HJ, Frye RL, Halperin JL, Kay GN, Klein WW, Levy S, McNamara RL, Prystowsky EN, Wann LS, Wyse DG, Gibbons RJ, Antman EM, Alpert JS, Faxon DP, Gregoratos G, Hiratzka LF, Jacobs AK, Russell RO, Smith SC, Jr., Alonso-Garcia A, Blomstrom-Lundqvist C, de Backer G, Flather M, Hradec J, Oto A, Parkhomenko A, Silber S, Torbicki A. ACC/AHA/ESC Guidelines for the Management of Patients With Atrial Fibrillation: Executive Summary A Report of the American College of Cardiology/American Heart Association Task Force on Practice Guidelines and the European Society of Cardiology Committee for Practice Guidelines and Policy Conferences (Committee to Develop Guidelines for the Management of Patients With Atrial Fibrillation) Developed in Collaboration With the North American Society of Pacing and Electrophysiology. *Circulation*. 2001;104:2118-50.
207. Wang Y, Cuculich PS, Woodard PK, Lindsay BD, Rudy Y. Focal Atrial Tachycardia after Pulmonary Vein Isolation: Noninvasive Mapping with Electrocardiographic Imaging (ECGI). *Heart Rhythm*. 2007;4:1081-1084.
208. Xi Q, Sahakian AV, Swiryn S. The effect of QRS cancellation on atrial fibrillatory wave signal characteristics in the surface electrocardiogram. *J Electrocardiol*. 2003;36:243-9.
209. Langendorf R, Pick A, Winternitz M. Mechanisms of intermittent ventricular bigeminy. I.

Appearance of ectopic beats dependent upon length of the ventricular cycle, the "rule of bigeminy". *Circulation*. 1955;11:422-30.

210. Langendorf R, Pick A. Mechanisms of intermittent ventricular bigeminy. II. Parasystole, and parasystole or re-entry with conduction disturbance. *Circulation*. 1955;11:431-9.

Vita

Yong Wang was born in Shangqiu, Henan, P.R. China. He received the degree of Bachelor of Engineering and Master of Science from Xi'an Jiaotong University in July 1999 and July 2002, respectively. He got his first two years' PhD training from July 2002 to July 2004 at Department of Biomedical Engineering at Case Western Reserve University under the guidance of Professor Yoram Rudy. He transferred to Washington University in Saint Louis in July 2004 together with his advisor, Professor Yoram Rudy. From July 2004 to May 2009, he was a graduate student and candidate for Ph.D. at Department of Biomedical Engineering at Washington University in Saint Louis.

Publications

Peer-Reviewed Journals

1. **Y. Wang**, Y. Rudy, "Application of the Method of Fundamental Solutions to Potential-based Inverse Electrocardiography". Ann Biomed Eng, 34: 1272-1288, 2006 (Featured paper as Journal Cover Story)
2. **Y. Wang**, P.S. Cuculich, P.K. Woodard, B.D. Lindsay, Y. Rudy, "Focal Atrial Tachycardia after Pulmonary Vein Isolation: Noninvasive Mapping with Electrocardiographic Imaging (ECGI)", Heart Rhythm Journal 2007; 4:1081-1084.
3. **Y. Wang**, R.B. Schuessler, R.J. Damiano, P.K. Woodard, Y. Rudy, "Noninvasive Electrocardiographic Imaging (ECGI) of Scar-Related Atypical Atrial Flutter", Heart Rhythm Journal 2007; 12:1565-1567
4. **Y. Wang**, L. Li, P.S. Cuculich, Y. Rudy, "Electrocardiographic Imaging of Ventricular Bigeminy in a Human Subject", Circulation: Arrhythmia and Electrophysiology, 2008; 1: 74-75
5. **Y. Wang**, Y. Rudy "Electrocardiographic Imaging (ECGI) of Normal Human Atrial Repolarization", Heart Rhythm Journal 2009; 6:582-583.
6. **Y. Wang**, P.S. Cuculich, L. Li, P.K. Woodard, M. N. Faddis, Y. Rudy "Characterization of EP substrate in Post-Myocardial Infarction Patients using Noninvasive Electrocardiographic Imaging (ECGI)" (In preparation)
7. **Y. Wang**, P.S. Cuculich, L. Li, B.D. Lindsay, Y. Rudy "Insights from Noninvasive Electrocardiographic Imaging (ECGI) of Ventricular Arrhythmias in Patients Undergoing Catheter Ablation" (In preparation)

8. P.S. Cuculich, **Y. Wang**, , L. Li, B.D. Lindsay, M. N. Faddis, R.B. Schuessler, R.J. Damiano, Y. Rudy “Characterization of Epicardial Activation in Humans with Diverse AF Patterns using Noninvasive ECG imaging (ECGI**)” (co-first author with P.S. Cuculich)** (In preparation)
9. **Y. Wang**, Y. Rudy “Real Time Electrocardiographic Imaging” (In preparation)

Book Chapter

1. Y. Rudy, **Y. Wang,** P. S. Cuculich, “Noninvasive Electrocardiographic Imaging (ECGI): Examples of Clinical Applications” In: Cardiac Electrophysiology: From Cell to Bedside, 5th edition, Elsevier Science Publisher, 2007 (In press)

Abstracts

1. **Y. Wang**, Y. Rudy, "Meshless Methods in Potential Inverse Electrocardiography". 28 IEEE EMBS Annual International Conference Proceeding , 2006 (Invited Talk)
2. **Y. Wang**, S. Ghosh, L. El-Esber, P. Cuculich, B.D. Lindsay, R.B. Schuessler, R.J. Damiano, P.K. Woodard, Y. Rudy “Noninvasive Electrocardiographic Imaging (ECGI) of Atrial Arrhythmias in Patients”, Gordon Research Conference on Cardiac Arrhythmia Mechanisms, Ventura Beach, California, March 18 – 23, 2007.
3. **Y. Wang,** P.S. Cuculich, P.K. Woodard, M.N. Faddis, Y. Rudy “Electrocardiographic Imaging (ECGI): Noninvasive Characterization of Electrophysiological (EP) Substrate in Post Myocardial Infarction (post-MI) Patients” Heart Rhythm Society's 29th Annual Scientific Sessions, San Francisco, California, May 14-17, 2008
4. **Y. Wang,** P.S. Cuculich, L.Li, J. Chen, M.N. Faddis, B.D.Lindsay, T.W. Smith, Y. Rudy , “Insights from Noninvasive Electrocardiographic Imaging (ECGI) of Ventricular Arrhythmias in Patients Undergoing Catheter Ablation” Heart Rhythm Society's 30th Annual Scientific Sessions, Boston, 2009

Patents and Inventions

1. **Y. Wang**, Y. Rudy, "System and Method for Meshless Noninvasive Electrocardiographic Imaging (ECGI)". USA Patent. Pending Serial No. PCT/US2006/28287 (Europe Coverage)
2. **Y. Wang**, Y. Rudy, “System and Method for On-Site and Real-Time Electrocardiographic Imaging (ECGI)”. USA Patent. Serial No. 61/087,875
3. **Y. Wang**, Y. Rudy, “System and Method for Noninvasive Endocardial Electrocardiographic Imaging (ECGI)”. Patent disclosure filed with Washington University in St. Louis, 2006.